Study of photoelectrodes with III-V epitaxial thin-films on Si substrate for photoelectrochemical water splitting

Mekan Piriyev

DOCTORAT MATIERE BRETAGNE MOLECULES LOIRE ET MATERIAUX

INSA RENNES

THESE DE DOCTORAT DE

L'INSTITUT NATIONAL DES SCIENCES APPLIQUEES RENNES

ECOLE DOCTORALE N° 596
Matière, Molécules, Matériaux
Spécialité : *Sciences des Matériaux*

Par

Mekan PIRIYEV

Study of photoelectrodes with III-V epitaxial thin-films on Si substrate for photoelectrochemical water splitting

Thèse présentée et soutenue à Rennes, le 15/12/2022
Unité de recherche : Institut FOTON (UMR 6082 / CNRS)
Thèse N° : 22ISAR 40 / D22 - 40

Rapporteurs avant soutenance :

Yamina ANDRE MCF (HDR), Institut Pascal, Université Clermont Auvergne
José PENUELAS MCF (HDR), Institut des Nanotechnologies de Lyon, École Centrale de Lyon

Composition du Jury :

Président :	Bruno FABRE	DR CNRS, ISCR, Université Rennes 1
Examinateurs :	Yamina ANDRE	MCF (HDR), Institut Pascal, Université Clermont Auvergne
	José PENUELAS	MCF (HDR), Institut des Nanotechnologies de Lyon, École Centrale de Lyon
	Murielle CHAVAROT -KERLIDOU	DR CNRS, LCBM, Université Grenoble Alpes
Dir. de thèse :	Charles CORNET	PR, Institut FOTON, INSA Rennes
Co-dir. de thèse :	Nicolas BERTRU	PR, Institut FOTON, INSA Rennes

DOCTORAT MATIERE BRETAGNE MOLECULES LOIRE ET MATERIAUX

INSA RENNES

Intitulé de la thèse:

Study of photoelectrodes with III-V epitaxial thin-films on Si substrate for photoelectrochemical water splitting

Mekan PIRIYEV

Résumé

Avec une densité énergétique élevée et de faibles émissions de carbone pendant son utilisation, l'hydrogène (H_2) est un combustible très prometteur pour réduire la dépendance énergétique mondiale aux énergies fossiles. Cependant, la production mondiale actuelle de H_2 est d'environ 50 millions de tonnes par an, avec plus de 95 % de cette production provenant de l'industrie des combustibles fossiles, principalement via le procédé de reformage du méthane, en raison de son faible coût (~2 €/kg H_2). [1] Ce procédé est associé à d'énormes émissions de carbone : pour 1 tonne d'H_2 produite via le reformage du méthane, 2,5 tonnes de CO_2 sont émises. [1,2]

Une méthode alternative est l'électrolyse, qui peut être considérée comme plus durable si l'apport d'énergie provient de sources renouvelables (énergie éolienne, hydraulique ou solaire). [2] Néanmoins, le coût du H_2 produit par électrolyse est relativement plus élevé en raison de l'utilisation de matériaux précieux et de la faible efficacité de conversion de l'électricité renouvelable en H_2. Par conséquent, la production renouvelable de H_2 à un coût plus abordable est un défi de grande importance pour rendre la technologie H_2 d'intérêt pratique. Dans ce contexte, les cellules photoélectrochimiques (PEC) sont apparues comme l'un des dispositifs prometteurs pour produire du H_2 vert, dans lesquels des photo-électrodes semi-conductrices sont utilisées pour convertir l'énergie solaire en énergie chimique sous la forme de molécules H_2 en dissociant l'eau.

Les propriétés physico-chimiques intrinsèques et les procédés de fabrication des photo-électrodes semi-conductrices sont des paramètres cruciaux pour que le dispositif PEC garantisse à la fois une efficacité solaire-hydrogène (STH) la plus élevée possible et un coût de production de H_2 le plus bas. [3–5] Les photo-électrodes semi-conductrices III-V possèdent de nombreux avantages pour cette technologie en raison de leurs excellentes propriétés optiques. Malgré des efficacités de conversion solaire-hydrogène très prometteuses déjà démontrées, le développement de photo-électrodes III-V fait face à des coûts élevés de fabrication, du fait du prix des substrats binaires III-V. Pour cela, le développement de couches minces à base de semi-conducteurs III-V sur des substrats bas coûts (par exemple le silicium) peut être considéré comme une stratégie de réduction des coûts. [6–9] De plus, l'utilisation de semi-conducteurs III-V épitaxiés offre théoriquement

un fort avantage en termes de flexibilité, car la bande interdite et la structure de bande de ces matériaux peuvent être ajustées à volonté grâce à l'association de différents semi-conducteurs III-V binaires (tels que InP, InAs, GaAs, GaP, GaSb, GaN, etc.) pour former des alliages ternaires ou quaternaires, avec un excellent contrôle de leur composition. [10]

L'objectif principal de ma thèse était de clarifier et d'améliorer les propriétés photoélectrochimiques (PEC) de photoanodes constituées de couches minces III-V sur substrats Si, en profitant de la forte collaboration entre l'Institut FOTON (élaboration des matériaux, propriétés structurales et optoélectroniques des semi-conducteurs) et l'Institut des Sciences Chimiques de Rennes-ISCR (photoélectrochimie et catalyse). La thèse est structurée en 5 chapitres :

Le chapitre 1 présente le contexte de recherche de la technologie de dissociation de l'eau en utilisant l'énergie solaire au sein de cellules PEC. Le concept de stockage d'énergie solaire sous forme de H_2 et le principe de fonctionnement de la dissociation solaire de l'eau dans une cellule PEC sont d'abord rappelés (**Figure I**). L'accent est mis sur les photo-électrodes semi-conductrices, avec une introduction à la physique des semi-conducteurs, aux interfaces métal/semi-conducteur et semi-conducteur/électrolyte. Sur cette base, les exigences en termes de matériaux pour le développement des cellules PEC en sont déduites. Enfin, une attention particulière est accordée à l'état de l'art et aux défis actuels dans le domaine des photo-électrodes à base de matériaux III-V et III-V/Si.

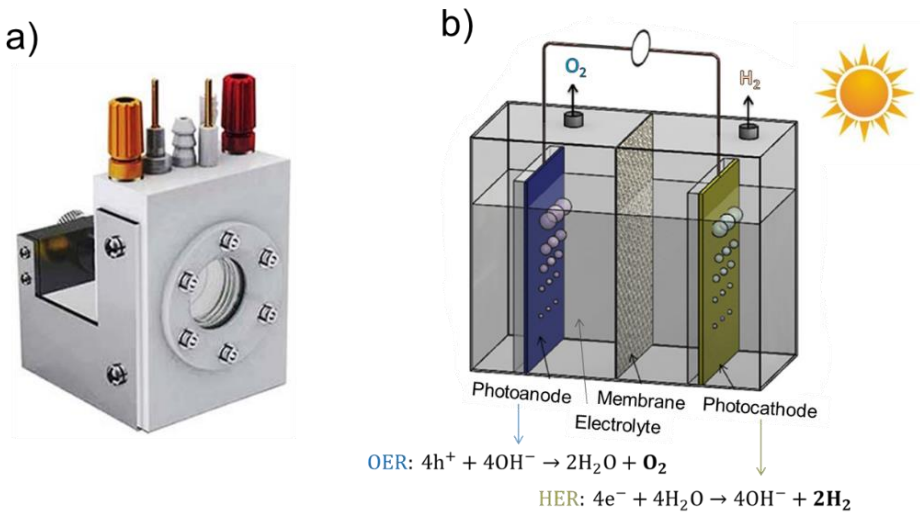

Figure I (a) Dispositif PEC à l'échelle du laboratoire utilisé pour la caractérisation des photo-électrodes, (b) Schéma de fonctionnement d'un dispositif PEC utilisé pour la production de H_2 et O_2 par dissociation de l'eau avec l'énergie solaire

Le chapitre 2 propose une description de l'élaboration et des caractérisations physico-chimiques des couches minces et des photo-électrodes de III-V/Si étudiées dans cette thèse. La croissance épitaxiale des couches minces III-V, les techniques de préparation des photo-électrodes et les méthodes de traitement de surface sont expliquées. Des techniques expérimentales comprenant des caractérisations structurales, optiques et photo-électrochimiques sont décrites avec les principes de fonctionnement et les paramètres utilisés correspondant. Les processus en jeu lors de la dissociation de l'eau sont détaillés, et une description du fonctionnement de la cellule photo-électrochimique est proposée.

Dans le **chapitre 3**, nous étudions les performances photoélectrochimiques (PEC) de photoanodes constituées d'une couche épitaxiale de GaAs (1 µm d'épaisseur) déposée sur un substrat de Si de type n et comparons ses performances à celles de photoanodes faites à partir de substrats GaAs commerciaux. L'étude structurale des échantillons GaAs/Si et du substrat commercial GaAs de référence est proposée avec la caractérisation par diffraction des rayons X (DRX) montré dans la **Figure II (a)**. Les caractérisations optiques et photoélectrochimiques ont ensuite été réalisées, montrant une densité de photo-courant étonnamment élevée de la photoanode épitaxiale GaAs/Si équivalente à celle mesurée pour la photoanode constituée du substrat GaAs commercial **Figure II (b)**.

L'origine de la haute densité de photo-courant est ensuite discutée, avec une analyse approfondie de l'efficacité de conversion photon-courant (IPCE) et de la densité de photo-courant mesurée sous éclairage monochromatique et accordable. La densité de photo-courant mesurée expérimentalement est ensuite analysée par rapport à celle calculée théoriquement en utilisant le coefficient d'absorption de l'échantillon et la densité spectrale du flux de photons du spectre solaire AM 1.5G. La contribution spectrale du substrat de Si est mise en évidence pour expliquer le photo-courant important mesuré pour la photo-anode GaAs/Si.

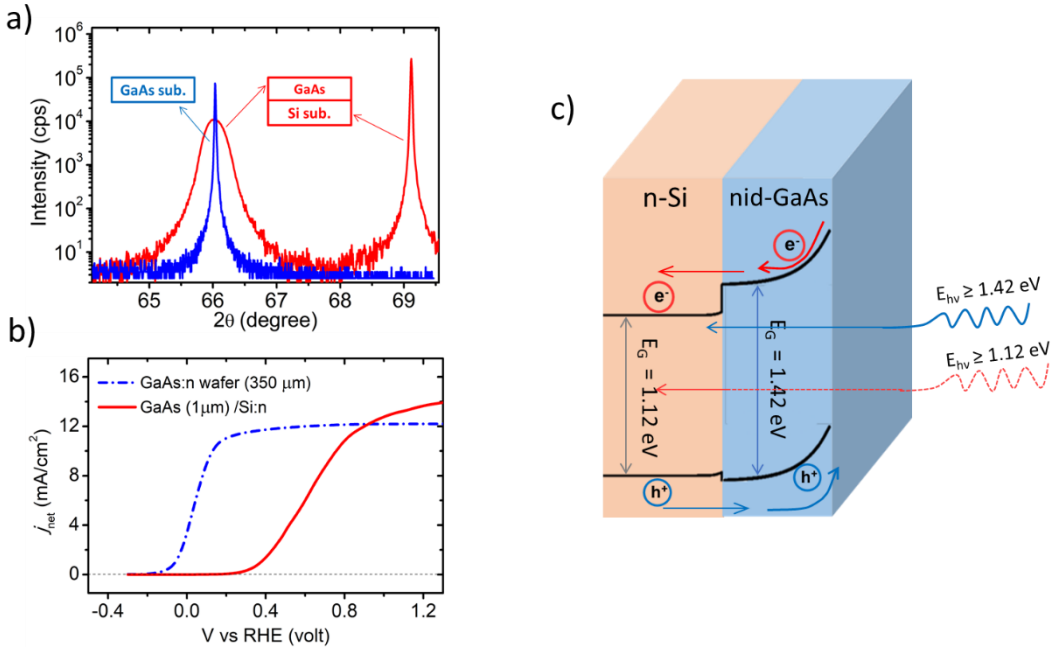

Figure II (a) Caractérisation par DRX de l'échantillon épitaxial GaAs (1 µm)/Si:n et du substrat GaAs:n (350 µm); (b) densité de photo-courant nette en fonction de la tension sous un éclairage à 1 soleil (100 mW/cm²); (c) illustration des niveaux d'énergie de la bande semi-conductrice pour la couche épitaxiale de GaAs sur substrat Si de type n, toutes deux en tant que couches photoactives

Dans le **chapitre 4**, nous étudions le concept d'ingénierie de bande avec des alliages $GaP_{1-x}As_x$ épitaxiés sur substrat Si et démontrons comment les propriétés optiques et photoélectrochimiques sont profondément impactées par les différentes natures de bande interdite et alignements de bandes en fonction de la composition de l'alliage (**Figure III)** L'amélioration des propriétés d'absorption optique est mise en évidence par une absorption efficace de la lumière dans la région visible du spectre solaire

et, par la suite, par l'augmentation de l'efficacité quantique résultant en une densité de photo-courant élevée pour les échantillons à bande interdite directe. La variation des alignements de bandes entre la photo-anode et l'électrolyte est étudiée plus en détail avec des mesures du potentiel en bande plate (V_{fb}) via des caractérisations de Mott-Schottky et affecte le potentiel d'apparition (V_{onset}) des photoanodes conçues. Ces observations confirment qu'il est possible d'utiliser l'ingénierie de bande avec les matériaux III-V pour adapter et contrôler très finement les propriétés photo-électro-chimiques des photo-électrodes.

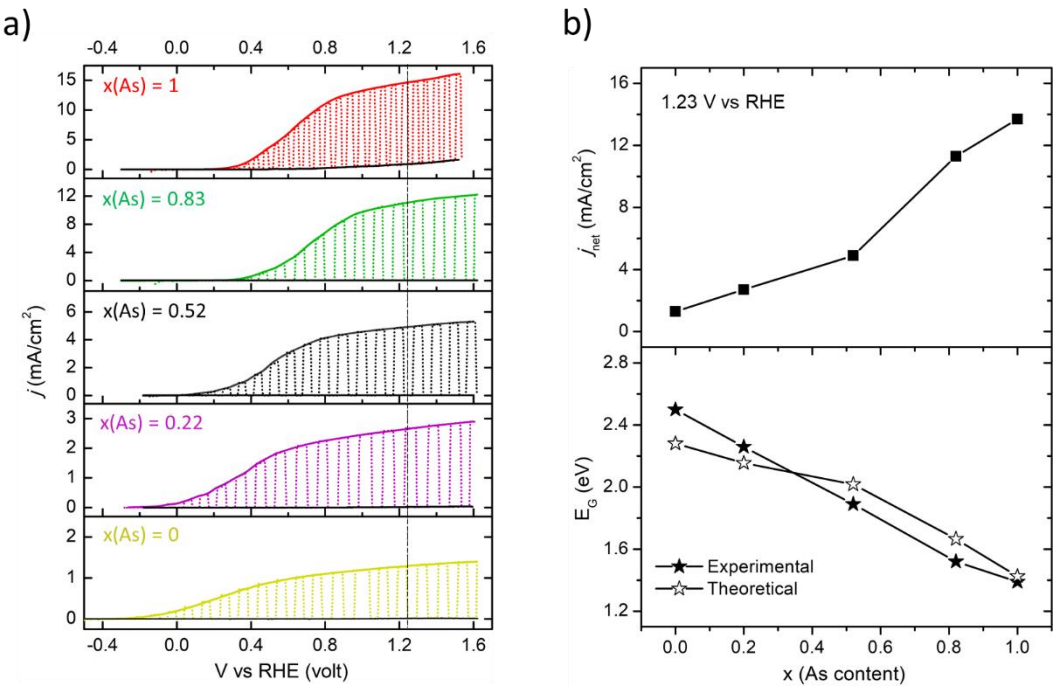

Figure III (a) Évaluation du photo-courant en fonction de la tension (j-V) pour les couches minces épitaxiales de 1 µm d'épaisseur d'alliages $GaP_{1-x}As_x$ épitaxiées sur Si avec les différentes compositions x(As) données en insert. Le potentiel d'oxydation de l'eau (1,23 V vs RHE) est marqué par une ligne pointillée noire; (b) évolution de la densité nette de photo-courant (j_{net}) à 1,23 V et de la bande interdite (E_G) en fonction de x(As) de l'alliage $GaP_{1-x}As_x$

Enfin, des résultats préliminaires concernant des tentatives de protection contre la corrosion des photo-anodes réalisées à partir de GaAs/Si épitaxial et du substrat GaAs commercial sont présentées dans le **chapitre 5**. Deux types de protections de surface ont été étudiées : 1) dépôt d'iridium métallique et de nickel par la technique de pulvérisation et 2) dépôt de couche atomique de TiO_2 par ALD. La mesure de la densité de photo-courant avec plusieurs balayages consécutifs et des mesures de stabilité ont été effectuées

pour évaluer la stabilité des photo-électrodes dans des électrolytes acides et alcalins. Les photo-anodes ont été étudiées plus en détail par microscopie optique, microscopie électronique à balayage et spectroscopie de rayons X à dispersion d'énergie pour étudier les changements de surface après les tests de stabilité (**Figure IV**) Même si une stabilisation efficace n'est pas démontrée ici, ces résultats donnent des premiers éléments de compréhension des mécanismes de corrosion en jeu dans ces photo-électrodes.

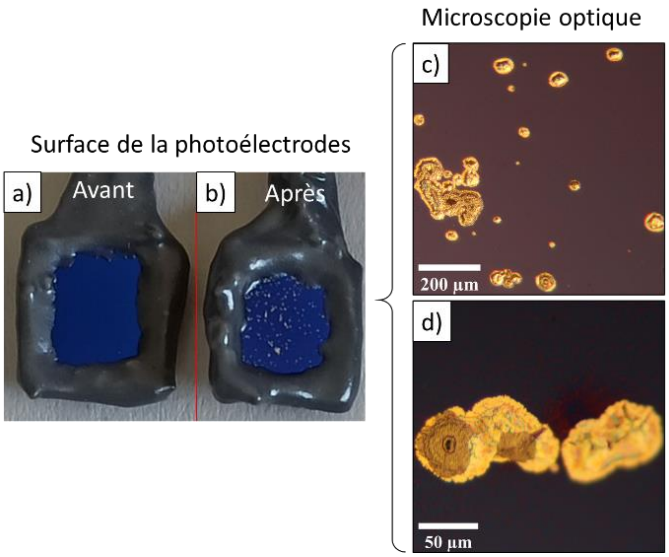

Figure IV La surface de la photo-électrode (a) avant et (b) après plusieurs minutes de caractérisation PEC. Images de microscopie optique à l'échelle de (c) 200 µm et (d) 50 µm

En conclusion, l'étude de photo-anodes à couches minces épitaxiales à base de semi-conducteurs III-V épitaxiés sur substrat silicium a été menée dans cette thèse en collaboration avec l'ISCR en étudiant leurs propriétés optiques, structurales et photoélectrochimiques et en les comparant avec photo-électrodes réalisées à partir de substrats commerciaux à coût élevé. Il est tout d'abord montré que les photo-électrodes III-V/Si peuvent atteindre des performances remarquables, comparables à celles de photo-électrodes faites à partir des substrats III-V natifs. Il est également montré expérimentalement que le concept « d'ingénierie des bandes » peut être utilisé pour la photo-électrochimie, pour contrôler les propriétés optiques et photoélectrochimiques et améliorer le fonctionnement des cellules photo-électrochimiques.

References

[1] T.J. Jacobsson, V. Fjällström, M. Edoff, T. Edvinsson, Sustainable solar hydrogen production: from photoelectrochemical cells to PV-electrolyzers and back again, Energy Environ. Sci. 7 (2014) 2056–2070. https://doi.org/10.1039/C4EE00754A.

[2] T. Abbasi, S.A. Abbasi, 'Renewable' hydrogen: Prospects and challenges, Renewable and Sustainable Energy Reviews. 15 (2011) 3034–3040. https://doi.org/10.1016/j.rser.2011.02.026.

[3] J. Tournet, Y. Lee, S.K. Karuturi, H.H. Tan, C. Jagadish, III–V Semiconductor Materials for Solar Hydrogen Production: Status and Prospects, ACS Energy Lett. 5 (2020) 611–622. https://doi.org/10.1021/acsenergylett.9b02582.

[4] M.R. Shaner, H.A. Atwater, N.S. Lewis, E.W. McFarland, A comparative technoeconomic analysis of renewable hydrogen production using solar energy, Energy Environ. Sci. 9 (2016) 2354–2371. https://doi.org/10.1039/C5EE02573G.

[5] J.H. Kim, D. Hansora, P. Sharma, J.-W. Jang, J.S. Lee, Toward practical solar hydrogen production – an artificial photosynthetic leaf-to-farm challenge, Chem. Soc. Rev. 48 (2019) 1908–1971. https://doi.org/10.1039/C8CS00699G.

[6] M. Alqahtani, S. Sathasivam, L. Chen, P. Jurczak, R. Piron, C. Levallois, A. Létoublon, Y. Léger, S. Boyer-Richard, N. Bertru, J.-M. Jancu, C. Cornet, J. Wu, I.P. Parkin, Photoelectrochemical water oxidation of GaP1−xSbx with a direct band gap of 1.65 eV for full spectrum solar energy harvesting, Sustainable Energy Fuels. 3 (2019) 1720–1729. https://doi.org/10.1039/C9SE00113A.

[7] L. Chen, M. Alqahtani, C. Levallois, A. Létoublon, J. Stervinou, R. Piron, S. Boyer-Richard, J.-M. Jancu, T. Rohel, R. Bernard, Y. Léger, N. Bertru, J. Wu, I.P. Parkin, C. Cornet, Assessment of GaPSb/Si tandem material association properties for photoelectrochemical cells, Solar Energy Materials and Solar Cells. 221 (2021) 110888. https://doi.org/10.1016/j.solmat.2020.110888.

[8] P. Kumar, P. Devi, R. Jain, S.M. Shivaprasad, R.K. Sinha, G. Zhou, R. Nötzel, Quantum dot activated indium gallium nitride on silicon as photoanode for solar hydrogen generation, Commun Chem. 2 (2019) 1–7. https://doi.org/10.1038/s42004-018-0105-0.

[9] L. Chen, Y. Léger, G. Loget, M. Piriyev, I. Jadli, S. Tricot, T. Rohel, R. Bernard, A. Beck, J. Le Pouliquen, P. Turban, P. Schieffer, C. Levallois, B. Fabre, L. Pedesseau, J. Even, N. Bertru, C. Cornet, Epitaxial III–V/Si Vertical Heterostructures with Hybrid 2D-Semimetal/Semiconductor Ambipolar and Photoactive Properties, Advanced Science. 9 (2022) 2101661. https://doi.org/10.1002/advs.202101661.

[10] I. Vurgaftman, J.R. Meyer, L.R. Ram-Mohan, Band parameters for III-V compound semiconductors and their alloys, Journal of Applied Physics. 89 (2001) 5815–5875. https://doi.org/10.1063/1.1368156.

Acknowledgements

In the first place, I would like to express my sincere gratitude to my supervisors Prof. Charles Cornet and Prof. Nicolas Bertru for the opportunity and inspiration they gave me to work on the subject that I am passionate. Their continuous guidance and support helped me to adapt fast and created in me curiosity for the research. I am truly thankful that my ideas were appreciated and welcomed. I am especially thankful for the techniques you taught me in scientific paper writing and presentation making.

I especially thank Dr. Yoan Léger for fruitful discussions and scientific explanations in semiconductor physics. In addition, I express my gratitude to all employees of FOTON Institute, especially, Dr. Christophe Levallois, Dr. Antoine Létoublon, Karine Tavernier, Julie.Le-Pouliquen, Julien.Lapeyre, Alex.Naim and Victor Fong for the instructions in experimental manipulation and warm-friendly work atmosphere. I would like to thank CMI Rennes and administrative staff of INSA Rennes (Justine.Gromaire) for their assistance in paperwork.

I express my appreciation to our collaborators Dr. Gabriel Loget (ISCR), Dr. Bruno Fabre (ISCR), Dr. Lionel Santinacci (CINaM) for their continuous support in scientific experiments and valuable discussions. I thank the reviewers and jury members for their efforts to further improve the thesis.

I acknowledge all PhD students (friends) I worked with during my PhD journey, especially, Dr. Lipin Chen, Hanh Vi Lê, Yiran Zhao, Joudi Dabboussi, Flora Zerbo, Ashanti Bergonzoni, Fan Fei and Eugène Bertin.

Lastly, but most importantly I thank my family for their constant support and endless love that was the main source of my motivation. I express my appreciation to Raimbault family, but mostly Lucinne for warm hospitality and shared good moments.

Thanks to everyone! (My apologies if I forgot you)

List of abbrevations

AFM	-	Atomic force microscopy	nid	-	Non-intentionally doped
ALD	-	Atomic layer deposition	OCP	-	Open-circuit potential
APB	-	Anti phase boundary	OER	-	Oxygen evolution reaction
BB	-	Band bending	PA	-	Photoanode
CA	-	Chronoamperometry	PEC	-	Photo-electrochemical cell
CBM	-	Conduction band minimum	PV	-	Photo-voltaic
CE	-	Counter electrode	QE	-	Quantum efficiency
CMP	-	Chemically mechanically polished	RE	-	Reference electrode
EDX	-	Energy-dispersive X-ray spectroscopy	RHE	-	Reversible hydrogen electrode
fb	-	Flat-band	RSM	-	Reciprocal space mapping
GB	-	Gartner Butler	SC	-	Semi-conductor
HER	-	Hydrogen evolution reaction	SCE	-	Saturated calomel electrode
IB	-	Integral breadth	SEM	-	Scanning electron microscopy
IPCE	-	Incident photon-to-current efficiency	SF	-	Stacking-fault
LSV	-	Linear sweep voltammetry	SRR	-	Strain Relaxation Rate
MBE	-	Molecular beam epitaxy	STH	-	Solar-to-hydrogen efficiency
MOCVD	-	Metalorganic chemical vapor deposition	SWS	-	Solar water splitting
MS	-	Mott Schottky	VBM	-	Valence band maximum
MT	-	Micro-twin	WE	-	Working electrode
NHE	-	Normal hydrogen electrode	XRD	-	X-ray diffraction

Contents

General introduction

Thanks to a high energy density and possible carbon free production and use, hydrogen (H_2) holds great promises to reduce global energy dependence on fossil fuels. Presently, the world H_2 production rate is ~ 50 millions of tons per year with more than 95% of this production being dependent on fossil fuel industry, mainly via steam methane reforming process, because of its low cost (~2 $/kg H_2). [1] However, this production process is associated to tremendous carbon emissions: for 1 ton of H_2 produced via steam methane reforming, 2.5 tons of CO_2 are released. [1,2] An alternative method is electrolysis, which can be considered as more sustainable if the energy input originates from the renewable sources (wind, hydro or solar energy). [2] Nevertheless, the cost of H_2 produced via electrolysis is relatively higher due the use of high-cost materials and modest conversion efficiency of renewable electricity to H_2 fuel. [3] Therefore, the renewable production of H_2 at a more affordable cost is a challenge of high importance to make the H_2 technology of practical interest. In this context, photoelectrochemical (PEC) cells have emerged as one of the promising devices to produce green H_2 via solar water-splitting, in which semiconductor photoelectrodes are used to perform the cathodic hydrogen evolution reaction (HER) and the anodic oxygen evolution reaction (OER) from the two most abundant resources: the sun and the water. [4,5] Despite the various recent research achievements in PEC water splitting technology, some issues still remain to be solved. Especially, the overall solar-to-hydrogen (STH) efficiency still needs to be improved [6] and the lifetime of known state-of-the-art photoelectrodes needs to be further increased. [7–9] Thus, the quest of a robust (long lifetime) and autonomous (working without applied bias) PEC cell having a high efficiency (STH >10%), with a cost-efficient approach motivated many researches in the past 10 years.

Semiconductor photoelectrodes are at the core of this technology. Therefore, their intrinsic physio-chemical properties and fabrication processes are crucial for the PEC device to guarantee both, the highest possible STH efficiency and the lowest H_2 production cost. [10,11] III-V semiconductor photoelectrodes are one of the obvious candidates for PEC water splitting materials, as record efficiencies were already obtained in the closely related fields of photovoltaic solar cells, photonic sensors and lasers, due to

their excellent optical properties. [12,13] Despite the very promising solar-to-hydrogen efficiencies demonstrated, the development of III-V photoelectrodes occurs at the expense of high substrate and fabrication cost when only expensive III-V binary substrates are used. [14] Nevertheless, the development of III-V thin films on earth-abundant substrates (i.e. silicon) is frequently considered as a cost reducing strategy. [15,16] First experimental demonstrations were given in 2019 by our research team at Institut FOTON and the group of Pr. Nötzel (South China Normal University). [17–19] In addition, the use of epitaxial III-V semiconductors provides theoretically a strong advantage in terms of flexibility, as the bandgap and band structure of these materials can be tuned at will through alloying of the different binary III-V semiconductors (such as InP, InAs, GaAs, GaP, GaSb, GaN, etc..) to form a ternary or a quaternary alloy and controlling the alloy's composition.

The main objective of my thesis was to clarify and improve the photo-electrochemical properties of photoanodes made of III-V thin films on Si substrates, taking advantage of the strong collaboration between Institut FOTON (materials elaboration, structural and optoelectronic properties of semiconductors) and Institut des Sciences Chimiques de Rennes-ISCR (photo-electrochemistry and catalysis). The thesis first assesses the performances of GaAs/Si epitaxial photoanodes, as compared to expensive GaAs ones. It then demonstrates how the concept of band engineering can be successfully applied to photo-electrochemistry, and how it affects the band lineups between the photoelectrode and the electrolyte. Preliminary studies on the development of protective layers are finally presented.

Thesis overview:

Chapter 1 introduces the research background of solar water splitting technology with PEC cells. The concept of solar energy storage in the form of H_2 and working principle of solar water splitting in a PEC cell is given shortly at the beginning. A focus is given on semiconductor photoelectrodes, with an introduction to semiconductor physics, metal/semiconductor and semiconductor/electrolyte interfaces. On this basis, material requirements for PEC development are inferred. Finally, a particular attention is given to

the current progresses and challenges of the state-of-the-art III-V and III-V/Si photoelectrodes development.

Chapter 2 gives the detailed description of the elaboration and physico-chemical characterizations of the III-V/Si thin-films and photoelectrodes studied in this thesis. The epitaxial growth of III-V thin films, photoelectrode preparation techniques, surface processing methods are explained. Experimental techniques including, structural, optical and photoelectrochemical characterizations are described with working principles and used parameters. Technical aspects of water splitting with energy requirements and detailed description of photoelectrochemical cell/setup is introduced.

Chapter 3 focuses on the in-depth comparison of photoelectrochemical (PEC) performances of the photoanodes made of a 1-μm thick epitaxial GaAs grown on n-type Si substrate and a commercial GaAs wafer. The structural investigation of the epitaxial GaAs/Si sample is first carried out and compared to the reference GaAs commercial wafer with X-ray diffraction (XRD) characterization. The optical and photoelectrochemical characterizations were then carried out, showing a surprisingly high photocurrent density of the epitaxial GaAs/Si photoanode equivalent to the photoanode made of the commercial GaAs wafer. The origin of the high photocurrent density is then discussed, with regards to Si substrate light absorption and photocurrent contribution by an in-depth analysis of the incident photon-to-current conversion efficiency (IPCE) and photocurrent density under tunable monochromatic light illumination. Experimentally measured photocurrent density is further analyzed relatively to the theoretically calculated one using the absorption coefficient of the sample and spectral photon flux density of the solar spectrum AM 1.5G.

Chapter 4 focuses on the possibility to use the concept of band engineering with $GaP_{1-x}As_x$ and demonstrates how the optical and photoelectrochemical properties are deeply impacted by different bandgap nature and band-lineups depending on the alloy's composition. The enhancement of optical absorption properties is evidenced with efficient light absorption in the visible region of solar spectrum and subsequently, in the increasing of quantum efficiency resulting in a high photocurrent density for direct bandgap configuration samples. The variation of band lineups between the photoanode

and the electrode was further investigated with flat-band (V_{fb}) measurements via Mott-Schottky characterizations and found to affect the onset potential of bandgap engineered photoanodes which is crucial as it describes the input energy in PEC water splitting.

Chapter 5 proposes a first investigation on the corrosion of bare and surface protected photoanodes made of the epitaxially grown GaAs and the commercial GaAs wafer. The two different surface protections were investigated: 1) by deposition of metallic iridium and nickel by sputtering technique, 2) atomic layer deposition of TiO_2. Photocurrent density with several consecutive scans and stability measurements were carried out to assess the stability in acid and alkaline electrolyte. The photoanodes were further studied with optical microscopy, scanning electron microscopy and energy-dispersive x-ray spectroscopy to investigate the surface changes after stability tests.

Chapter 1

III-V/Si photoelectrodes: motivations and issue

Chapter 1. III-V/Si photoelectrodes: motivations and issues

1.1 Green energy storage through hydrogen

Sustainable green energy technologies have become more crucial than ever to achieve carbon neutrality and reduce our negative impacts on the environment. Until now, the amount of CO_2 released in the atmosphere associated to human activity is tremendously high (~34 Gigatonnes in 2021) and it still has to be reduced drastically to stay below an increasing by 1.5ºC of the earth surface temperature. [20] Driven by the consequences of global warming, most of the countries as well as world leading industrial companies have targeted to reduce CO_2 and greenhouse gas emissions. While these targets imply a massive reduction of energy consumption worldwide, the large-scale implementation of carbon-free, sustainable and renewable energies (e.g., wind, hydroelectric, solar) and the improvement of their conversion efficiency is also highly required to help mitigating the detrimental influence of fossil fuels energy scarcity on our everyday life in the upcoming years. The main drawback associated to the use of some renewable energies is the lack of regularity due to intermittency of available sources (e.g. wind, solar energy), which naturally questions our ability to store this energy in a clean and sustainable way. [21]

Amongst the renewable energy sources, solar energy is the most abundant, but was only poorly exploited in the previous century. Solar energy is a decentralized and inexhaustible natural resource, with a magnitude of the available solar power striking the earth's surface of 173 000 TW, meaning that in 1 hour it provides an energy equivalent to the 1-year world energy consumption. From years 2010, the situation changed and the solar energy harvesters started to contribute significantly to the global electricity production (**Figure 1. 1**). Today, around 4% (850 TWh-1000 TWh) of the yearly global electricity production originates from solar energy. [20]

To convert solar energy into usable energy, the most advanced technology uses photovoltaic (PV) solar modules, which efficiencies, robustness, payback period and energy payback time have been significantly improved in the last past years. With this approach, however, the intermittent electricity produced is stored through electro-

chemical storage in batteries (e.g. Lithium-ion batteries), with challenging issues of lifetimes, toxicity, capacity, cost, recycling and materials earth abundancy.

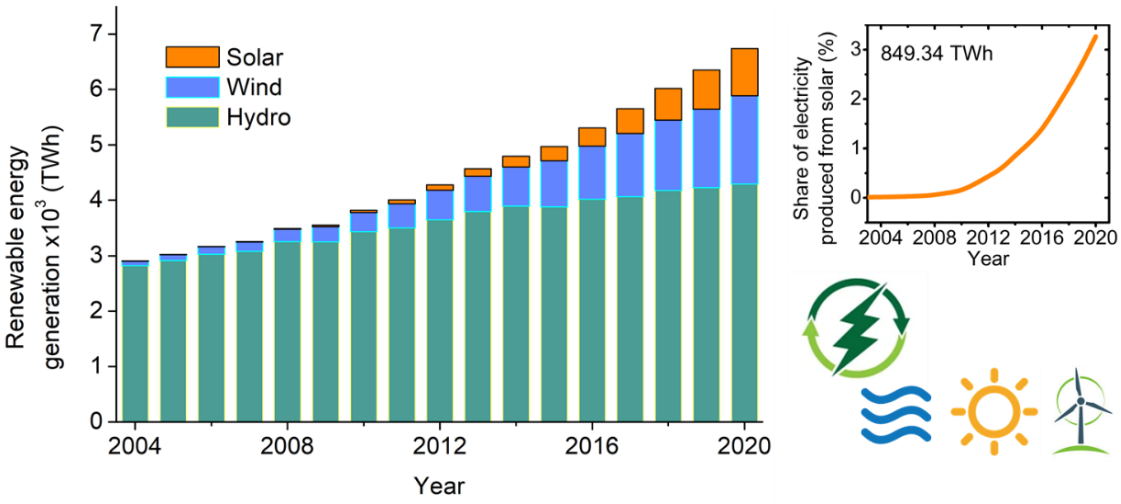

Figure 1. 1 Growing tendency of the renewable energy generation. Adapted from [22]

Electrochemical energy storage is based on forming chemical bonds using the available energy at a given time. When the supply is cut, the chemical bonds that were made are cleaved releasing the energy that can be used in the form of electrical energy.

Recently, great attention has been focused on hydrogen (H_2) as a potential promising energy vector among other available chemical fuels, as it has an interesting energy density (142 MJ/kg), which is approximately 2.6 times higher than the methane based fossil fuels. [23] Moreover, it is a carbon-free energy precursor producing only water when combined with oxygen, thus leading to zero CO_2 emission during its use. Global H_2 production volume for 2021 is 70 million tons and is expected to increase in a large extent in the upcoming years. [24]. Up to now, H_2 was principally produced from fossil fuels, hydrocarbon steam reforming process which is not sustainable in the long term. Indeed, only 5% of the produced H_2 comes from renewable sources. [25] In this work, we focus on the direct production of hydrogen, using the sun energy to promote electrolysis of water.

1.2 Solar water splitting with photoelectrochemical cells

1.2.1 Solar water splitting

Solar water splitting (SWS) aims at generating green H_2 from sun and water only. Over the years, different SWS approaches have been developed, which can be classified in indirect methods and direct methods, as illustrated in **Figure 1. 2 (a,b)**. As shown in **Figure 1. 2 (b)** , the indirect approach uses at least two separate components: (i) the light absorber (usually a PV-cell) and (ii) the water-splitting/electrolysis component (electrolyzer). [26] In this case, renewable electricity is first produced by PV-cells, and subsequently transferred to the electrolyzer as an input energy to drive water splitting reactions. The PV-electrolyzer technology is mature and has a high technology readiness level.

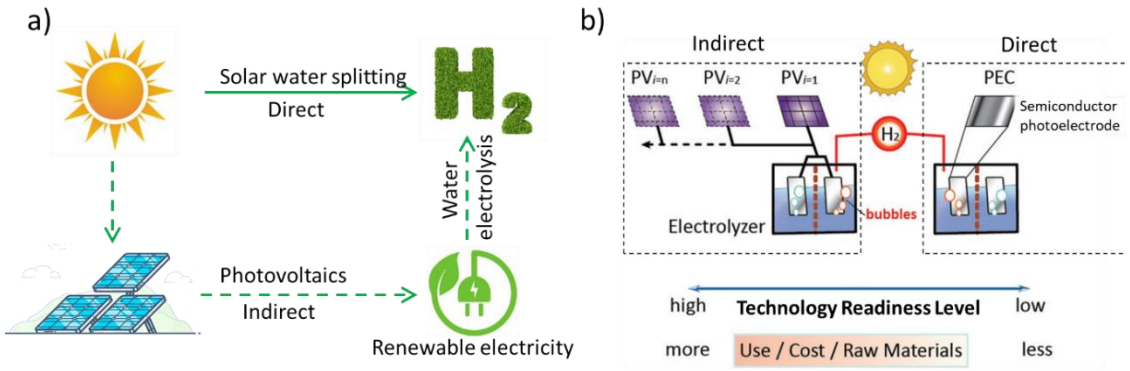

Figure 1. 2 (a) Direct and indirect approaches for green hydrogen production via solar-water splitting; (b) comparison between operating principles of PV-electrolyzer systems (indirect) and PEC systems (direct) (b). Adapted from [26]

Although solar-to-hydrogen (STH) energy conversion efficiency above 10% can be easily obtained by wiring an efficient photovoltaic array to an electrolyzer stack, the high cost of the individual components (PV-cell and electrolyzer) and the system complexity makes the indirect approach less competitive with the conventional steam reforming of methane in terms of H_2 production costs.[11] In the direct approach, both the light absorbing and water splitting components are assembled together into a single system referred as the Photoelectrochemical (PEC) cell. In this case, the device performance is directly influenced by the physical property of the semiconductor photoelectrodes. The concept

of photoelectrode was first introduced in the pioneering work of Fujishima and Honda [27] This approach is simpler, and may also lead to lower fabrication costs. But PEC cells are less technologically mature, still in their early stage of development, as compared to the indirect PV-Electrolyzer devices. [26] Nevertheless, there is a large room for improvement of PEC cells efficiencies in terms of materials developments [28], catalysts [29], stability [8] and device design optimization. [30] Indeed, PEC cells hold great promises for realizing solar hydrogen production at an industrial scale considering the world record STH efficiencies obtained for a PEC-based system (19.3%), which competes with the one obtained with PV-Electrolyzer systems. [6,31] However, the complexity of the developed photoelectrodes presented in these works make the device high-cost with a limited lifetime. For these reasons, no PEC cell is commercialized up to now. The common target STH efficiency required for a PEC cell is 10% with a lifetime of at least 10 years in order to compete with the current industrial hydrogen production technology. [30] The production of such a PEC cell should also be cost-efficient. [3] Thus, the development of new cost-efficient and high performances materials capable of absorbing the full solar spectrum, together with robust protective layers remains a core task of the research in this field.

1.2.2 PEC cell with semiconductor photoelectrodes

A PEC cell is a device that contains semiconductor photoelectrodes immersed in an aqueous solution (electrolyte) to produce chemical fuels (H_2, O_2, methanol, etc) using solar energy. [32,33]. The device consists of two electrodes immersed in the liquid electrolyte with at least one electrode exposed to the light. PEC water splitting system is displayed in **Figure 1. 3** containing the semiconductor photocathode and photoanode dipped in an electrolyte, separated by a polymer membrane (proton exchange membrane). A brief description of processes that occur at the photoanode (n-type semiconductor) is illustrated as well in **Figure 1. 3.** In the following, a first and short description of the physical processes involved in photoelectrodes is provided. The absorption of light with energy higher than that of the bandgap of the semiconductor ($E_{hv} > E_G$) generates electron-hole pairs (e^-/h^+) in the semiconductor material (process I in **Figure 1. 3**). The photo-generated charges are then separated thanks to the band bending between the semiconductor and the electrolyte (process II in **Figure 1. 3**) With a proper design, these

charges are transferred to the electrolyte to feed the oxygen evolution reaction (OER) for O_2 production in the case of a photoanode, or the hydrogen evolution reaction (HER) for H_2 production in the case of a photocathode.

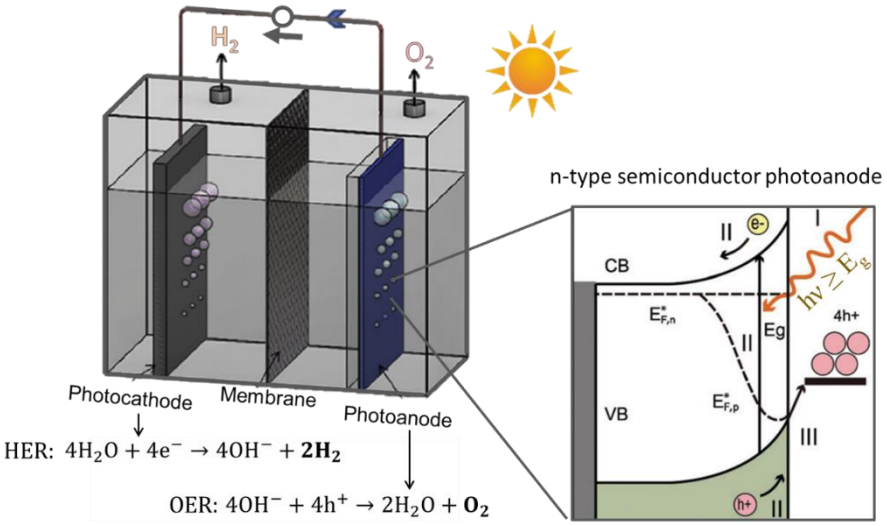

Figure 1. 3 Operation principle of a PEC water splitting system, and overview of the physical processes occurring at the n-type semiconductor photoanode. The main processes driving the water splitting in the photoanode are: (I) light absorption, (II) subsequent separation/ transportation of photogenerated charges and (III) water oxidation reaction (OER). The same processes are also considered for photocathodes, but in this case, the water reduction reaction (HER) is considered.

The band bending and charge carrier separation processes will be explained in detail in an upcoming section. Usually, photoanodes are made of n-type semiconductors with holes (h^+) driving the OER, and photocathodes are made of p-type semiconductors with electrons (e^-) driving the HER. A polymer membrane (e.g., a proton exchange membrane (PEM)) is used to separate gaseous products while maintaining the electrolyte ionic conductivity. The oxidation and reduction reactions to split the water into O_2 and H_2 take place simultaneously; this is why the optimization of both reactions is prominent to achieve the highest efficiency of the PEC water-splitting system. Roughly, for application purposes and high STH efficiencies, scientists will target (i) the highest H_2 or O_2 production rates, which means the highest possible photocurrent density, j (mA/cm^2) in the absence of corrosion, and (ii) unassisted water splitting, which means that it is not needed to apply an external bias to start the reaction. These performances are usually assessed by measuring the (j - V) curve firstly, where j is the photocurrent density, and V

the applied potential with respect to a reference electrode (will be explained in details in next chapters).

Generally, for an efficient PEC operation, and a realistic hydrogen production, the optimal semiconductor composing the photoelectrodes should present:

1. High absorbance of the solar spectrum, which is related to its band gap values and its nature (direct vs indirect);
2. Good transport properties (high mobility and long recombination time of minority carriers in the depletion zone);
3. Sufficient photovoltage for unassisted water splitting (theoretically >1.23 V);
4. High stability in harsh conditions to prevent corrosion and decomposition, while promoting efficient catalytic activity;
5. Low fabrication cost;
6. Appropriate position of the conduction band relatively to the H^+/H_2 redox potential for HER and position of the valence band energy relatively to O_2/OH^- redox potential for OER.

The results presented in this work will be constantly confronted to these criteria for assessment of the photoelectrode operation. In the following, we present a more detailed description of some of these aspects, and remind useful fundamental knowledges about semiconductor physics, and electrochemistry.

1.3 Semiconducting photoelectrodes

Understanding the general physical properties of the semiconductor materials used in this work is of prime importance, as the development of semiconductor photoelectrodes is at the heart of this thesis. In this section, we present and discuss the physical properties of semiconductors, and metal-semiconductor or semiconductor-electrolyte heterojunctions, with respect to photoelectrodes operation.

1.3.1 Bands and Fermi level in semiconductors

Semiconductors is a class of materials intermediate between metals (without bandgap) and insulators (with a large bandgap), where energy bands originate from the coupling between electronic states of the numerous individual atoms as illustrated in **Figure 1. 4**. Consequently, they present a small but opened bandgap (E_G). The electronic states located below this gap are occupied with electrons at T = 0 K and belong to the valence band (VB). The electronic states above the bandgap are empty at T = 0 K and belong to the conduction band (CB).

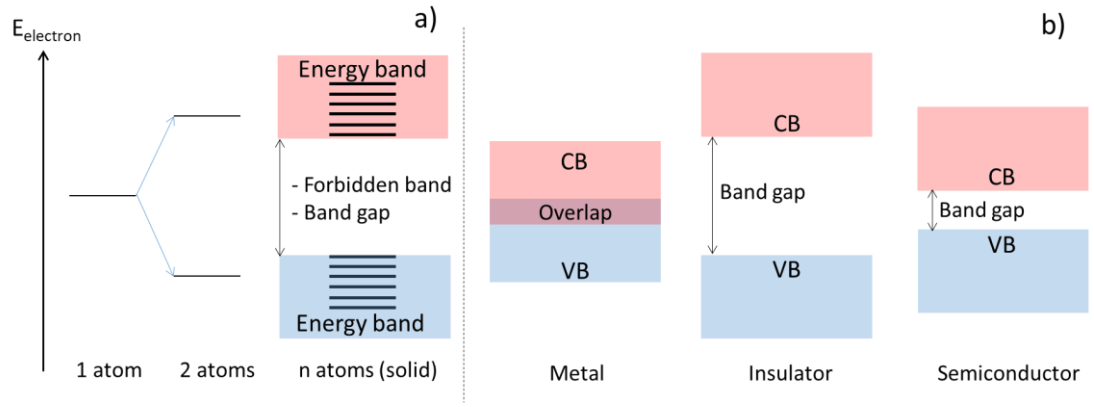

Figure 1. 4 (a) General illustration of the splitting of energy levels in a material, and (b) relative positioning of the conduction bands (CB) and valence bands (VB) for metals, insulators and semiconductors

The bandgap, E_G (usually expressed in eV) is equal to the difference between the minimum of the CB (E_{CB}) and the maximum of the VB (E_{VB}). E_G is a critical parameter that primarily defines light absorption properties of the semiconductor and varies in the range of 0.1 to 4 eV for semiconductor materials and above 4eV for insulators. [34] In a semiconductor the electrons in the VB can jump into the CB when they get sufficient external energy ($E > E_G$), e.g., with increasing temperature or by receiving photons. The process is called "excitation" and leaves behind a hole (h^+) in the VB. As a result, the number of electrons in the CB increases and thus the conductivity as well.

Statistically, the general distribution of electrons over all the available energy levels in a semiconductor can be described by the Fermi-Dirac approximation [34] which allows defining the so-called Fermi level (E_F). E_F is the energy level where the probability

of finding one electron per available state is equal to 0.5 and corresponds to the chemical potential of electrons in the semiconductor. [35] These parameters are commonly used to distinguish metals (E_F is located in the VB or in the CB which leads to a good electron conduction), from semiconductors and insulators. E_F is located at the mid-gap for an intrinsic semiconductor (**Figure 1. 5)**, where the electron densities (n) and hole densities (p) in the CB and VB are considered to be the same. The electrons or holes densities can be increased by introducing dopants with the aim of increasing material conductivity. The doping of the intrinsic semiconductor with some electron donor dopants increases electron density (n) making the semiconductor "n-type" with majority charge carriers being electrons.

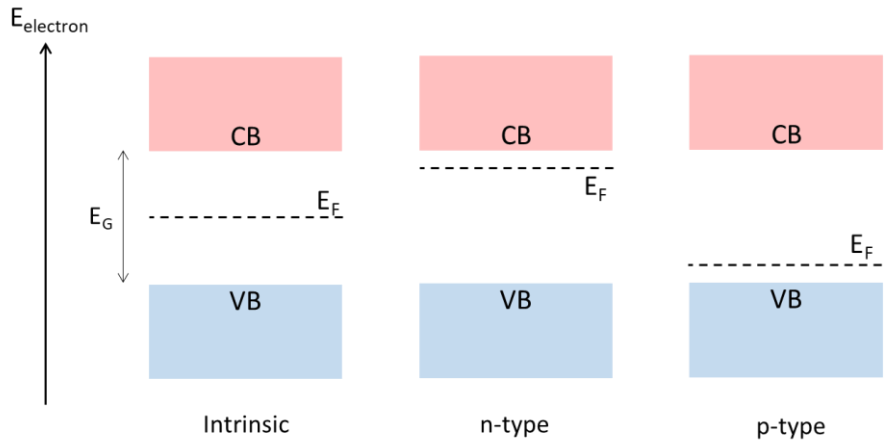

Figure 1. 5 Schematic illustration of the relative positioning of the Fermi level for an intrinsic, n-type and p-type semiconductor

On the contrary, electron acceptor dopants increase the hole density (p) making the semiconductor p-type with majority carriers being holes. E_F thus varies with the type and magnitude of the doping: E_F is shifted close to the CB (VB) for the n-type (p-type) semiconductor that has relatively a larger (smaller) electron density than the intrinsic semiconductor meaning that the probability for the electron existence is increased (decreased) due to the additional (missing) electrons induced by dopants.

1.3.2 Solar spectrum, band structure and bandgap in semiconductors

The band structure of a semiconductor defines its ability to absorb efficiently the solar radiation. The AM 1.5G solar spectrum, corresponding to the standard illumination

conditions (1-sun or 1000 W/m²), covers a broad spectral range between Infrared and Ultraviolet, as shown in **Figure 1. 6** with a maximum spectral irradiance in the visible range. A conventional semiconductor starts to absorb the light when the energy of the radiation becomes larger than E_G; the higher the energy of the photons, the larger the absorption coefficient, and thus the larger the number of photo-generated carriers. However, solar energy harvesting devices are known to be limited by other processes (e.g., recombinations, thermal losses or impedance matching), so that carriers photogenerated with an energy much larger than the band gap cannot be used for the solar harvesting application considered. This is known as the Shockley–Queisser limit, and explains the fraction of the effectively usable power with a crystalline Si photovoltaic solar cell observed in **Figure 1. 6**.

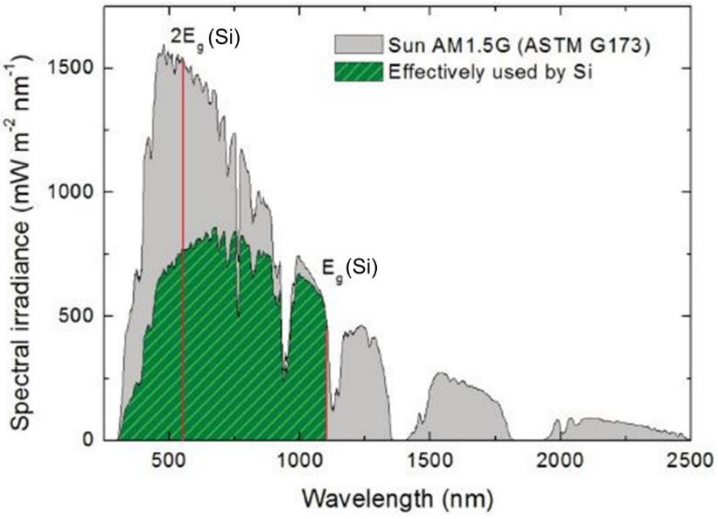

Figure 1. 6 Spectral irradiance of solar AM 1.5G spectrum and the power effectively usable by a crystalline Si photovoltaic solar cell. Adapted from [36]

In this context, considering a single absorber configuration, it has been predicted that a solar device would reach its optimum efficiency by using a semiconductor with a bandgap around 1.3 eV [37]. Efficiency of such device could even be improved by associating two or more absorbers with different bandgaps, to harvest a larger portion of the solar spectrum. In the case of a tandem association of materials, the ideal bandgap association for optimum efficiency is 1.7eV/1.1eV [37].

The nature (direct or indirect) of the band structure also strongly impacts the performances of solar devices. As described in **Figure 1. 7**, the relative positioning of the

CB Minimum (CBM) and of the VB Maximum (VBM) at a given electron momentum in the crystal (k-vector) in the Brillouin zone determines whether the band structure is direct or indirect. In the case of direct band gap semiconductors, E_{CB} and E_{VB} have the same k-vector, meaning that the transition of an electron from the VB to CB can be achieved upon absorption of a photon with an energy hv equivalent to the band gap of the semiconductor. While, the indirect bandgap semiconductors, the E_{CB} does not coincide with the E_{VB} and a change in momentum is thus needed together with the band-to-band transition. An additional phonon is required to enable the transition of an electron from the VB to the CB. [38]

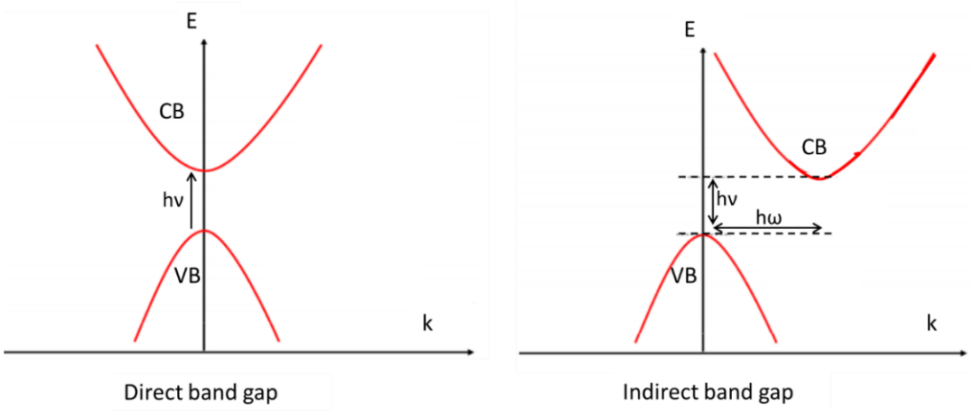

Figure 1. 7 Illustration of the electron transition from the valence band (VB) to conduction band (CB) (left) for the direct bandgap and, (right) indirect bandgap

As a consequence, indirect and direct band gap semiconductors have different absorption properties. Due to the energetic requirements in order to change the momentum of electrons, the absorption coefficient is relatively smaller for indirect band gap semiconductors, and increase more slowly above the bandgap energy. [39] This difference between indirect and direct bandgaps has also some consequences on the design of solar devices. Indeed, the light absorption depth, defined as the inverse of the absorption coefficient ($1/\alpha$ in cm) is used to determine the thickness of light absorbers. Indirect band gap semiconductor absorbers are designed to be much thicker (>100 µm for Si solar cells) than the direct band gap ones (~1µm for direct bandgap III-V solar cells) in order to absorb the full portion of the solar light. The first case leads to high material consumption, whereas the latter one can be used only as a thin-film with low material consumption.

1.3.3 Metal - semiconductor junction

As briefly mentioned above, and highlighted in this thesis, the ability to transfer charge carriers to the electrolyte is conditioned by the ability to bend the bands of the semiconductor, in a controlled way, at the vicinity of the semiconductor/electrolyte interface. To some extent, the semiconductor/electrolyte heterojunction has some similarities with the semiconductor/metal Schottky junction model case. In a first approximation, one can consider that the electrolyte behaves similarly as a metal, which Fermi energy level would correspond to the electro-chemical potential of the electrolyte (more details will be given in the upcoming sections).

The physics of the metal/semiconductor junction is generally rationalized by the Schottky-Mott rule and the junction is referred as the "Schottky junction". [34] The work function (Φ) is an important parameter that governs the physics of the Schottky junction. It is defined as the minimum energy required to extract an electron from the material. [34] Considering a Schottky junction formed between a metal with a work function Φ_m and a semiconductor with a work function Φ_s, a situation where $\Phi_m \neq \Phi_s$ will automatically lead to a charge transfer through the interface. **Figure 1. 8** displays the energy band diagrams of a metal and n-type semiconductor. The first case corresponds to the situation where the metal work function is larger than that of the semiconductor ($\Phi_m > \Phi_s$) (**Figure 1. 8 (a) top**). In this case, when the two materials are in contact, equilibration of the Fermi levels will occur and electrons will transfer from the semiconductor to the metal (**Figure 1. 8 (b) top**). The transfer of electrons will occur until the Fermi level of the metal ($E_{F,m}$) and semiconductor ($E_{F,s}$) equilibrate. At the equilibrium, the depletion layer will be established at the vicinity of the interface. In this region, the metal is negatively charged and the semiconductor is positively charged due to the semiconductor-to-metal electron transfer. As a consequence, a gradient of electron concentration appears in the n-type semiconductor (smaller electron density near the interface, larger electron density in the bulk). The electric field induced by charge redistribution is thus responsible for the so-called "band bending" near the interface. The region where the bands are bent is called space charge region or depletion layer which strongly depends on the nature and level of the doping in the semiconductor. The depletion layer has the ability to separate the

charges. In the present case the light induced holes (h^+) are attracted towards the interface, whereas the electrons (e^-) are repelled.

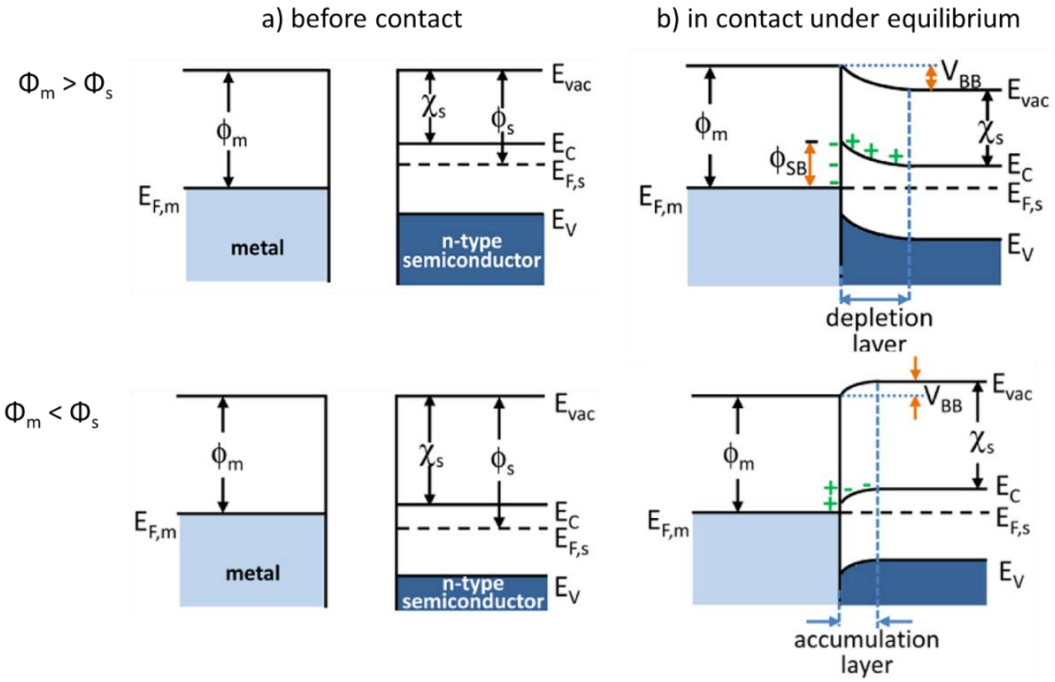

Figure 1. 8 (a) Energy band diagrams of a metal and a n-type semiconductor before contact and (b) in contact under equilibrium. E_{vac} is the vacuum energy, E_C and E_V are the energies of the conduction band minimum and valence band maximum, $E_{F,s}$ and $E_{F,m}$ are the Fermi energy levels of the semiconductor and of the metal, Φ_{SB} is the Schottky barrier height, V_{BB} is the magnitude of the band bending Φ_s and Φ_m are the work functions of the semiconductor and of the metal, χ_s is the electron affinity of the semiconductor. Adapted from ref [40]

On the contrary, when the metal work function is smaller than that of the semiconductor ($\Phi_m < \Phi_s$), **Figure 1. 8 (a) bottom**, an accumulation layer is formed instead of a depletion layer, where the electrons are accumulated in the space charge region due to the electron transfer from the metal to the semiconductor as shown in **Figure 1. 8 (b) bottom**. As a consequence, the band bending and distribution of charges in the space charge region will be opposite to the prior case. Generally, the energy bands bend upward toward the interface and electrons flow from the semiconductor to the metal when $\Phi_m > \Phi_s$, and the inverse mechanism is observed when $\Phi_m < \Phi_s$.

The magnitude of the band bending (V_{BB}) is defined as the difference between the work function of the metal and that of the semiconductor,

$$V_{BB} = |\Phi_m - \Phi_s| \quad (1.1)$$

Moreover, the Schottky barrier that prevents the charge flowing backward is formed at the interface under equilibrium, and the height of it also depends on the work function of the metal (Φ_m) and the electron affinity of the semiconductor (χ_s) as shown in the equation below,

$$\Phi_{SB} = (\Phi_m - \chi_s) \quad (1.2)$$

The electron affinity of the semiconductor (χ_s) in **Figure 1. 8** represents the energy difference between the minimum of the conduction band (CB) and the vacuum energy level (E_{vac}).

From this general introduction on the physics of semiconductor/metal heterojunctions, we can now introduce with more details the physics and chemistry of the semiconductor/electrolyte junction, in the dark or under illumination.

1.3.4 Semiconductor – electrolyte junction

The semiconductor – electrolyte junction is one of the most important components in a PEC cell for solar water splitting, as the oxidizing and reducing photogenerated charges are transferred to the reaction sites through this interface. Gerischer's model is widely used to describe the physics and the phenomena occurring at the junction when the semiconductor and the electrolyte are brought into contact. [41] Unlike solid semiconductors, the liquid electrolyte does not have an intrinsic Fermi level. So the electrochemical potential of the electrolyte, referred as E_{Redox}, originates from the electrochemical potentials of the different active species in the solution (H^+ and OH^- in case of water) and depends on the concentration of ions, the interaction between them and their solvation energies. [41,42] The E_{Redox} is considered as the Fermi level of the electrolyte in analogy to Fermi levels in solid semiconductors or metals, even if the two concepts are distinct.

When a semiconductor is in contact with an electrolyte with E_{Redox} different than that of the semiconductor ($E_{F,s}$), charge transfer occurs at the semiconductor/electrolyte interface until equilibrium is reached. As a first example, a junction between a n-type semiconductor and an electrolyte is considered, with $E_{F,s}$ larger than E_{Redox} (Note that potentials and energies vs. vacuum use inverted sign conventions. Here, I will use the energy scale to explain the physics). In this case, the electrons flow from the semiconductor to the electrolyte, as shown in **Figure 1. 9 (a)**.

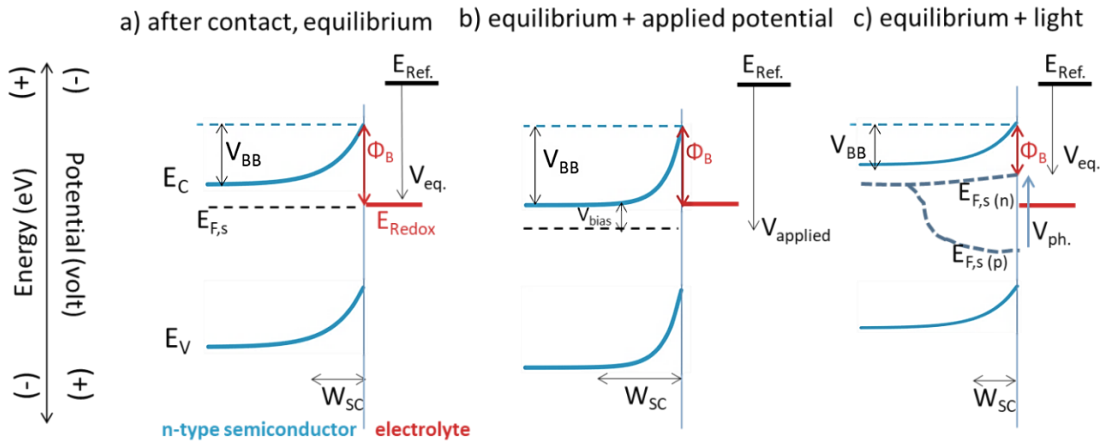

Figure 1. 9 Energy band diagram for an n-type semiconductor in contact with an electrolyte for three different configurations: a) equilibrium b) under applied potential and c) under illumination. $E_{F,s(n)(p)}$ are the quasi Fermi level of electrons and holes; V_{ph} is the photovoltage; V_{BB} is the magnitude of band bending; Φ_B, W_{SC} are the barrier height and depletion layer width.

$E_{F,s}$ will decrease to equilibrate with E_{Redox}. Thus, at the equilibrium without illumination and without applied bias, the Fermi levels of the semiconductor and the electrolyte are exactly at the same potential V_{eq} (or $V_{ocp\text{-}dark}$ as shown in potentiostat). The gradient of electrons concentration (lower near the interface, larger in the bulk semiconductor) is thus formed at the vicinity of the semiconductor/electrolyte interface (see the previous section), and the energy bands of the semiconductor are bent upward toward the interface.

Inverted configuration is obtained for a p-type semiconductor, with the electrons being transferred from the electrolyte to the semiconductor and with the bands of the semiconductor bending downward toward the interface (we consider that $E_{F,s} < E_{Redox}$ for the p-type). [41,42] In response to the charge accumulation at the semiconductor

/electrolyte interface, due to the presence of a depletion layer in the semiconductor, a thin and charged molecular layer (typically <1nm) forms in the electrolyte near the interface. This layer, referred usually as "Helmholtz layer" is negatively (positively) charged if the semiconductor is of n-type (p-type).

The difference between the Fermi level of the semiconductor and the one of the electrolyte defines the magnitude of the band bending (V_{BB}) at the equilibrium. This parameter varies also with external parameters (applied bias or illumination). The induced interfacial electric field assists spatial separation of the photogenerated charge carriers in the semiconductor; holes (h^+) are attracted, whereas electrons (e^-) are repelled from the interface. The inverse is valid for the p-type semiconductor. Additionally, the energy barrier that prevents the charge flowing to the opposite direction is formed at the interface under equilibrium that makes charge separation more efficient. There are several factors that influence the interfacial electric field and thus charge carrier separation/ transportation. Particularly, the width of the depletion layer (W_{SC}) which can be calculated using the equation (1.3). It corresponds to the characteristic distance where the bands are bent and is typically in the order of hundreds of nanometers. [43]

$$W_{SC} = \left(\frac{2\varepsilon\varepsilon_0}{eN_D}\left|V - V_{fb}\right|\right)^{1/2} \tag{1.3}$$

Where, ε is the relative dielectric constant, ε_0 is the permittivity of the vacuum, e is the electronic charge, N_D is the donor density and V_{fb} is the flat-band potential. V_{fb} is a crucial parameter which corresponds precisely to the parameter V_{BB} at equilibrium (no applied bias, no illumination). Knowledge of this parameter gives a direct access to the relative positioning of the semiconductor bands with respect to the electrochemical potential of the electrolyte E_{Redox}. [44] Experimentally, this parameter can be determined from a capacitance measurement performed on the semiconductor-electrolyte junction. Details will be given in next chapter.

In the case of the n-type semiconductor, applying a positive potential shifts the Fermi level of the semiconductor downward and increases the band bending leading to the extension of the space charge region (larger W_{SC}) as shown in **Figure 1. 9 (b**).

Consequently, the effect of the induced interfacial electric field becomes more pronounced which better separates and drives the photogenerated charge carriers to the reaction sites and reduces the electron-hole recombination probability. On the contrary, a negative bias applied will tend to flatten the bands, until the flat-band situation is reached. Beyond the flat-band configuration, band bending will be inverted. The band-bending and V_{fb} influences significantly the onset potential (V_{onset}), the starting point of PEC reaction (explained in chapter 2). Overpotential (delayed V_{onset}) is mostly observed in practical measurements depending on the physical properties of the material (Helmholtz layer, surface defects) and the electrolyte. Especially for the materials used in water OER, where the reaction kinetics is sluggish, larger overpotentials remain as an issue to be solved. [45] The use of water OER catalysts and passivation layer has been demonstrate to reduce the overpotential. [46]

The depletion layer is further affected by light, as the e^- / h^+ density is increased upon light absorption. Depending on the density of free carriers, the Fermi level of the semiconductor is split into 2 quasi-Fermi levels: one for the electrons, and the other for the holes ($E_{F,s(n)}$ and $E_{F,s(p)}$ respectively), as presented in **Figure 1. 9 (c**), magnitude of which depends on light intensity and surface recombination rates. Higher light intensity and lower surface recombination rates result in a larger splitting of Fermi levels. Generally, the light absorption is assumed to affect mostly the density of minority carriers. In the case of n-type semiconductor, the resulting $E_{F,s(n)}$ level under illumination will be thus eventually slightly shifted close to its initial position (without light), whereas $E_{F,s(p)}$ will experience a more significant displacement toward the VB, leading to the increase of the overall oxidizing power of the material. On the contrary, for the p-type semiconductor, the $E_{F,s(n)}$ will be shifted more importantly toward the CB, whereas the $E_{F,s(p)}$ will remain almost unchanged near the VB, which will thus increase the overall reducing power of the material. This explains why the n-type semiconductors are generally used as photoanodes for the OER, whereas the photocathodes for HER are made of p-type semiconductors. The difference between $E_{F,s(n)}$ and $E_{F,s(p)}$ is one of the key parameters characterizing the PEC process and is referred to as the photovoltage, V_{ph} [47] with a maximum value always smaller than the band gap energy. The photovoltage quantifies the voltage induced by the light itself in the semiconductor depletion zone. The

larger the photovoltage, the lower applied bias will be requested to use the photoelectrode in a PEC cell, and thus the larger STH efficiency will be expected.

1.4 Semiconductor photoelectrodes: material requirements

Since the first demonstration of PEC water splitting using a metal oxide semiconductor electrodes, [27] it appeared clearly that semiconductor materials are well adapted to be used as photoelectrodes if they can provide enough input energy to split the water molecules into gaseous O_2 and H_2 (>1.23 V) from the sun radiation. As stated previously, this can be done in a realistic way (STH > 10%, lifetime > 10 years) only if the semiconductor has (i) a good visible light absorption coefficient, (ii) enhanced charge transportation properties, (iii) suitable CB and VB energy band positions and (iv) a strong stability in aqueous solution. Moreover, the semiconductor photoelectrode should remain cost-efficient and easily fabricated to guarantee a low levelized cost of hydrogen. Finding all these qualities in one semiconductor is very challenging, thus many research efforts in the recent years have been devoted to find new materials that possess all the desired characteristics. In the following, we focus on the material requirements needed to achieve efficient photoelectrodes.

1.4.1 Band gap, depletion layer and diffusion length

As stated previously, for a good visible light absorption, the individual semiconductor or the semiconductor stack should have a suitable band gap to absorb a large portion of the solar spectrum. On the other hand, without any external applied bias (unassisted water splitting), the individual semiconductor or the semiconductor stack should present at least a 1.23 eV difference between the E_{CB} and the E_{VB} in the stack (so at least a 1.23 eV bandgap in the case of a single material) to provide sufficient photovoltage for the water splitting reaction. The absorption of photons leads to the generation of charge carriers and subsequently electrical current in the whole circuit, composed of the semiconductor, the electrolyte and the connectors. This electrical current is referred as photocurrent (or photo-induced current). The photocurrent density, j (photocurrent divided by the effective surface area of the electrode) is a widely used quantitative parameter to compare the performance of the semiconductor electrodes.

Using the spectral irradiance of the solar spectrum (AM 1.5G) and photon's energy (hv) at each specific wavelength, it becomes possible to calculate the theoretical maximum value of the photocurrent density ($j_{theoretical}$), without considering e^-/h^+ recombination and assuming that one absorbed photon creates one e^-/h^+ pair.

$$j_{theoretical} = e \times \int_{\lambda_{min}}^{\lambda_{max}} \Phi_0(\lambda) \times [1 - exp(-\alpha(\lambda) \times d)] \qquad (1.4)$$

Where, $\Phi_0(\lambda)$ is the spectral photon flux of the simulated solar light (AM 1.5G), $\alpha(\lambda)$ is the absorption coefficient of the material, d is the thickness, λ is the photon wavelength and e is the elementary charge.

The value of $j_{theoretical}$ is directly related to the bandgap energy and the nature of the band gap (indirect-direct) of the material. The growing trend of the $j_{theoretical}$ as a function of the band gap energy and corresponding demonstrations with various materials are given in **Figure 1. 10**. [30]

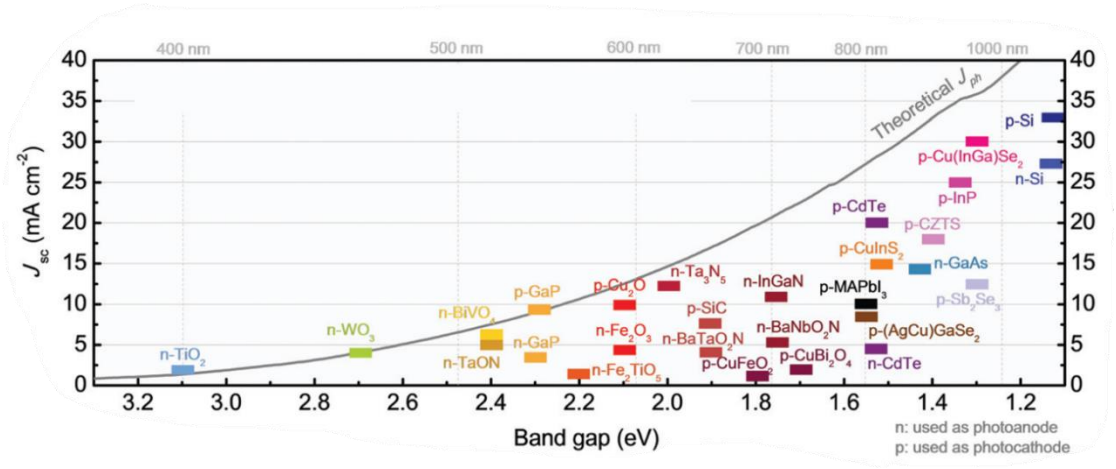

Figure 1. 10 Photocurrent density under short circuit conditions (photoanode @ 1.23 V vs. RHE, photocathode @ 0.0 V vs. RHE) under 1-sun illumination. Solid grey line is the $j_{theoretical}$ and colored bars are experimental demonstrations with various different materials. Adapted from [30]

The difference observed between the theoretical (solid grey line) and achieved (colored rectangles) photocurrents is quite obvious and can be explained with losses induced e.g., by charge recombinations or parasitic resistances. From this description, we

can easily understand that a larger bandgap will lead to a potentially larger photovoltage, but with a lower density of photo-generated carriers. On the other hand, a smaller bandgap will lead to a smaller photovoltage, but with a larger density of photo-generated carriers. A trend is thus to be considered for efficient PEC operation.

Charge transportation is mainly defined by the mobility (μ) and diffusion length of the minority carriers (h^+ for the n-type and e^- for the p-type semiconductors). The minority carriers with a longer lifetime and faster mobility can propagate over longer distances before recombination and favor a higher charge collection efficiency. [34] The carrier's lifetime can be also affected by doping concentration or crystal defects. For example, a very high doping decreases the diffusion length as well as induces a small space charge region. Considering the internal losses, such as charge recombination beyond the diffusion and depletion layer as illustrated in **Figure 1. 11**, the photocurrent density (j) can be re-calculated using Gärtner's model by the equation shown below,

$$j = eI_0\left(1 - \frac{\exp\left(-\alpha W_{SC}\right)}{1 + \alpha L_{min}}\right) \tag{1.5}$$

where, e is the charge of an electron, I_0 is the incident photon flux, L_{min} is the diffusion length of minority carriers, α is the absorption coefficient and W_{SC} is the width of the depletion layer. The formula takes into account only the charges photo-generated within the diffusion and depletion layer by subtracting the amount of charges recombined beyond this region from the total amount of the absorbed photons. General illustration of the model is given in **Figure 1. 11 (a).** Nevertheless, the charge recombination is known to occur even in the space charge region, at the surface states. This is expected to result in an even smaller photocurrent and with a potential loss causing delayed onset potential (V_{onset}). **Figure 1. 11 (b)** shows the difference in photocurrent density with and without recombination in the space charge region.

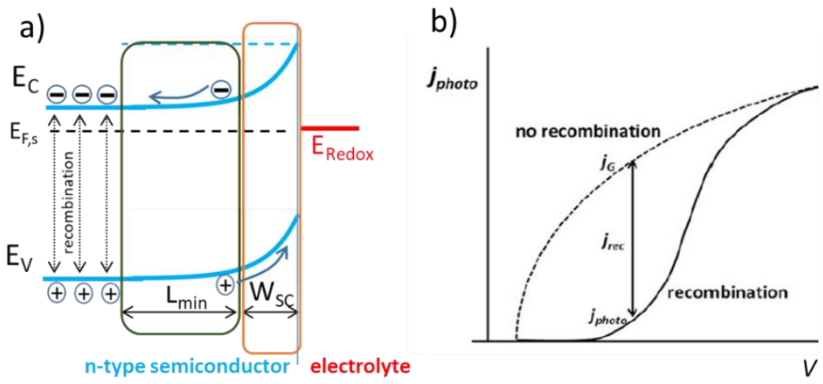

Figure 1. 11 (a) Schematic illustration of the Gärtner's model showing the recombination of the charges beyond the diffusion length, L_{min} and depletion layer length, W_{SC}; (b) Delayed onset potential (V_{onset}) and smaller photocurrent are obtained, as a result of recombinations in the space charge region. The j_G is the current predicted by the Gärtner equation, j_{photo} is the experimental photocurrent ($j_{photo} = j_G - j_{rec}$). Adapted from [35]

In this case one has to apply a greater external potential to have the same amount of the photocurrent when the recombination was not considered. It was already mentioned above, that applied potential increases the band bending and thus increases the driving force for the transport of the charges through the semiconductor / electrolyte interface. Accordingly, it appears clearly that the width of the depletion layer (W_{SC}) and diffusion length of the carriers (L_{min}) are as important as having a suitable bandgap for a large range light absorption.

1.4.2 Positioning of the energy band edges

In order to perform the water OER/HER reaction with high selectivity and lower overpotentials, the E_{CB} and E_{VB} should be well aligned with the reduction and oxidation redox potentials of water. More specifically, the CB (VB) of the semiconducting material has to be higher (lower) than the corresponding redox potential energy level in order to be able to drive in an unassisted way the water splitting reaction (without external applied voltage). **Figure 1. 12 (a)** shows the ideal case, where both energy band positions of the semiconductor straddle the water HER and OER potentials energy levels. It means in this ideal case this semiconductor can be both used for water oxidation and reduction reactions.

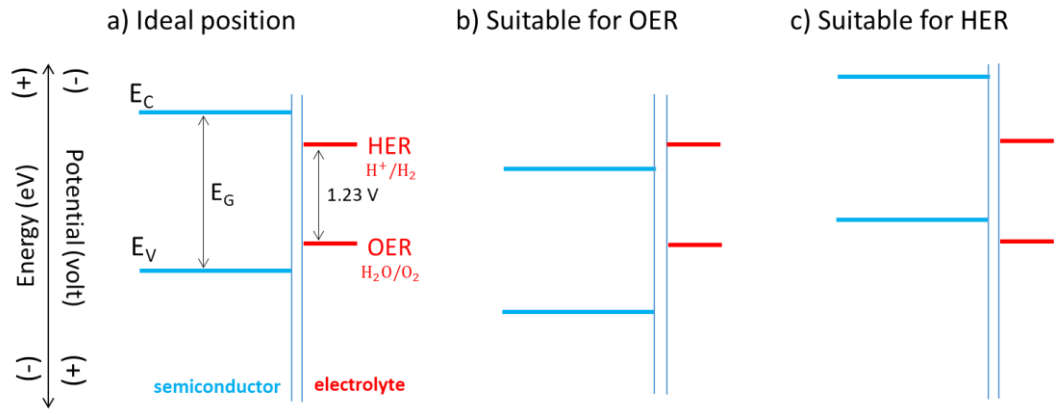

Figure 1. 12 (a) The relative positioning of the semiconductor band edges with respect to the water redox potentials that are suitable for both unassisted HER and OER; (b) for unassisted OER only and (c) for unassisted HER only. Band alignments are given without equilibration of Fermi Levels, applied bias or illumination.

In more practical way, a n-type (p-type) semiconductor is considered for the OER (HER), as the majority of known semiconductors do not fulfill simultaneously these two requirements for OER and HER. Instead, the usual strategy is to select one semiconductor suitable for OER and another one for HER. **Figure 1. 12 (b)** shows a possible band alignment suitable for the OER reaction. In this case, photogenerated holes could likely drive the OER, while electrons would require external potential to drive the HER. **Figure 1. 12 (c),** on the contrary, shows a possible band alignment suitable for the HER reaction. Here, photogenerated electrons could likely drive the HER, while holes would require external potential to drive the OER.

1.4.3 Stability of semiconductor photoelectrodes

The high reactivity of semiconductor surfaces with electrolytes makes stability issues critical in PEC cell development. Such stability issues are more crucial in strong acidic or alkaline electrolytes. Generally, unprotected PEC cell photoelectrodes corrode and their performances drop drastically with time. [48] While a lifetime longer than 10 years is required for a practical use of PEC system, [3] a typical operation time for best known photoelectrodes is in the range of few hundreds of hours. [8] The semiconductor photoelectrodes in PEC cell are known to corrode through chemical, electrochemical and photoelectrochemical corrosion. Chemical corrosion involves only chemical actions that lead to degradation of the material without necessity of net charge transfer across the

solid-electrolyte interface. Electrochemical and photoelectrochemical corrosion, however, require a net charge transfer between the semiconductor and the electrolyte. [48] The stability of a semiconductor against electrochemical /photoelectrochemical corrosion is based on so called thermodynamic anodic/cathodic self-decomposition potentials, $E_{p,d}\,(pH)$ and $E_{n,d}\,(pH)$ that are dependent on pH of the surrounding electrolyte [49,50]. For a binary compound semiconductor MX, the self-decomposition reactions can be either anodic or cathodic as written below,

$$MX + zh^{+} \rightarrow M^{z+}_{(aq)} + X\ (anodic) \tag{1.6}$$

$$MX + ze^{-} \rightarrow M + X^{z-}_{(aq)}\ (cathodic) \tag{1.7}$$

Electrochemical corrosion occurs without illumination, by involving only the majority charge carriers (electrons for n-type, holes for p-type). For instance, the n-type semiconductors undergo cathodic decomposition, if the potential ($E_{n,d}$) is located at a lower energy than the Fermi level E_F of the semiconductor. For the p-type semiconductors electrochemical corrosion is likely to occur through anodic decomposition if the potential ($E_{p,d}$) is located at a higher energy than the Fermi level E_F. [50] To summarize, the electrochemical corrosion can occur if,

$$p-type\ semiconductor: E_{p,d} > E_F\ (reaction\ (1.6) \tag{1.8}$$

$$n-type\ semiconductor: E_{n,d} < E_F\ (reaction\ (1.7)) \tag{1.9}$$

As a consequence, as the Fermi level of semiconductors is located in their bandgap, the semiconductor is considered as thermodynamically stable against anodic self-decomposition, if the ($E_{p,d}$) is located below the E_{VB}. The same applies for the cathodic self-decomposition, if the ($E_{n,d}$) is above the energy level of the E_{CB}. **Figure 1. 13** shows the calculated anodic decomposition ($E_{p,d}$ red bars), cathodic decomposition ($E_{n,d}$ black bars) potentials, as well as positions of energy bands, CB (blue columns), VB (green columns) for many state-of-the-art semiconductor materials at pH=0.

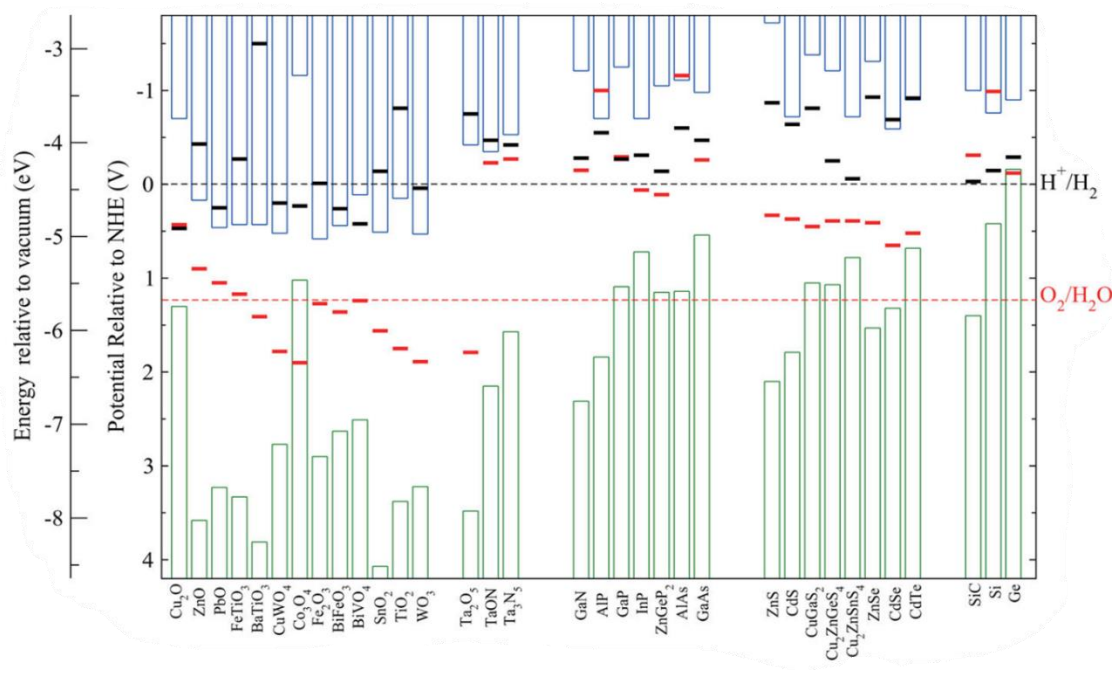

Figure 1. 13 Calculated anodic ($E_{p,d}$ red bars), cathodic ($E_{n,d}$ black bars) self-decomposition potentials for various semiconductor materials at pH=0, with corresponding CB and VB band alignments. Adapted from ref [51]

For the metal oxide semiconductors, i.e., ZnO, $BaTiO_3$, SnO_2, TiO_2, etc., the ($E_{n,d}$) is located above than the CBM. As the Fermi level of n and p-doped semiconductors is located within the bandgap, it is expected that ($E_{n,d} > E_F$). Thus, these semiconductors are expected to be stable against cathodic self-decomposition. In contrast, for III-V compounds (GaP, GaAs, InP, etc.), the ($E_{n,d}$) is located far below than the E_{CB} ($E_{n,d} < E_F$). Therefore, III-V compounds are expected to be prone to cathodic decomposition. In terms of anodic self-decomposition potential, for most of the semiconductors, the ($E_{p,d}$) is located far above the VB. As a consequence, the anodic self-decomposition is expected for the majority of p-type semiconductors.

The previous discussion does not take into account the presence of other redox couples or solvent decomposition reactions. Especially, in the general context of hydrogen production through water splitting, the solvent decomposition reactions are the HER and OER, which should be promoted. **Figure 1. 14 (a-d)** illustrates schematically some specific situations, with the semiconductor and solvent decomposition potentials and energy bands of the p and n-type material. In the first case considered (a), the n-type material has a potential ($E_{n,d}$) located below the CBM and is thus expected to be unstable against cathodic self-decomposition. However, the solvent decomposition potential

($E_{n,solvent}$) is below ($E_{n,d}$) of the semiconductor and thus the material is protected against cathodic self-decomposition by solvent decomposition. In the second case considered (b), the p-type material is likely not to be protected and remains unstable because the ($E_{p,d}$) is located above than the ($E_{n,solvent}$).

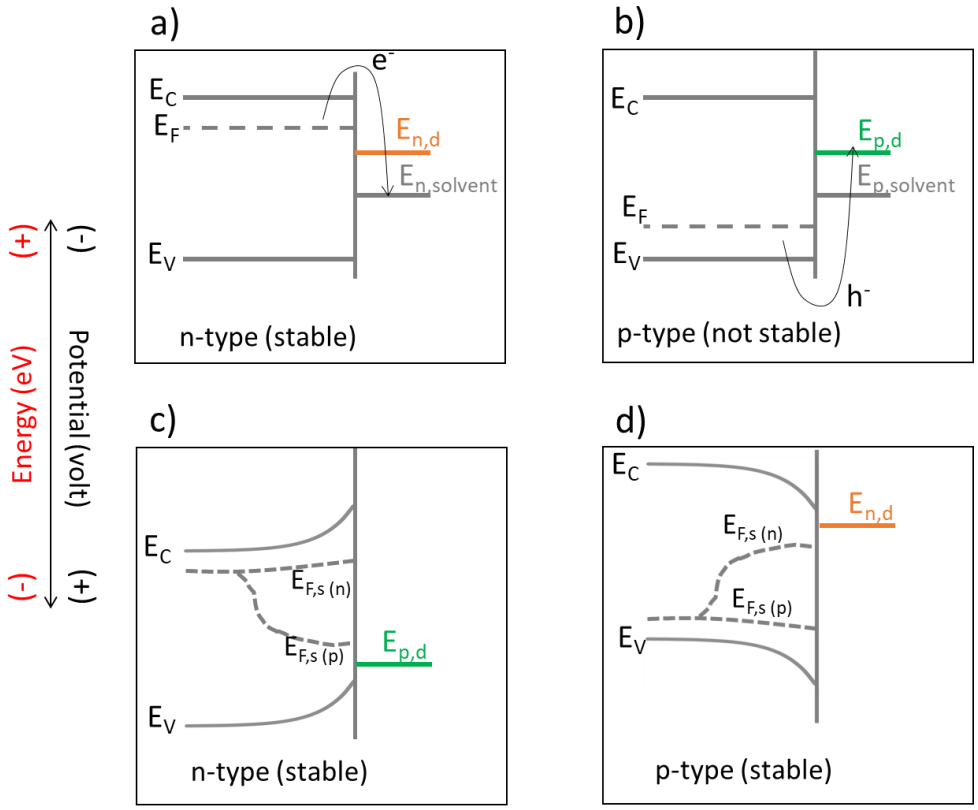

Figure 1. 14 Schematic illustration of some specific configurations of band alignments, including non-illuminated semiconductor decomposition potentials, solvent (electrolyte) decomposition potentials and VBM and CBM for (a) n-type, or (b) p-type semiconductor; Illustration of the semiconductor stability against photocorrosion of the illuminated (c) n-type, (d) p-type. The energetic position of minority carrier quasi-fermi levels ($E_{F,s\,(n)}$, $E_{F,s\,(p)}$) at the surface and that of anodic and cathodic decomposition potentials ($E_{p,d}$, $E_{n,d}$) are shown.

This analysis is valid if the rate of the solvent decomposition reactions is higher than that of semiconductor decomposition. Kinetics of the water-decomposition for instance, affects largely the stability of the semiconductor used, as the semiconductor self-decomposition and HER/ OER reactions are in competition. [52] For example, it has been observed that an electrodeposited Pt catalyst on a GaInP photocathode enhanced the kinetics of HER and thus stabilized the electrode against cathodic decomposition [53].

Until now, we considered semiconductor self-decomposition in the dark, where only majority carriers contribute to the semiconductor decomposition (anodic decomposition for the p-type and cathodic one for the n-type sample). As shown in previous paragraph, under illumination, concentrations of minority carriers increase and their quasi-fermi levels move quickly with illumination. In photocorrosion, the semiconductor decomposition occurs with minority carriers (h^+ for the n-type, e^- for the p-type). Thermodynamic stability of the semiconductor is now defined by the relative energy positions of the quasi-Fermi levels ($E_{F,s\,(n)}$, $E_{F,s\,(p)}$) at the semiconductor surface and the respective anodic and cathodic self-decomposition potentials ($E_{p,d}$, $E_{n,d}$) as shown in **Figure 1. 14 (c-d)**. For instance, thermodynamic stability against photocorrosion is achieved for a n-type semiconductor (c) when the anodic self-decomposition potential, $E_{p,d}$ is located below the minority carrier quasi-fermi level ($E_{p,d} < E_{F,s\,(p)}$) for some given illumination conditions and surface recombination rates. [54] For a higher illumination or lower surface recombination rate, the semiconductor may undergo photocorrosion, if the pseudo-Fermi level $E_{F,s\,(p)}$ shifts at a lower energy than $E_{p,d}$. In a similar way, a stable situation is depicted for the p-type semiconductor (d) as well and the stability criteria is given by $E_{n,d} > E_{F,s\,(n)}$.

To summarize, the stability of a semiconductor photoelectrode depends on the relative energy position of the anodic/cathodic decomposition potentials, the solvent decomposition reactions and the quasi fermi levels. [50] In general, the stability issue appears much more critical for the semiconductors that are used for water oxidation reaction (photoanodes) than for photocathodes due to the slower kinetics and higher energy requirement of OER. [55]

1.5 III-V/Si materials for photoelectrodes: promises and issues

III-V materials have been used for years both academically and industrially in the field of photonics, taking advantage of their excellent optical and electronic properties, their robustness for long life-time devices, and the possibility to control at the nanoscale their optoelectronic properties. It also emerged recently as a promising solar energy harvesting material's family for photoelectrodes [30] or solar cells [56], establishing

world record performances, but without finding any large scale industrial outcome because of their prohibitive fabrication cost (they are used in aerospace applications for instance). Beyond their excellent optical performances, the promises and issues related to their fabrication, alloying and their possible integration on Si are discussed in this section.

1.5.1 Accurate control of interfaces and doping profiles

By using Molecular Beam Epitaxy (MBE) or Metal Organic Vapor Deposition (MOCVD) facilities, the lattice-matched monocrystalline III-V layers can be deposited epitaxially without noticeable bulk crystal defects or interfacial defects formation. High quality heterojunctions including different III-V compounds with excellent optoelectronic properties can thus be elaborated. Also, during the epitaxy of the III-V semiconductor, dopants can be incorporated with a very fine control of the concentration and spatial distribution. These possibilities are at the origin of the development of high-performance optoelectronic devices (HEMT transistors, laser or LEDs), or of energy harvesting devices (photoelectrodes and solar cells). In solar cell technologies, it allowed the achievement of complex multijunction tandem cells architectures, with record solar energy conversion efficiency (45 %). [57] In PEC technologies, by combining multiple absorbers, high photovoltage and unassisted water splitting was achieved. The first demonstration has been reported by Khalesev and Turner with the Pt/$GaInP_2$/GaAs multijunction photoelectrode which showed unassisted water splitting with a promising photocurrent density of 10 mA/cm^2 and a STH efficiency of 12.4%. [58] This approach was further developed resulting in world record STH efficiencies, which will be detailed in an upcoming section.

1.5.2 Bandgap engineering with III-V alloys

The mainstream monocrystalline growth facilities cited in the previous section (MBE and MOCVD) are not only able to provide a high quality III-V material but can also be used to combine two binary III-V compounds, to form a ternary III-V alloy (or even a quaternary alloy) with a high accuracy on the composition of the alloy. **Figure 1. 15** gives the bandgap energy as a function of the lattice parameter of some common III-V semiconductors. Circular dots represent binary III-V semiconductors, while the dashed

(indirect bandgaps) and solid lines (direct bandgaps) represent the ternary alloys connecting the binary III-V materials. From this figure, it can be seen that the precise and fine tuning of the alloy composition offered by epitaxial facilities allows also a fine tuning of the bandgap, and thus of the band positions. This property is very interesting for PEC applications.

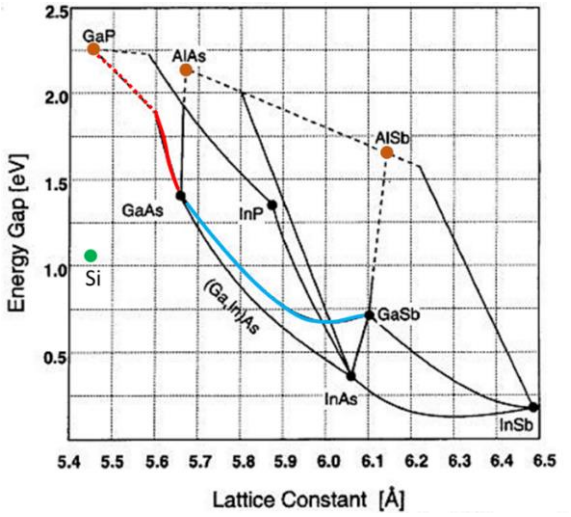

Figure 1. 15 Plot of the energy gap of III-V semiconductor as a function of the lattice constant. Indirect band gap semiconductors (brown circle) and their alloys (dashed line), direct band gap (black circle) and their alloys (solid line). Adapted from ref [59]

Indeed, it means that the position of the conduction band (CB) and valence band (VB) edges could also be adjusted at any specific oxidation reduction reactions. [60] Moreover the nature of the bandgap (indirect-direct) can be modified to enhance solar energy harvesting capabilities. For example, GaP has a large, and indirect bandgap of 2.26 eV and therefore, absorbs a small part of the solar spectrum. The incorporation of Sb (or As) to form GaP(As,Sb) alloys, allows to get a direct band gap, and subsequently a stronger light absorption. As shown in **Figure 1. 15** the band gap of $GaP_{1-x}As_x$ can be tuned all along the red line by controlling the elemental composition of the alloy, i.e., the band gap of the GaPAs alloy (red line) can be modulated from the one of GaAs (1.42 eV) to that of GaP (2.26 eV) through the fine control of As or P elements. This can thus be made easily in epitaxial facilities, but simultaneously, it also changes the lattice parameter of the grown crystal, which can generate some crystal defects, and have a drastic influence on the device performances (this will be further discussed in the thesis). Surprisingly, in the PEC literature, bandgap engineering was only used considering stacks of different

materials with different bandgaps, but having the same lattice parameters, such as GaAs/AlAs/GaInP or AlInAs/GaInAs/InP. PEC performances of several photoelectrodes based on lattice matched materials have been reviewed. [10]

1.5.3 Crystal defects and monolithic integration on Si substrate

Since the early development stages of optoelectronic devices for photonics or photovoltaics, a clear correlation was made between the crystal quality of the III-V semiconductors and the ultimate performances of the developed devices. Fundamentally, this can be easily understood, as crystal defects which possess dangling bonds are commonly understood as non-radiative recombination centers, thus capturing a part of the electrons going through the defects. The most common crystal defect developed during the epitaxy is the dislocation. A dislocation is the defect encountered when an atomic row of atoms is missing or added to the perfect III-V crystal. [61] Especially, misfit dislocations appear when the epitaxial materials don't have the same lattice parameter than the substrate (see **Figure 1. 16 (a)**). This is why most of the materials scientists preferentially worked on lattice-matched materials to develop devices for photonics and energy. Nevertheless, strategies were found to overcome the dislocation issue, and impressive demonstrations were obtained with metamorphic devices in the field of photovoltaics [56] or lasers [62].

Additionally, the monolithic integration of III-V semiconductors on silicon substrates also leads to several additional specific defects, on which the research team of Institut FOTON developed a recognized expertise. Especially, stacking faults (SFs) and microtwins (MTs) are planar defects that alter the crystallographic plane order and are found in close-packed structures where the atomic layers are arranged in a certain stacking order (see **Figure 1. 16 (b)** and **(c)**). Their appearance was found to be related to inappropriate Si substrate chemical/thermal preparation, or inappropriate growth initiation conditions. [63,64] Finally, beyond SFs and MTs, antiphase domains may form in the III-V epilayers, due to the different crystallographic structures of III-V semiconductors (Zinc-Blende, except for GaN), and Si (Diamond). These antiphase domains correspond to a rotation by 90° in-plane of the III-V crystal, and are separated by Anti-Phase Boundaries (APBs) (**see Figure 1. 16 (d)**). These structural defects, whose

generation mechanisms were clarified recently, [61,65,66] were found to provide to the samples original physical properties, and possible beneficial impact on some photoelectrodes performances. [18]

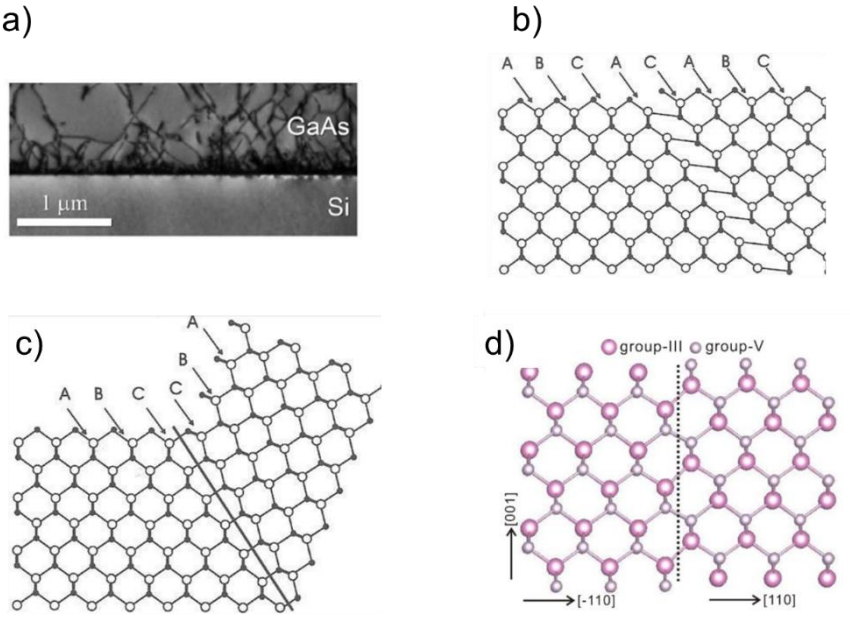

Figure 1. 16 (a) Cross-sectional transmission electron microscopy (TEM) image of crystal dislocations propagating through the GaAs grown on Si substrate; (b) illustration of an intrinsic stacking fault; (c) microtwins and (d) atomic configuration of a stoichiometric APBs adapted from [67]

1.6 III-V and III-V/Si photoelectrode performances: a state-of-the-art

Since the first demonstration of solar-water splitting with TiO_2 in 1972, [27] many research works have been conducted on oxide semiconductors especially on Fe_2O_3, [68] $BiVO_4$ [69] and WO_3 [70]. With these materials, the reported maximum photocurrent densities obtained for a bare photoelectrodes are below 5 mA/cm^2 at 1.23 V vs RHE. The origin of these poor performances can be related to the intrinsic properties of oxide semiconductors. Indeed, they present large and indirect band gaps, limiting the absorption of solar photons, and low carrier diffusion lengths restraining photocarrier collection and thus photocurrents. Nevertheless, oxide semiconductors are earth abundant and low-cost materials. Therefore, significant research efforts was done to improve the light harvesting efficiency of metal oxide semiconductor-based PEC cells. [46,71] On the other hand,

photoelectrodes composed of binary III-V semiconductors were also deeply investigated showing very promising performances, but at a much higher cost, and facing the intrinsic problem of their poor stability (already discussed in previous sections). In the following, we present some of the typical performances of different III-V single photoelectrodes, p-n junctions or multi-junctions architectures and review the attempts to integrate them on silicon. In this state-of-the-art, we will focus on three fundamental parameters, which are of critical performance to develop an efficient PEC cell: (i) the maximum photocurrent achieved (traducing the ability to convert solar light into chemical fuel without considering corrosion), (ii) the onset potential (the smaller the better for a photoanode, and the larger the better for a photocathode), traducing the ability to drive the OER and HER reactions, (iii) the lifetime of the device, as it is one of the main drawbacks of III-V semi-conducting photoelectrodes.

1.6.1 InP photoelectrodes

Among III-V semiconductors, indium phosphide (InP) is one of the promising candidates for PEC applications. The material has a direct band gap of 1.34 eV close to the optimum one for wide-range sunlight absorption and excellent electronic properties [72]. Its conduction band edge is higher than the water reduction potential (HER) and thus InP have mainly been used for photocathodes with recorded photovoltages resulting in V_{onset} of 0.62 and 0.84 V vs. RHE and a maximum photocurrent density of ~24 mA/cm^2 (0 vs RHE). [73,74] As discussed previously, the corrosion in aqueous electrolyte is one of the major drawbacks for InP based photoelectrodes operating in a PEC system with a lifetime of less than 2 h. Nevertheless, the use of thin-film protection layers has successfully increased the photoelectrode durability. [73]

1.6.2 GaN photoelectrodes

Gallium nitride (GaN) is a III/V semiconductor that is mainly used in blue light-emitting diode fabrication. It has a Wurtzite crystal structure and a direct band gap (3.4 eV). Due to its large band gap, GaN absorbs only a small fraction of the solar spectrum and low photocurrents are expected (< 5mA/cm^2). However the valence edge energy of GaN is located well below OER reaction energy and is favorable for photoanode

elaboration. [75] Bare-GaN photoanodes were studied by Kamimura et al [76]. They show a photocurrent density of 1.1 mA/cm^2 (1.23 V vs. RHE) with a V_{onset} of -0.25 V in a neutral phosphate buffered electrolyte solution (pH=7). The application of cobalt phosphate catalyst on a bare-GaN slightly improve the photocurrent density reaching 1.5 mA/cm^2 [76]. Although the catalyst modification suppressed surface recombination, the stability tests reveal that the photoanode has corroded in 1 h due to the high oxidizing potentials. The well-known metal-oxide passivation layers such as, Al_2O_3 and Fe_2O_3 have been tried on the bare-GaN photoelectrodes and the lifetime of photoelectrode has been successfully increased by several hours. [77,78]. Studies have shown that GaN nanostructures, especially those exhibiting N-terminated surfaces are resistant against oxidation and photocorrosion. For example, stable photocatalytic solar water splitting has been demonstrated on InGaN with N-terminated nanowire arrays without any extra surface protection layers. [79]

1.6.3 GaP photoelectrodes

Gallium phosphide (GaP) is one of the mature, extensively studied III-V binary semiconductor, as it has an appropriate bandgap (2.26 eV) to provide high photovoltage and suitable energy band positions. The material was extensively studied as photocathode [80–83] due to the appropriate positioning of the CB relatively to the water HER potential. Malizia et al., demonstrated p-GaP photocathodes with increased V_{onset} and stability by sputtering n-type metal oxides (n-TiO_2, n-Nb_2O_5) onto bare p-GaP photocathodes. [81] As a result, p-GaP/n-TiO_2/Pt photocathodes showed a photocurrent density of 1.45 mA/cm^2 at 0 V vs. RHE with a V_{onset} of 0.71 V. The photocathode was stable for 24 h without any degradation in 1 M $HClO_4$ (pH~0). Whereas, the bare p-GaP had a lower V_{onset} (0.52 vs. RHE), with similar photocurrent density (1.25 mA/cm^2) but started to decompose within 6 h. Although the metal-oxide sputtered p-GaP photocathode showed a promising PEC performance in terms of V_{onset} and stability, the resulted photocurrent density under 1-sun illumination was small (~1.4 mA/cm^2). The small photocurrent of GaP can be attributed to the large and indirect band gap of the material that leads to a poor light absorption (α_{GaP} = 10^2 - 10^3 cm^{-1} just above 2.26 eV). The nanowire geometry with the crystal structure of wurtzite type was found to be a promising approach to improve the light absorption properties of GaP. [84] Standing et al, have extensively

studied p-GaP photocathodes for the PEC water reduction, reporting a similar photocurrent density (~1.4 mA/cm^2 at 0 V vs. RHE) for both planar "zinc-blende" and nanowire (NW) "wurtzite" p-GaP photocathodes. [82] Nevertheless, the photocathodes with NW geometry were improved significantly by applying the MoS_x and Pt catalyst obtaining 10 mA/cm^2 at 0 V vs. RHE and V_{onset} of 0.76 V. Moreover, the p-GaP(NW)/Pt photoelectrode was stable for 5 h in 1 M $HClO_4$ (pH~0) without any applied protection layer. The authors claimed that modifying the geometry from planar to nanowire and application of Pt catalyst enhances light absorption as well as the kinetics of water HER.

GaP photoanodes were scarcely studied, due to the sluggish hole-transfer kinetics leading to high overpotentials to enable water OER. Besides, corrosion of GaP is more prominent in anodic potential than the cathodic one. Despite the harsh conditions of water OER and corrosion issue associated, [51] significant efforts have been made to explore the potentials of GaP and to employ as PEC water splitting photoanodes. For instance, Hu et al., demonstrated nGaP photoanodes protected with an amorphous ALD grown TiO_2 passivation layer in combination with Ni catalysts to improve the stability and charge transfer kinetics. [85] As a result, nGaP/TiO_2/Ni photoanode showed a photocurrent density of 2.3 mA/cm^2 at 1.23 V vs. RHE. The photoanode was stable for 5 h in 1 M KOH (pH=14) and started to decompose after. Alqahtani et al., applied CoO_x as a catalyst onto a TiO_2 protected GaP photoanodes and achieved a good stability for 24 h in 1 M NaOH (pH=14). [86] However, the recorded photocurrent density for both, bare-nGaP (nGaP/TiO_2/CoO_x) 0.18 mA/cm^2 (0.56 mA/cm^2) at 1-sun illumination was ~10 times smaller than the values reported in the literature. [18,87]. Bagal et al., have reported recently a simpler strategy to protect GaP photoanodes, where the authors investigated a photo-deposited NiOOH co-catalyst on the GaP thin films. GaP photoanode with photo-deposited NiOOH co-catalyst showed a photocurrent density of 1.28 mA/cm2 at 1.23 V vs. RHE with V_{onset} at -0.03 V. [88] Furthermore, the photoanode with NiOOH co-catalyst was stable for 11 h at applied potential of 0.2 V vs. RHE in 0.5 M H_2SO_4 (pH~0) solution, while bare-nGaP started to corrode after 1.5 h.

1.6.4 GaAs photoelectrodes

Gallium arsenide (GaAs) is another efficient material of the III-V family, used mostly in photovoltaic industry or laser technology. It possesses a direct band gap (1.42 eV), and high charge carrier mobilities (e.g. electron mobility up to 8500 cm^2/Vs and hole mobility of 400 cm^2/Vs). [89] A perfect 1-μm thick GaAs thin-film photoelectrode could result in ~30 mA/cm^2 under 1-sun illumination (theoretical maximum photocurrent density of GaAs). [30] The recorded experimental values for GaAs photoelectrodes are however lower (~20 mA/cm^2 as a photocathode, ~14 mA/cm^2 as a photoanode). [85,90] As any other III-V material, GaAs is prone to corrosion and decomposes rapidly. Several studies have been conducted to investigate the electrochemical behavior of GaAs in different aqueous solutions with the aim of exploring the degradation mechanism. [91,92] It was mentioned that the material suffers from rapid photocorrosion resulting in a dissolution of the formed corrosion products. Moreover, photocorrosion is more pronounced in oxidation reaction where six elementary charge carriers are required for anodic dissolution of one formula unit, while cathodic corrosion occurs at slower rate. [93]

Young et al., have investigated 2 μm-thick epitaxial p-GaAs photocathodes for water HER, obtaining a remarkable cathodic photocurrent density of 22 mA/cm^2 at -0.57 V vs. RHE. [90] The photocathode had a V_{onset} of -0.15 V and a stability of 120 h with minimal etching in 3 M H_2SO_4 (pH~0) solution. The observed stability is in strong contrast to $GaInP_2$ and InP which decompose within 2 h. [94,95] The findings of authors from surface analysis experiments (XPS) support that corrosion occurs in a much slower rate and it is likely due to the formation of elemental As during the water HER.

1.6.5 p-n single and multi-junction photoelectrodes

GaAs photoanodes, based on n/p bulk junction were successfully demonstrated by Hu et al., showing a photocurrent density of 14.3 mA/cm^2 at 1.23 V vs. RHE with stable operation for 25h in 1 M KOH (pH=14) thanks to an ALD-grown electronic defective TiO_2 passivation layer and an optically transparent Ni OER co-catalyst. [85]. Alternative surface passivation layers such as monolayer of graphene [96] and in-situ

electrodeposited Nickel-borate surface catalysts [97] have been also studied, showing a saturated photocurrent density of ~20 mA/cm^2 but with limited stability, lasting for about 8 h.

Studies on multi-junction photoelectrodes based on GaAs have been conducted as well to demonstrate unassisted water splitting. Recently Kang et al [98] reported ultra-thin GaAs n/p bulk junctions immersed in an electrolyte, used as a photoanode or as a photocathode by changing the surface exposed to the electrolyte and the protective layer deposited on top surface. They demonstrated that two series connected n/p GaAs electrodes can supply a sufficient photovoltage to drive water splitting with sunlight as only energy input. A solar to hydrogen efficiency of 13.1 % was measured. The latest record for PEC cells, has been obtained on metamorphic three junction tandem cell (GaInP/GaInAs)/TiO_2/RuO_x with a 19.3 % STH efficiency under 1-sun illumination in which materials with dissimilar lattice parameters are stacked. [31] However, these structures are very complex and costly and their practical use remains questionable.

1.6.6 III-V/Si photoelectrodes

Despite the excellent performances of multijunction III-V photoelectrodes, the practical application of such a complex structured photoelectrodes made of expensive commercial wafers is very limited for terrestrial applications due to their prohibitively high cost and complexity. Indeed, a 2-inch silicon wafer price is ~30 EUR, whereas a GaAs wafer is ~500 EUR. A techno-economical manufacturing analysis conducted by Shaner et al., claims that the III-V substrate cost corresponds to 90% of the final PEC device cost that operates with III-V photoelectrodes. [11] In this context, integration of III-V semiconductors in the form of thin-films on earth-abundant Si substrates is considered as cost reducing and thus as a more sustainable approach. [10,18,99]

While many research works were mostly carried out using commercial substrates with binary III-V semiconductors, only few researches have been focused on the use of III-V semiconductors on Si substrate for PEC applications. [18,99–101] Wu et al., have proposed to use a 1.7 eV band gap GaAsP nanowire photocathode monolithically grown on Si substrate. The GaAsP (NW)/Si photocathode with integrated Pt catalysts showed a

photocurrent density of 4.5 mA/cm^2 at 0 V vs. RHE and a recorded V_{onset} of ~0.5 V. [102] The authors stated that, despite low surface coverage of the self-catalyzed NW the resulted STH value (0.5%) was relatively high as compared to other wafer scale NW photocathodes published previously. [80,103] Alqahtani et al., have studied planar GaP grown on Si substrate as a photocathode for water HER, demonstrating a photocurrent density of -0.4 mA/cm^2 at 0 V vs. RHE. [100] The relatively low photocurrent density was attributed to the indirect band gap of GaP and the small thickness of GaP thin-film. Recently, the first planar III-V nitrides photoelectrodes on Si substrate were demonstrated by Nötzel et al., who reported a photocurrent density of 13.6 mA/cm^2 at 1.23 V vs RHE, which was further improved by using surface quantum dots activated structures. [19] Simultaneously, the demonstration of planar Zinc-Blende GaPSb photoanode grown on Si substrate was realized by our group, showing a remarkable photocurrent >10 mA/cm^2 at 1.23 V vs RHE and stability for 5 h in 1 M KOH (pH=14) electrolyte. [17]. In addition to the promising photocurrent densities obtained with III-V semiconductors grown on a low-cost Si substrate, alloying of III-V are known for the capability of engineering the bandgap energy and band lineups between the photoelectrode and the electrolyte which is of great interest for PEC devices. Assessment of $GaP_{1-x}Sb_x$ alloys grown on Si was studied experimentally and theoretically revealing the advantages of the material in terms of light harvesting capabilities or band gap engineering properties. [101] Later on, the study was further extended to other III-V/Si materials systems, i.e., GaP, GaPSb and GaAsP alloys grown on Si with the measured V_{onset} in the range of 0.12 and 0.45 V vs RHE and the photocurrent density equals to 1.0, 7.8 and 11.3 mA/cm^2, respectively at 1.23 V vs RHE [18]. However, the lifetime of the photoanodes were several minutes (< 30 min) which is not surprising for bare III-V photoanodes.

Above-mentioned the state-of-the-art III-V photoanodes are summarized in **Table 1.1** below to compare later with the photoanodes developed in this thesis.

Photoanode	j (mA/cm^2)	V_{onset} (V vs. RHE)	Stability	Electrolyte	Ref
InP	5.5	0.05	15 min	0.5 M HCl	[30] [46]
GaN	1.1	-0.25	1 h	Phosphate buffer	[76]
GaP	~2	-0.03	5 h (protected)	0.5 M H_2SO_4 1 M NaOH	[18] [51] [85]
GaAs	10-14	-0.02	15 min	0.5 M H_2SO_4 1 M NaOH	[85] [97] [128]
InGaN/Si	13.6	0.6	n/a	0.1 M Na_2SO_4/H_2SO_4	[19]
GaPSb/Si	12	0.6	5 h (protected)	1 M KOH	[17]
GaP/Si	1	0.12	< 30 min	0.2 M H_2SO_4	[18]

Table 1.1 State-of-the-art III-V photoanodes reported in this thesis

1.7 Objectives of the thesis

The main objective of the thesis is to assess the potential of the $GaP_{1-x}As_x$ alloy grown monolithically on Si substrate for anodic operation, in order to develop cost-efficient photoelectrodes for solar hydrogen production with simple designs. Obviously, the use of Si substrate reduces significantly the fabrication cost, as it is a low-cost (second most abundant element on earth) material, widely used in the microelectronic industry. Thanks to the strong light absorption within III-V materials, the absorber's thickness can be as well reduced to few microns or lower. As a result, the consumption of expensive elements is limited in the proposed structure design and a drastic cost reduction is anticipated for PEC devices. Moreover, alongside the superior optoelectronic properties (enhanced light absorption, high electron-hole mobility), we here study the ability to tune at will the composition of $GaP_{1-x}As_x$ alloys, to take advantage of bandgap engineering capabilities. The band gap energy, as well as the relative position of the conduction and valence band edges can be precisely tuned with the elemental composition, in order to achieve a large range absorption of the solar spectrum, high efficiency in photon-to-electron conversion and more importantly an ideal positioning of the band energy levels relative to the underlying Si substrate and water redox potentials.

This dissertation builds on the promising results obtained by FOTON Institute in collaboration with University College London for $GaP_{0.7}Sb_{0.3}$ photoelectrode grown on

Si substrate, and prolongs the collaboration with ISCR-Rennes (G. Loget, B. Fabre) initiated in the framework of L. Chen's PhD thesis. The thesis will focus first on the comparison/benchmarking of a GaAs/Si photoelectrode, as compared to a GaAs one (chapter 3). Then, the applicability of the bandgap engineering concept to a photoelectrode operation will be studied (chapter 4), and the stability issue of III-V/Si photoelectrodes will finally be discussed and addressed (chapter 5).

Chapter 2

Experiments: growth, structural, optical and electro-chemical characterizations of photoelectrodes

Chapter 2. Experiments: growth, structural, optical and electro-chemical characterizations of photoelectrodes

This chapter presents a detailed description of the elaboration and physico-chemical characterizations of the III-V/Si thin-films and photoelectrodes studied in this work.

2.1 Molecular Beam Epitaxy

To date, mainstream experimental setups used to grow monocrystalline III-V thin-films are mainly metalorganic chemical vapor deposition (MOCVD) and molecular beam epitaxy (MBE). Both of these methods can be used to grow a quality-controlled epitaxial thin films of III–V semiconductors with high precision in thickness, composition and doping. While MOCVD growth is based on chemical reactions of organometallic compounds with a high deposition rate, MBE uses direct physical deposition from metal precursors and/or active gases with no carrier gases being used and a low deposition rate. Thus, while MOCVD is preferred for growing faster III-V epilayers on large scale wafers (up to 12 inches), MBE results in ultra-pure, homogeneous monocrystalline films with highly tunable thicknesses and compositions but usually on smaller wafers (typically up to 4 inches).

Solid Source MBE (SSMBE) is the technique to synthesize thin-film crystals, where the feedstock ultrapure materials (Ga, P and As in this work) are heated and evaporated from effusion cells towards the substrate (Si in this work) in Ultra-High Vacuum conditions (see **Figure 2. 1)** A detailed description of the experimental setup used in this thesis is presented elsewhere. [63] The evaporated molecules or atoms flow towards the substrate starting nucleation and subsequently the epitaxial growth. Due to their low vapor pressure, group-III atoms have a near-to-unity sticking coefficient, and consequently govern the III-V growth rate. As a consequence, the accurate control of III-III-V alloys compositions is usually assumed to be easier than the ones of III-V-V alloys, as group-V atoms do not permanently stick to the surface at growth temperature. It is commonly accepted that the epitaxial process is mainly governed by the mobility and diffusion length

of group-III atoms at the sample surface, which is strongly impacted by the growth temperature T_g and the V/III flux ratio. These are the two most important parameters in MBE.

In my thesis, most of the samples studied are made of 1 µm-thick $GaP_{1-x}As_x$ alloys with different As contents, x(As), grown on a 350-µm thick Si substrate in a RIBER compact 21 solid source MBE reactor. The growth of the thin-films is monitored in-situ by the Reflection High-Energy Electron Diffraction (RHEED) system and fluorescent screen which are inserted in the MBE reactor as illustrated in **Figure 2. 1**

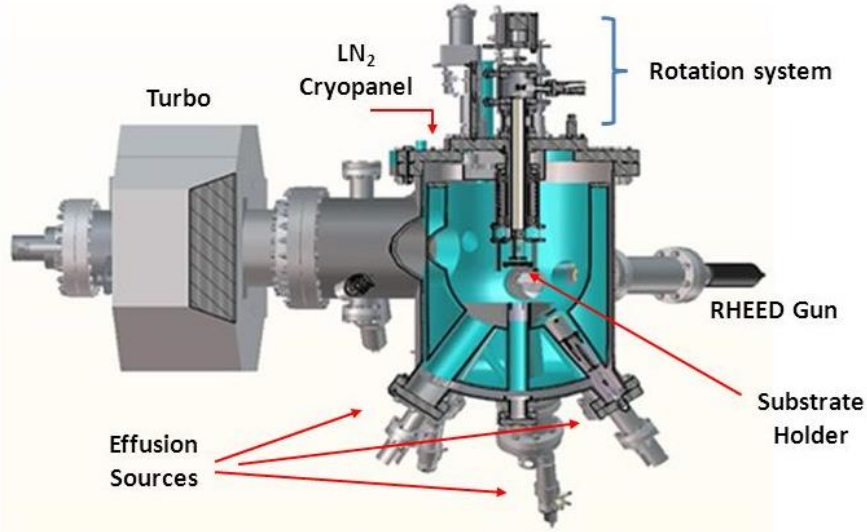

Figure 2. 1 Schematic illustration of the MBE growth chamber

Before the epitaxial growth of $GaP_{1-x}As_x$ layer, the Si substrate was cleaned with HF 1% solution for 90 seconds, followed by ultraviolet-ozone (UV-O_3) surface treatment for 5 minutes. The process is repeated 2 more times with overall cleaning time in HF (1%) of 180 seconds and UV-O_3 treatment for 15 minutes. The cleaned Si substrate was directly transferred to the RIBER compact 21 epitaxial chamber and heated up to 800^{o}C for ten minutes for dehydrogenation and cooled down to the $GaP_{1-x}As_x$ layer growth temperature (cca. 500^{o}C). The group-III element (Ga) is generated from a conventional Knudsen effusion cell containing pure metallic source. While the elements of group-V (P, As) are released in the form of tetramers (P_4, As_4) from thermal evaporation cell and subsequently cracked by the valved-cracker into P_2 and As_2 molecules. During the epitaxial growth the

group-III and group-V atoms are supplied simultaneously. The samples grown in this thesis were not intentionally doped [61,65]. The characterization techniques I used to investigate the as-grown thin-film materials are presented in the following.

2.2 X-ray diffraction

X-ray diffraction (XRD) is a non-destructive technique used to characterize the crystal structure qualitatively and quantitatively. XRD is done by irradiating a sample with a monochromatic X-ray irradiation (at a wavelength (λ)) and by measuring the intensities and diffraction angles of the X-rays that are scattered by the sample. The technique provides information related to the crystal structure of the sample, such as the lattice constant, the crystallinity, the stress relaxation status, or the presence of crystal defects.

In this thesis, XRD is particularly used to characterize the structural quality, elemental composition and relaxation rate of $GaP_{1-x}As_x$ alloys epitaxially grown on Si substrate by measuring ω/2θ and reciprocal space maps (RSM) around different Bragg peaks using X-ray Smartlab Rigaku diffractometer (sealed tube Cu source). A parabolic multilayer mirror and a 2 bounce Ge (220) monochromator are used for beam definition and monochromatization. The detection is ensured by using a Hypixis 3000 detector working either in 1D mode for reciprocal space maps (RSM) or 0D mode for line scans. The Bragg equation ($n\,\lambda = 2\,d_{hkl}\,sin\theta$) is the basis to understand XRD **(Figure 2. 2 (a))**, where the d_{hkl} is the spacing between a particular set of planes with (*hkl*) being the Miller indices, the θ is the angle of incidence at which a diffraction peak is measured, and *n* is an integer that represents the 'harmonic order' of the diffraction. A typical XRD ω-2θ scan recorded around the (004) diffraction peak for a $GaP_{1-x}As_x$ alloy grown on a Si substrate, with x(As) = 0.5 is represented in **Figure 2. 2 (b).** The lattice constant of the epilayer (a_{sample}) can be obtained from the corresponding value of 2θ at which a maximum of intensity is observed, using the equation shown below:

$$a_{sample} = \frac{\lambda}{2\sin\theta}\sqrt{h^2 + k^2 + l^2} \qquad (2.10)$$

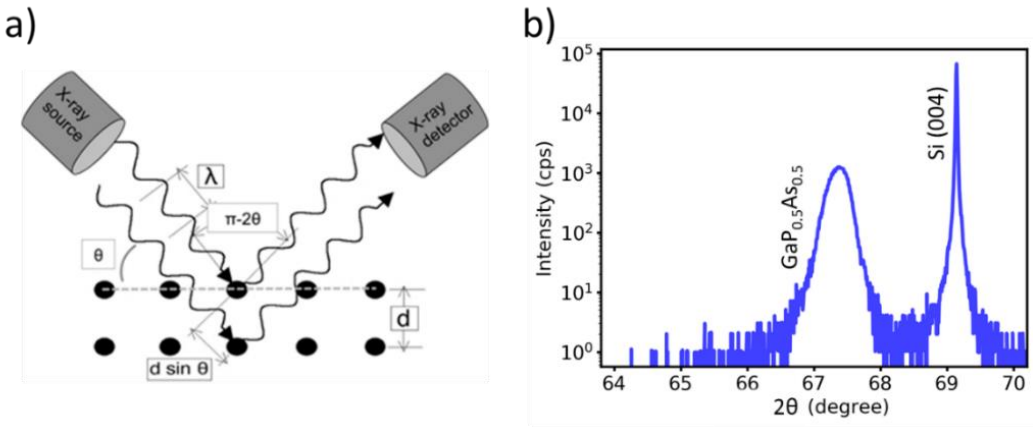

Figure 2. 2 (a) Schematic representation of the XRD technique, (b) XRD profile around the (004) Bragg peak for a $GaP_{1-x}As_x$ sample with x(As)=0.5, grown on Si substrate

The lattice constant of the epilayer (a_{sample}) can be obtained from the corresponding value of 2θ at which a maximum of intensity is observed, using the equation shown below:

$$a_{sample} = \frac{\lambda}{2\sin\theta}\sqrt{h^2 + k^2 + l^2} \tag{2.11}$$

After measurement of the lattice constant of the epilayer, it is possible to infer the approximative value of x(As) in $GaP_{1-x}As_x$ alloy using the Vergard's law as shown in equation below,

$$x(As) = \frac{a_{sample} - a_{GaP}}{a_{GaAs} - a_{GaP}} \tag{2.12}$$

Based on the lattice constants of GaP (a_{GaP}) and GaAs (a_{GaAs}) from the literature, the calculated x(As) for the studied sample here is 50%. However, this simple view is only valid for perfectly plastically relaxed epilayers, without taking into account stress of the strain. The precise value of the lattice constant and thus of the composition x(As) in a $GaP_{1-x}As_x$ alloy strongly depends on the strain state of the epilayer which is usually unknown or uncertain in the case of thick (>50nm) and metamorphic layers. Therefore, it is crucial to determine the plastic relaxation rate, R (%), of the epilayer. In order to calculate R (%), reciprocal space mappings (RSM) around (224), (-224) and (004)

reflections can be performed. [64,104] **Figure 2. 3** shows the RSM around the (224) Bragg peak for the same GaPAs/Si sample, where in-plane and out-of-plane lattice constants [64] can be deduced from the equations shown below:

$$a_L^{//} = a_{sub}\frac{S_{sub}^{//}}{S_L^{//}} \tag{2.13}$$

$$a_L^{\perp} = a_{sub}\frac{S_{sub}^{\perp}}{S_L^{\perp}} \tag{2.14}$$

where $a_L^{//}$ (parallel, in-plane) and $a_L^{\perp}$ (perpendicular, out-of-plane) are the lattice constants of the epitaxial layer, a_{sub} is the lattice constant of the Si substrate, and the $S_L^{//}$, $S_L^{\perp}$, $S_{sub}^{//}$and $S_{sub}^{\perp}$ are the positions in the reciprocal space coordinates of the observed intensity maxima corresponding to the layer (*L*) and the substrate (*sub*) diffraction spots in the RSM in the directions parallel (corresponding to S_x) and perpendicular (corresponding to S_z) to the surface. [64,104]. The corresponding free of strain cubic lattice constant of the GaPAs epilayer ($a_L^{free\ of\ strain}$) is then given by:

$$a_L^{free\ of\ strain} = \frac{a_L^{\perp} - \alpha a_L^{//}}{1-\alpha} \tag{2.15}$$

where $\alpha = \frac{e_{zz}}{e_{xx}} = -2\frac{C_{12}}{C_{11}}$ and $C_{12,}C_{11}$ are the X-ray elastic constants of GaAs. The R (%) can now be determined from the RSM, using the equation below:

$$R\ (\%) = \frac{a_L^{//} - a_{sub}}{a_L^{free\ of\ strain} - a_{sub}} * 100 \tag{2.16}$$

Consequently, when the epilayer is fully plastically relaxed, $a_L^{//} = a_L^{free\ of\ strain} \rightarrow R(\%) = 100$, while when it remains pseudomorphic (strained), R (%) = 0, as illustrated in **Figure 2. 3** assuming no rotation and no shear strain. The full relaxation line (black dashed line), which goes through the center of the RSM peak of Si and the origin point (S_z=S_x=0) is plotted together in the RSM plot (**Figure 2. 3).**

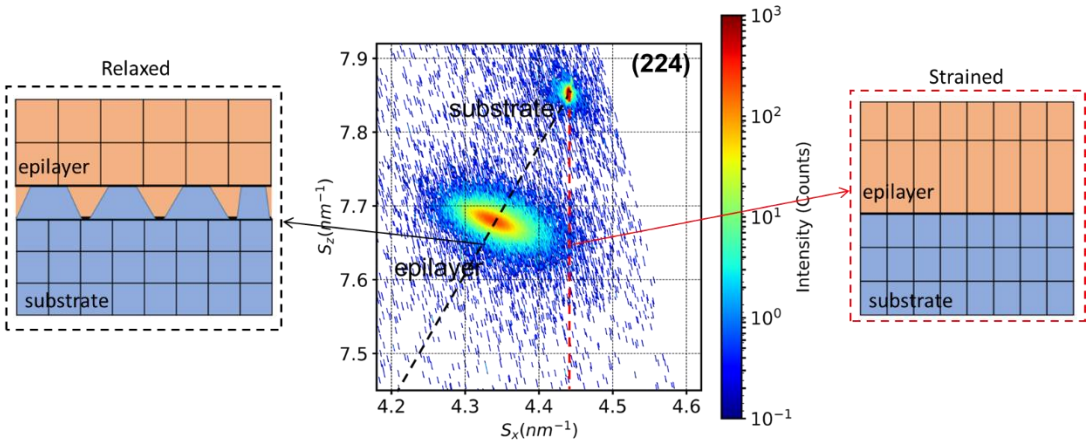

Figure 2. 3 RSM around the (224) Bragg peak for the $GaP_{0.5}As_{0.5}$/Si sample (S_x and S_z are the projected coordinates in the right-handed Cartesian representation, with z axis parallel to the surface normal). The black (red) dashed lines and corresponding images represent a fully plastic relaxation (perfectly strained) line.

The RSM signal corresponding to the maximum intensity diffracted by the epilayer appears around the full relaxation line, indicating that the GaPAs alloy is almost fully relaxed. Otherwise, when a perfectly strained pseudomorphic epilayer is grown the maximum of intensity of the epilayer is vertically aligned on the substrate peak (red dashed line). Any intermediate case (between the red and the black lines) would indicate a partial relaxation of the crystal. In conclusion, from these measurements, one can determine with a good accuracy the compositions and relaxation rates of metamorphic epilayers, which give crucial information for further device operation analysis.

2.3 Atomic Force Microscopy

Atomic Force Microscopy (AFM) is a scanning probe microscopy with resolution in the order of fractions of nanometers. It is a simple technique to use that can be applied on various solid or soft materials to characterize the topography of the sample. AFM gathers information by touching the surface with a very sharp tip typically made of Si_3N_4 or Si on a deformable cantilever. Depending on the interaction between the sample surface and the tip, a small variation in force (Van Der Waals force, capillarity force, electrostatic force or magnetic force) can deflect a laser beam reflecting on the cantilever. The deflection is measured with diode sensors, and converted into information on the surface morphology, to build the 2D image of the sample surface. A standard AFM

apparatus consisting of an optical system with a laser source (illuminating the extreme edge of the cantilever) reflected toward the quadrant photodiode detector that records the cantilever's spatial variation is illustrated in **Figure 2. 4 (a)**. The sample is placed on a cylindrical piezoelectric stage which allows the sample to move in x, y axis to scan all the required area and z axis to keep the tip and surface interaction force (referred as the set point) constant.

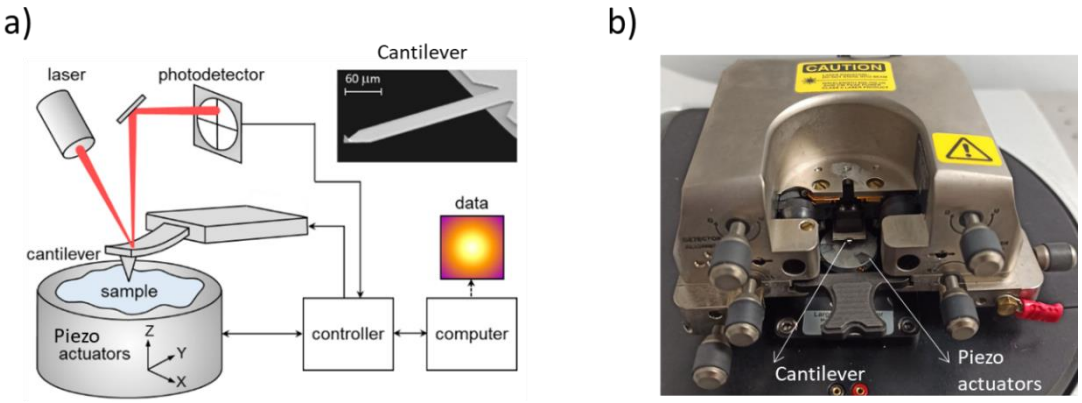

Figure 2. 4 (a) Operating principle of AFM, adapted from [105] and (b) Veeco di Innova AFM setup of the FOTON institute at INSA Rennes

In my thesis the surface of the MBE-grown samples were characterized using an AFM 2007 Veeco di Innova experimental setup presented in **Figure 2. 4 (b)** allowing producing 100×100 μm^2 images with a lateral resolution of 15 nm and a vertical resolution of 0.2 nm in standard conditions. The measurements were performed in two working modes**:** 1) contact and 2) tapping mode. In the contact mode, the interactive force between the tip and the sample is repulsive. The tip scans the sample surface maintaining the cantilever's vertical deviation (Z) at a constant level. The piezoelectric stage is moved accordingly to maintain the tip/sample interaction force constant by tuning the set-point. The tapping mode uses both attractive and repulsive forces alternatively. The cantilever vibrates at high frequency and therefore, the signal detected at the photodiodes alternates as well. The amplitude of the vibration is sensitive to the force between the tip and the sample surface, which changes with the distance between them. As compared to the contact mode, the tapping mode is preferred for soft surfaces or when one wants to prevent tip damaging, as the tip is not in direct contact with the surface.

2.4 Spectroscopic Ellipsometry

Spectroscopic ellipsometry is a non-destructive optical technique mainly used to determine optical constants and thickness of thin films, bi (or multilayered) samples. This technique is based on the change in the polarization state of light as it is reflected at a particular incidence angle (~70° for group III-V or IV semiconductors) from the studied sample. The technique has the advantage of being able to get information even on very thin layers, such as native oxides at the surface of materials (from few angstroms to several tens of microns). In this thesis, a Horiba UVISEL 2 spectroscopic ellipsometer is used to characterize the optical constants (*n*,*k*), absorption coefficients (α), thickness and roughness of $GaP_{1-x}As_x$ alloys epitaxially grown on Si substrate.

Spectroscopic ellipsometry uses a model-based approach [106,107] to determine the above-mentioned parameters deduced from the measurement of ψ and Δ. Both of these quantities describe the output of elliptical polarization state after linearly polarized light is reflected by the sample. Through the well-known ellipsometry formula, the polarization change can be described by an amplitude ratio (tan Ψ) and a phase difference (Δ):

$$\frac{r_p}{r_s} = \tan \Psi . exp\{i\Delta\} \qquad (2.17)$$

where, the r_p and r_s are respectively the complex Fresnel reflection coefficient for p and s polarization. Usually, other variables, i.e., typical I_s and I_c parameters as a function of the photon energy (eV) can be used to display a measurement in ellipsometry. They derive from Ψ and Δ through the following relations:

$$I_s = \sin(2\psi).\sin(\Delta) \qquad I_c = \sin(2\psi).\cos(\Delta) \qquad (2.18) - (2.19)$$

Thus, *Is* and *Ic* parameters are then comprised between -1 and 1 and can be fitted as shown in **Figure 2. 5 (a)** by using a dispersion model including adjustable parameters where *n* and *k* are linked together through Kramers-Kronig relations. In our case, a simple but robust Tauc-Lorentz model with two oscillators has been used to achieve a good agreement between the measurements and the model.

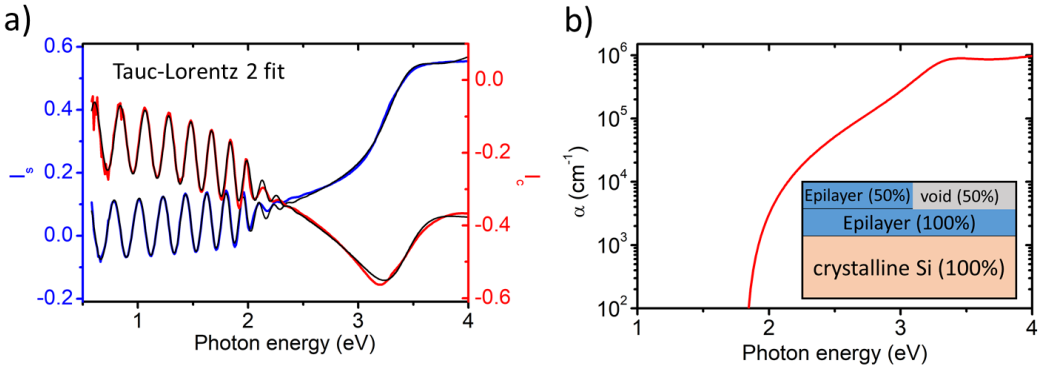

Figure 2. 5 (a) Raw data I_S (blue) and I_C (red) are fitted with a Tauc-Lorentz model with 2 oscillators (black), (b) Absorption coefficient deduced from the imaginary part of the refractive index (k). The stacking layers model used to describe the metamorphic III-V epilayers grown on Si substrate is illustrated in the inset

As the samples studied in this thesis have a root-mean-square (rms) roughness of around 10 nm, a third layer containing a mixture of epilayer and void is applied to account for the sample roughness (inset of **Figure 2. 5 (b)**). Following a successful fit of the raw data, the complex refractive index with the real (n) and imaginary (k) parts, thickness and roughness of the different layers can be extracted as an output of the fit. **Figure 2. 5 (b)** shows the absorption coefficient (α in cm^{-1}) deduced from the imaginary refractive index (k) with the following relationship:

$$\alpha = \frac{4\pi k}{\lambda} \tag{2.20}$$

where λ is the photon wavelength in cm

2.5 Photoelectrode preparation

Photoelectrodes from the epitaxial $GaP_{1-x}As_x$/Si samples and the commercial GaP, GaAs wafers were prepared by cleaning the sample in the ultrasound cleaner for 10s and subsequently dried with N_2 gas. The backside was slightly scratched and Gallium-Indium eutectic (99.99%, Alfa Aesar) and silver paste (Electron Microscopy Sciences) were applied to make an ohmic contact (**Figure 2. 6 (a)**). The geometric surface area was defined using an epoxy resin (EA 3423, Henkel from Loctite) covering the backside and

the edges of the photoelectrode as shown in **Figure 2. 6 (b).** The surface area was systematically evaluated for each individual electrode using ImageJ software where the area of interest is selected manually from the photo with a calibration grid. Note that the rough estimation of the electrode surface in this work, may impact the values obtained for the current densities, which are consequently given with a ~10% uncertainty.

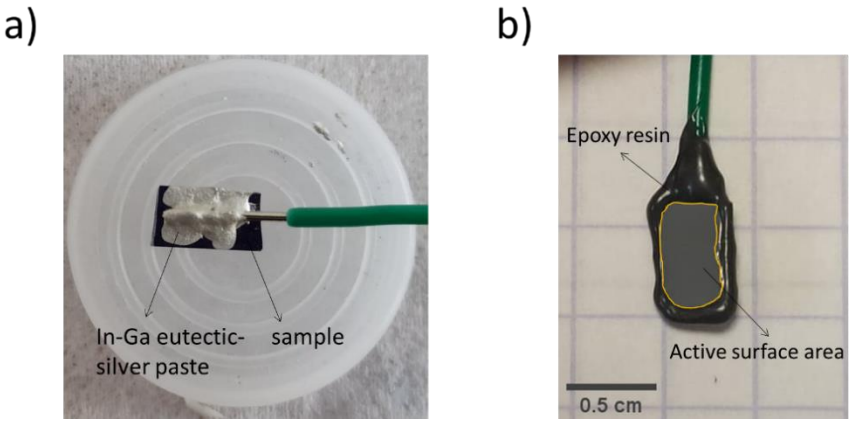

Figure 2. 6 (a) Thin-film sample and low-resistance wire back contact and (b) as-prepared photoelectrode with the surface area selected in orange line

2.6 Technical aspects of water splitting and PEC characterization

2.6.1 Thermodynamics, stability and energy diagrams

Although the dissociation of water offers a convenient way to produce carbon-free H_2, the energy required by the process is approximately 4 times larger than the energy required for the production of H_2 by conventional steam reforming of methane (excluding the heat of methane combustion). [3] A minimum total Gibbs free energy of 237.2 kJ per mol of H_2 is needed for the production of H_2 by water dissociation in standard conditions (temperature = 293 K and pressure = 1 atm). It also requires an additional energy of 48.7 kJ/mol to account for the entropy variation of the reaction ($T\Delta S°$). [108] The energy balance of the stoichiometric water splitting reaction e is summarized below in **Figure 2. 7.** The Gibbs free energy change $\Delta G°_{water}$ can be expressed from the Nernst equation, in terms of number of electrons transferred to the reaction (n) multiplied by the Faraday

constant (F) and change in standard electrochemical potential ($E^o = E^o_{reduction} - E^o_{oxidation}$) as shown below:

$$\Delta G^o_{H_2O} = -nFE^o \tag{2.21}$$

Standard electrochemical potential (E^o) in standard temperature and pressure conditions is mostly used in electrochemistry rather than $\Delta G°_{water}$ as it allows to define a relative energy scale to compare the change in free energy for different electrochemical reactions.

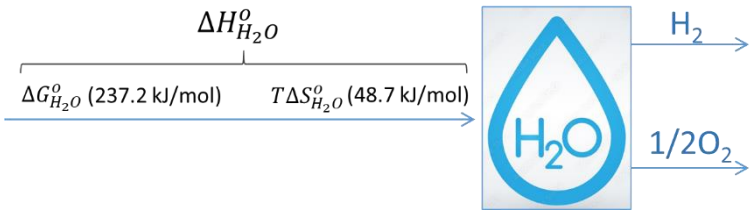

Figure 2. 7 Stoichiometric products of water splitting reaction with the corresponding energy balance

The water splitting reaction includes two half reactions: oxygen evolution reaction (OER) and hydrogen evolution reaction (HER) occurring in acidic conditions (pH = 0). For these two reactions, E^o can be written as follows,

$$2H_2O_{(aq)} + 4h^+ + 4e^- \rightleftharpoons 2H_{2\,(g)} + O_{2\,(g)} \qquad E^o = -1.23\,V\ vs\ NHE \tag{2.22}$$

$$\boldsymbol{OER}: 2H_2O_{(aq)} + 4h^+ \rightleftharpoons O_{2\,(g)} + 4H^+ \qquad E^o{}_{H_2O/O_2} = 1.23\,V vs\ NHE \tag{2.23}$$

$$\boldsymbol{HER}: 4H^+ + 4e^- \rightleftharpoons 2H_{2\,(g)} \qquad E^o_{H^+/H_2} = 0\,V\ vs\ NHE \tag{2.24}$$

In this case, E^o for both OER and HER reactions are defined relatively to the normal hydrogen electrode (NHE). The NHE is a reference electrode based on the hydrogen half-cell reaction, constructed by immersing a platinum electrode in an acidic solution (pH = 0, solution of 1N normal concentration, for protons, 1N = 1M). The E^o for the overall water splitting reaction is negative, thus reaction is not spontaneous but rather demands energy to be completed. The pH of the solution can shift the potential energy for water splitting, as the decomposition of water is kinetically related to the concentration of

protons (H^+) and hydroxyl ions (OH^-). The pH dependency with the Nernstian relation for water OER (2.23) and HER (2.24) can be written as follows,

$$E_{H^+/H_2} = E^o_{H^+/H_2} - 0.059 * pH \quad (2.25)$$

$$E_{H_2O/O_2} = E^o{}_{H_2O/O_2} - 0.059 * pH \quad (2.26)$$

The values of thermodynamic water oxidation and reduction potentials are dependent on the electrolyte pH following a Nernstian equation, shifting with a value of -59 mV per pH unit. This variation can be observed in the simplified Pourbaix diagram of water shown in **Figure 2. 8 (a).** Water is thermodynamically stable between the blue and orange lines corresponding to water OER and HER, respectively.

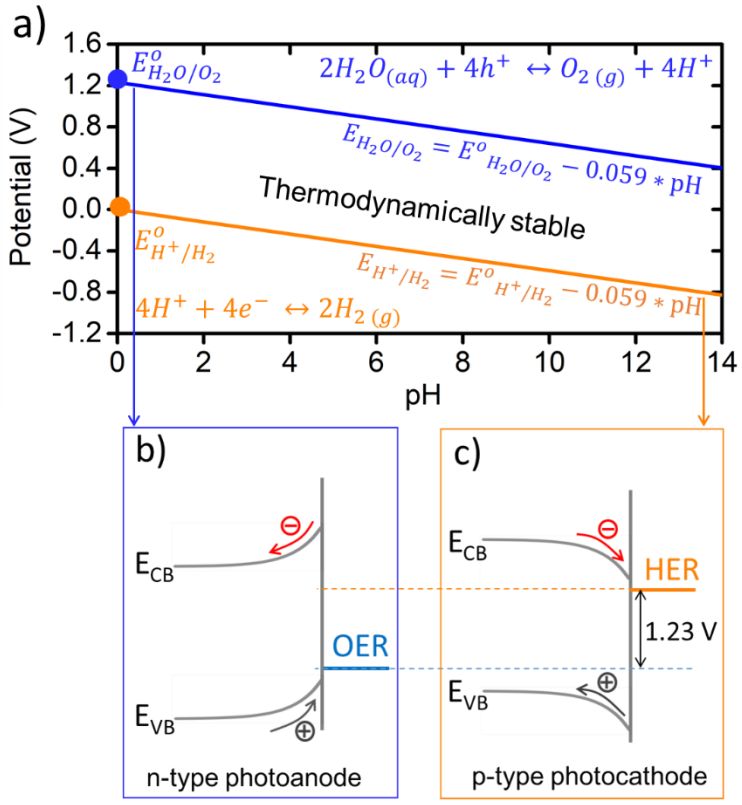

Figure 2. 8 (a) Evolution with the pH of the electrochemical potential for water oxidation (blue), reduction (orange), (b-c) with the corresponding semiconductor photoelectrode energy bands at pH~0. Thermodynamically stable region for H_2O is indicated between the blue and orange lines. Adapted from ref [49].

Considering all the external energy that have to be added to the system in order to split water molecules into gaseous H_2 and O_2, the process is taking place at higher energies

than the Gibbs formation energy of water ($\Delta G°_{water}$) which is equivalent to 237.2 kJ/mol or 2.46 eV/molecule of H_2O. (Since two electrons are used per molecule of H_2O, it corresponds to 1.23 eV per electron). [108] An additional energy, referred to as overpotential (η), is required to overcome the activation energy barriers and ohmic losses in order to successfully split water molecules. For instance, commercial water splitting systems typically operate at a cell voltage of 1.8 – 2 V. [30]

In this thesis, the photoelectrodes made of $GaP_{1-x}As_x$ alloys epitaxially grown on Si substrates were studied for photoelectrochemical water splitting (chapter 1) rather than for electrochemical water splitting, but keeping similar technical aspects. The only difference is that the required energy has to be provided by the sun, resulting in a minimum theoretical photovoltage (V_{ph}) of 1.23 V in the semiconductor photoelectrode. **Figure 2. 8 (b-c)** illustrates the relative position of energy bands (E_C and E_V), V_{ph} for the photoanode (OER) and for the photocathode (HER).

It was already mentioned previously that the positions of the energy bands (E_C and E_V) relatively to the water redox potentials (OER/HER) is of great importance and significantly impacted by the change in pH of the electrolyte. [110,111] For instance, the energy bands as well as the Fermi level (E_F) for an n-doped (10^{18} cm^{-3}) GaAs material are expected to shift by ~55 mV vs NHE per unit of pH (when the impact of surface states, and surface reactions are neglected). [110] As a result, band-alignment between the semiconductor and electrolyte changes, as the Fermi levels of both semiconductor (E_F) and electrolyte ($E_{F,redox}$) are impacted by the pH of the solution. However, the use of one Fermi level for the electrolyte ($E_{F,redox}$) that has multiple redox potentials (i.e., HER: H^+/H^2 , OER: H_2O/O_2, etc) and different concentration of active species is a subject of controversy. Nevertheless, $E_{F,redox}$ depends on redox potentials of the different active species in the solution and their concentration, the interaction between them as well as solvation energies. The precise value of $E_{F,redox}$ is not yet given in the literature due to the difficulty of calculations. Below, **Figure 2. 9** illustrates the change in the position of energy bands and water HER/OER potentials for two different cases (pH = 0 and 14).

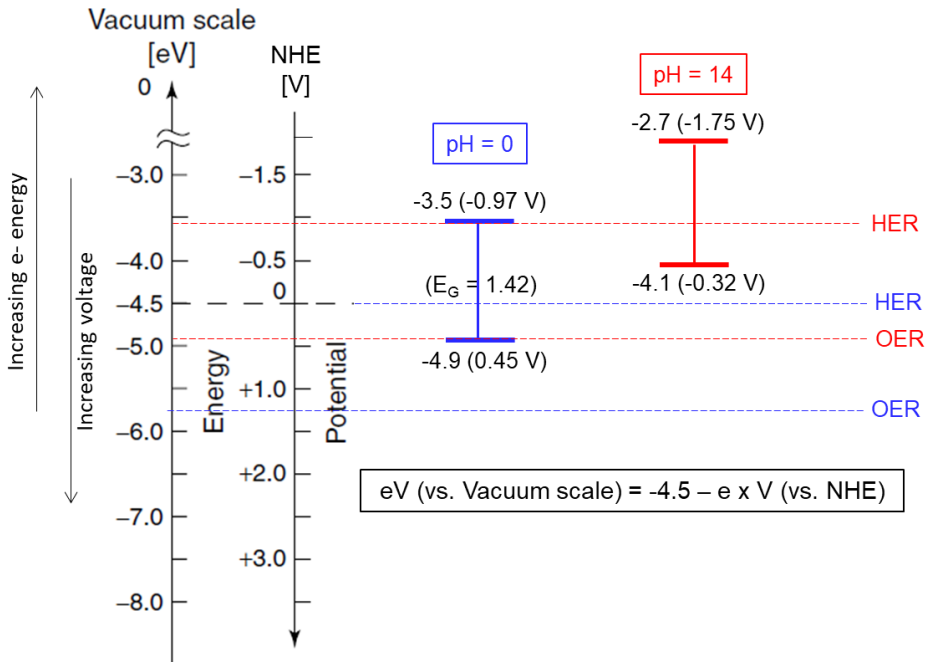

Figure 2. 9 Energy band levels of GaAs relatively to the water HER/OER potentials in eV (vs. Vacuum) and V (vs. NHE) at pH=0 (blue) and pH=14 (red). Adapted from [110,112] The equation in the inset represents the relation between eV vs. Vacuum and V vs. NHE

In electrochemistry the energy levels of oxidation-reduction reactions (including water splitting) are reported in terms of electrochemical potentials vs. the standard hydrogen electrode (SHE) or NHE. In solid state physics the semiconductor band energy levels are generally represented in absolute scale (eV vs. vacuum scale). In order to be able to discuss the band-alignment between the semiconductor energy bands and water redox potentials, these energy scales are linked through the absolute vacuum scale with a correspondence between -4.48 eV [113] on the vacuum scale and the "zero volt" reference in NHE. As a result, the absolute energy scale (eV vs. Vacuum) can be transformed into NHE or vice-versa using the relation indicated in the inset of **Figure 2. 9**

2.6.2 Description of the PEC setup

To investigate PEC properties of the photoelectrodes studied in this work, a laboratory scale three-electrode PEC experimental setup was used (as shown in **Figure 2. 10 (a)).** It is composed of a working electrode (WE) which is the photoelectrode to be studied, a reference electrode (RE) and a counter electrode (CE), all connected to the external potentiostat.

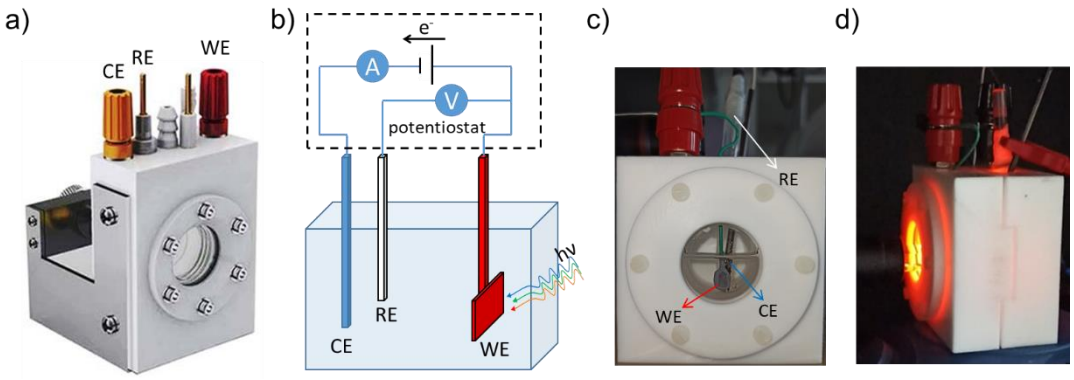

Figure 2. 10 (a) laboratory scale standard PEC cell, with (b) schematic illustration of the 3-electrode configuration operating at oxidation reaction with an n-type semiconductor as a photoanode, (c) PEC cell developed in Institut FOTON in this thesis (d) during the PEC experiment under red light (656 nm) illumination.

The illumination of the photoelectrode is realized using a solar simulator AM 1.5G with the power density of 100 mW/cm^2 (referred often as 1-sun). [114] Here, I will describe the PEC cell with each electrode individually in details as it is the most prevalent experimental tool used to characterize PEC properties of the samples in this work.

2.6.2-a Working electrode (WE) and counter electrode (CE)

Photoelectrodes on which the reaction of interest occurs, are referred as working electrodes (WE). Especially, photoanodes or photocathodes can be considered for the electrochemical oxidation and reduction reactions, respectively. The counter electrode (CE) acts as a charge collector, and takes up electrons or holes if the WE is performing oxidation or reduction reaction, respectively. The electric current (ampere, A) generated during the electrochemical reaction is measured between the WE and the CE which are both connected to the potentiostat (**Figure 2. 10 (b)).**

2.6.2-b Reference electrode (RE)

The electrochemical potential of the electrode is measured relatively to the reference electrode. Therefore, an additional third electrode is required in order to study the influence of the external applied bias potential (V_{bias}) on the performance of the WE. Practically, the potential of a photoelectrode is measured with respect to another electrode

that has a constant and stable potential. Introducing a reference electrode (RE) in the cell thus allows measuring precisely the potential of the WE performing oxidation or reduction reactions. One might refer to the measurement of the potential difference between WE and CE using a conventional multimeter. However the voltage difference measured in this case is dependent on the overall cell current that could lead to some experimental errors. [43,115] The advantage of using a RE is that the potential difference between the WE and the RE is independent on the current flow. There are several types of REs, the choice of which depends on the nature of the used electrolyte and pH. Although the normal hydrogen electrode (NHE: H^+/H_2), saturated calomel (SCE: Hg/Hg_2Cl_2) and silver chloride (Ag/AgCl) REs are widely used in most experimental setups, [116] recent literature has reported on the advantages of using the virtual reversible hydrogen electrode (RHE) scale to alleviate the influence of the pH and to avoid confusion in the interpretation of measurements. The virtual RHE electrode scale takes into account the pH of the solution in relation to the reference potential applied in the reaction. Conversion of the experimentally used RE such as NHE, SCE and silver chloride electrode to the RHE scale is done as follows:

$$E_{RHE} = E_{NHE} + 0.059 * pH \rightarrow E_{RHE} = E_{NHE}\ at\ pH = 0 \quad (2.27)$$

$$E_{RHE} = E_{SCE} + 0.059 * pH + E^o_{SCE}(0.241) \quad (2.28)$$

$$E_{RHE} = E_{Ag/AgCl} + 0.059 * pH + E^o_{Ag/AgCl}(0.197) \quad (2.29)$$

Initially, the PEC setup from Institut des Sciences Chimiques de Rennes (ISCR) consisting of a solar simulator AM 1.5G with 1-sun illumination intensity (100 mW/cm^2) and Zahner potentiostat were used in collaboration to perform PEC measurements on the first studied samples. During the second year of my thesis, we developed a PEC setup in Institut FOTON which is dedicated to PEC experiments under monochromatic light excitation with lasers of different wavelength. In this thesis, the PEC measurements under 1-sun illumination were conducted with the PEC setup of ISCR, whereas the PEC measurements under monochromatic light were performed using the PEC cell developed in Institut FOTON. For both setups the same PEC cell (developed in this thesis) was used. It consists in a working electrode (WE) being the photoanode of interest, an Ag/AgCl in saturated NaCl solution reference electrode (RE) and a graphite rod counter electrode (CE). **Figure 2. 10 (c-d)** displays the PEC cell developed during this thesis with all

electrodes assembled and connected to the potentiostat operating under red light illumination (656 nm). The set of PEC measurements performed for the samples studied in this thesis is described below.

2.6.2 Linear sweep voltammetry

Linear sweep voltammetry (LSV) is a voltametric method where the current at the photoelectrode is measured while sweeping the voltage at the RE linearly with time. Generally, the LSV is measured in three different conditions: with light, in dark and alternated light (on-off). The resulted current under light illumination is called photocurrent and usually normalized with photoelectrode active surface area. Thereafter, the photocurrent becomes a photocurrent density (*j*) and the LSV measurement is further referred as "*j*-V". The result of the measurement is plotted as *j*-V plots with y-axis expressed in (mA/cm^2) and x-axis in (volt vs RHE) which is calculated from the as-measured voltage with the RE (Ag/AgCl) using the equation (2.29). The value of *j* is very important as it is related directly to the photon-to-electron conversion efficiency of the material and the ability to extract the photo-generated carriers for contributing to oxidation and reduction processes. The materials capable of generating higher *j* are generally targeted for the solar energy harvesting devices. Another important parameter that can be extracted from the *j*-V curves is the onset potential (V_{onset}) that defines the ability of producing high photovoltage (V_{ph}). As a general trend, a photoanode (photocathode) having a low (high) V_{onset} is expected to have a large V_{ph}, which is particularly interesting for the un-assisted PEC water splitting, as most of the input energy required is produced in this case from solar energy. On the contrary, a large V_{onset} of a photoanode implies usually a small V_{ph}, which is less interesting for un-assisted water splitting, as more energy is needed from external bias to enable the PEC operation. As an illustration, **Figure 2. 11** shows a typical *j*-V curve obtained from a photoanode of $GaP_{1-x}As_x$ alloy with x(As)=0.8, where a photocurrent of 11.3 mA/cm^2 at water oxidation potential (1.23 V vs RHE) and a V_{onset} of 0.38 V vs RHE is measured.

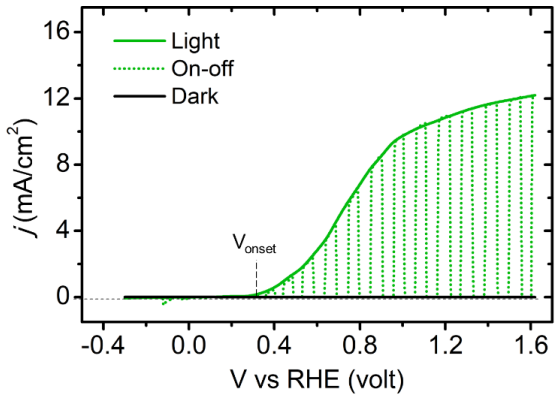

Figure 2. 11 Typical j-V curve for a photoanode of $GaP_{1-x}As_x$ alloy with x(As)=0.8, measured in 0.2 M H_2SO_4 (pH = 0.35) under 1-sun illumination

2.6.3 Open-circuit potential and photovoltage

In PEC water splitting, the open-circuit potential (OCP) is the equilibrium potential between the electrode and the electrolyte. At OCP in the dark (OCP_{dark}), the photoelectrode potential is determined by the equilibrium potential of the redox system (in other words, the Fermi level of the electrolyte, E_{redox}). [35] However, different photoelectrode materials show different OCP_{dark} even if the measurement is performed in the same electrolyte. This can be attributed to different surface acidity, and surface reactions of the semiconductor photoelectrode. [35] Under light, the OCP is determined at $j = 0$ as shown in **Figure 2. 12 (a)**. OCP under illumination provides insights such as conductivity type (n or p) and flat-band potential (V_{fb}). For the n-type semiconductors, the OCP under illumination shifts toward negative potentials vs RHE, as compared to the dark OCP. The inverse is valid for the p-type semiconductors. [115] Under high illumination intensity, the band bending decreases, tends to be flat and it becomes possible to estimate the flat-band potential V_{fb} (see chapter 1). However, high intensity illumination may cause a strong photocorrosion and the estimated values in this case might be misleading. **Figure 2. 12 (a)** shows the j - V curve in the dark and light calculated from Gartner equation for the illustration of the OCP in the dark, light and V_{ph} which is (OCP_{dark} - OCP_{light}). [35] In addition, the experimental OCP vs Time plot obtained for a bare GaAs:n wafer used in this thesis is shown in **Figure 2. 12 (b)** with corresponding energy bands.

In literature, the V_{ph} is mainly determined with 1-sun illumination at a given specific power density (100 mW/cm^2) in order to compare to other research works. In this thesis we have performed the V_{ph} measurements in the same three-electrode PEC cell experimental setup used for the LSV experiments. As an illumination source we have used 1-sun illumination (AM 1.5G) with 100 mW/cm^2

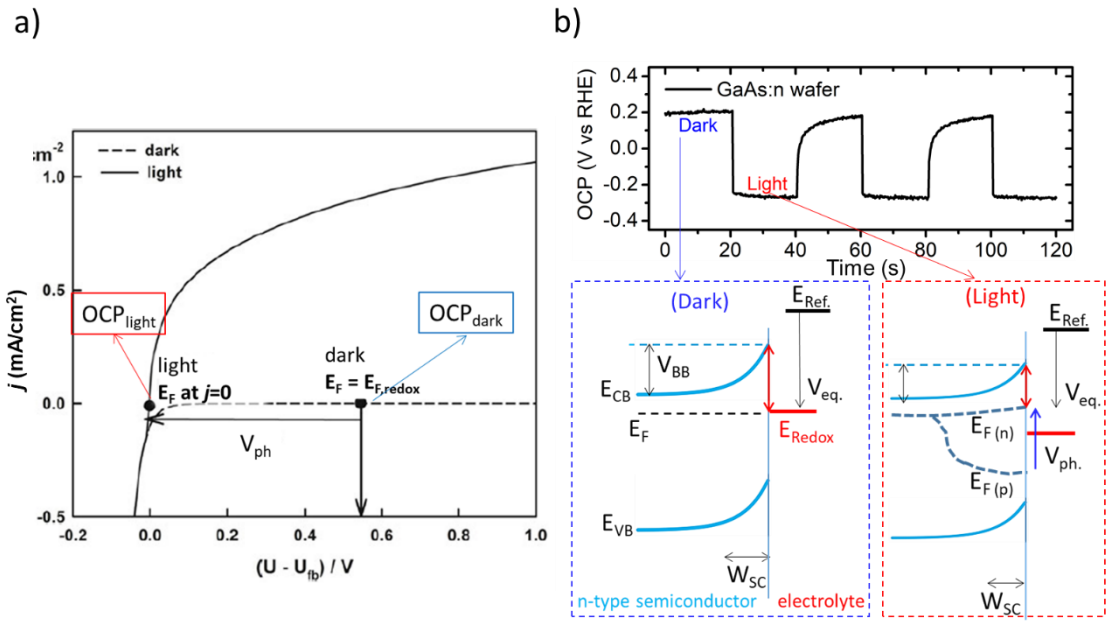

Figure 2. 12 (a) j-V curve in the dark and light for illustration of the OCP and V_{ph} adapted from [35]; (b) Experimentally measured OCP vs Time measured in the dark and light with the corresponding photoelectrode energy bands for GaAs:n wafer used in this thesis.

2.6.4 Flat-band potential

Together with the OCP and the V_{ph}, it is important to determine the flat-band potential (V_{fb} see chapter 1) as this parameter helps to elucidate the band-alignments of a semiconductor relatively to water redox potentials. The most common way to estimate the V_{fb} is by measuring the differential capacitance of the electric double layer at the semiconductor-electrolyte interface, often referred as Mott-Schottky experiment. [117] The measured capacitance of the interfacial double layer ($C_{Interface}$) mainly includes the semiconductor capacitance (C_{SC}) and the Helmholtz layer capacitance in the electrolyte (C_H) which are connected in series ($1/C_{Interface} = 1/C_{SC} + 1/C_H$). As the potential drop occurs mainly in the semiconductor depletion layer, the C_{SC} varies (decreases) with the extent of band bending, while C_H is expected to remain constant, hence it is often assumed

that ($C_H >> C_{SC}$), such that $1/C_{Interface} \approx 1/C_{SC}$. The reciprocal of the square of C_{SC} vs applied voltage or potential drop (V) gives Mott-Schottky (MS) plot as shown in **Figure 2. 13 (a)**. However, in experimental data, Mott-Schottky plots may contain a non-negligible contribution of C_H. For instance, in **Figure 2. 13 (b)** theoretical values of $1/C_{SC}^2$ are compared with $1/C_{Interface}^2$ as a function of the potential drop associated to the semiconductor band bending with different doping densities (N_D). In this case, $1/C_{Interface}^2$ has to be corrected by the $1/C_H^2$ in order to obtain reliable estimation of V_{fb}, particularly for highly doped semiconductors where the approximation is not valid anymore. In practice, even after correction by C_H, the perfectly linear MS plot is not always guaranteed, due to other factors (surface states, non-uniform doping, defect density, etc) that may influence the band bending.

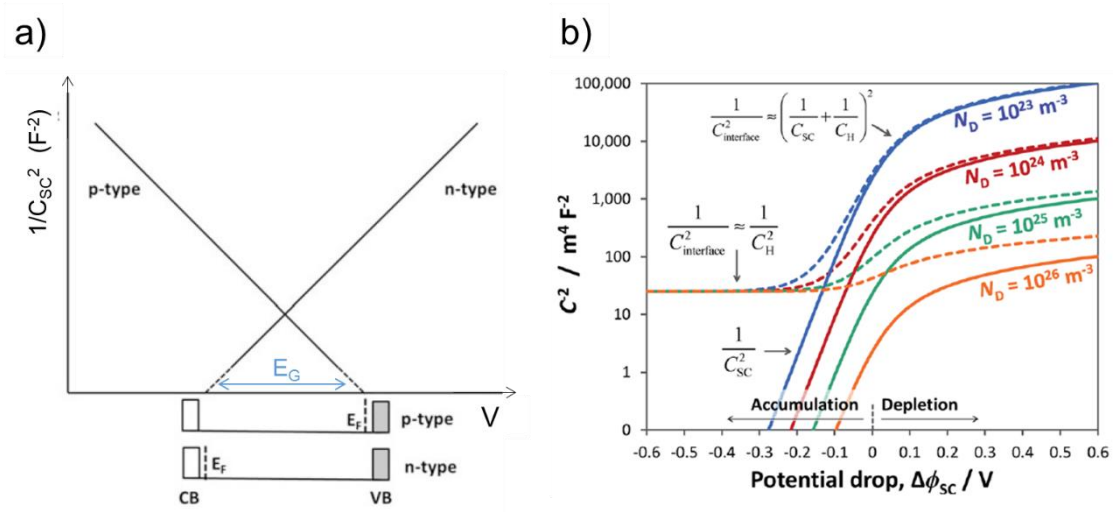

Figure 2. 13 (a) Schematical illustration of the ideal MS plots for the same material doped p-type and n-type with the corresponding E_F, E_G and relative positions of energy bands adapted from [35]; (b) Theoretical values of $1/C_{Interface}^2$ (dashed-line) and $1/C_{SC}^2$ (solid-line) as a function of semiconductor band bending for the given doping densities (N_D) adapted from [44]

From the experimental measurement of the capacitance, the Mott-Schottky equation further makes the link between the measured C_{SC} and V_{fb} as follows:

$$\frac{1}{{C_{SC}}^2} = \frac{2}{eN_D A^2 \varepsilon_0 \varepsilon_r}\left(V - V_{fb} - \frac{kT}{e}\right) \tag{2.30}$$

where, ε_r is the relative permittivity of the semiconductor, ε_o is the permittivity of vacuum, A is the surface area, e is the charge of an electron, N_D is the free carrier density,

k is the Boltzmann constant, *T* is the temperature and *V* is the applied potential. The V_{fb} can be extracted from the x-intercept of the $1/C_{SC}^2$ (y-axis) of the linear portion of the MS plot as shown in **Figure 2. 14.** The N_D can be extracted from the slope of the MS plot and is generally compared to the known doping of a semiconductor to check the validity of the MS measurement. Furthermore, the relative position of the energy bands can be determined. N-type semiconductors with the N_D in the range of 10^{18} cm^{-3} usually show a negative V_{fb} that corresponds to E_F closer to the CB and thus it can be assumed that $V_{fb} \sim E_{CB}$. The opposite is observed for the p-type semiconductors ($V_{fb} \sim E_{VB,}$ for the p-type). For the same semiconductor of type n and p, the difference between V_{fb} gives the band gap (E_G) of the respective semiconductor (**Figure 2. 13 (a)**).

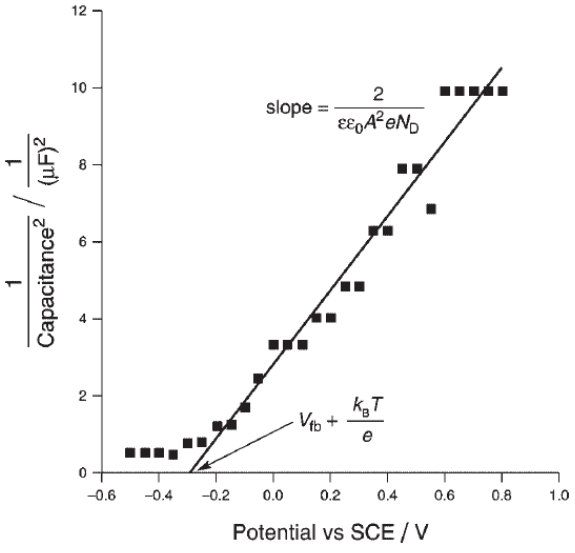

Figure 2. 14 Mott–Schottky plot measured for ZnO in 7 × 10^{-4} M $K_3[Fe(CN)_6]$ in 1 M KCl. Adapted from [117]

Together with the concept of band bending and V_{fb} it is possible now to interpret a typical experimental *j*-V curve, i.e., obtained with a n-type GaAs wafer. **Figure 2. 15** displays the experimental *j*-V curve of an n-type GaAs photoanode and the corresponding band bending situations at different applied positive potential (anodic) for illustration. (i) At a negative potential (cathodic) lower than the V_{fb}, the electron accumulation layer is formed at the semiconductor/electrolyte interface and electrons partially can be transferred to the electrolyte, subsequently resulting in a cathodic current, without illumination. (ii) While the bands are flat at V_{fb}, no space charge layer is formed to separate light induced charge

carriers and thus the resulting current is zero. (iii) Increasing the potential at a value larger than V_{fb}, a space charge layer is formed to separate and transport photo-generated charge carriers towards the electrolyte to enable the redox reaction. This results first in a small photocurrent, subsequently increasing with the applied potential due to increased spatial extent of the depletion layer. (W_{SC}). (iv) The photocurrent saturates when a larger positive potential is applied. In this case, all the light-induced charge carriers can reach the semiconductor-electrolyte interface, provided that they can diffuse in the semiconducting material. In this case photocurrent is limited by the diffusion length of minority carriers (L_{min}).

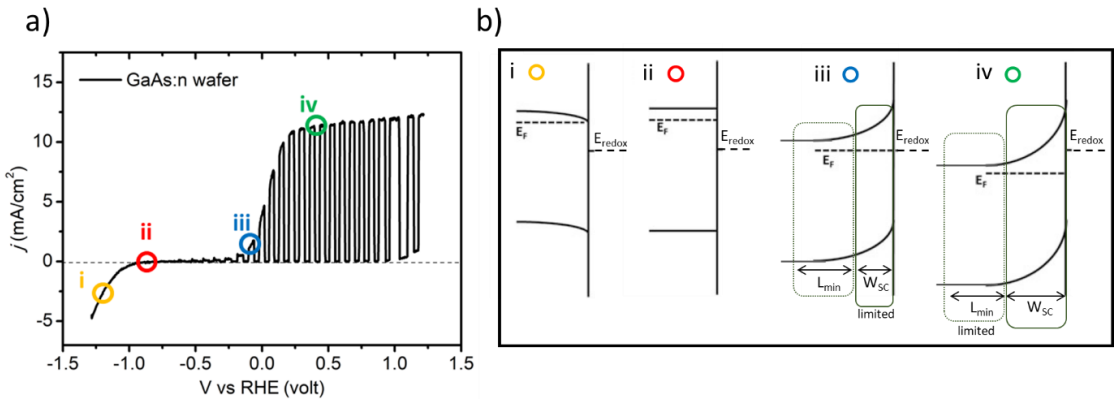

Figure 2. 15 (a) Correlation between the experimental j-V curve of an n-type GaAs and (b) band diagram model of an n-type semiconductor at different applied potential

2.6.5 Chronoamperometry

Chronoamperometry (CA) is the electroanalytical technique to measure the stability or time dependent behavior of the photoelectrode. The general concept of the CA is to measure the current of the cell as a function of time. The CA is usually performed in the dark (under illumination) to test the electrochemical stability (photoelectrochemical stability) under a specific applied voltage. In this case, stability of the photoelectrode can be assessed from the change of the photocurrent density over a certain period of time. Overall, this gives an idea of the lifetime of the photoelectrode.

2.6.6 Incident Photon-to-Current Efficiency

Incident Photon-to-Current Efficiency (IPCE) also known as the Quantum Efficiency (QE) is an important metric to establish what is the spectral response of a semiconductor photoelectrode. According to its definition, IPCE measures the ratio of electron flux, $n_e(\lambda)$ that is generated in the photoelectrode to the overall photon flux, $n_{ph}(\lambda)$ that shines on the respective photoelectrode, in a range of wavelengths. The IPCE measurement gives an idea of how many charge carriers are generated per incident photon, how efficiently they are transported to the space charge region and transferred through the interface to the electrolyte. [115] The IPCE is described in the form of mathematic equation shown below,

$$IPCE(\lambda) = \frac{n_e(\lambda)}{n_{ph}(\lambda)} = \frac{I(\lambda)}{P * A} * \frac{h * c}{\lambda * e} \tag{2.31}$$

where, $I(\lambda)$ is the photocurrent at a given wavelength (λ), P is the power density of the illumination source, A is the area of the electrode, h is the Planck's constant, c is the speed of light in vacuum and e is the charge of an electron.

In this thesis, the IPCE measurements were performed with a CIMPS-QE IPCE 3 workstation (Zahner) with a TLS03 light source tunable in the 1.2 - 4.2 eV range (**Figure 2. 16 (a)**). The three-electrode PEC cell and potentiostat used were identical to those used for the classical $j - V$ characterizations. The applied potential was (0.8 – 1) V vs RHE. The input parameters were set as following: the light modulation frequency 1 Hz, the settling time 5 s, and the number of counts 25. The final result was provided by Thales software in the form of photocurrent efficiency (A W^{-1}) or IPCE (%) as shown in **Figure 2. 16 (b)**. In order to verify the consistency of the measurements, the integral of the photocurrent efficiency (A W^{-1}) together with the AM 1.5G solar spectrum were used to obtain the integrated photocurrent density ($j_{integrated}$) and then compared with the results of the LSV measurement.

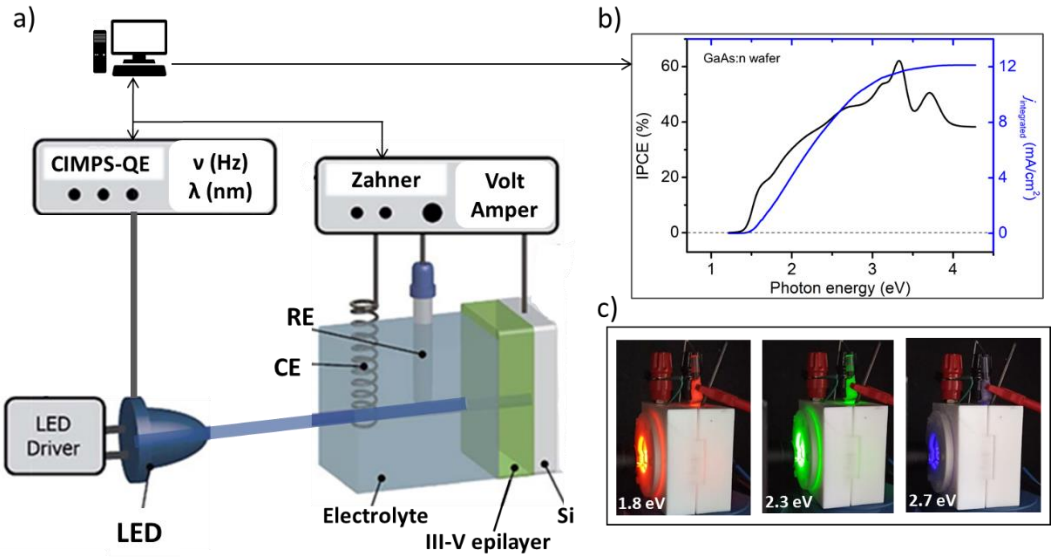

Figure 2. 16 (a) Schematic representation of IPCE measurement with (b) the measured IPCE curve and integrated photocurrent for GaAs:n wafer and (c) PEC cell under different photon energy illumination

Chapter 3

Dual band gap operation of GaAs/Si photoelectrode

Chapter 3. Dual bandgap operation of GaAs/Si photoelectrode

Building on the promising results in solar water-splitting demonstrated with a planar GaPSb thin-film photoanode grown epitaxially on a low-cost Si substrate, [17] I study in this chapter the ability to achieve similar results, but with the mainstream GaAs semiconductor, known for years in the field of photonics or photovoltaics, monolithically integrated on silicon. This chapter presents an in-depth comparison between the photoanode performances of a 1-µm thick epitaxial GaAs grown on n-type Si substrate and a photoanode made of a commercial GaAs wafer.

3.1 Introduction

Solar water-splitting technology to produce green hydrogen was discussed earlier in chapter 1. As a reminder, the ideal photoelectrode material should combine simultaneously (*i*) a large light absorption with solar energy harvesting capabilities over the largest solar spectral range, (*ii*) a bandgap and band lineups appropriate to drive the water splitting half-reactions at lower overpotential, (*iii*) a longer lifetime of operation and (*iv*) low fabrication costs, for instance through the choice of Earth-abundant materials. III-V semiconductors show a great potential for solar water splitting due to remarkable intrinsic physical properties leading to large light absorption and enhanced mobility for charge carriers and efficient charge transfers to the electrolyte, thus leading to high photocurrent densities and large solar-to-hydrogen (STH) efficiencies. [10,46] As a result, relatively high-efficiency photoelectrodes were achieved with III-V semiconductors, as compared to oxide semiconductors or traditional silicon. [30] Despite the excellent optoelectronic properties of III-V semiconductors, their poor stability (against corrosion) in aqueous electrolytes was pointed out in the pioneering work of Khalesev and Turner, showing nevertheless promising photocurrent densities of 10 mA/cm^2 with a Pt/GaInP$_2$/GaAs photoelectrode under 1-sun illumination. [58] This issue was recently fixed by application of thin-film materials as protective layers, [9,118,119] especially metal-oxide layers as a protection for III-V photoelectrodes. [85,86,88] For instance Hu et., successfully demonstrated an n/p$^+$ GaAs-based photoanode operating at a photocurrent density of 14.3 mA/cm^2 with a stable operation for more than 25 h thanks to a TiO_2 passivation layer and an optically transparent Ni OER co-catalyst. [85] This

proposed passivation method was further confirmed for a $GaP_{1-x}Sb_x$ photoanode, indicating that this approach can be transposed to a large variety of other III-V materials. [17] Although photoelectrodes with III-V multi-junctions architectures composed of series-associated p-n junctions are complex to fabricate, with multiple doping steps and necessary tunnel junctions, they are the best solutions so far to increase the junction voltage. Thus, the most of research works dealing with III-V photoelectrodes were carried out using commercial binary III-V substrates, [10]. The development of these III-V technologies occurs at the expense of high substrate and fabrication costs and sustainability issues with the use of toxic materials or critical resources for their production. [120]

The reduction of the fabrication cost motivated the development of III-V thin films or nanostructures photoelectrodes on Si. [82,99,101,121] Recently, planar III-V nitrides photoelectrodes on silicon substrate were employed by Nötzel et al., who reported a photocurrent density of 13.6 mA/cm^2 at 1.23 V vs RHE, which was further improved by using surface quantum dots activated structures. [19] Simultaneously, the first planar Zinc-Blende III-V photoelectrode grown on a silicon substrate was demonstrated by our laboratory, by using a GaPSb alloy, producing a photocurrent density of 10 mA/cm^2 at 1.23 V vs RHE. [17] This work was further extended to other III-V/Si materials systems, i.e., GaP and GaAsP alloy grown on Si with the measured photocurrent density equals to 1.0 and 11.3 mA/cm^2, respectively. [18] But still, in these various demonstrations, the Si substrate was considered as a starting template for further photo-active III-V material regrowth, which performances are usually governed by the crystal defects density generated during III-V/Si heteroepitaxy. [18] Despite the advantages of using the III-V/Si association as a dual-bandgap architecture highlighted in reference [101], the spectral contribution of the Si substrate itself to the photoresponse of a planar III-V/Si photoelectrode has never been reported so far.

From this perspective, in the following sections will be given the details of material growth, photoelectrode elaboration, characterization methods and discussion of results. The wide-range potential of the epitaxial GaAs/Si thin-film photoelectrode is specifically assessed based on structural, optical, photoelectrochemical characterizations and compared to a reference n-doped commercial GaAs wafer. Experimentally measured

photocurrent density is relatively analyzed to the theoretically calculated one using the absorption coefficient of the sample and spectral photon flux density of the solar spectrum AM 1.5G. [114,115] Additionally, photoelectrochemical characterization under tunable monochromatic light source is used to investigate the large photocurrent measured with a GaAs/Si photoanode. The interest of using such a simple dual-bandgap architecture as a single photoelectrode is finally discussed. In this chapter, the "Dual-bandgap" simply refers to the association of two different materials with two different bandgaps, and "dual bandgap operation" means that the carriers photo-generated in both materials (the GaAs epilayer and the Si substrate) can contribute to the electro-chemical redox reaction.

3.2 Material growth and photoelectrode elaboration

For this study, a 1-µm thick GaAs thin film was grown in a bi-domain configuration (i.e., with emerging antiphase boundaries as described in reference [18]) by Molecular Beam Epitaxy (MBE) on a HF-chemically prepared Si substrate [001] (n-type, Ph-doped $5x10^{14\text{-}15}$ cm^{-3}, with a thickness of 350 µm) misoriented by 6^0 off toward [110] direction. The substrate was heated at 800°C for 10 min to desorb hydrogen. Following the preparation of the 350 µm-thick Si substrate, 1 µm-thick GaAs layer was epitaxially grown at 500°C with a growth rate of 0.24 ML/s in a conventional continuous MBE growth mode. Beam Equivalent Pressure V/III ratio was set to 7.36. It should be noted that the GaAs epilayer was non intentionally doped (nid), and epitaxial strategies to annihilate antiphase boundaries (APBs) were not used leading to emerging APBs. [18,61] In addition, a homoepitaxial nid GaAs (1 µm) was grown on an n-doped GaAs [100] (350 µm) for comparison of photoelectrochemical properties. A commercial n-doped GaAs wafer [100] (350 µm in thickness) was used as reference material to compare the structural and optical properties as well as photoelectrochemical performances.

After the growth of a 1-µm thick GaAs thin-film on Si substrate (GaAs/Si), and on GaAs substrate (GaAs/GaAs), the photoanodes (PA) of GaAs/Si, GaAs/GaAs samples and the GaAs wafer were prepared by cleaning the sample in the ultrasound cleaner for 10 s and subsequently dried with N_2 gas. The backside was slightly scratched and metallic contact was made using Gallium-Indium eutectic, silver paste and conductive wire

(chapter 2). The geometric surface area was defined using an epoxy resin covering the backside and the edges of the PA (**Figure 2. 6**) and calculated using ImageJ software.

3.3 Structural characterization of GaAs/Si and GaAs wafer

The structural characterization of the epitaxially grown GaAs (1 μm)/Si:n and the reference GaAs:n wafer (350 μm) was first carried out using X-Ray Diffraction in the conventional ω/2θ mode. **Figure 3. 1 (a)** shows XRD ω/2θ scans performed in the vicinity of Si (004). A thin Bragg peak is first observed at 69.13° for the GaAs/Si sample, corresponding to the Si substrate. A well-defined Bragg peak is also observed at a 2θ angle (66.02°) for the epitaxial GaAs/Si, very near from the position of the commercial GaAs wafer peak (66.06°), both giving a mean lattice constant of 0.565 ± 0.002 nm corresponding to the lattice constant of the bulk GaAs. [89] However, the Bragg peak for the 350 μm GaAs wafer Bragg peak appears narrow with an integral breadth (IB) of 0.018°, comparable to the Si one and resolution-limited. In contrast, the Bragg peak associated to the 1 μm GaAs epitaxial layer (IB of 0.294°) is much broader than what is expected for a good quality layer with the same thickness (expected IB of 0.043°). The strain relaxation rate was inferred from the space reciprocal maps (RSM) shown in **Figure 3. 1 (b-d)** around the (004), (224) and (-224) directions, giving a mean R of 97±2 % (R = 100%, indicates a fully plastically relaxation while R = 0% fully strained structure).

From the Bragg peak position in conventional ω/2θ scan and reciprocal space mappings it is clear that (*i*) the GaAs grown on the Si substrate is almost fully relaxed (and consequently its intrinsic physical properties can be compared directly to the bare GaAs wafer) and that (*ii*) GaAs/Si has a large density of crystal defects (induced by the relaxation process or the polar-on-non-polar epitaxy), namely micro-twins, misfit dislocations and antiphase boundaries. [61,122] These crystal defects are expected in bi-domain and mismatched III-V/Si samples when no strategies are used to bury or annihilate them. [65,66]

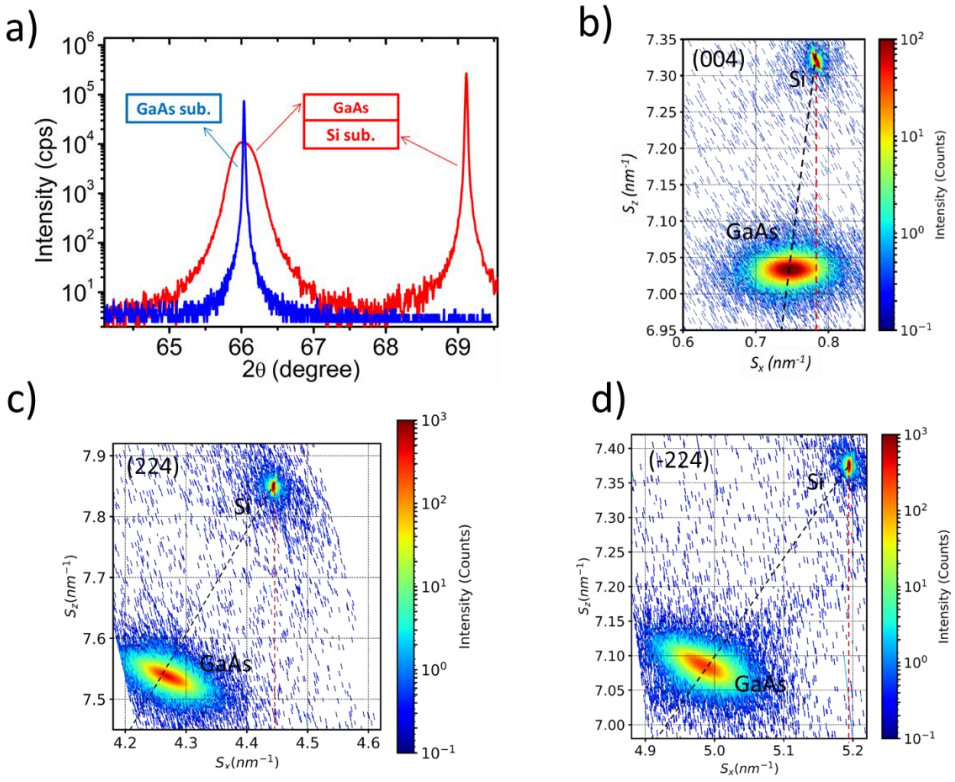

Figure 3. 1. (a) XRD ω/2θ scan performed in the vicinity of Si (004) with the Bragg peaks of the epitaxial GaAs (1 µm)/Si sample (red) and the GaAs (350 µm) wafer (blue); reciprocal space mappings around (b) 004, (c) 224 and (d) -224 showing the Si substrate and the epilayer. Black (red) dashed line corresponds to a fully plastically relaxation (fully strained) line

To further investigate the sample morphology, tapping mode atomic force microscopy (AFM) and scanning electron microscopy (SEM) were performed. The 10 x 10 µm² AFM image of the GaAs/Si sample is given in **Figure 3. 2 (a)**. An AFM image at the same scale for the GaAs wafer is given for comparison in **Figure 3. 2 (b)**. Epitaxial GaAs/Si sample surface reveals a root-mean-square (rms) roughness of 9.2 nm, higher than the one measured for the GaAs wafer (0.7 nm). This roughness is not really surprising and has to be related to the presence of numerous crystal defects in the GaAs epilayer grown on Si. [65] **Figure 3. 2 (c-d)** shows the tilted-top and side view SEM images for the epitaxial GaAs/Si sample. The Si substrate and the 1-µm thick GaAs epilayer can be easily distinguished from the two different contrasts of the side view SEM image. Roughness of the epitaxial GaAs/Si sample surface is thus confirmed over a scale larger than the AFM one.

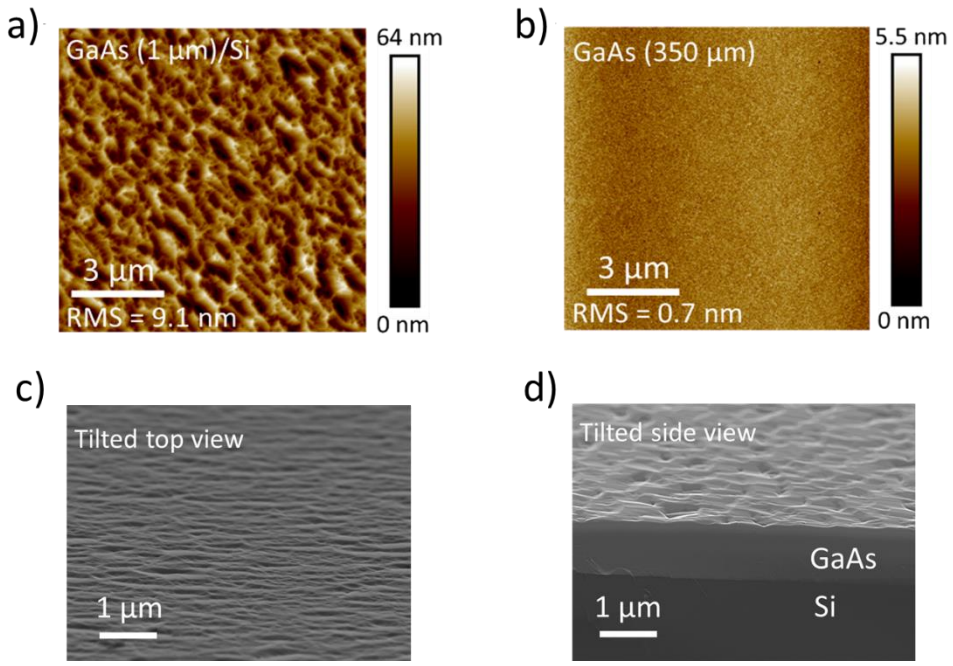

Figure 3. 2 (a) AFM image of the GaAs/Si sample and (b) of the commercial GaAs wafer morphology with a rms roughness of 9.2 nm and 0.7 nm, respectively; (c-d) Tilted top and side view SEM images of the GaAs/Si sample.

3.4 Characterization of optical properties

3.4.1 Light absorption coefficient (α) with spectroscopic ellipsometry

Optical properties of the epitaxial 1 µm-thick GaAs epilayer grown on Si substrate (GaAs/Si) were studied with A Horiba UVISEL 2 spectroscopic ellipsometer. The optical constants were measured at room temperature in the photon energy range of 0.6 – 4.2 eV and subsequently fitted with Tauc-Lorentz with 2 oscillators model in order to calculate thickness, roughness and absorption coefficient of the chemically mechanically polished (CMP) GaAs/Si sample. **Figure 3. 3 (a)** shows the experimental ellipsometry spectra for CMP-GaAs/Si, where the variation of the I_s (green) and I_c (orange) parameters as a function of the photon energy is plotted. The black lines correspond to the fitting curves obtained after adjusting the parameters of the Tauc-Lorentz 2 model. After fitting the raw data, the complex refractive indexes with the real (n) and imaginary (k) parts were extracted and plotted in **Figure 3. 3 (b)**.

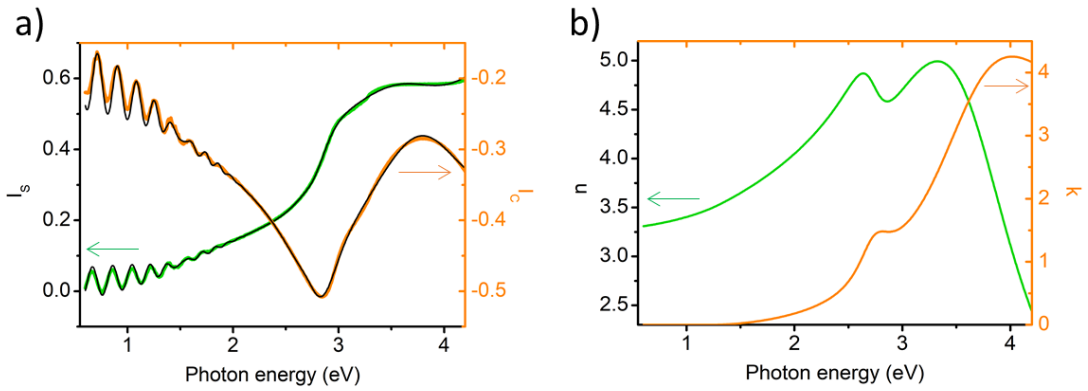

Figure 3. 3 (a) Is (green) and Ic (orange) ellipsometry parameters and fitting curves with Tauc-Lorentz 2 model (black); (b) optical constants n (real part) and k (imaginary part) extracted from the fitting data for the GaAs/Si sample.

The extracted values for the thickness (roughness) were 1.03±0.08 µm (0.01 µm) that are in good agreement with the SEM and AFM measurements. The absorption coefficient of the sample is then deduced from the imaginary (k) part of the refractive index as follows:

$$\alpha = \frac{4\pi k}{\lambda} \tag{3.32}$$

λ is the photon wavelength in (cm), α is the absorption coefficient and is given in **Figure 3. 4.** The optical constants used for the calculation of (α) for the reference GaAs wafer were extracted from the ref. [39]. The extracted absorption spectra, given in **Figure 3. 4** indicates that light absorption lies within the same order of magnitude for both GaAs/Si and GaAs wafer, and therefore that crystal defects do not affect significantly carrier photogeneration in GaAs.

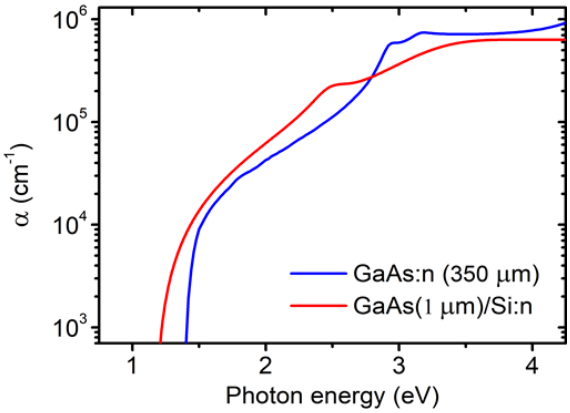

Figure 3. 4 Absorption coefficient determined for the GaAs epilayer in GaAs/Si (red) and for the reference GaAs wafer (blue)

3.4.2 Fraction of the photons absorbed from the solar spectrum AM 1.5G and theoretical photocurrent density

From the absorption coefficient measurements, and assuming zero electron-hole recombination, it becomes possible to evaluate the maximum theoretical photocurrent density ($j_{theoretical}$) generated in the two photoanodes. [115] For comparison, this calculation is first performed by considering only the epitaxial GaAs thin layer (1 μm) and the commercial GaAs wafer (350 μm) as photoactive layers. In this regard, the fraction of the photon flux absorbed by each GaAs layer in both samples ($\Phi_{sample}(\lambda)$) is calculated from its thickness (d_{sample}), its absorption coefficient ($\alpha_{sample}(\lambda)$), and the spectral photon flux of the simulated solar AM 1.5G ($\Phi_0(\lambda)$) using the equation below:

$$\Phi_{sample} = \Phi_0(\lambda) \times \left[1 - exp\left(-\alpha_{sample}(\lambda) \times d_{sample}\right)\right] \quad (3.33)$$

Figure 3. 5 (top) superimposes the solar spectral photon flux $\Phi_0(\lambda)$ (black solid line) and absorbed photon flux $\Phi(\lambda)$ for the 350 μm-thick commercial GaAs wafer (blue solid line), and the 1μm-thick GaAs layer in GaAs/Si sample (red solid line)

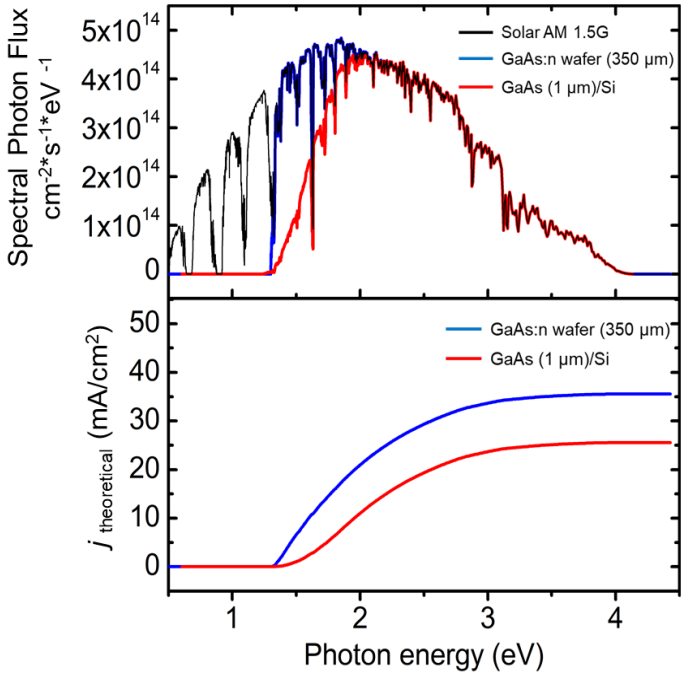

Figure 3. 5 Fraction of the photons absorbed by GaAs from the spectral photon flux of the AM 1.5G solar spectrum (black) for the 350-µm thick GaAs wafer (blue) and 1-µm thick GaAs layer (red) from GaAs/Si sample (top); $j_{theoretical}$ (mA/cm^2) calculated neglecting e^-/h^+ recombination (bottom)

Assuming that each photon absorbed generates one electron/hole pair, the total number of the absorbed photons multiplied by the electric charge (e) gives the maximum current density that can be produced as shown below,

$$j_{theoretical} = N_{photons\ absorbed} * e = \int_{E_{min}}^{E_{max}} \Phi_{sample} * e \qquad (3.34)$$

Figure 3. 5 (bottom) shows the deduced maximum integrated current density $j_{theoretical}$ for the epitaxial 1-µm GaAs layer as the red solid line (commercial 350 µm GaAs wafer as the blue solid line) with a photocurrent density at saturation equal to 25.5 mA/cm^2 (35.2 mA/cm^2), in close agreement with that calculated in references [30,115]. The difference in photocurrent densities between the two configurations is thus mostly related to the difference of GaAs thicknesses considered (1 µm vs 350 µm), the impact of which is enhanced when the absorption is lower (at energies near the GaAs bandgap).

3.5 Photoelectrochemical (PEC) characterization

PEC characterizations were carried out in a standard three-electrode configuration consisting of a working electrode (PA fabricated from the epitaxial GaAs/Si, GaAs/GaAs samples and the commercial GaAs wafer), a reference electrode (Ag/AgCl in saturated KCl), and a counter electrode (graphite rod). The used electrolyte was an aqueous 0.2 M H_2SO_4 solution (measured pH = 0.35). The solar light was simulated by a solar simulator (LS0106, LOT Quantum Design) equipped with an AM 1.5G filter with the measured power of 100 mW/cm^2. A Zennium potentiostat (Zahner) was used and potential was scanned at a rate of 50 mV/s. The measured potential vs Ag/AgCl reference electrode was converted to the comparable reversible hydrogen electrode (RHE) using the equation shown below,

$$E_{RHE} = E_{Ag/AgCl} + 0.197 + 0.059\,pH \tag{3.35}$$

3.5.1 Linear sweep voltammetry (LSV)

The crystal defects were considered for years as device killers in the field of III-V/Si photonics or photovoltaics. [123,124] Especially, these defects are usually considered as non-radiative recombination centers, hampering efficient transport in photoelectric devices. Thus, relatively lower photoelectrochemical (PEC) performance in terms of photocurrent density and quantum efficiency would be expected for the epitaxial GaAs/Si sample, as compared to the almost defect-free commercial GaAs wafer. In order to examine PEC properties, the photoanodes (PA) of GaAs/Si, GaAs/GaAs and the GaAs wafer were prepared as described in chapter 2. The net photocurrent density (j_{net}) was determined from the difference between photocurrent density of the electrode under 1-sun illumination (AM 1.5G, 100 mW cm^{-2}) and under dark conditions ($j_{net} = j_{light} - j_{dark}$) for the GaAs/Si PA, GaAs/GaAs PA and GaAs wafer PA and represented as a function of the applied potential in reversible hydrogen electrode scale (RHE) in **Figure 3. 6** Surprisingly, a slightly (but significantly) higher photocurrent is obtained at 1.23 V for the GaAs/Si PA (j_{net} = 13.74 mA/cm^2) as compared to the GaAs PA (j_{net} = 12.22 mA/cm^2). A similarly shaped *j*-V curve was obtained for the epitaxial GaAs/GaAs photoanode (PA) when compared to the epitaxial GaAs/Si PA. Importantly, the observed j_{net} at 1.23 V vs.

RHE for the GaAs/GaAs PA (7.94 mA/cm^2) is significantly smaller than the GaAs/Si PA, which could be related to the amount of charge carriers photogenerated and successfully transported to the electrolyte.

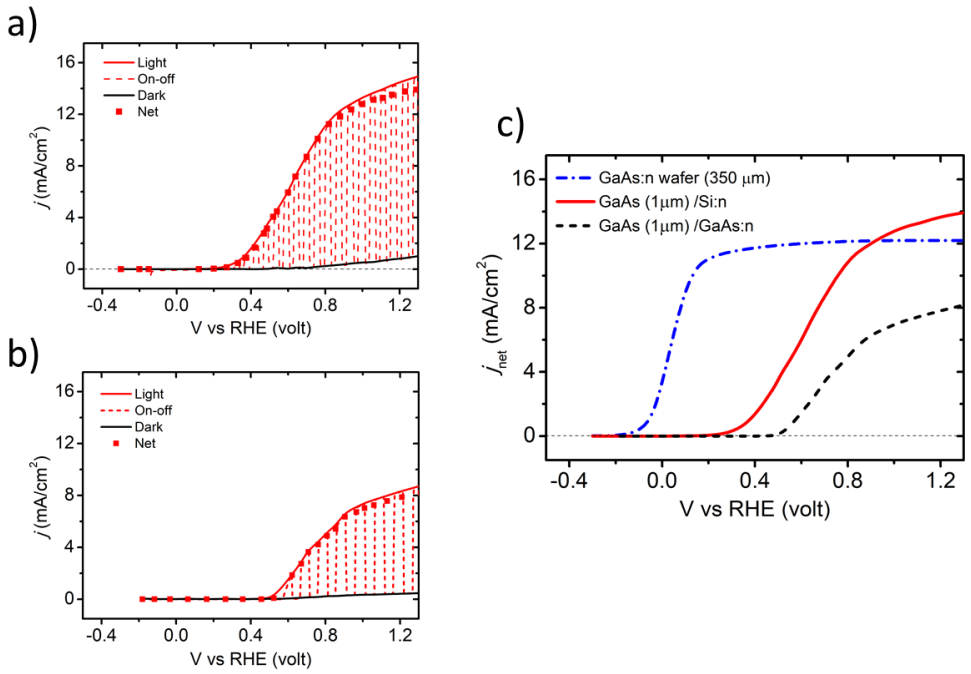

Figure 3. 6 Photocurrent density as function of applied voltage (j-V) recorded under light, chopped light and in the dark for (a) GaAs/Si PA; (b) GaAs/GaAs PA and (c) net photocurrent density ($j_{net} - V$) for the GaAs wafer (350 μm) PA (blue dashed-dotted line), the epitaxial GaAs (1 μm)/Si PA (red solid line) and the epitaxial GaAs (1 μm)/GaAs PA, respectively.

This result indicates that GaAs/Si sample with a large density of defects also generates the highest photocurrent which seems, at first, contradictory with previous reports using III-V/Si for photonics or photovoltaics. The high photocurrent of GaAs/Si suggests that (*i*) carriers transport in photoelectrodes is not affected by the crystal defects in the same way as in photonic or photovoltaic devices, [18] and (*ii*) there are additional contributions to the photocurrent, beyond the GaAs one, giving rise to higher photocurrent, which will be discussed in the upcoming sections.

Additionally, onset potentials (V_{onset}) of 0.38 V, 0.48 V and -0.08 V are extracted for GaAs/Si, GaAs/GaAs and GaAs, respectively, showing that the V_{onset} is significantly larger for both, GaAs/Si PA and GaAs/GaAs PA when benchmarked to GaAs wafer PA. The delay in V_{onset} can be attributed to the influence of interfaces in epitaxial samples.

The V_{onset} and the slope are convoluted with kinetics of OER reaction. As no catalysts were used in this study, the slopes of *j*-V curves are compared relatively and estimated to be 0.028, 0.016 and 0.049 Siemens/cm^2 for GaAs/Si, GaAs/GaAs and GaAs PA, respectively

3.5.2 Mott-Schottky and depletion layer width (W_{SC})

One can expect that, GaAs/Si will lead to a depletion width that extends much further into the bulk because of its nid low doping. Therefore, the electric field in the GaAs/Si would lead to enhanced carrier collection and thus higher photocurrent obscuring other loss channels. However, the recombination occurs not only in the bulk, but also in the depletion layer at the surface states and interfacial defects. [125] Nevertheless, in the absence of recombinations in the depletion layer, only the minority carriers generated within the distance of diffusion width (L_D) can be separated efficiently and transferred through the interface for redox reaction. [46,126] L_D is expected to be in the range of 3 – 10 μm [127] for GaAs. In case if the width of the depletion layer in GaAs/Si has a similar (or larger) value than the value of $L_{D,}$ the measured photocurrent would correspond only to the collection of photocarriers generated in the depletion layer, and thus a continuous increase of the photocurrent with the applied potential should be observed. On the contrary, a plateau is observed in the photocurrent of the GaAs/Si photoanode as shown in **Figure 3. 6 (c)**. This plateau is usually related to a diffusion regime in which the current is limited by the collection of photocarriers within the diffusion width $L_{D,}$ which is being larger than the depletion width.

To verify this experimentally, the Mott Schottky analysis for GaAs/Si was performed and the apparent doping density for GaAs/Si is determined to be 7.25x10^{17} cm^{-3} from 1/C^2 slope as shown in **Figure 3. 7 (a)**. The observed high-doping density likely results from the presence of antiphase boundaries in the material, which are electrically active and act as donor defects. [18] The width of the depletion layer as a function of the doping density is calculated using the equation below and plotted in **Figure 3. 7 (b)**.

$$W_{SC} = \sqrt{\frac{2\varepsilon_r \varepsilon_0 (V - V_{fb})}{N_D e}} \tag{3.36}$$

where, ε_r is the relative permittivity constant of GaAs (12.9), ε_o is the permittivity of vacuum (8.85 x10^{-14} F cm^{-2}), N_D is the doping density (7.25x10^{17} cm^{-3}), e is the charge of an electron (1.6 x10^{-19} C), V is the potential at the equilibrium (OCP_{dark}) and V_{fb} is flat-band potential from MS measurement (0.57 V).

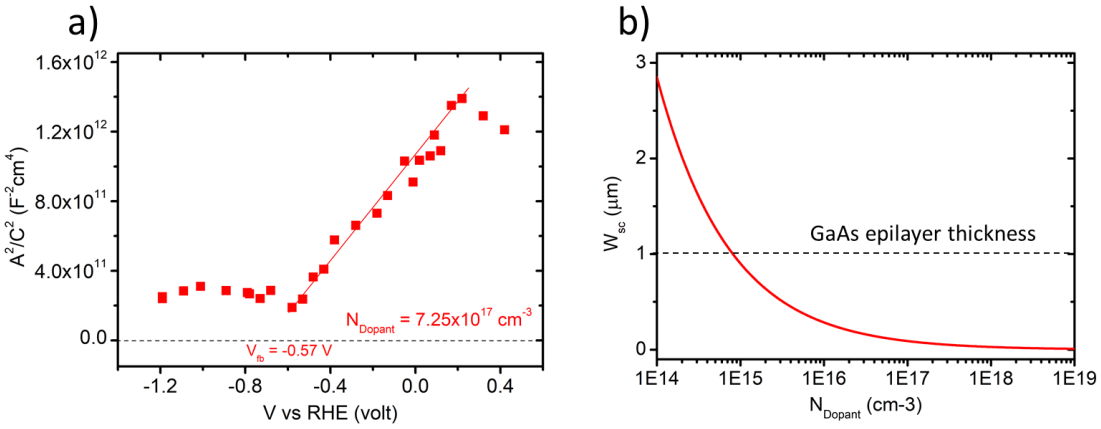

Figure 3. 7 (a) Mott-Schottky plot measured in the dark for the epitaxial GaAs on Si substrate showing the V_{fb} and N_D in inset; (b) Width of the depletion layer (W_{SC}) as a function of doping density (N_D) in LOG scale. Thickness of the GaAs epilayer (1 µm) is shown in inset.

It appears to be that; the width of the depletion layer (77 nm, for the apparent doping density for GaAs/Si) does not extend into the bulk in GaAs/Si and is below than the thickness of the epilayer. This confirms that photogenerated carriers collection is in diffusion regime in GaAs/Si, limited firstly by the diffusion width and secondly by the width of depletion layer.

3.5.3 Open-circuit potential (OCP)

Open circuit potential (OCP) measurements were carried out in the same three-electrode cell at the equilibrium to investigate the influence of the light on the studied samples, as shown in **Figure 3. 8**. Photopotential (V_{ph}) was then inferred from the difference between OCP measured in light and dark ($V_{ph} = OCP_{light} - OCP_{dark}$). A lower V_{ph} is obtained for the epitaxial GaAs/Si (0.22 ± 0.05 V), GaAs/GaAs (0.18 ± 0.02 V) than

for the GaAs (0.45 ± 0.03 V), confirming that the GaAs/Si PA requires a higher applied external voltage to enable photoelectrochemical charge transfer. This is consistent with the larger V_{onset} measured for the epitaxial GaAs/Si PA, and related to the presence of additional interfaces, in the case of GaAs/Si (Si/GaAs/electrolyte) and GaAs/GaAs (GaAs/GaAs/electrolyte) that may lead to potential drop at the hetero-interface. Please note that, GaAs/Si (GaAs/GaAs) is an epitaxial stack of nid GaAs and n-type Si substrate (n-type GaAs substrate), and thus does not involve multiple p-n junctions to be a tandem structure. Therefore, an increase in V_{ph} or decrease in V_{onset} is not expected for the epitaxial samples.

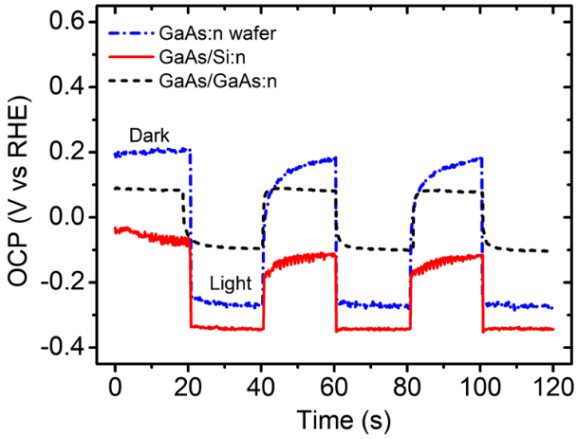

Figure 3. 8 OCP measurements for the GaAs wafer PA (blue dashed-dotted line), the epitaxial GaAs/Si PA (red solid line) and GaAs/GaAs PA (black dashed line) in 0.2 M H_2SO_4 electrolyte (measured pH=0.35) under simulated AM 1.5G illumination

3.5.4 Quantum efficiency of GaAs/Si and GaAs wafer photoanodes

Quantum efficiency or incident photon-to-current conversion efficiency (IPCE) was measured for the epitaxial GaAs/Si and GaAs PA using a tunable wavelength light-emitting diode (LED) illumination source (details in chapter 2) with the external applied potential at 0.8 V vs RHE. **Figure 3. 9 (a)** shows the IPCE curve and integrated photocurrent density ($j_{integrated}$) plot extracted from IPCE data for the GaAs/Si and GaAs PA where a maximum of IPCE around 60% was observed for both PA.

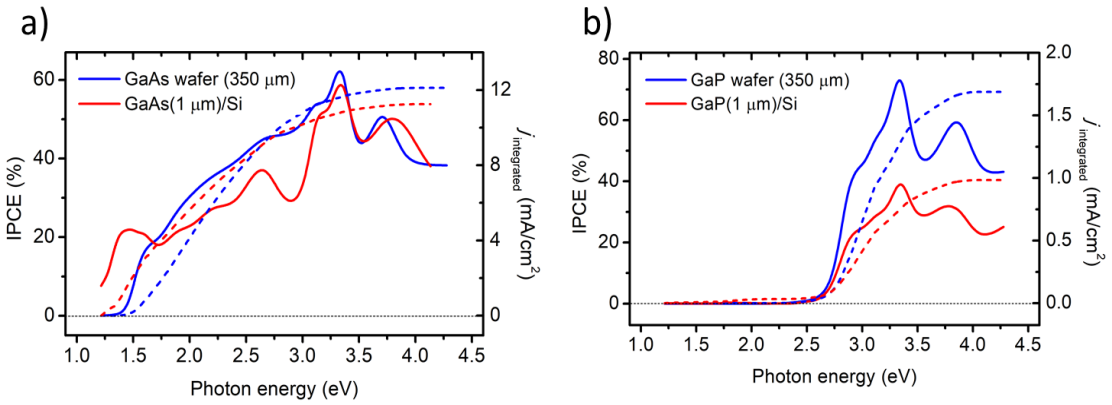

Figure 3. 9 (a) IPCE measured for the GaAs wafer and GaAs/Si PA; (b) GaP wafer and GaP/Si PA in the energy range of (1.21 - 4.2) eV at 0.8 V vs RHE

The $j_{integrated}$ at saturation was estimated to be 11 mA/cm^2 and 12 mA/cm^2 for GaAs/Si and GaAs, respectively, showing a good consistency of the measurements with the *j*-V voltammetric curves plotted above in **Figure 3. 6 (b)**. As expected, the GaAs wafer PA has a zero IPCE (no photoresponse) in the photon energy below 1.42 eV which corresponds to the bandgap of GaAs. [89] Whereas, this is not the case for the GaAs/Si that has a non-zero IPCE value below 1.42 eV. This sub-bandgap photoresponse could be mainly due to the Si substrate contribution to the photocurrent. While there is a possibility of Si substrate to be optically active in the case of the GaAs/Si PA, it does not appear to be a general trend for all III-V/Si associations; for instance, it is not the case for GaP/Si PA (**Figure 3. 9 (b)**). Indeed, below 2.7 eV (direct band gap of GaP), IPCE is near to 0 for both PA made of the GaP wafer and the GaP/Si sample, meaning that there is no sub-bandgap photoresponse contrary to the GaAs/Si PA. A more quantitative picture can be given through additional measurements of the photocurrent density under specific wavelength monochromatic excitation.

3.5.5 Photocurrent density under tunable monochromatic light illumination

Monochromatic light source with light-emitting diodes (LED) was used in order to study the response of the photocurrent density as a function of photon energy for the epitaxial GaAs/Si sample as it has two layers where both might be photoactive. The three-electrode PEC cell and potentiostat used for this experiment were identical to those used

for the classical ($j - V$) characterizations. The photocurrent density at 0.8 V vs RHE was measured with LED light at three different excitation energies (E_{exc}). The spectral information of each source is reported in **Table 3. 1**. The first E_{exc} (1.89 eV) was set to a photon energy significantly larger than the bandgap of GaAs. The second E_{exc} (1.36 eV) was set to a photon energy just below the bandgap of GaAs and the third one (1.23 eV) was chosen to lie significantly below the bandgap of GaAs. All the E_{exc} are however larger than the Si bandgap (1.12 eV). **Figure 3. 10 (a)** displays the photocurrent density measured alternatively at different E_{exc} and in dark conditions for the reference GaAs PA, showing a photocurrent density of 0.56 mA/cm^2 measured at E_{exc} = 1.89 eV. For the E_{exc} smaller than the band gap of GaAs (1.42 eV), it can be observed that the reference GaAs PA is not responding as the photocurrent is close to zero. In contrast to the reference GaAs, the epitaxial GaAs/Si PA results in a smaller but significant net photocurrent density equal to 0.12 mA/cm^2 and 0.07 mA/cm^2 even at smaller E_{exc} energies (1.36 and 1.23 eV) than the bandgap of GaAs (**Figure 3. 10 (b)**). These experiments show unambiguously that the Si substrate is photoactive in the GaAs/Si PA.

LED	Energy (eV)	Spectral width (eV)	Power density (mWcm^{-2})
1	1.89	0.08	5.7
2	1.36	0.03	2.3
3	1.23	0.03	3.5

Table 3. 1 Photon energy, spectral width and power density of the tunable monochromatic LED illumination source extracted from Thales software that controls LED source.

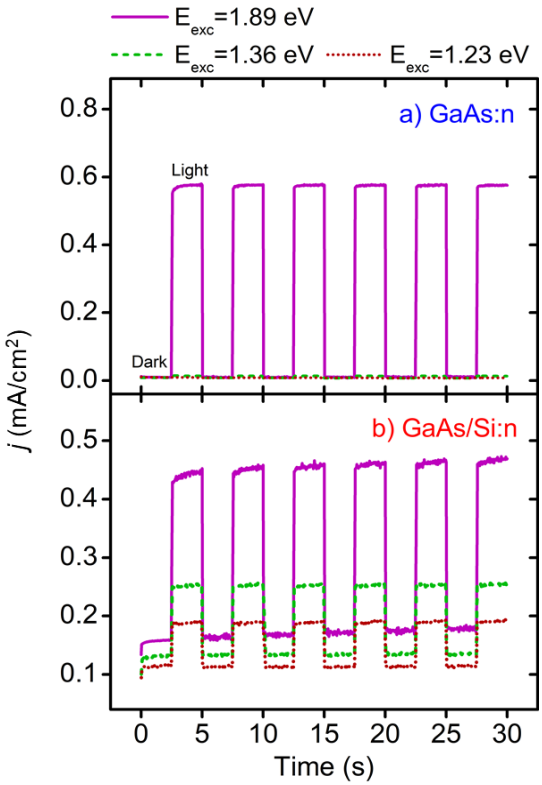

Figure 3. 10 (a) Photocurrent density measured under tunable monochromatic light illumination for GaAs wafer; (b) GaAs/Si PA at an applied potential of 0.8 V vs RHE

3.6 Discussion

To further clarify the high photocurrent obtained for GaAs/Si PA, a photoactive 350 µm-thick Si layer was added to the model in order to recalculate the fraction absorbed photons from the spectral photon flux of solar AM 1.5G spectrum and the maximum possible photocurrent density $j_{theoretical}$ that can be generated. Results are shown by green curves in **Figure 3. 11.** From these calculations, one can easily observe that the addition of Si as a photoactive material allows the absorption of the solar photon flux at lower energy **Figure 3. 11 (top)**. This results in a photocurrent density starting at lower energy, and reaching a higher saturation value of 41.1 mA/cm^2 as shown in **Figure 3. 11 (bottom).**

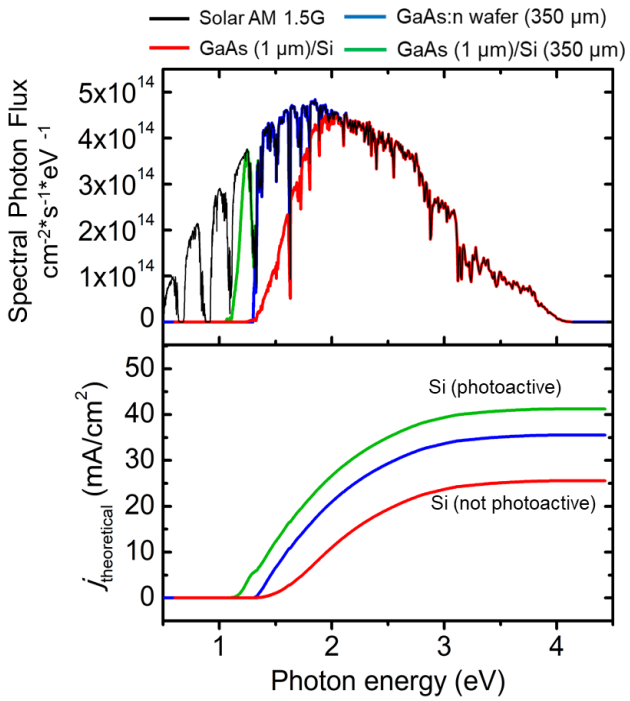

Figure 3. 11 Fraction of the photons absorbed by GaAs from the spectral photon flux of the AM 1.5G solar spectrum (black) for the 350-µm thick GaAs wafer (blue), 1-µm thick GaAs layer (red) from GaAs/Si sample and 1-µm thick GaAs epitaxial layer grown on 350-µm thick Si substrate (green) (top); corresponding $j_{theoretical}$ (mA/cm^2) calculated neglecting e^-/h^+ recombination (bottom)

This therefore explains why the photocurrent reached with GaAs/Si PA is higher than the one measured with the reference GaAs PA, and gives the hope to reach even improved performances for single photoelectrodes with such dual bandgap configuration. These results also highlight that carriers photogenerated in the Si material are surprisingly able to cross the GaAs/Si interface, and the whole GaAs layer despite the hetero-interface band offsets and the GaAs crystal defects. The photocurrent density of bare n-type Si substrate PA without GaAs epitaxial layer is in the range of 0.1 mA/cm^2, which is attributed to the presence of insulating SiO_x native oxide. Following the dipping of the bare n-type Si photoanode into HF (10%) for 2 min to remove SiO_x from the surface, the photocurrent density is increased 2x times reaching ~0.2 mA/cm^2 (**Figure 3. 12**).

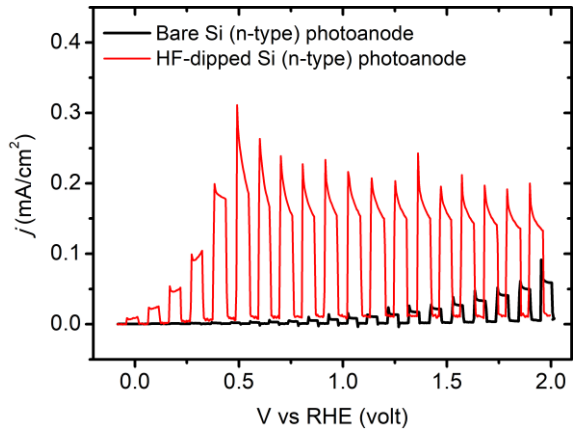

Figure 3. 12 Photocurrent density vs voltage (j - V) curve for the bare and HF-dipped n-type Si photoanode under 1-sun illumination

Here, it is interesting to note that the photoactivity of Si is not systematically observed for other III-V materials grown on Si substrates. As shown previously, similar analysis was performed on comparable GaP/Si sample and GaP wafer (**Figure 3. 9 (b)**). In this case, the IPCE for both epitaxial GaP/Si and GaP PA increases massively above 2.7 eV (direct bandgap of GaP) and shows a close to zero value below that energy indicating that Si substrate does not contribute to the PEC activity of the GaP/Si PA. We attribute this difference between the two materials systems to the relative positioning of the III-V semiconductor bands and their band lineup with the bands of Si, which are different (**Figure 3. 13**).

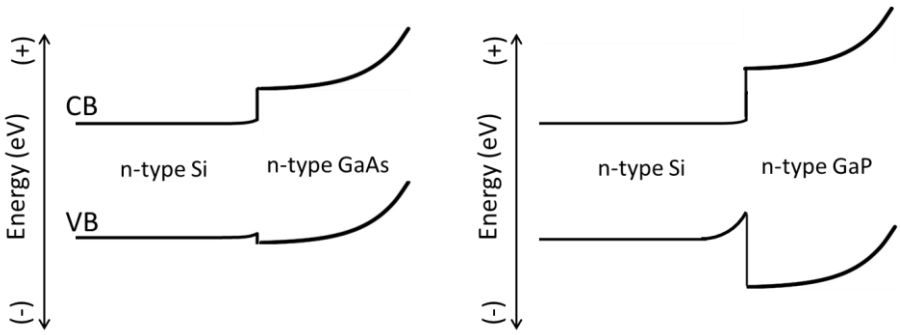

Figure 3. 13 Relative positioning of the III-V semiconductor energy bands and their band lineup with the energy bands of Si (represented for illustration).

Indeed, as the valence band (VB) of Si is well aligned with the VB of GaAs [112], the minority charge carriers, i.e., the photogenerated holes, can be easily transferred from Si

to GaAs. Therefore, the amount of the effective charges used in oxidation process increases which consequently results in an enhancement of the photocurrent. In the case of GaP/Si, the VB maximum of Si is significantly higher than that of GaP, thus it will impose an energy barrier for the transfer of the photogenerated holes from Si to GaP. It is worth to mention that, without any protective layers, epitaxial GaAs/ Si, GaAs/ GaAs and GaAs wafer PA are not expected to drive Oxygen Evolution Reaction (OER), but photocurrents are likely to originate from III-V photocorrosion which is already highlighted in references [7,9,17,128] Nevertheless, we believe that this does not change the main finding of this study i.e. the contribution of the silicon substrate in the generated photocurrent, as photocorrosion is a redox reaction taking place as a result of photoelectrochemical charge generation and transportation. Nevertheless, the large photocurrent detected with the GaAs/Si PA is intriguing and potentially of great interest for water splitting applications. Consequently, the development of efficient dual-bandgap III-V/Si single photoelectrodes is conditioned by the choice of an appropriate III-V semiconductor, which band lineups with Si are favorable to promote photoelectrochemical charge transfer.

3.7 Summary

In this chapter, we demonstrated that the photoelectrode composed of a thin-film GaAs epilayer (1 μm) grown on a low-cost Si substrate can operate in a dual-band gap mode, where carriers photo-generated in both the GaAs layer and the Si substrate can contribute to the electro-chemical reaction. We especially show that despite crystal defects and additional band offsets, the GaAs/Si dual-bandgap photoanode allows reaching higher light-limited net photocurrents than those obtained with photoelectrodes fabricated from commercial defect-free bare 350-μm thick GaAs substrates. The set of experiments carried out in this chapter highlight that the participation of carriers photogenerated in the Si substrate is found to be the origin of enhanced photocurrent. Notwithstanding the high photocurrent density of GaAs/Si PA, the photoanode onset potential (V_{onset}) is relatively larger than the one of the GaAs wafer photoanode and the origin of it is mainly attributed to the influence of interfaces (Si/GaAs/electrolyte) and surface states on its performance, as well as the potential drop due to the presence of the Si. Nevertheless, the demonstration of high photocurrent density, as well as quantum

efficiency with a simple material design, opens prospects for the development of high-efficiency dual-bandgap III-V/Si photoelectrodes with other III-V materials.

Chapter 4

Alloys of III-V thin films on Si substrate with Photoelectrode/Electrolyte band engineering

Chapter 4. Alloys of III-V thin films on Si substrate with Photoelectrode/Electrolyte band engineering

The concept of band engineering between photoelectrode and electrolyte to achieve desired materials properties and thus, higher photoelectrochemical (PEC) water splitting efficiency has a great significance for the development of hydrogen fuel chain. In this chapter, we demonstrate bandgap engineering with III-V alloys, specifically GaPAs alloys grown epitaxially on a low-cost Si substrate, and how the optical and photoelectrochemical properties are deeply impacted by different band-lineups.

4.1 Introduction

In the general context of carbon-free energy policy and global energy/ environmental crisis, the development of green hydrogen production technologies (i.e., hydrogen produced from renewable energies) has attracted much researches in the last past years. [30,129] The energy potential of hydrogen and solar water splitting PEC cells have been extensively discussed in chapter 1. It was already mentioned in above chapters that semiconductor photoelectrodes are at the heart of this technology and combine simultaneously several characteristics such as (i) a good light absorbtion, (ii) appropriate energy band positions and (iii) low fabrication costs, for instance through the choice of earth-abundant materials to render higher solar-to-fuel conversion efficiency with affordable cost. Finding all these qualities in one material is very challenging, thus many research efforts have been devoted to find new materials that possess most of the desired characteristics. [6,30]

III-V semiconductors have been used for years in the field of photovoltaic solar cells, sensors or photonics, both at academic and industrial levels, because of their remarkable optical properties, leading to world record performances for various applications. [56,130] Most of these achievements were made possible thanks to the ability of materials scientists to tune at will the bandgaps and bandlineups in III-V materials stacks. This strategy, often referred to as “bandgap engineering” or “band engineering”, [60] consists in alloying different binary III-V semiconductors (such as InP,

InAs, GaAs, GaP, GaSb, GaN, etc.) to form a ternary or a quaternary alloy, with targeted bandgap properties for laser emission or light harvesting in solar cells. [72] Over the years, different epitaxial setups have been developed to guarantee the ultimate control of III-V semiconductors alloys composition, such as Molecular Beam Epitaxy (MBE) or Metal-Organic Chemical Vapor Deposition (MOCVD), with a III-V alloy composition control typically better than 1% over a 4 inches wafers in industrial grade experimental setups.

The use of III-V semiconductors as photoelectrodes in PEC cells have also been emerged with promising performances, yet most of the studies focus on the use of binary compound semiconductors based on expensive III-V commercial wafers. [10,31,58] While PEC cell performances with relatively high photocurrents and photovoltages were demonstrated with this approach, [73,85,86,98] the bandgap and the relative positioning of the semiconductor bands with respect to the redox levels of the electrolyte are however fully determined by the physical intrinsic properties of the binary III-V semiconductor, and thus fundamentally reducing the maximum efficiency that can be reach by the cell. On the other hand, few photoelectrodes using ternary III-V alloys semiconductors were proposed in complex architectures, [10,46] such as the monolithic multiple-junction photoelectrode (GaInP/GaInAs)/TiO_2/RuO_x used to run unassisted water splitting with 19% of Solar to Hydrogen (STH) record efficiency. [31] In these devices, alloying is mostly used to adjust the bandgaps of the multiple absorbers to the sunlight spectrum and ensure the current matching between the two p-n junctions. Despite excellent performances, the optimization of the semiconductor band alignment with water redox levels was not considered. More recently, operating photoelectrodes with monocrystalline III-V thin films directly grown on Si substrates were demonstrated, leading to a drastic reduction of their fabrication cost. [17–19,99] Following this strategy, bandgap engineering was proposed theoretically to address the issue of band alignments between the semiconducting photoelectrodes and redox levels of the electrolyte, but without experimental proof of the concept in electrochemistry. [101]

In this chapter, we study the photoelectrochemical and optical properties of photoelectrodes, made from $GaP_{1-x}As_x$ alloys epitaxially grown on a low-cost Si substrate. We show that, optical and photoelectrochemical properties can be finely

adjusted through the control of the As content, x(As) in the alloy. With composition change, the absorbing edge is tuned from 1.39 eV to 2.41 eV. The nature of the band structure (indirect-to-direct) is also modified as deduced from the change of photon-to-current conversion efficiency. The flat-band potentials (V_{fb}) determined from Mott-Schottky (MS) measurements are associated to the variation of energy bands and onset potentials (V_{onset}), respectively, depending on elemental composition of $GaP_{1-x}As_x$ alloys. However, the variation range is found to be lower for the energy bands and systematically higher for the onset potentials, which is interpreted by the high surface recombination and low hole transfer kinetics of bare photoelectrodes without passivating and catalysts layers.

4.2 Sample growth and photoelectrode elaboration

In this study, a 1-µm thick $GaP_{1-x}As_x$ thin films were grown in a bi-domain configuration [18] by Molecular Beam Epitaxy (MBE) on a HF-chemically prepared Si substrate (n-type, Ph-doped $5x10^{14-15}$ cm^{-3}) with a thickness of 350 µm. The substrate was heated at 800°C for 10 min to desorb hydrogen. Following the preparation of the 350 µm-thick Si substrate, 1 µm-thick $GaP_{1-x}As_x$ epilayers were grown at 500°C in a conventional continuous Molecular Beam Epitaxy (MBE) growth mode. **Table 4. 1** summarizes the important growth parameters of the epitaxial $GaP_{1-x}As_x$ alloys, including a targeted x(As), Beam Equivalent Pressure V/III ratio, epilayer thickness and MBE growth rate. It should be noted that the GaAs epilayer was not intentionally doped (nid), and epitaxial strategies to annihilate antiphase boundaries (APBs) were not used. In addition, a commercial n-doped GaAs, GaP wafers (1 to $5 \cdot 10^{18}$ cm^{-3}) with thickness of 350 µm were used as a reference sample to compare with epitaxially grown GaAs and GaP.

	Alloys				
x(As)	**1**	**0.83**	**0.52**	**0.22**	**0**
V/III ratio	7.4	5.7	5.1	3.9	8.7
Epilayer Thickness (µm)	1	1	1	1	1
MBE growth rate (ML/s)	0.24	0.24	0.24	0.24	0.24

Table 4. 1 Alloys of $GaP_{1-x}As_x$ grown epitaxially on Si substrate with arsenide content x(As), Beam Equivalent Pressure V/III ratio, epilayer thickness and MBE growth rate

Prior to the preparation of the photoanodes (PA), all the epitaxial $GaP_{1-x}As_x$ alloys on Si ($GaP_{1-x}As_x$ /Si) were cleaned in ultrasound cleaner for 10s with ultrapure water and subsequently purged with the flow of N_2 gas. The backside was scratched to make the Ohmic contacts using Gallium-Indium eutectic (99.99%, Alfa Aesar) and silver paste (Electron Microscopy Sciences). The electrochemically active surface area was defined using an epoxy resin (EA 3423, Henkel from Loctite) covering the backside and the edges of the PA (**Figure 2. 6**) and was calculated using ImageJ software.

4.3 Structural characterization

Structural characterization of the epitaxial $GaP_{1-x}As_x$ /Si alloys were carried out using X-Ray Diffraction (XRD) in the conventional ω/2θ mode. **Figure 4. 1 (a)** shows a superimposed plot of ω/2θ scans performed in the vicinity of Si (004) for the alloys of $GaP_{1-x}As_x$ /Si with different x(As).

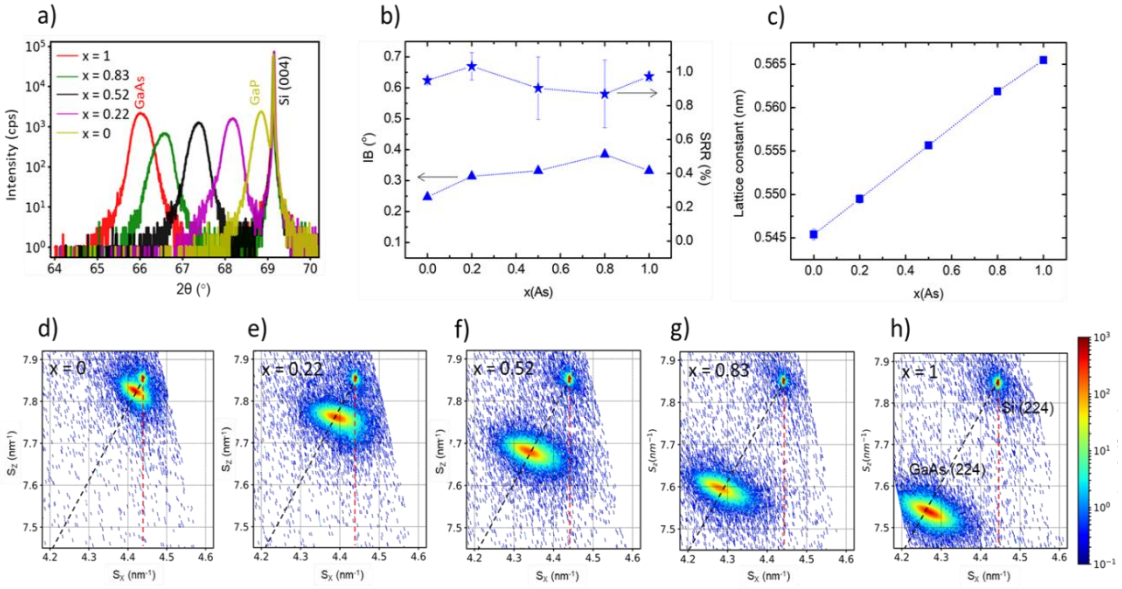

Figure 4. 1 (a) XRD ω/2θ scan performed in the vicinity of Si (004); (b) evolution of the integral breadth (IB) of the epilayer Bragg peak (triangle) and strain relaxation rate (SRR) (star) as a function of x(As); (c) evolution of the calculated lattice constant (square) as a function of x(As); and (d-h) RSM showing the Si substrate and the epilayer in (224) direction with black dashed line (fully plastically relaxation) and red dashed line (fully elastically strained). x in inset refers to x(As) of $GaP_{1-x}As_x$ /Si alloys.

The ω/2θ scans exhibit a common thin Bragg peak which is observed at 69.13° for all the samples, that corresponds to the Si substrate. The other well-defined Bragg peaks are

related to $GaP_{1-x}As_x$ layers with the Integral Breadth (IB) (**Figure 4. 1 (b),** triangle markers) similar for all samples, showing a similar crystal quality independently of the alloy composition. The position of the Bragg peak of $GaP_{1-x}As_x$ epilayers depends on both, the alloys composition and the strain status of the epilayer. In order to separate both effects and to determine $GaP_{1-x}As_x$ alloys composition accurately, the Reciprocal Space Maps (RSM) were recorded in 224, (**Figure 4. 1 (d-h)**), -224 and 004 (**Figure 4. 2**) directions.

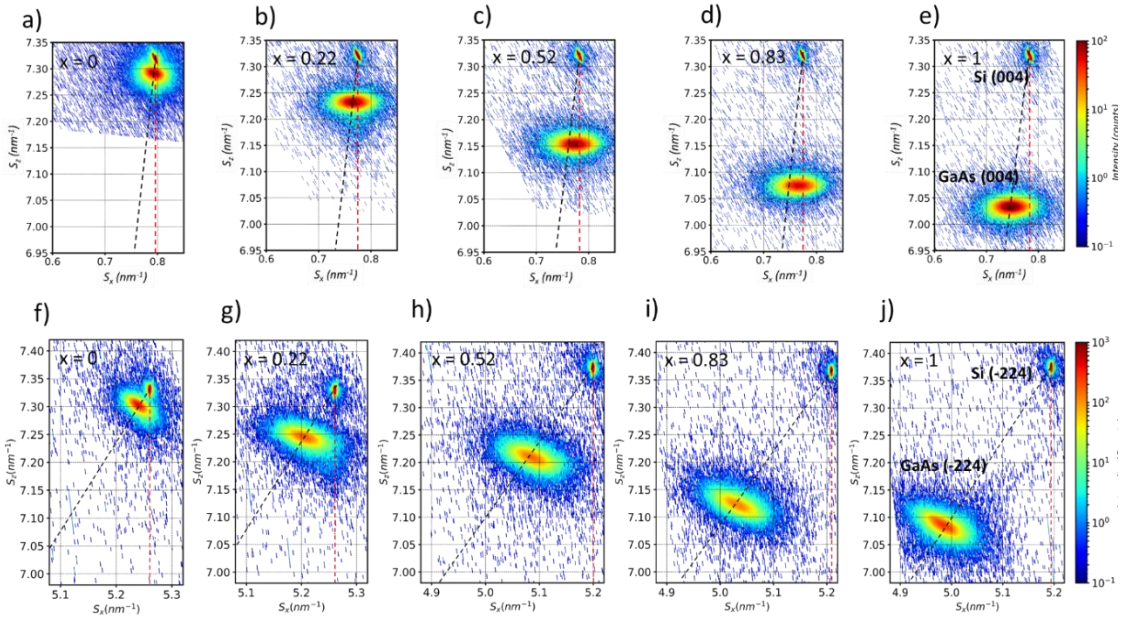

Figure 4. 2 Space Reciprocal Maps (RSM) showing the Si substrate and the epilayer (a-e) at 004 reflection and (f-j) at -224 reflection. In inset black dashed line (fully plastically relaxation) and red dashed line (fully elastically strained), x refers to x(As) of $GaP_{1-x}As_x$ /Si alloys

The Strain Relaxation Rate (SRR) was then inferred, SRR = 1 corresponds to fully plastically relaxation and SRR = 0 to fully elastically strained structure (illustrated in chapter 2). Considering all the RSM recorded for $GaP_{1-x}As_x$ /Si epitaxial alloys, the calculated mean value for SRR is higher than 0.8 (**Figure 4. 1 (b)** – star markers) indicating that the epitaxial samples are close to fully plastically relaxation. The observed change in S_z values for the $GaP_{1-x}As_x$ epilayer which is decreasing for the higher x(As) is attributed to the evolution of the 2θ values of the $GaP_{1-x}As_x$ alloy Bragg peaks indicating that the lattice constant increases with the x(As) as shown in **Figure 4. 1 (c),** which is in a good agreement with the theoretical lattice parameter of GaP (0.54505 nm) and GaAs (0.56532 nm). [131] From the SRR values and the Bragg peak positions, the real As content, x(As) of $GaP_{1-x}As_x$ alloys is calculated with the corresponding mean values of

1.0±0.02, 0.83±0.02, 0.52±0.01, 0.22±0.02 and 0.01±0.01, respectively, showing a good consistency with the initial targeted x(As) values before epitaxial growth, illustrating the very fine control of III-V alloys compositions that can be reached with MBE.

4.4 Surface characterization

Furthermore, to investigate sample morphology, tapping mode atomic force microscopy (AFM) and scanning electron microscopy (SEM) were used. **Figure 4. 3** depicts the set of 5 x 5 μm^2 AFM images of the epitaxial samples with different x(As) as well as for the commercial GaP and GaAs wafers. All $GaP_{1-x}As_x$ alloys present similar morphology, independently to different x(As), revealing a root-mean-square (rms) value in the range of 5 – 9 nm.

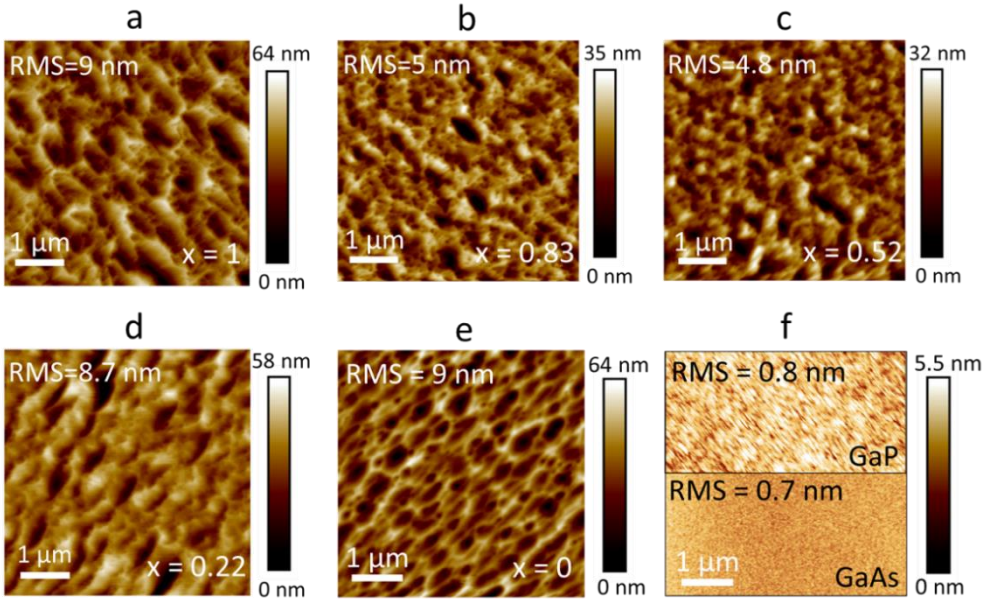

Figure 4. 3 (a-e) AFM image of surface morphology of the epitaxial $GaP_{1-x}As_x$ alloys with different x(As) shown in inset as x and (f) the commercial GaP and GaAs wafers. Inset includes the rms value and corresponding scale bar

However, the rms of the epitaxial samples are higher than the one measured for the commercial GaP, GaAs wafers (~0.8 nm). The higher surface roughness observed for the epitaxial samples is attributed to the growth of a polar material as GaP, GaAs on a non-polar Si substrate [132], as well as used specific growth processes. [61,65]

The SEM image of the sample with one high and low rms value is shown in **Figure 4. 4** to compare the sample morphology over a larger scale. SEM image at the same scale is given for the GaAs wafer as well for comparison in **Figure 4. 4 (f)**. From the side-view SEM image, the 1-µm thick (targeted thickness) $GaP_{1-x}As_x$ epilayer and Si substrate can be easily distinguished from two different contrasts. In overall, from structural and surface characterizations, it is clear that (i) 1-µm thick $GaP_{1-x}As_x$ alloys were epitaxially grown on a low-cost Si substrate with precise control of x(As) content and with (ii) similar surface and crystal quality independently to different x(As).

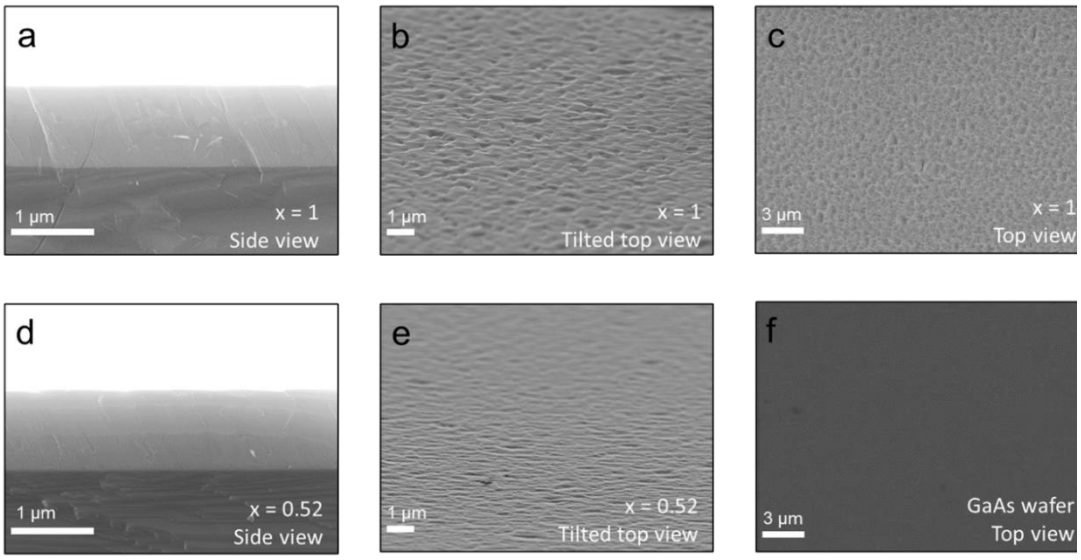

Figure 4. 4 SEM images for the 1 µm-thick epitaxial $GaP_{1-x}As_x$ alloy with high roughness: (a) side view, (b) tilted top view and (c) top view; low roughness: (d) side view, (e) tilted top view; (f) commercial GaAs wafer from the top view, x in inset refers to x(As)

4.4 Characterization of optical properties

A Horiba UVISEL 2 spectroscopic ellipsometer were used to characterize light absorption properties of the epitaxial thin-film $GaP_{1-x}As_x$ alloys grown on Si substrate. In this perspective, the optical constants were measured at room temperature in the photon energy range of 0.6 – 4.2 eV and subsequently fitted with Tauc-Lorentz with 2 oscillators model in order to calculate the energy gap (E_G), thickness and roughness, respectively. Absorption coefficient (α) was deduced from the imaginary part of the optical index (k) resulted after the fitting. In order to increase the accuracy of the fitting with given models, the samples surface was smoothened with chemically mechanically polishing (CMP).

Figure 4. 5 shows the experimental ellipsometry spectra for CMP $GaP_{1-x}As_x$ alloys, where the variation of the I_s (blue) and I_c (red) parameters as a function of the photon energy is plotted. The black lines correspond to the fitting curves obtained after adjusting the parameters of the Tauc-Lorentz 2 model.

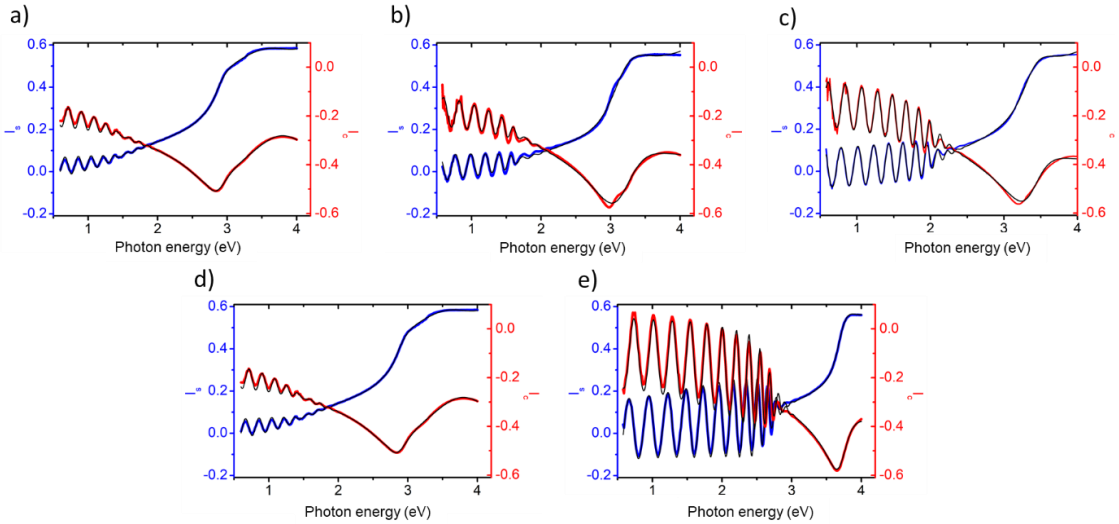

Figure 4. 5 Experimental ellipsometry spectra of the I_S (blue), I_C (red) parameters and fitting curve with Tauc-Lorentz model (black) for $GaP_{1-x}As_x$ alloys with (a) x(As)=1; (b) 0.83; (c) 0.52; (d) 0.22 and (e) 0, respectively

The extracted values for the energy gap (E_G), thickness and roughness are given in **Table 4. 2**.

	Alloys				
x(As)	**1**	**0.83**	**0.52**	**0.22**	**0**
E_G (eV)	1.39	1.46	1.81	2.18	2.41
Thickness (µm)	0.942	0.816	0.836	0.866	0.722
Roughness (µm)	0.011	0.017	0.009	0.013	0.011

Table 4. 2 Energy gap (E_G), thickness and roughness values extracted from the fitting of the raw ellipsometry data

The observed slightly difference between the values of extracted and real thickness (~1 µm) is associated to CMP polishing and small uncertainties of the ellipsometry fitting models. The absorbtion coefficient of the sample is then deduced from the imaginary (k) part of the refractive index extracted from the fitting as follows:

$$\alpha = \frac{4\pi k}{\lambda} \tag{4.37}$$

λ is the photon wavelength in (cm) and α is the absorption coefficient. **Figure 4. 6** shows the measured absorption spectra of $GaP_{1-x}As_x$ alloys with different x(As), indicating the evolution of the light absorption at different photon energy depending on the alloy's composition.

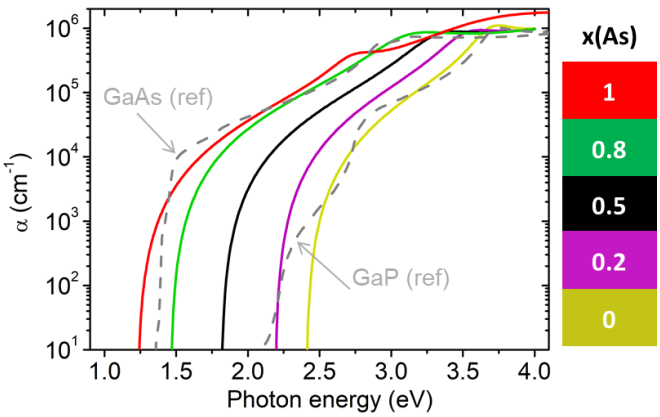

Figure 4. 6 Optical absorption spectra for the epitaxial $GaP_{1-x}As_x$ alloys grown on Si substrate, including bare GaP[39] and GaAs[39] for comparison

Light absorbtion spans from 2.41 eV to 1.39 eV highlighting that, optical properties of the material become tunable with the control $GaP_{1-x}As_x$ elemental composition. The absorption spectra of GaP, GaAs wafers from [39] is also given in the same plot in order to compare with the epitaxial alloys especially with x(As) = 0 (GaP) and x(As) = 1 (GaAs) showing that absorption coefficient lies within same order of magnitude for both commercial wafers and epitaxial samples, and therefore that crystal defects do not alter significantly the light absorption in epitaxial $GaP_{1-x}As_x$ alloys.

4.5 Photoelectrochemical (PEC) characterization

PEC characterizations were carried out in a standard three-electrode configuration consisting of a working electrode (photoanode (PA) fabricated from $GaP_{1-x}As_x$ alloys and commercial GaAs, GaP wafers), a reference electrode (Ag/AgCl in saturated KCl), and a

counter electrode (graphite rod). The used electrolyte was an aqueous 0.2 M H_2SO_4 solution (measured pH = 0.35). The solar light was simulated by a solar simulator (LS0106, LOT Quantum Design) equipped with an AM 1.5G filter with the measured power of 100 mW/cm^2. The polychromatic light was simulated with tunable wavelength light-emitting diode (LED). A Zennium potentiostat (Zahner) was used and potential was scanned at a rate of 50 mV/s. The measured potential vs Ag/AgCl reference electrode was converted to the comparable reversible hydrogen electrode (RHE) using the equation below,

$$E_{RHE} = E_{Ag/AgCl} + 0.197 + 0.059\,pH \tag{4.38}$$

4.5.1 Incident photon-to-electron conversion efficiency (IPCE)

The incident photon-to-electron conversion efficiency (IPCE) was measured in a three-electrode PEC cell under illumination with a tunable wavelength light-emitting diode (LED) with the photon energy range of (1.2 – 4.2) eV. The external applied potential was 1 V vs RHE. **Figure 4. 7 (a)** shows the IPCE curves as a function of photon energy for the epitaxial $GaP_{1-x}As_x$ alloys with different x(As).

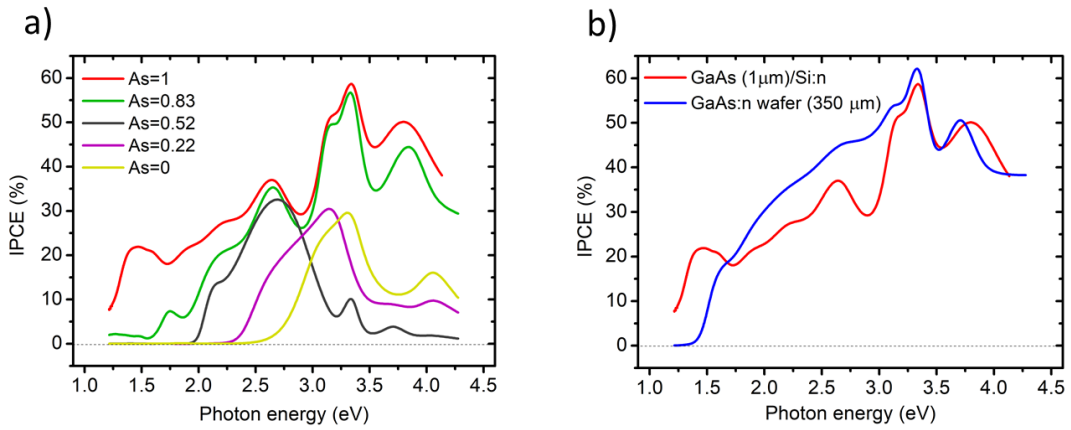

Figure 4. 7 (a) IPCE spectra for the 1 µm-thick epitaxial $GaP_{1-x}As_x$ alloys grown on Si substrate measured under polychromatic light at 1 V vs RHE applied potential; (b) IPCE spectra of GaAs (1 µm) epilayer and bare GaAs:n wafer (350 µm) measured in the same conditions for comparison

A clear shift of the IPCE edges is observed depending on the elemental composition of the alloys. For the higher x(As) alloys, the IPCE edge is observed at smaller photon

energy, highlighting the capability of high x(As) alloys to absorb more in visible region. This trend is related to the bandgap evolution of $GaP_{1-x}As_x$ alloys with different x(As) as confirmed by spectroscopic ellipsometry measurements (**Figure 4. 6**). Moreover, the observed IPCE edge fronts for x(As)=0 and x(As)=0.22 alloys are less abrupt than the those with higher x(As) alloys.

Additionally, the low x(As) alloys (0, 0.22 and 0.52) exhibit the IPCE of ~30% at maximum, whereas the IPCE values up to 60% is achieved for the higher content x(As) alloys (0.83 and 1), meaning that the higher x(As) alloys are capable of absorbing more photons and subsequently generating more charge carriers for the photoelectrochemical redox reaction. While the decrease in photon energy is due to the band gap shift toward smaller values, the shape and the magnitude of IPCE curve is associated to the indirect-to-direct band gap transition, which is expected to occur at x(As) = 0.52 for $GaP_{1-x}As_x$ alloys. [72]

The IPCE measurement performed at the same conditions for the commercial nearly defect-free GaAs:n wafer (350 µm) is given in **Figure 4. 7 (b)** for comparison with x(As) = 1 (GaAs) epitaxial alloy grown on Si substrate. Despite emerging defects and smaller thickness, GaAs (1 µm) epitaxial alloy exhibit a similar IPCE efficiency to the commercial GaAs wafer, which is intriguing and was not expected (details in chapter 3). This means the charge carriers photogeneration and transport in photoelectrodes is not affected by the crystal defects in the same way as in photonic or photovoltaic devices [18] and 1 µm-thick GaAs/Si epitaxial sample is able to produce the IPCE of similar magnitude as the commercial 350 µm-thick GaAs wafer. The surprising photoelectrochemical performance of the GaAs/Si sample is related to the sub-bandgap photoresponse of Si substrate and extensively studied in chapter 3. These results demonstrate high optical and transport properties of epitaxially grown GaAs on Si substrate. Moreover, it strengthens the potential of thin III-V layers on cheap silicon substrate for low cost photoelectrode elaboration.

4.5.2 Flat-band potential (V_{fb}) and band-lineups

Flat-band (V_{fb}) measurements with Mott-Schottky (MS) characterization were further performed in the dark for the photoanodes of $GaP_{1-x}As_x$ alloys in 0.2 M H_2SO_4 electrolyte (measured pH = 0.35) using the same three-electrode photoelectrochemical cell. As shown in **Figure 4. 8**, the MS plots exhibit a positive slope indicating that the epitaxial $GaP_{1-x}As_x$ alloys present an n-type doping.

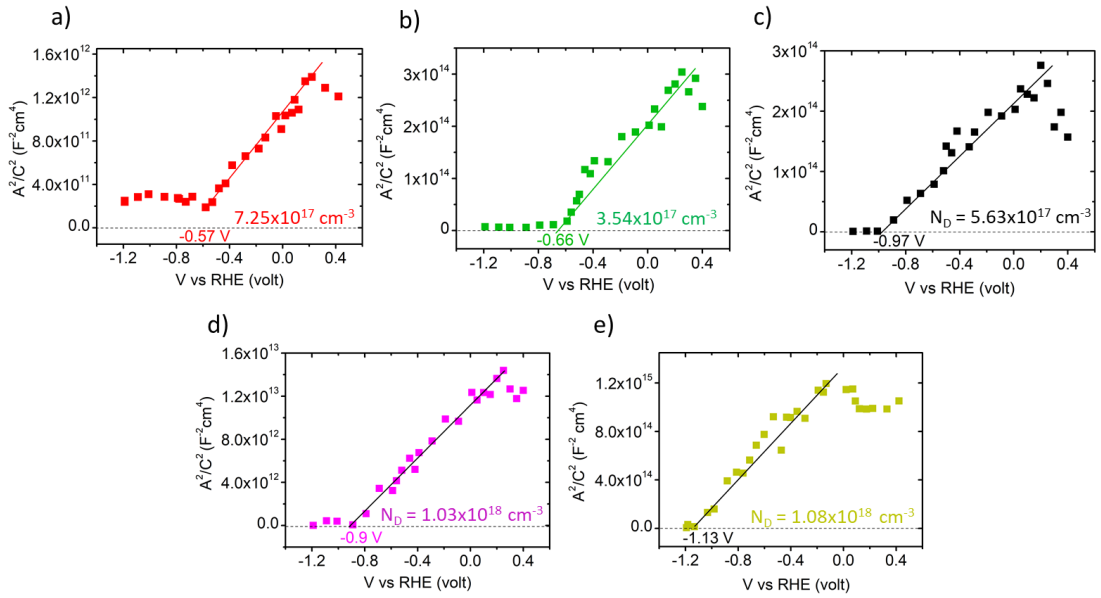

Figure 4. 8 Mott-Schottky analysis performed in the dark for $GaP_{1-x}As_x$ alloys with different x(As): (a) 1, (b) 0.83, (c) 0.52, (d) 0.22 and (e) 0, respectively. The x-intercept of the y-axis (A^2/C_{SC}^2) of the linear portion indicate the flat-band potential (V_{fb})

Donor densities in the range of 10^{17} and 10^{18} cm^{-3} are measured, which are unexpectedly large values for non-intentionally doped III-V layers grown by MBE. Although contamination (e.g. by carbon atoms) of the Si surface prior to III-V overgrowth cannot be excluded, [133,134] theses large values measured are more likely explained by the presence of antiphase boundaries in the layers that have been shown to be electrically active and potentially with a donor-like behavior. [18,135] Flat-band potentials (V_{fb}) versus Reversible Hydrogen Electrode (RHE) deduced from the A^2/C^2 intercept with the potential x-axis are plotted for the different samples in **Figure 4. 9** (green diamonds). The large values of donor concentrations determined from MS measurements, enable approximation that Fermi level coincides with the conduction band (CB) levels. In this case, V_{fb} corresponds to CB levels versus RHE. By adding bandgap energy determined

from spectroscopic ellipsometry measurements, valence band (VB) positions are deduced (black diamond) The theoretical expected evolution of the different energy bands of interest for $GaP_{1-x}As_x$, corresponding to the different valleys of the Brillouin zone (Γ, L, X) are superimposed with experimental values in **Figure 4. 9**, similarly to previous works. [72,101,112] Note that in the semiconductor research community, the CB edge energy is usually referred versus vacuum level (and defined as electron affinity). In order to compare energy versus RHE and versus vacuum, we consider that the chemical potential for electrons under RHE is shifted by -4.48 eV on the vacuum level. [113] From GaAs photoelectrode measurements, the measured flat-band potential of -0.57 V vs. RHE leads to an electron affinity equal to 3.89 eV, in good agreement with the well documented 4.07 eV value. [136]. Surface dipoles and/or surface states could explain the small difference between these two values.

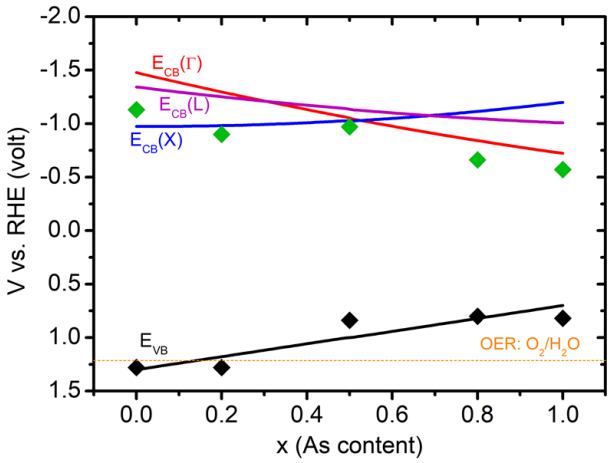

Figure 4. 9 Experimental flat-band potential (green diamond) as a function of x(As) of $GaP_{1-x}As_x$ alloys measured from Mott-Schottky plot, inferred further as E_{CB}. The E_{VB} (black diamond) deduced from the measured flat-band potential and the band gap. Theoretical Γ, X and L valleys of the CB and the VB as a function of x(As) are calculated [72], considering linear evolution of the VB from x(As)=0 to x(As)=1 [112] OER potential of 1.23 V is shown as an orange dashed line.

As expected, a weak evolution of the CB energy and a large change of the VB energy is observed on the theoretical curves in **Figure 4. 9**, as a function of the x(As), with an indirect (X) to direct (Γ) cross-over for x(As)=0.5 [72,137]. The first observation that can be made is the remarkable agreement between the CB and the VB evolutions predicted theoretically and the positions of the one deduced from the flat-band potential and ellipsometry measurements. This not only validates experimentally with unprecedented

accuracy the band bending model used for years in photo-electrochemistry to describe the semiconductor/electrolyte junction, [41] but also implies that, thanks to the fine control of III-V alloys composition provided by epitaxial techniques, one can adjust precisely the position of the VB with respect to the energy levels of the electrolyte.

In addition, the O_2/H_2O water redox potential was positioned in **Figure 4. 9**, and crosses the valence band maximum for a x(As) composition below 0.2. For a rapid and energetically optimal OER, the valence band should straddle the O_2/H_2O level.[46,115] Therefore, in the present study, OER is not expected to occur for photoelectrodes with x(As) contents above 0.2. By extension, we deduce that accurate control of any III-V alloy composition allows such optimization, whatever the III-V compound considered, on the anodic or on the cathodic side.

4.5.3 Linear sweep voltammetry (LSV)

The current vs voltage (*j*-V) measurements were performed further to analyze the influence of different energy band positions of $GaP_{1-x}As_x$ alloys on the PEC performance of photoanodes. The *j*-V measurements were carried out using the same three-electrode PEC cell containing 0.2 M H_2SO_4 electrolyte (measured pH=0.35) under light illumination with AM 1.5 G (100 mW/cm^2) dark and chopped light. **Figure 4. 10 (a)** shows the *j*-V plots recorded on $GaP_{1-x}As_x$ alloy photoelectrodes versus reversible hydrogen electrode (RHE) for the different x(As) contents.

At first, we observe an increase of the net photocurrent density (j_{net}) with the composition x(As) of the $GaP_{1-x}As_x$ alloys used to fabricate PAs. A photocurrent density of 14.62 mA/cm^2 and 1.34 mA/cm^2 at 1.23 V is measured for x(As)=1 (GaAs/Si) and for x(As)=0 (GaP/Si) PAs, respectively. The photocurrent increase is particularly significant for the alloys with x(As) beyond 0.52 as shown in **Figure 4. 10 (b)**. This evolution is the consequence of a strong light absorption with low-bandgap alloys and indirect-to-direct bandgap transition (more photons are absorbed) which occurs at x(As) ~ 0.5. These trends are in good agreement with the IPCE measurements shown in **Figure 4. 7 (a)** and band structures presented in **Figure 4. 9**

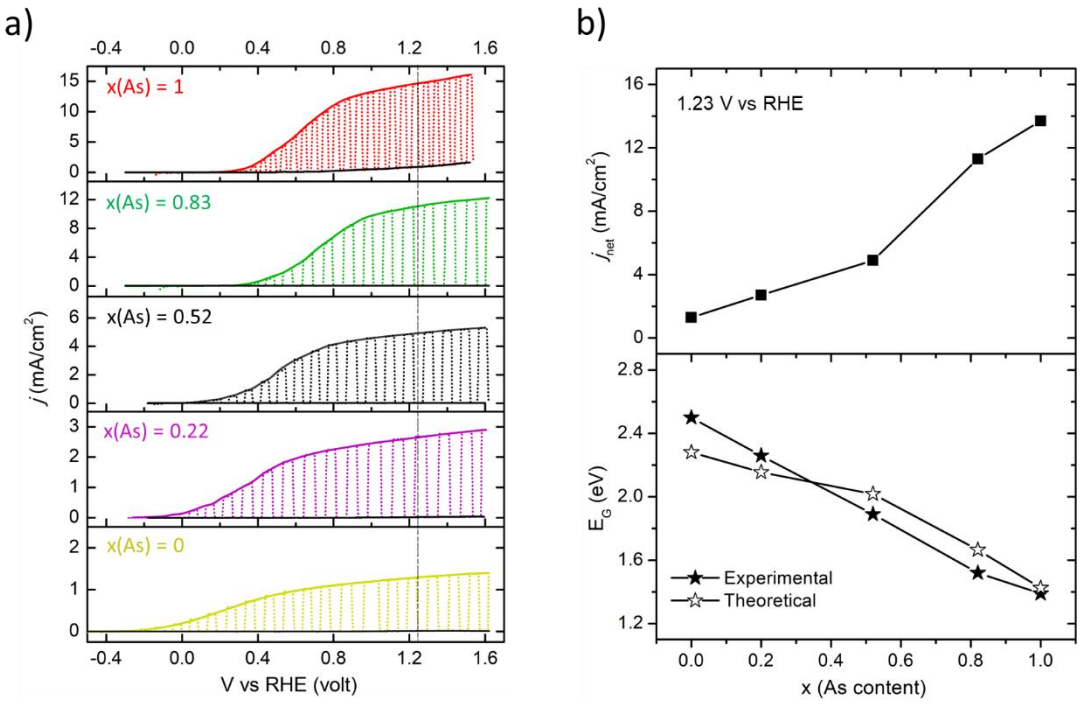

Figure 4. 10 (a) Photocurrent vs voltage (j-V) curves for the epitaxial thin-films of $GaP_{1-x}As_x$ alloys with different x(As) described in inset. The water oxidation potential (1.23 V vs RHE) is marked as a black dotted line; (b) evolution of the net photocurrent density at 1.23 V vs. RHE and the energy gap as a function of x(As)

The photocurrent density measured at 1.23 V for the PAs made from GaAs and GaP substrates is 12.22 mA/cm^2 and 1.27 mA/cm^2, respectively (**Figure 4. 11**). The measured photocurrents of PAs made of native substrates have thus in first approximation the same values than the corresponding epitaxial III-V/Si ones. This result is therefore, a confirmation of the good optical and transport quality of the III-V epilayers grown on the cost-efficient Si substrate despite the low thickness of the thin-film layers deposited.

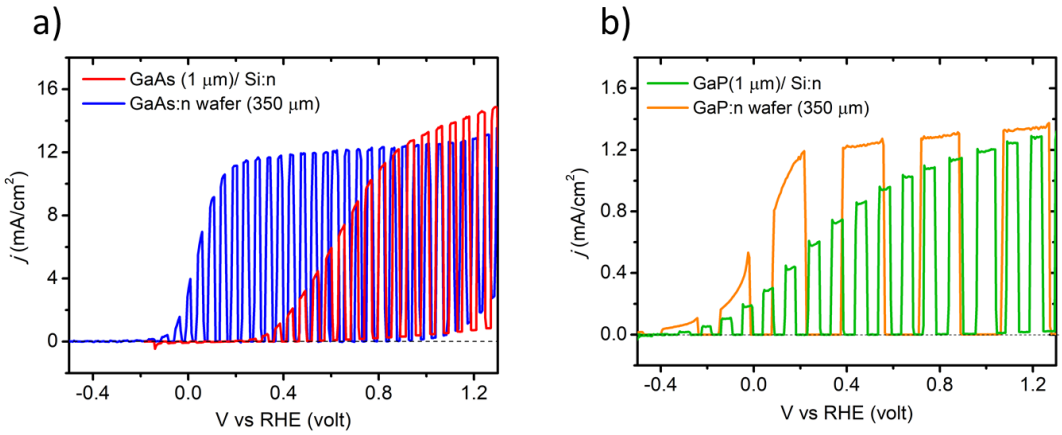

Figure 4. 11 (a) Photocurrent density vs applied voltage (j – V) curves for the commercial 350 μm-thick GaAs, (b) GaP wafer in comparison with the 1 μm-thick $GaP_{1-x}As_x$ with x(As) = 1 (GaAs) and x(As) = 0 (GaP) grown on Si substrate measured under 1-sun illumination in 0.2 M H_2SO_4

Second, it is clearly seen that the onset potential (V_{onset}), the potential where a measurable photocurrent is detected, is changing according to the elemental composition of the $GaP_{1-x}As_x$ alloy. The relative positions of the energy bands, particularly the valence band (VB) is mostly influencing the V_{onset} of the anodic photocurrent besides the kinetics of charge transfer and charge recombinations at surface states. [138]. The V_{onset} as a function of x(As) is plotted in **Figure 4. 12**. The V_{onset} increases for the higher x(As) alloys, meaning that higher external potential has to be applied to enable the photoelectrochemical charge transfer. Especially for the samples with x(As) 0.22, 0.52 and 0.83, the change is obvious with corresponding V_{onset} values of 0.21 V, 0.37 V, and 0.55 V vs. RHE, respectively.

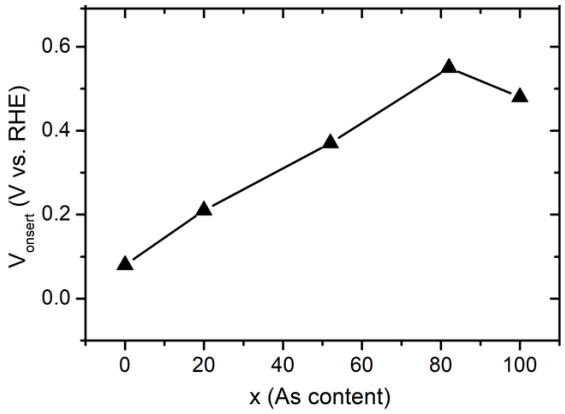

Figure 4. 12 Evolution of the onset potentials (V_{onset}) as a function of x(As) from $GaP_{1-x}As_x$ alloy

Considering an ideal photoanode (without surface/interface recombinations), for any potential more anodic than V_{fb}, the band bending will drive photo-generated holes to the solid/liquid interface, and a photocurrent is detected. Thus, V_{onset} and V_{fb} are identical for an ideal photoanode. In the present work, a large difference can be seen between the apparent values of V_{onset} and the measured V_{fb}, especially for large As contents. Such a difference can be analyzed following Gärtner-Butler (GB) approach, an alternative method to determine the V_{fb} by analyzing the experimentally recorded *j*-V curves. [44] With this analysis, for an ideal photoelectrode, the intercept of the square of the net photocurrent, j_{net}^2 with the potential axis (V vs. RHE) should allow the determination of V_{onset} that corresponds in theory to V_{fb}. As shown in GB analysis of x(As)=1 (GaAs/Si) sample (**Figure 4. 13 (a)**), at potential higher than 1 V, a good agreement with the model is observed and by fitting this part, the V_{fb} is estimated at -0.21 V vs. RHE. However, in the range of potential lower than 1 V, a second and different linear slope can be fitted, with the intercept directly related to the observed delayed V_{onset}. In this range the photo-generated minority carriers recombine with majority carriers, possibly in surface states or accumulate at the interface due to the slow kinetic of surface reactions. [125]

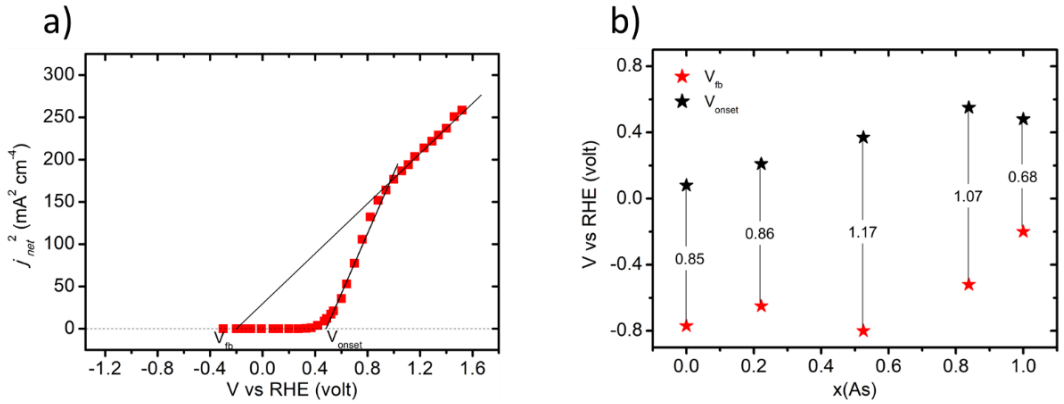

Figure 4. 13 (a) Gärtner-Butler (GB) analysis of the experimentally measured j-V curve of the x(As)=1 (GaAs/Si) sample, the slopes for V_{fb} and V_{onset} are shown in inset; (b) evolution of the V_{fb},(red star markers) the V_{onset} (black star markers) and their differences determined with GB analysis as a function of the composition x(As) in the alloys

A similar tendency is observed for all the other alloys of $GaP_{1-x}As_x$ (**Figure 4. 14**). The V_{onset} and V_{fb} deduced from GB analysis and the difference between are shown in **Figure 4. 13 (b).** We interpret these large differences as the consequence of surface/interface states in the samples that will need to be improved in future works. A decrease of the

offset has been reported by using deposition of surface state passivating layers [119,125] and (or) OER catalysts [139]. In order to fully demonstrate the potential of III-V alloys/silicon photoelectrodes, studies on surface passivating layers and (or) catalysts are required.

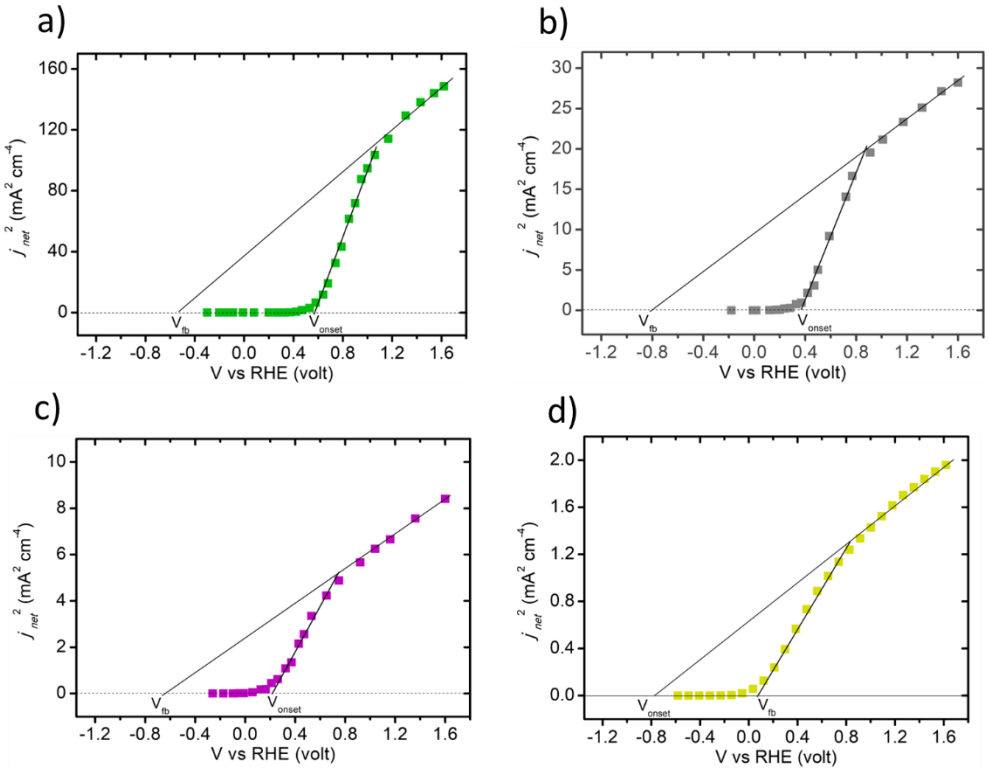

Figure 4. 14 Gärtner-Butler (GB) analysis of the experimentally measured j-V curves for the x(As) (a) 0.83, (b) 0.52, (c) 0.22 and (d) 0, the slopes for V_{fb} and V_{onset} are shown in inset

4.6 Discussion

The CB and VB positions of $GaP_{1-x}As_x$ alloy changes drastically as a function of x(As), so does the nature of the band gap, influencing mainly the optical and photoelectrochemical properties of the material that are of great interest for solar energy harvesting devices. As shown in **Figure 4. 10 (b)**, the alloys with higher x(As) have smaller bandgap which is more suitable to absorb large range of the solar spectrum and thus it is clearly observed that these samples are capable to produce large photocurrent. As a consequence, the quantum efficiency for the samples with x(As) 0.83 and 1 is relatively larger than those with lower x(As) and are potentially of great interest for the solar energy harvesting devices. On the other hand, the alloys with lower x(As) reveal a

relatively smaller V_{onset} which is particularly interesting for the un-assisted solar water splitting. However, the alloys with lower x(As) absorb relatively smaller fraction of the solar spectrum with smaller efficiency due to the indirect bandgap configuration.

Nevertheless, the $GaP_{1-x}As_x$ alloys are intriguing and potentially of great interest as the important photoelectrochemical properties as well as the optical bandgap can be tuned through the fine control of x(As). For instance, the desired photocurrent density (>10 mA/cm2) and the V_{ph} (>1.23 V) for the PEC water splitting could be achieved by elaboration of the connected multi-absorber tandems. The alloys of x(As) 0, 0.22 and 0.52 with E_G varying in between 1.8 – 2.5 eV could be used as top absorber, whereas the alloys with x(As) 0.83 and 1 as bottom absorbers exceeding 25% the overall STH efficiency.[140]

4.7 Conclusion

In this chapter, we demonstrated band gap engineering on the epitaxial $GaP_{1-x}As_x$ alloys grown on a low-cost Si substrate through the control of alloy's composition. Especially, we show that, the bandline-ups and bandgap configuration can be relatively tuned with respect to the desired application in solar energy harvesting devices. The experimental results highlight that engineering of the $GaP_{1-x}As_x$ bandgap deeply impacts the optical and photoelectrochemical properties which is intriguing and shows the potential interest in photoelectrochemical water splitting. In addition, the alloys with x(As) 0 (GaP) and 1 (GaAs) exhibit a competitive photocurrent density compared to the commercial III-V wafers which are x10 times more expensive than our laboratory grown materials. These results strengthen our approach for low cost and efficient photoelectrodes fabrication. However, the measured onset potentials are quite high and huge offset between flat band and onset potential is observed. These indicate that the photoelectrodes suffer from high surface recombination and (or) poor surface kinetics. Studies on passivating and (or) catalysis layers are in demand to fully demonstrate the potential of III-V alloys/silicon photoelectrodes.

Chapter 5

Protection of $GaP_{1-x}As_x$ /Si photoanodes against corrosion: First attempts

Chapter 5. Protection of GaAs/Si photoanodes against corrosion: First attempts

Despite the promising results of the epitaxial III-V/Si thin-film photoelectrodes discussed in previous chapters, the stability remains as one of the primary challenges. In this chapter, preliminary stability studies are conducted on epitaxial 1-µm thick GaAs grown on Si substrate and commercial n-doped GaAs photoanodes (i) without any protective layer, (ii) with Ir, Ni metal depositions by sputtering and (iii) with TiO_2 atomic layer deposition (ALD) protective layers. Results are discussed to identify developments axis.

5.1 Introduction

As described in chapter 1, the semiconductor photoelectrode's thermodynamic stability under illumination can be estimated from the anodic/cathodic self-decomposition potentials. If the anodic self-decomposition potential ($E_{p,d}$) is located above the water OER energy level ($E_{p,d} > E_{OER}$ in E_{VAC} scale), the photocorrosion of the photoanode is dominant over the water OER. [50,51] The majority of the state-of-the-art III-V semiconductors, including InP, GaP and GaAs as well as Si (group IV) are thermodynamically unstable for water oxidation reaction. [51,93] Whereas, photocorrosion is less severe when these materials are used as photocathodes, as the cathodic self-decomposition potential ($E_{n,d}$) is located above the water HER energy level ($E_{n,d} > E_{HER}$ in E_{VAC} level) [51]. It also depends on the nature and acidity of the electrolyte. Thanks to the recent research efforts, various protective layers have been proposed. [8,9]. The application of the ultra-thin transition metal oxide layers as a protection layer have been proven to be effective to extend the photoelectrode's lifetime and applicable to most of the unstable photoelectrodes. [9,85] A general working principle of the protection layers is illustrated in **Figure 5. 1**. In the case of n-type photoanode having $E_{p,d} > E_{OER,}$ it can be protected by applying a thin layer of a material that have $E_{p,d}' < E_{OER}$ as illustrated in **Figure 5. 1 (a-b)**. Similar approach is valid for the p-type photocathode (**Figure 5. 1 (c-d)).**

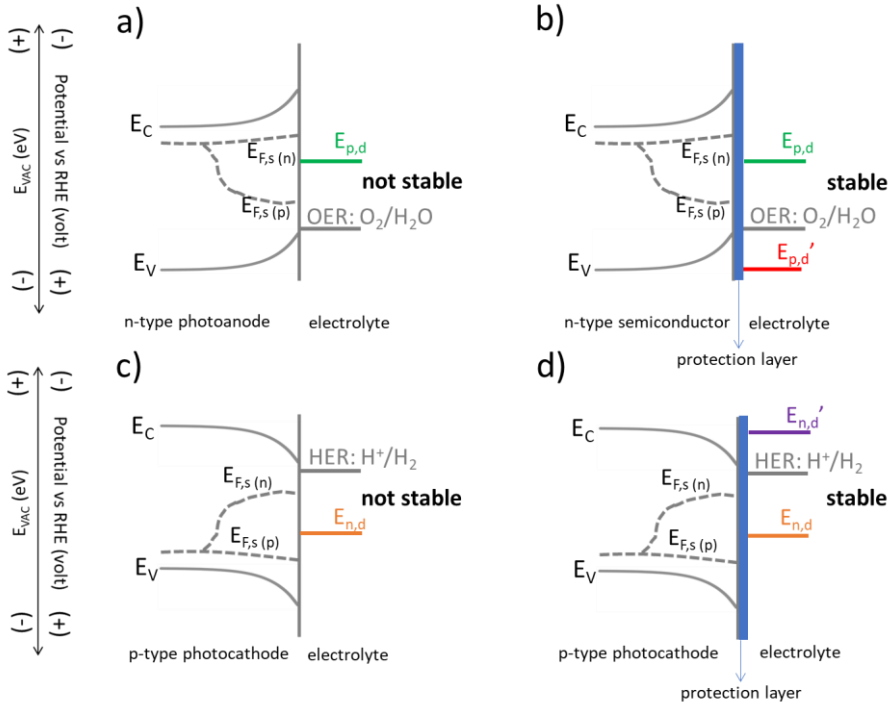

Figure 5. 1 Schematic illustration of an n-type photoanode (a) not stable, (b) stable with a protection layer; p-type photocathode (c) not stable, (d) stable with a protection layer.

Kinetics of water redox reactions and charge transfer as well play a crucial role in the stability of the semiconductor photoelectrodes. For instance water OER is kinetically sluggish and in competition with photoanode self-decomposition reaction. [7,52] Catalysts are mainly found to be solution to increase the rate of water OER and subsequently increase the lifetime of the photoelectrode. In addition, several surface passivation strategies have shown to improve the surface chemical properties by surpassing the recombinations at surface states and thus improving charge transfer kinetics. [119] Therefore, the application of the catalysts together with passivation or protective layers with the robust stability in acidic/alkaline solutions is a must to have a longer lifetime of operation.

Considering photocathodes (for the HER), p-type semiconductors have been first protected with metal layers. As an example, a p-type Si photocathode was found to be stable for 60 days in 1M HCl (pH = 0) by using a metallic platinum coating. [141] Generally, noble metals such as Pt, Ru and Ir are used, but some other non-noble metals have been also tested. [85,88] The deposition of metal leads to the formation of a Schottky

junction (chapter 1**)** between metal and semiconductor and introduce a new way to control the built-in electric field and thus the charge separation. The metal work function is therefore, a critical parameter to choose the correct metal. Despite the simplicity of the metal deposition approach, its application as protective layers is limited due to parasitic light absorption/reflection loss by these metallic layers. A large decrease in the photocurrent is usually observed after the deposition of the metal with a large thickness. In addition, several metal oxide semiconductors have been considered as a protective layer, i.e., TiO_2 (E_G = 3.2 eV) is the most widely used, owing to its optical transparency for the photons with $h\nu \leq 3$ eV and suitable E_{CB} close to HER potential. Turner and coworkers demonstrated high stability of p-$GaInP_2$ photocathode protected with a 35-nm TiO_2 layer functionalized by a cobaloxime molecular catalyst for several hours in H_2 production with a current density of $\sim 9\ mA\ cm^{-2}$ at 0 V vs RHE. [142] In addition to TiO_2, n-type Nb_2O_5 layers have shown good stability and high light-limited photocurrents for p-GaP photocathodes. [81] In general, the metal oxides have poor catalytic activity and thus co-catalyst such as Pt and Ru are deposited to speed-up the reaction kinetics.

The photoanodes protection issues are substantially different than those of photocathodes. [9,119] Unprotected non oxide photoanode materials oxidize under OER conditions by forming an insulating layer, sometimes soluble in electrolyte. [128,143] Only a few OER catalysts (IrO_x, RuO_x) are stable under acidic OER conditions and thus most of the attention has been devoted to protection in alkaline electrolytes (pH=14). [139] The band alignment of TiO_2 is normally unfavorable for the OER and the photogenerated holes are expected to be blocked at the semiconductor/TiO_2 interface. However, quite good performances have been reported for some photoanodes protected by TiO_2 layers, [17,85,144,145] demonstrating efficient hole transport through the amorphous TiO_2. Hole tunneling through the thin TiO_2 layer and/or hole transfer by hopping via TiO_2 defect states have been proposed to explain the hole transport observed. [85,145] NiO_x and CoO_x present better band positions to ensure hole transfer and are quite stable in alkaline electrolytes (though unstable in acid) and has been tested for GaP photoanode protection. [86,88]

5.2 Stability of bare GaAs:n and GaAs/Si photoanodes

At first, the stability of bare photoanodes (PA) of the commercial GaAs:n wafer was studied as a reference material without any protection layer. Then, the stability of epitaxial thin-film GaAs/Si:n PA was investigated to compare the stability of the PA of two materials in similar conditions.

5.2.1 GaAs:n photoanode

The stability of 350-µm thick commercial n-doped (1-5x10^{18} cm^{-3}) GaAs wafer photoanode without any protection layer was analyzed at an applied external potential of 0.8 V vs. RHE in the dark and under illumination**. Figure 5. 2** shows the chronoamperometry results at 0.8 V vs. RHE with corresponding *j*–V curves recorded before (0h), at 10h and after (20h), respectively.

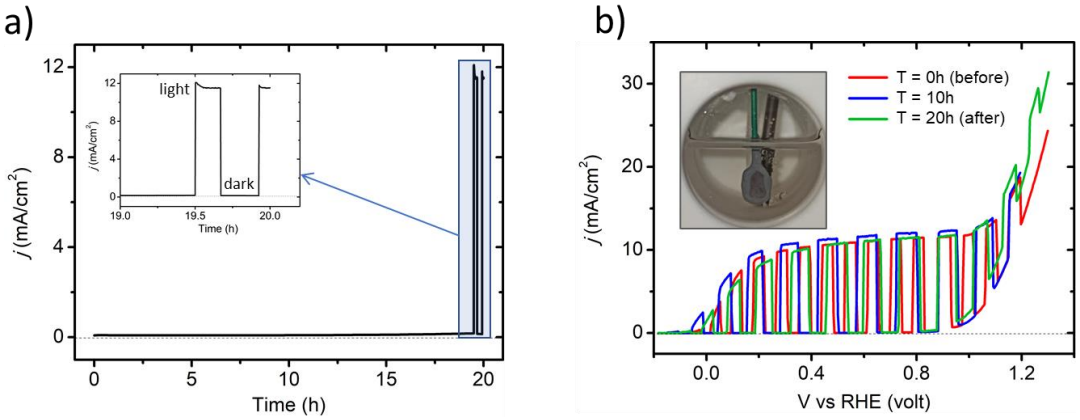

Figure 5. 2 (a) Photocurrent density vs. Time (chronoamperometry) in the dark at 0.8 V vs. RHE for GaAs:n wafer photoanode, inset shows a magnified version of the graph at T~20 h; (b) j - V curves recorded at 0h, 10h and 20h after chronoamperometry, inset shows the inside of the PEC cell after 20h stability test.

Despite the known issues of GaAs stability, the current density in the dark remains steady close to 0 mA/cm^2 indicating a good stability within 20h. At the end of the chronoamperometry measurement, the light (1-sun illumination) was turned ON, in order to check if the photoanode is still photoactive. In the inset of **Figure 5. 2 (a),** one can clearly observe that 1-sun illumination results in a photocurrent density of ~12 mA/cm^2 which is similar to the photocurrent density obtained at the beginning of the

chronoamperometry experiment for the bare-GaAs:n photoanode. The *j* – V curves before (0h), at 10h and after (20h) were recorded and plotted in **Figure 5. 2 (b)**, in order to check if the photoanode is still photoactive. The observed similarity in the *j* – V curves and the intact surface of the photoelectrode after stability test (inset of **Figure 5. 2 (b))** suggests that the bare-GaAs:n photoanode remained stable and photoactive after 20h of stability test performed in the dark. As explained in chapter 1, the corrosion of an n-type GaAs in the absence of light may occur mainly via cathodic self-decomposition with the majority carriers (electrons, e^-). N-type GaAs has a cathodic self-decomposition potential, $E_{n,d}$ located below the E_C and is thus expected to be unstable against cathodic self-decomposition. [51] However, considering the solvent decomposition potential, $E_{n,solvent}$ is located below $E_{n,d}$ for the n-type GaAs semiconductor (**Figure 1. 14 (a)** in chapter 1), and thus the material can be protected against cathodic self-decomposition by the solvent decomposition. [50]

Under illumination, the density of the minority carriers (holes, h^+) increases vastly in the case of the n-type semiconductor and enables the oxidation reaction that can be either oxidation of the semiconductor itself (photocorrosion) or solvent (water) depending on the relative position of the anodic self-decomposition potential, $E_{p,d}$. In the case of n-type GaAs, the $E_{p,d}$ is located above the water oxidation (O_2/H_2O) potential, [51] meaning that the anodic self-decomposition of an n-type GaAs is more favorable than the water oxidation. **Figure 5. 3** shows chronoamperometry result obtained at 0.8 V vs. RHE under 1-sun illumination with the corresponding *j* - V curves recorded before (0 h), at 4 h and 8 h of chronoamperometry.

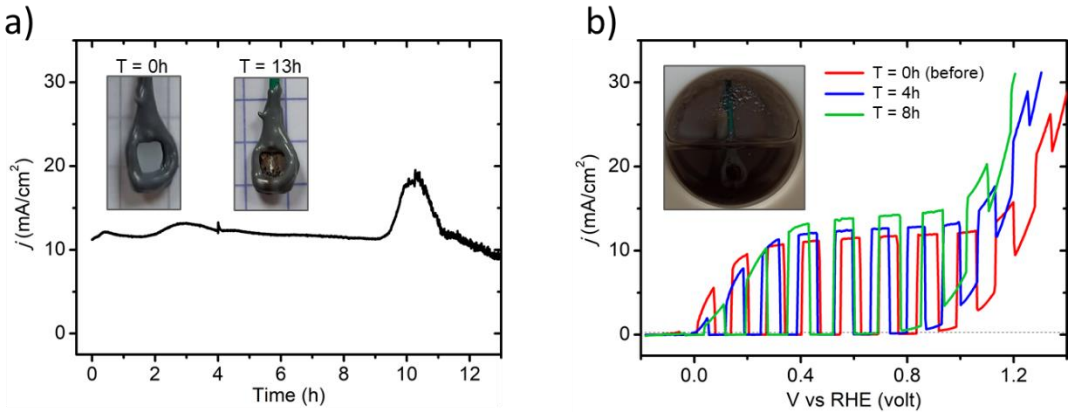

Figure 5. 3 (a) Evolution of photocurrent density as a function of time at 0.8 V vs. RHE under 1-sun illumination, inset shows the photoelectrode surface before T=0h, after T=13h; (b) j-V curves recorded before (0h), 4h and 8h of chronoamperometric activity, inset shows the inside of PEC cell after stability test.

Unstable photocurrent density as function of time **(Figure 5. 3 (a))** and *j* – V curves recorded at different time intervals **(Figure 5. 3 (b))** indicate photocorrosion of the bare-GaAs PA. Moreover, bare-GaAs PA studied in this thesis has a photovoltage, V_{ph} of ~ 0.45 V (**Figure 3. 8**), which is not sufficient to split water on its own as the minimum V_{ph} required is 1.23 V. Thus, the photocurrent observed at lower voltages than the 1.23 V vs. RHE is mostly the consequence of GaAs photocorrosion. As a result, the surface of the photoelectrode changed completely, showing a complete etching of the 350-µm thick GaAs:n wafer after ~13h of the chronoamperometric test. In a first approximation, assuming that the etching is uniform and linear, the estimated etching rate of bare-GaAs photoanode is ~0.45 µm/min in our experimental conditions (0.8 V vs. RHE, 1-sun illumination, 0.2 M H_2SO_4 electrolyte with measured pH of ~0.3). Moreover, the electrolyte solution in PEC cell as shown in the inset of **Figure 5. 3 (b)** turned into darker color, indicating the electrolyte contamination with photocorrosion products of GaAs as they are partially soluble in the solution. [93,128,143] It is known from the literature, that six elementary charge carriers are required for the anodic corrosion of GaAs. [91,146] A two-step process is proposed for the overall anodic corrosion reaction of GaAs in acidic conditions (pH=0), [91,143] in which Ga is selectively etched first, leaving behind As^0 which is subsequently oxidized and dissolved,

$$GaAs + 3h^+ \rightarrow Ga^{3+} + As^0 \quad (5.39)$$

$$As^0 + 3h^+ + 2H_2O \rightarrow HAsO_2 + 3H^+ \quad (5.40)$$

and thus, the overall reaction for the GaAs anodic corrosion can be written by the sum of the first process (5.39) and the second process (5.40),

$$GaAs + 6h^+ + 2H_2O \rightarrow Ga^{3+} + HAsO_2 + 3H^+ \quad (5.41)$$

Following the interpretation of the chronoamperometry and *j* - V results for the GaAs:n wafer PA, one may observe that current density in the dark and under-illumination increases exponentially beyond applied voltage of 1 V vs. RHE. This is attributed to the tunneling of the excess of majority charge carriers (electrons) through the narrow depletion layer caused by the very sharp band-bending in the case of the highly doped n-type GaAs. [147]

5.2.2 GaAs/Si:n photoanode

The stability of 1-µm thick epitaxial GaAs/Si:n PA is now studied in the same experimental conditions under 1-sun illumination than the ones used for the bare GaAs:n PA. The two PA are similar, from the surface material point of view, however, GaAs/Si:n photoanode is thinner, grown epitaxially on a n-type Si substrate and thus it has a relatively higher defects density, including APBs that have been found to impact PEC water splitting properties. [18] **Figure 5. 4** shows the evolution of the photocurrent density as function of time at an applied potential of 0.8 V vs. RHE under 1-sun illumination. The photocurrent density has decreased from 11 mA/cm^2 to ~0 mA/cm^2 after 125 s of the chronoamperometric activity. The strong decrease is confirmed with the corresponding *j* – V voltametric curves as well, recorded at T=0 s (before) at 60 s and 120 s. Such an evolution of the *j* can be associated to the etching of the photoactive layer (1-µm thick epitaxial GaAs layer from GaAs/Si PA). At 125 s of chronoamperometry, the measurement was stopped in order to check the surface of the photoelectrode.

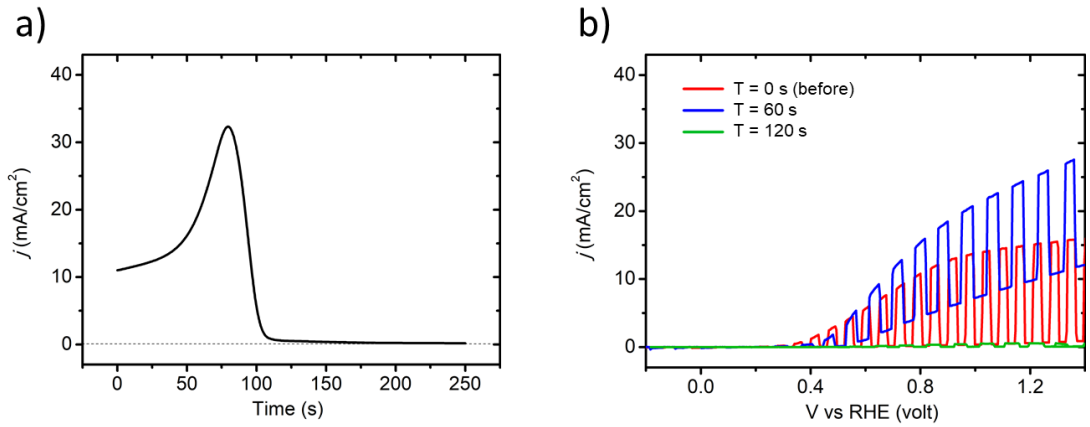

Figure 5. 4 (a) Photocurrent density vs. Time at 0.8 V vs. RHE under 1-sun illumination for 1-µm thick GaAs/Si:n photoanode; (b) j – V curves obtained before chronoamperometry (0 s), at 60 s and 120 s, respectively.

Figure 5. 5 shows the surface and surface profile of the photoelectrode after 125 s of the chronoamperometric activity.

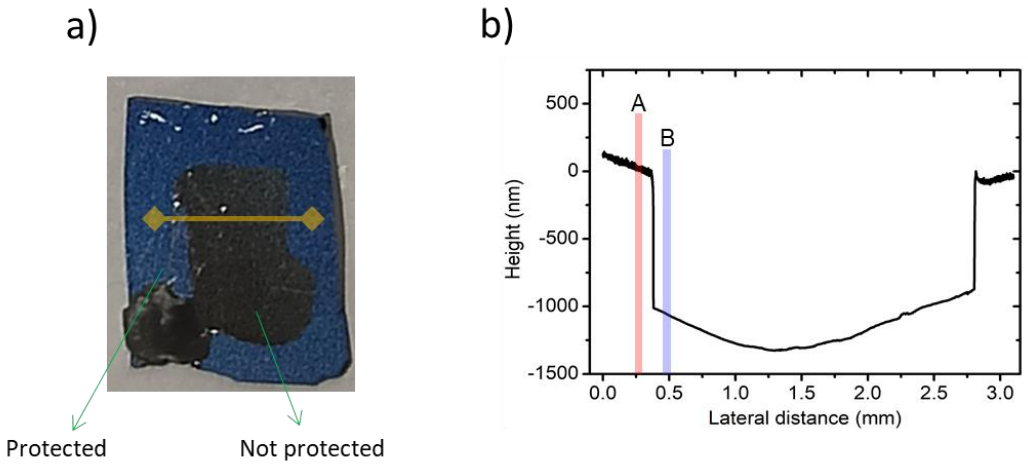

Figure 5. 5 (a) Surface of the photoelectrode after 125 s of chronoamperometry; (b) surface profile measured with profilometry along the yellow line (lateral distance)

The epoxy layer was removed after dipping the photoelectrode in dichloromethane solution for 30 min. As shown in **Figure 5. 5 (a),** the photoelectrode surface change can be observed from the color difference: a lighter bluish color is observed for the part where it was protected by epoxy resin, whereas the surface that was in contact with the electrolyte has a darker blue color. Surface profile of the photoelectrode (**Figure 5. 5 (b))** shows a clear step between the point A and B, which is equivalent to 1.02±0.05 µm

(thickness of the GaAs epilayer). From these results, the etching rate was calculated for the GaAs/Si PA, and found to be ~0.48 μm/min (very close to the one of GaAs:n wafer PA). The AFM was performed to characterize the surface of GaAs/Si PA before and after the stability test. In **Figure 5. 6**, it can be clearly observed that surface of the GaAs/Si PA is changed after 125 s chronoamperometry, revealing a smaller roughness with RMS value of 0.5 nm for the etched GaAs/Si PA.

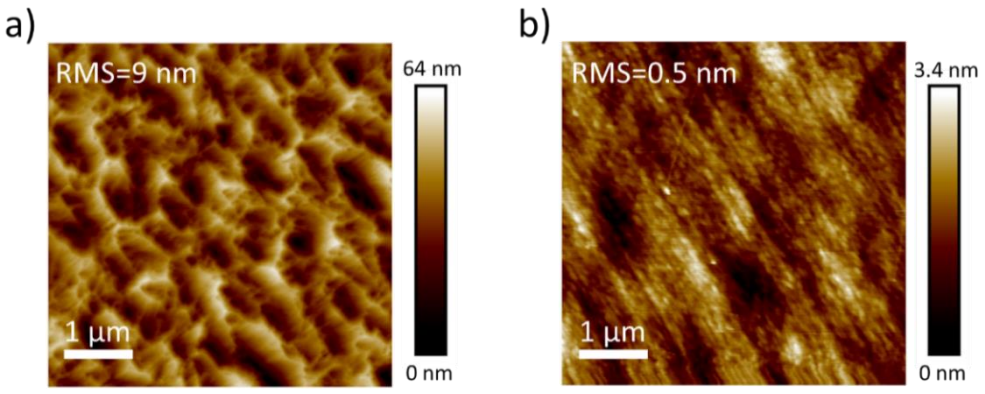

Figure 5. 6 Atomic Force Microscopy (AFM) images of the sample surface for the GaAs/Si PA (a) before; (b) after 125 s of chronoamperometry at 0.8 V vs. RHE under 1-sun illumination

It was mentioned above that, the anodic photocorrosion of GaAs involves six elementary charges and starts with the anodic oxidation of Ga species to Ga^{3+} leaving behind As^0 which is subsequently dissolved in the electrolyte (etching). GaAs/Si PA photocorrosion seems to follow a similar path as the 1-μm thick photoactive GaAs layer is etched as a result of material self-decomposition.

5.3 Application of metallic layers as a cocatalyst and protection against corrosion

To prevent photocorrosion while promoting PEC water oxidation, the epitaxial thin-film GaAs-Si photoanodes should be physically protected with a thermodynamically stable layer. The work function of the deposited stable layer has to be suitable with the semiconductor's one to ensure an efficient charge transportation in case of thick deposited metal layers. Metals having relatively high work functions (which is usually preferred for efficient hole transport at the semiconductor/metal interface), such as Platinum (Pt),

Iridium (Ir) and Nickel (Ni), seem adapted for GaAs that has a lower work function. Additionally, these metals are catalytically active to improve the kinetics of water OER and thus avoiding possible corrosion reactions. In this context, we have deposited a thin layer of Iridium (Ir) or Nickel (Ni) via a sputtering technique mainly for the purpose of protection against corrosion. In the following, the results obtained after these attempts are presented and discussed.

5.3.1 GaAs-Si photoanode protected with iridium

Iridium (Ir) is a noble metal known for its catalytic properties in multiple redox reactions, including water oxidation. [148,149] According to the Pourbaix diagram shown in **Figure 5. 7**, iridium has a robust stability in acidic electrolyte which is in favor of PEC water splitting. [150]

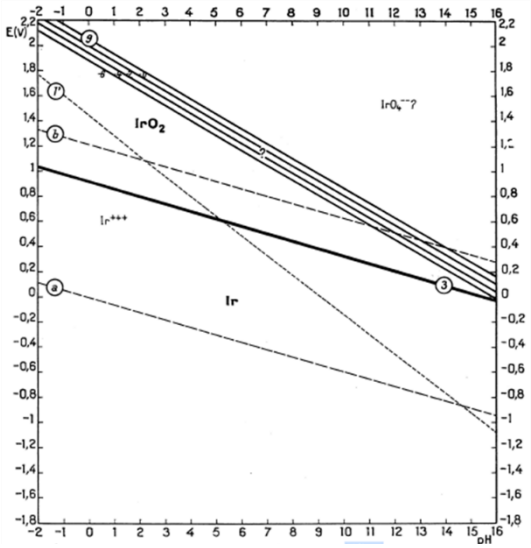

Figure 5. 7 Pourbaix diagram of iridium. Adapted from [49]

Metallic layer of iridium with thickness of 4-nm was deposited via sputtering technique following the same recipe that was developed and successfully demonstrated for Si photoelectrodes in Institut des Sciences Chimique de Rennes (ISCR). Prior to the deposition of the metal, thin-film GaAs-Si was cleaned in acetone (3 min), iso-propanol (3 min) and ultrapure water (5min) in ultra-sound cleaner. The photoelectrodes of Ir-deposited GaAs-Si samples were prepared using the standard procedure described in chapter 2, and were immediately tested for PEC water oxidation as photoanodes. **Figure**

5. 8 shows the *j* - V curve measured under 1-sun illumination in 0.2 M H_2SO_4 electrolyte (measured pH=0.3) for the as-grown GaAs-Si and for the Ir-coated GaAs-Si PA. It can be clearly observed that the photocurrent density recorded at 1st *j* - V curve for the 2 PA is different with a slightly delayed onset potential (V_{onset}) by 0.2 V vs. RHE for the Ir-coated GaAs-Si PA. The delay in V_{onset} is associated to the newly formed Schottky junction between metal (Ir) and semiconductor (GaAs-Si) that affects the built-in electric field and thus charge separation.

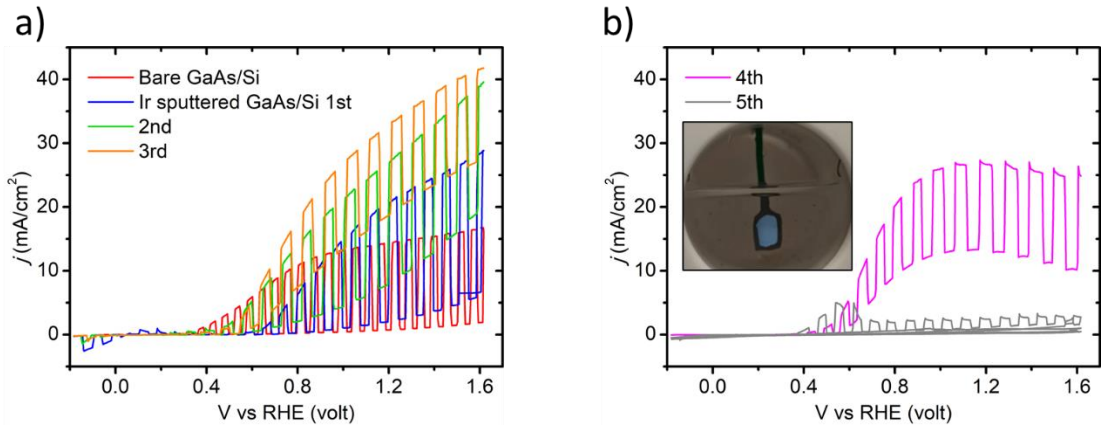

Figure 5. 8 (a) Photocurrent density as a function of applied voltage (j - V) curve measured under 1-sun illumination in 0.2 M H_2SO_4 (pH=0.3) for bare and Ir-coated GaAs-Si PA for the 1st, 2nd and 3rd scans; (b) 4th and 5th scans

Moreover, the magnitude of the current density in the dark and under illumination differs from each other and increases successively for the 2nd and 3rd *j* - V scans of Ir-coated GaAs-Si PA. The observed unstable current density can be associated to the photocorrosion of the PA. The photocurrent decreases down to 0 mA/cm^2 for the 5th *j* - V curve and the presence of several tiny black particles in the electrolyte solution (inset of **Figure 5. 8 (b)**) indicates the etching of the GaAs photoactive layer regardless of the deposited thermodynamic stable layer of iridium. These results indicate that the recipes used to protect Si PA cannot be directly transferred to GaAs/Si PA, and that further in-depth study (on surface preparations, thicknesses, deposition processes, etc.) is needed for further III-V PA developments using Ir as a protection layer.

5.3.2 GaAs-Si photoanode protected with nickel

Nickel is another promising candidate to protect GaAs-Si PA from photocorrosion with relatively lower cost than iridium. Research studies demonstrated catalytic activities of Ni in the form of metallic layers and nanoparticles for water oxidation reaction, which is of interest for PEC water splitting. [151–153] In contrast to iridium (discussed above), nickel has a very low stability in acidic electrolytes. Nevertheless, its stability in alkaline electrolytes (pH~14) lasts for a couple of hours. [152] With the same technique used to deposit iridium, a 4 nm-thick nickel layer was deposited onto the cleaned GaAs-Si sample. The Ni-coated GaAs-Si PA was investigated for PEC water oxidation in 1 M KOH electrolyte (pH=14) in the dark and under 1-sun illumination. As shown in **Figure 5. 9 (a)**, the first 4 scans of *j* - V curves measured in the dark show a current density below 0.5 mA/cm^2, which increases subsequently up to 2.5 mA/cm^2 after some additional scans (see the 13th scan and subsequent ones) for the Ni-coated GaAs-Si PA.

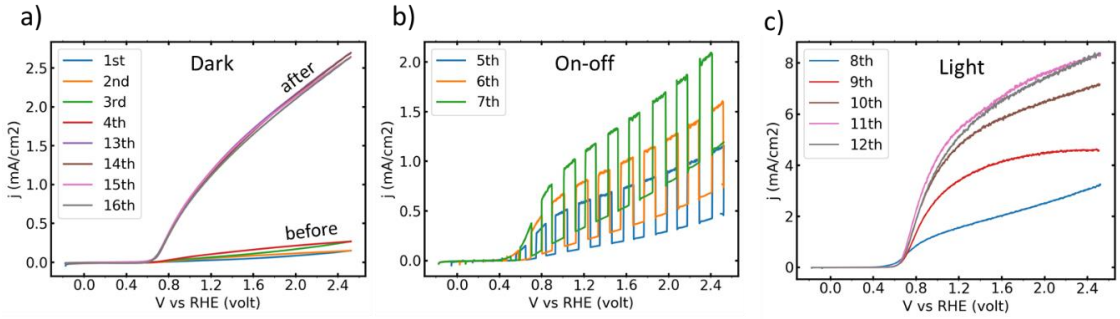

Figure 5. 9 (a) (j - V) curves measured in the dark for Ni-deposited GaAs-Si PA in 1 M KOH (pH=14) electrolyte before and after PEC characterization; (b) under chopped light of 1-sun illumination; (c) and steady light conditions

The resulted current density in the dark and its change toward higher values after few PEC characterizations is associated to the self-corrosion and surface change of the photoelectrode. After the 4th scan in the dark, the *j* - V curves were measured under chopped (5th - 7th) and continuous wave 1-sun illumination (8th - 12th scans) showing an increased photocurrent density up to 8 mA/cm^2 (**Figure 5. 9 (b-c)).** Moreover, the surface of the photoelectrode is changed at the end of PEC characterization by forming a reddish-pink colored surface (**Figure 5. 10**). The increased current density with the number of *j* - V scans and the surface change observed after the PEC characterization is associated to the corrosion of the Ni-coated GaAs-Si PA, likewise to the Ir-coated one.

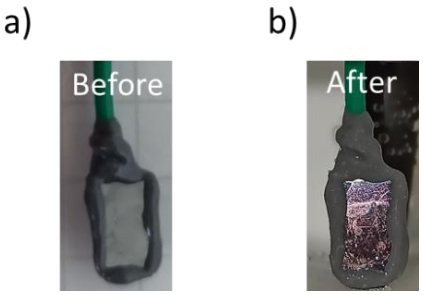

Figure 5. 10 (a) Surface of the Ni-coated GaAs-Si PA before; and (b) after PEC characterization.

The photoanodes of GaAs-Si with a 4-nm thick deposited iridium and nickel layers were corroded after a couple of minutes, whereas at least an hour of stability could be expected. [152,153] The main reason for the failure is expected to be the high roughness of the GaAs-Si sample. As shown in **Figure 5. 6 (a),** the epitaxial 1-µm GaAs grown on Si substrate presents a roughness with the RMS of 9 nm. Therefore, the surface of GaAs-Si might present one or several un-covered parts after the deposition of iridium/nickel, where the corrosion of GaAs initiates and spreads over as the current density in the dark and under illumination increases first and decreases down to ~0 mA/cm^2 after photocorrosion of the entire photoactive GaAs layer. In addition, the adhesion of the metallic iridium and nickel layers on GaAs surface could be another reason of the failure to protect against photocorrosion. To check these assumptions, the same work has been performed with photoanodes made of native GaAs substrates.

5.3.3 GaAs:n photoanode protected with iridium or nickel

In order to verify the influence of the roughness on the protection efficiency of iridium and nickel layers, here we have used the same technique to deposit iridium or nickel onto a commercial GaAs:n wafer that has a relatively low roughness, with a typical RMS value below 1 nm.

First, the PEC characterization was carried out for the Ir-coated GaAs:n photoanodes. As shown in **Figure 5. 11**, the 1st *j* - V curve measured under chopped light is very different than that of the bare GaAs:n wafer with the delayed V_{onset}. The difference between the dark and light current density is very small indicating that the Ir-coated GaAs PA does

not have a strong photo-response. The parasitic light absorption and charge transfer barriers imposed by iridium could be the two main reasons.

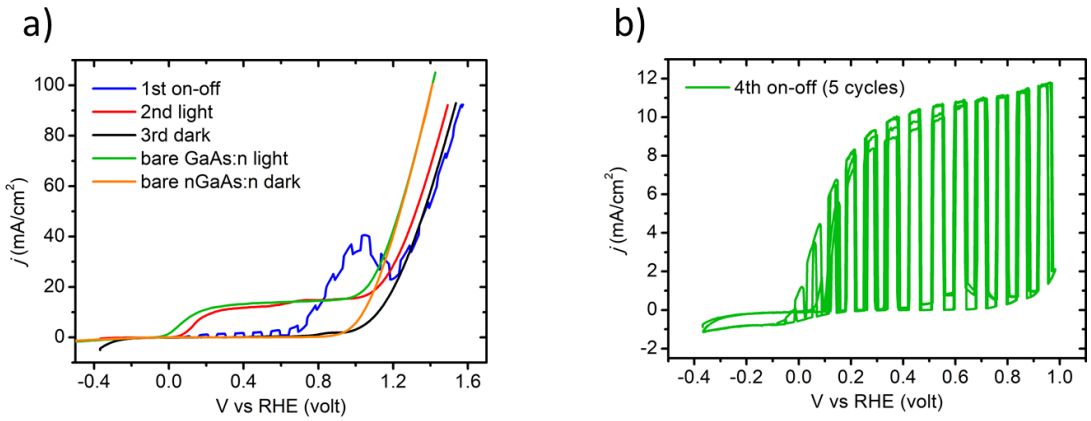

Figure 5. 11 (a) (j – V) curves measured for Ir-coated GaAs:n PA and bare GaAs:n PA; (b) several cycles recorded for Ir-coated GaAs:n PA under chopped light. The measurement was carried out in 0.2 M H_2SO_4 (pH = 0.3) with 1-sun illumination.

Moreover, it exhibits an increasing bump at 1 V vs. RHE that could be assigned to the redox change of iridium. The 2nd and 3rd *j* - V scans measured in the light and dark are similar to the *j*-V curves obtained for the bare GaAs PA. Nevertheless, all the *j*-V curves exhibit a strongly increasing current density in the dark and under light beyond 1 V vs. RHE, which is attributed to the tunneling of electrons through a very thin depletion layer as described previously. The 4th *j* - V curve as well, with several scans performed under chopped light is very similar to the bare GaAs PA. These results suggest that the deposited layer of iridium with the thickness of 4 nm is removed from the surface after the 1st *j* - V scan, possibly either after the corrosion underneath areas of the Ir film or imperfect adhesion between Ir film and the GaAs wafer.

Second, the PEC characterization was carried out on a Ni-coated GaAs PA, which is prepared exactly in the same way as the Ir-coated GaAs PA. As shown in **Figure 5. 12**, likewise to the previous cases, the current density is not stable until the 3rd and 4th scans measured in the dark and under light. Similarly, to the peeling-off of the deposited iridium layer, a 4-nm thick deposited nickel was likely removed after few minutes of PEC characterization. The shape of the 2nd *j* - V curve of the Ni-coated GaAs PA is similar to the one of the bare GaAs PA.

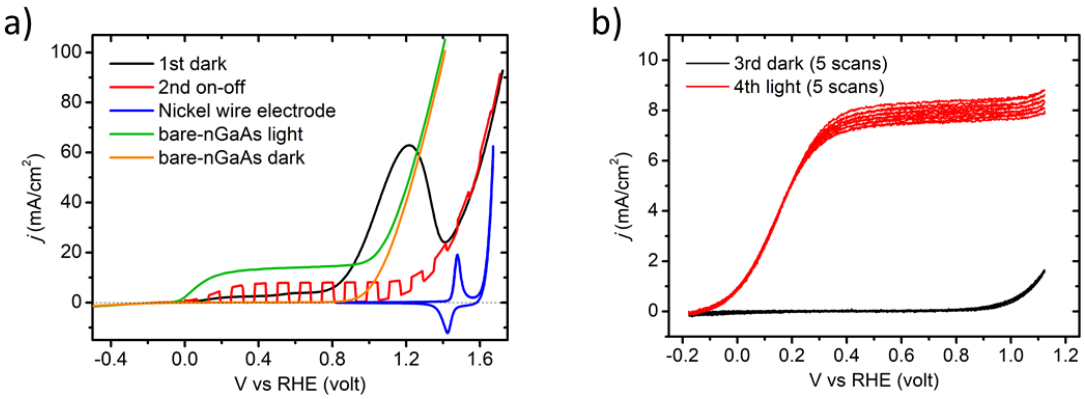

Figure 5. 12 (a) (j – V) curves measured for Ni-deposited GaAs PA, nickel wire electrode and bare nGaAs wafer; (b) several cycles recorded in the dark and under light of 1-sun illumination for Ni-deposited GaAs PA. The measurement was carried out in 1 M KOH (pH=14) under 1-sun illumination

However, in terms of potential (V vs. RHE), the *j* – V curve of the Ni-coated GaAs PA is delayed by few millivolts, that could be due to an additional interface formed after nickel deposition imposing a barrier for charge transportation. The *j* - V curve with the nickel wire electrode is measured as a reference with a reversible photocurrent spike at ~1.4 V vs. RHE corresponding to Ni^{2+}/Ni^{3+} redox change (blue curve of **Figure 5. 12 (a)**). The increasing photocurrent at 1.6 V vs. RHE is associated to the water OER which should not be assimilated to the current density of the GaAs PA, that results from the tunneling of electrons through a narrow depletion layer caused by the high doping.

5.4 Titanium dioxide (TiO_2) protected GaAs-Si and GaAs:n

Deposition of thin, conformal surface protection layers, especially titanium dioxide (TiO_2) using atomic layer deposition (ALD) to mitigate semiconductor corrosion has had success in recent years. [9,85,144] As mentioned above, a 100-nm thick ALD deposited TiO_2 layers provided a 20 h robust protection against corrosion for an n-p^+ GaAs photoanode during water oxidation reaction. [85] Considering the band energy alignment between TiO_2 and GaAs, the photogenerated holes are expected to be blocked at the GaAs/TiO_2 interface and thus making the water oxidation reaction unfavorable. However, efficient hole transport through the un-annealed amorphous TiO_2 layer with a high density of electronic defect states and good PEC performance with a photocurrent density >10mA/cm^2 have been demonstrated for some photoanodes protected by a TiO_2

layer. [17,85] Hole tunneling through the thin TiO_2 layer and/or hole transfer by hopping via TiO_2 defect states have been proposed to explain the hole transport observed. [85,145] As TiO2 has a mild catalytic property, other co-catalysts such as Ni, CoO_x or ruthenium-aqua complexes have been used together in combination with TiO_2 layer to increase the water OER kinetics which is also crucial to avoid the photoelectrode self-decomposition. [139]

Keeping in mind the roughness of the GaAs-Si sample, here we have targeted two samples to be protected with TiO_2: (i) a chemically mechanically polished GaAs-Si (CMP GaAs-Si) sample and (ii) a pristine GaAs-Si (GaAs-Si) one. **Figure 5. 13** shows the schematic illustration and corresponding AFM images of the two GaAs-Si samples on which a 50 nm-thick TiO_2 layer was deposited using ALD by our collaborators at CiNAM (L. Santinacci). Further, a 8 nm-thick nickel layer (catalyst) was deposited using sputtering technique as described above. The Ni/TiO_2–coated GaAs-Si photoanodes (PA) were prepared using the procedure described in chapter 2**.** Photoelectrochemical, surface and elemental composition characterizations were carried out to study the stability of Ni/TiO_2–coated GaAs-Si PA and discussed in the following sections.

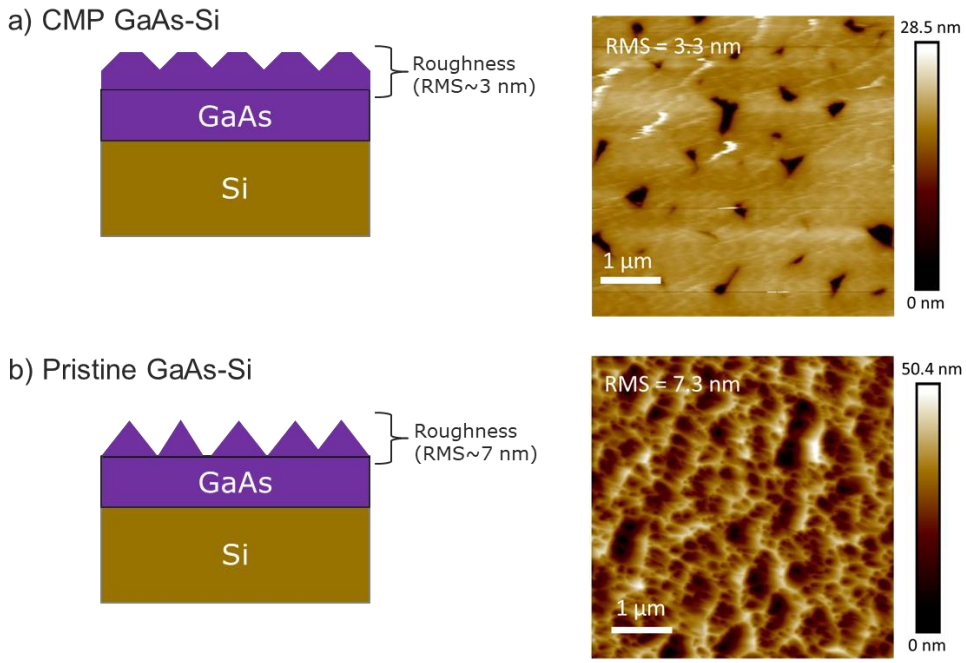

Figure 5. 13 Schematic illustration of the (a) CMP GaAs-Si sample and (b) the pristine GaAs-Si sample with corresponding surface AFM images. The scale bar and RMS are indicated in inset.

5.4.1 CMP GaAs-Si protected with TiO_2 and Ni as a catalyst

To reduce the surface roughness of GaAs-Si, and thus favor the conformal deposition of TiO_2 on the surface, the sample first underwent chemical mechanical polishing (CMP). AFM image plotted in **Figure 5. 13 (a)** shows a smoothened surface and decreased roughness by two times as a result of CMP. The ALD deposition was performed using a Tetrakis(dimethylamino) titanium (TDMAT) and deionized water (ρ = 18.2 MΩ · cm) according to the recipe described elsewhere. [154] Afterwards, the received samples (TiO_2/GaAs-Si) were annealed in FOTON Institute cleanroom at T_a = 450 ^oC under N_2 atmosphere for 2 h to get rid of the Ti precursor ligands that are dissolved when the films are immersed in the electrolyte and to transform the amorphous layer into the polycrystalline anatase. On the surface of the annealed samples, a 8 nm-thick layer of nickel was deposited via sputtering technique used previously. Hereafter, Ni/TiO_2–coated CMP GaAs-Si PA were prepared after rinsing the sample with ultrapure water and drying it with the flow of N_2 gas. Photoelectrochemical measurements were carried out in a three-electrode PEC cell in the dark and under 1-sun illumination in 1 M KOH (pH=14) electrolyte and plotted in **Figure 5. 14**. The current density in *j* - V curves measured in

the dark (1st – 5th scans) increases successively with the number of scans, indicating instability of the photoanode when higher anodic potential is applied (**Figure 5. 14 (a)**). The *j* - V curves measured under light (6th – 12th scans) decrease then down to 1 mA/cm^2 as corrosion deteriorates the photoelectrode surface (**Figure 5. 14 (b)).**

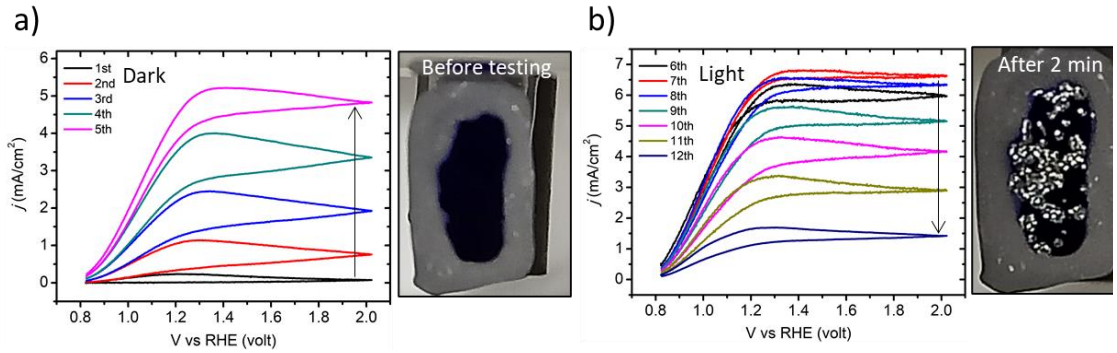

Figure 5. 14 (a) Photocurrent density as a function of applied voltage for CMP Ni/TiO$_2$/GaAs-Si PA measured in the dark; (b) under light in 1 M KOH (pH=14) electrolyte with the corresponding images of the PA surface before testing and after 2 min of PEC activity, respectively

The surface of the photoelectrode changes after 2 min of PEC activity as a result of corrosion by forming small circular dots that multiply to cover the whole surface. From the optical microscopy images plotted in **Figure 5. 15**, it seems that the PA surface was peeled-off during its operation.

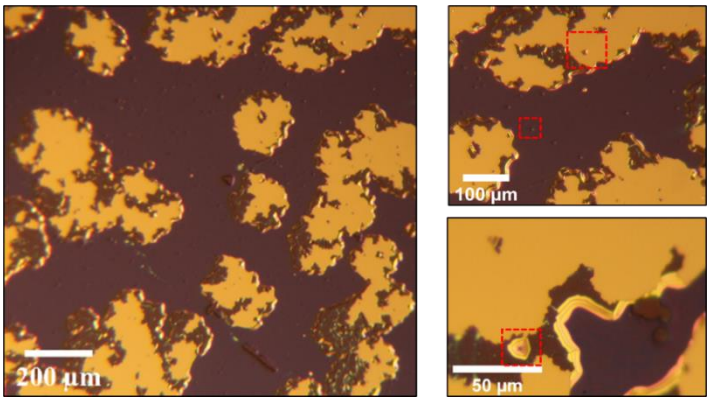

Figure 5. 15 Optical microscopy images of the CMP Ni/TiO$_2$/GaAs-Si PA after 2 min of PEC characterization

As TiO_2 is supposed to be stable in alkaline electrolyte, [9] the etching of the photoelectrode likely starts at the GaAs surface underneath. Moreover, the presence of

several holes can be observed at the surface where the corrosion could initiate first at those sites. One may wonder if the holes present at the surface were formed after PEC characterization or were already existing before.

The SEM and EDX measurements were carried out to check the sample surface, and elemental composition before PEC characterization. As shown in **Figure 5. 16 (a)**, several large holes were already present before PEC characterization. EDX analysis performed at two different selected areas (spectrum 1 and 2) show a different elemental composition indicating that the two areas are chemically modified (**Figure 5. 16 (b)**). Especially, while the expected atoms and compositions are measured in area 2, it was not possible to measure any contribution of the GaAs or the Ni to the EDX signal in area 1, which seems to be an area where the Si is directly covered by the TiO_2. Either CMP processing of the GaAs-Si sample before TiO_2 and Ni deposition or annealing afterwards could be the main reasons for the presence of these holes at the surface of the CMP Ni/TiO_2/GaAs-Si sample. In the next section, we consequently study the properties of a similar PA, where the CMP polishing was not used.

a)

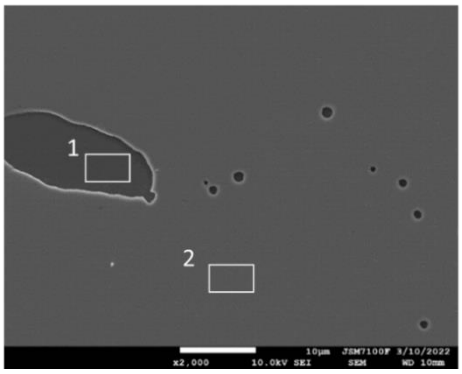

b)

Element	% atomic **"spectrum 1"**	% atomic "**spectrum 2**"
O	22.31	35.41
Si	76.62	5.17
Ti	1.06	2.29
Ni	-	0.52
Ga	-	26.60
As	-	30.00
Total:	100.00	100.00

Figure 5. 16 (a) SEM image of the CMP Ni/TiO_2/GaAs-Si sample before PEC characterization; (b) results of EDX elemental composition analysis of the spectrum 1 and 2 listed in the table form

5.4.2 Pristine GaAs-Si protected with TiO_2 and Ni as a catalyst

It is obvious that uncomplete coverage of the GaAs-Si surface will lead to the corrosion of the photoelectrode. Assuming that corrosion starts initially at the pinholes that are presumably generated during the CMP processing of GaAs-Si sample and that

corrosion spreads all over the surface by etching the GaAs underneath in the Ni/TiO_2/GaAs-Si PA, we now study a pristine GaAs-Si with an ALD deposited TiO_2 of 50 nm and 8 nm-thick layer of Ni deposited by sputtering technique, as described above. TiO_2 and Ni deposition on the pristine GaAs-Si sample took place in the same batch than that of the CMP GaAs-Si sample. The TiO_2 deposited GaAs-Si sample was annealed at the same temperature (T_a = 450 ^oC) under N_2 atmosphere for 2 h and followed by the deposition of a 8 nm-thick Ni layer. The PEC characterization was then carried out on the Ni/TiO_2/GaAs-Si PA and plotted in **Figure 5. 17**. The current density in the dark is close to 0 mA/cm^2 at the beginning, which increases subsequently up to 5 mA/cm^2 **(Figure 5. 17 (a))**. This indicates corrosion of the Ni/TiO_2/GaAs-Si PA in the dark when higher anodic potential is applied, similarly to the CMP Ni/TiO_2/GaAs-Si PA. Current density under light has a similar behavior, starting at 3 mA/cm^2 at the beginning, increasing up to almost 6 mA/cm^2 and then decreasing down to > 1 mA/cm^2 after several successive scans **(Figure 5. 17 (b))**. The decrease of the photocurrent density can be related to the deterioration of the Ni/TiO_2/GaAs-Si PA as a result of corrosion although TiO_2 layer was deposited as a protection layer.

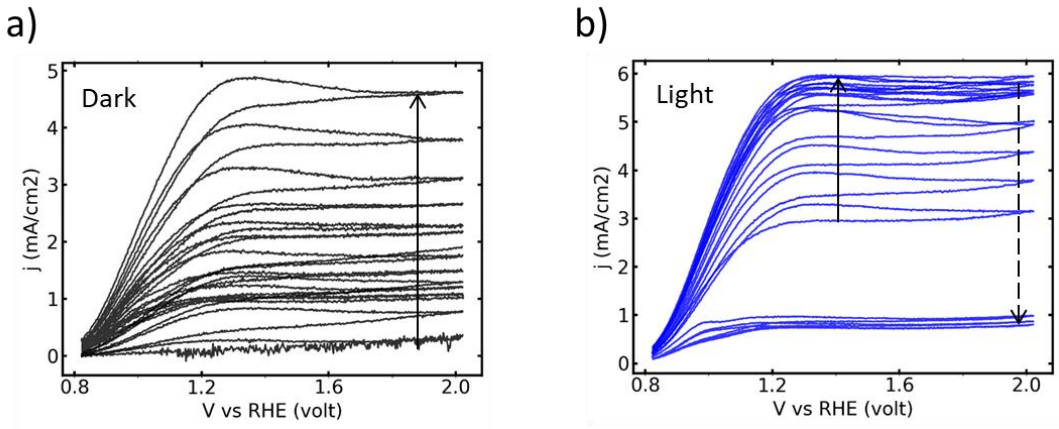

Figure 5. 17 Photocurrent density as a function of applied voltage for Ni/TiO_2/GaAs-Si PA measured (a) in the dark; (b) under light with several cycles in 1 M KOH (pH=14) electrolyte.

In order to analyze if the corrosion of the Ni/TiO_2/GaAs-Si PA occurs in the same way as the CMP-processed Ni/TiO_2/GaAs-Si PA, the optical microscopy images were taken on the surface of the samples after 2 min of PEC activity and shown in **Figure 5. 18**

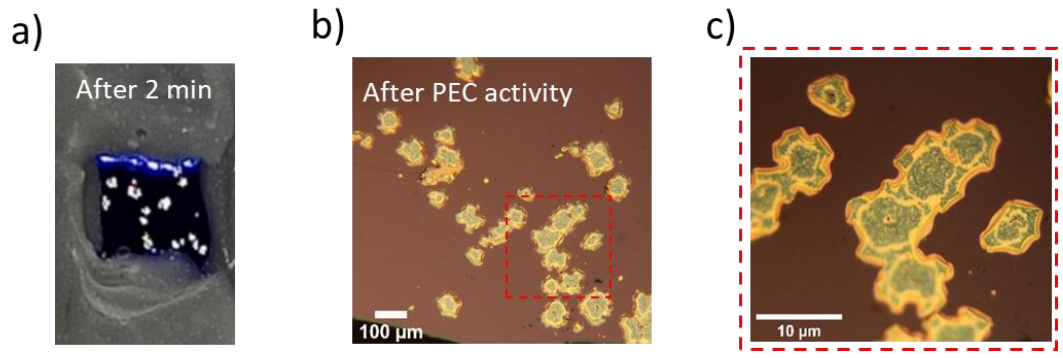

Figure 5. 18 (a) Surface of the Ni/TiO_2/GaAs-Si PA; and (b) optical microscopy images taken after 2 min of the PEC activity with 100 µm scale, and (c) zoomed area in 10 µm scale

Similarly, the circular dots started to form when the photoelectrode was immersed into 1 M KOH electrolyte and biased with anodic potential. The optical microscopy images show similar corrosion pits as the ones observed for the CMP Ni/TiO_2/GaAs-Si PA (**Figure 5. 15).** Only the corrosion rate seems slightly lower than the one of the CMP-polished sample, maybe due to the lower density of pits.

SEM characterization together with EDX elemental composition analysis were carried out on the PA surface and results are given in **Figure 5. 19**. As observed in **Figure 5. 19 (a)**, corrosion starts at a specific area where it is etched forming a hole that spreads all over the surface by time. The elemental composition was analyzed with EDX at 4 different areas: s1 and s2 where the sample surface is still intact, s3 and s4 are etched as a result of corrosion as shown in **Figure 5. 19 (b).** It is clearly observed that the elemental composition is identical at the intact surface area (s1 and s2), and elements such as Ga and As from the photoactive GaAs are present with a similar atomic percentage (% at.). The Si substate is not detected due to the thick coverage of the other materials (>1µm). Whereas, GaAs photoactive layer is not detectable anymore in the etched area of the surface (s3 and s4), which can be explained with corrosion and subsequent dissolution of the GaAs products in the electrolyte. Interestingly, despite the GaAs etching underneath, TiO_2 and Ni layers are still detected in the etched area, suggesting that the TiO_2/Ni membrane was at least roughly preserved during the GaAs etching and lies directly on the silicon surface after the PEC operation. As a consequence, the use of the CMP processing cannot explain the low stability of the PA during PEC operation.

a)

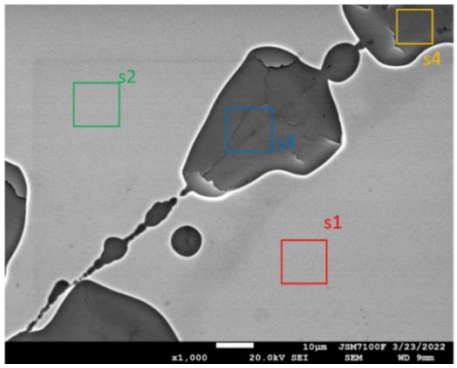

b)

Element	% at.“s1”	% at.“s2”	% at.“s3”	% at.“s4”
O	39.62	38.89	19.93	20.24
Si	-	-	78.94	78.64
Ti	2.07	2.06	0.95	0.96
Ni	0.25	0.39	0.18	0.16
Ga	27.07	26.86	-	-
As	31.00	31.79	-	-
Total:	100.00	100.00	100	100

Figure 5. 19 (a) SEM image at the damaged area of Ni/TiO_2/GaAs-Si PA surface after 2 min of PEC activity and (b) EDX elemental composition analysis at the specific selected areas

Interestingly, **Figure 5. 20** shows the SEM images of unpolished (without CMP) Ni/TiO_2/GaAs-Si before PEC activity and corresponding EDX elemental analysis results. Ni/TiO_2/GaAs-Si before PEC activity has a similar elemental composition than the s1 and s2 area from **Figure 5. 19** where the layer remained intact. In this sample, large holes such as the one presented in **Figure 5. 16** for the sample polished (with CMP) are not visible. This allows to conclude (i) that the CMP process developed initially in our Lab for GaP/Si materials, creates holes in GaAs/Si samples (through GaAs peeling off), as the chemical treatments still need to be adapted to this material, and (ii) that corrosion can occur in other places than the large holes generated during the CMP (**Figure 5. 16**). This process is expected to start in pinholes that have a much smaller scale than the one observed with CMP. Presently, the exact reason on why corrosion starts in s3 and s4 areas are not known. From the SEM image it can be observed a higher surface roughness for Ni/TiO_2/GaAs-Si. Taking into account that the ALD deposition of TiO_2 layer is normally perfectly conformal, a 50-nm thick TiO_2 layer is expected to fully cover the surface of pristine GaAs-Si, and thus provide a robust protection against corrosion. Nevertheless, the photoelectrode surface has started to change after 2 min of PEC activity due to corrosion of the sample (s3 and s4 areas in **Figure 5. 19**)

a)

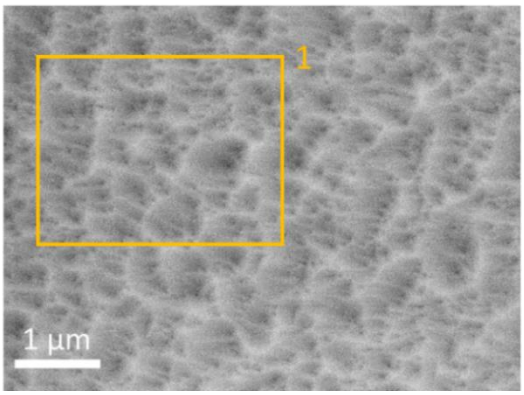

b)

Element	% at. **1**
O	37.97
Si	-
Ti	2.24
Ni	0.39
Ga	28.28
As	31.11
Total:	100.00

Figure 5. 20 (a) SEM image of Ni/TiO_2/GaAs-Si PA before PEC activity, and (b) EDX elemental composition analysis at selected area "1"

5.4.3 GaAs:n commercial wafer protected with TiO_2

To avoid the impact of the surface roughness and annealing conditions, we have tested a PA made of GaAs:n commercial wafers, protected with a TiO_2 layer which was annealed in CiNAM following the procedure already used for the protection of Si. [145] In the similar way as for the previous samples (CMP GaAs-Si and pristine GaAs-Si), a 50-nm thick TiO_2 layer was deposited via ALD technique with a Tetrakis(dimethylamino) titanium (TDMAT) precursor and deionized water (ρ = 18.2 MΩ cm). [145,154] Whereas, the annealing of the as-deposited GaAs:n/TiO_2 samples were done in CiNAM (Marseille) at T_a = 450 ^oC under ambient air for 2 h as it was supposed to be done for all the samples according to references [145,154]. Photoanodes of GaAs:n/TiO_2 samples were characterized in PEC water oxidation using the same three-electrode cell in the same electrolyte solution (1 M KOH, pH=14) under 1-sun illumination**. Figure 5. 21 (a)** shows a photocurrent density (*j*) as function of applied voltage (V) for the pristine GaAs:n wafer PA. It was already mentioned above that highly doped ($N_D = 10^{18}$ cm^{-3}) GaAs exhibits an exponentially increasing current density in the dark and under light beyond 1 V vs. RHE due to tunneling of electrons through narrow depletion layer. Similarly, the increasing current density is observed for the TiO_2/GaAs:n PA, but with a delayed potential of ~0.3 V as shown in **Figure 5. 21 (b)**, indicating that TiO_2/GaAs:n PA is still vulnerable to corrosion at higher anodic potentials.

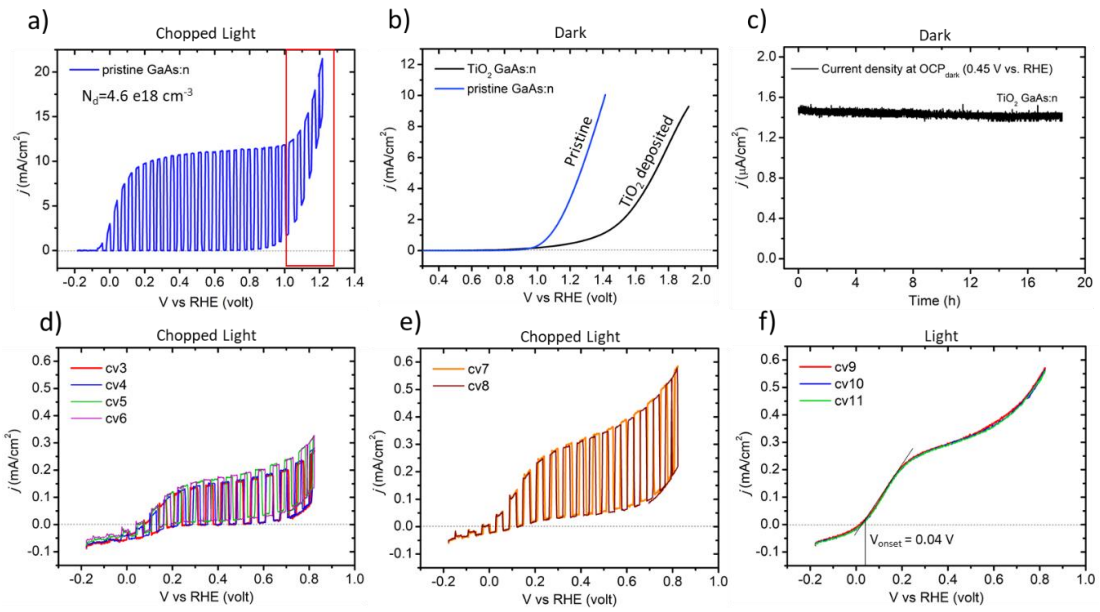

Figure 5. 21 Photoelectrochemical (PEC) characterization of the photoanodes: j-V curve of (a) pristine GaAs:n under chopped light;(b) j-V curve of TiO_2 GaAs:n and pristine GaAs:n PA in the dark ; (c) chronoamperometric stability test of TiO_2 GaAs:n PA at OCP in the dark; (d-e) j-V curves of TiO_2 GaAs:n PA under chopped light and (f) under 1ight of 1-sun illumination

This result is surprising as one could expect that electron tunneling would be avoided for GaAs:n/TiO_2 as the charge separation and transportation is supposed to be influenced by the newly formed built-in potential between GaAs:n and TiO_2. Nevertheless, a good stability is achieved at open-circuit potential (OCP) in the dark. The current density decreased slightly, staying mostly steady within 10 h at 1.5 μA/cm^2. However, photocorrosion of the GaAs:n/TiO_2 PA still remains an issue. Following the 1st and 2nd *j* – V scans, further PEC characterization was performed with the chopped light and plotted in **Figure 5. 21 (d-e)** with the photocurrent density in the y-axis (in the same scale) for different *j* – V scans. It is clearly observed that photocurrent density has evolved slightly in between the 3rd – 6th, and increased after for the 7th and 8th ones as a result of surface changes during PEC activity. From the *j*-V measurement performed under light (9th – 11th) scans, it is possible to extract the onset potential (V_{onset}) which equals to ~0.04 V vs. RHE. Taking into account the photovoltage (V_{ph}) of TiO_2 protected GaAs:n PA measured with 1-sun illumination (**Figure 5. 22**), the V_{onset} (0.04 V) is far below than the desired value for the water OER, which equals to 1.6 V vs RHE measured experimentally with Ni wire electrode (**Figure 5. 12**). Thus, the photocurrent density of TiO_2 protected GaAs:n

PA measured below 1.3 V (1.6 – $V_{ph\ (TiO2\ GaAs:n)}$) can be associated to the self-decomposition or other PEC redox reaction.

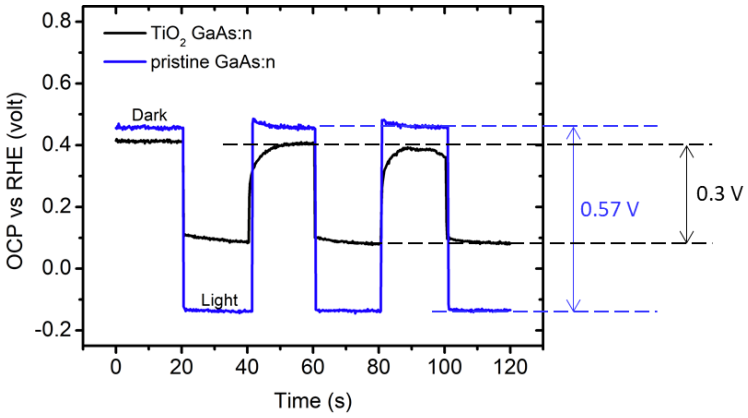

Figure 5. 22 Open-circuit potential (OCP) and photovoltage (V_{ph} = OCP_{dark} – OCP_{light}) measured for TiO_2 GaAs:n and pristine GaAs:n photoanodes.

Indeed, the surface change observed after several minutes of PEC activity under light with applied anodic bias indicates that the majority of the measured photocurrent density does not originate from the water OER, but, from the self-corrosion of the TiO_2 GaAs:n PA (**Figure 5. 23**). Self-corrosion of TiO_2 GaAs:n PA leads to the formation of the circular dots or etching pits **(Figure 5. 23 (b))** similarly to the previous samples with ALD deposited TiO_2 layer. Despite the use of standard annealing conditions, there might exist few/several micro/nano pinholes at the surface where the electrolyte may reach the bulk GaAs and initiate corrosion underneath the TiO_2 layer.

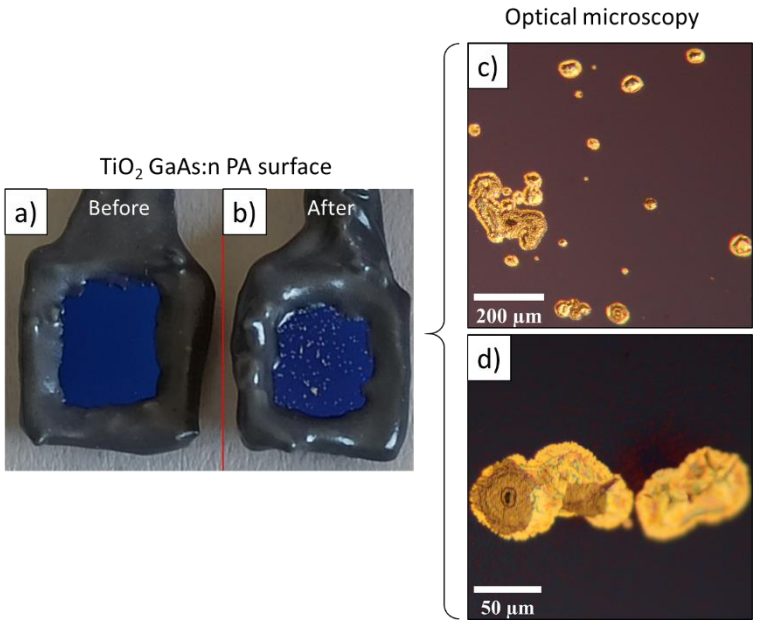

Figure 5. 23 (a) Surface of TiO_2 GaAs:n PA before and (b) after several minutes of PEC characterization. Optical microscopy images at the scale of (c) 200 µm and (d) 50 µm

5.5 Discussions and conclusions

Despite the convenient use of sputtering technique to deposit the layers of Ir and Ni, in this work we did not succeed in providing a robust protection against anodic corrosion of III-V photoanodes. Similar strategies have been used for Si and it is interesting to compare the results. In the case of Si photoanodes, the stability was demonstrated over a couple of hours when the photoanodes were coated with a thin layer of Ir-IrO_x (20 nm-thick layer). [155] The measured photocurrent density started to decrease after 10 h of activity. It is not the case for GaAs photoanodes studied in this work, where the corrosion of the GaAs starts rapidly at the surface pinholes, as one surface hole is enough for the electrolyte to reach the bulk GaAs surface and starts corrosion underneath. [128,155] It was already mentioned that once GaAs starts corroding, the corrosion products are soluble leading to the dissolution or peeling-off of the deposited metallic layer. On the contrary, the corrosion product of Si is mainly SiO_2 which is not soluble and remains at the surface as a passivation layer extending the protection efficiency of the deposited metallic layer (**Figure 5. 24**). From these preliminary studies, a number of different strategies could be used to improve the protection of III-V/Si samples. For instance, thicker metal layers could be ideal for

minimizing the surface pin-holes, however, it may lead to the pinned Fermi levels at the surface or impeded photoelectrochemical junction that can block the charge transfer. More complex metal oxides could also be considered. In any design, the parasitic metal light absorption will have to be taken into account. In any cases, the precise understanding of corrosion processes on coated III-V/Si samples will require in-depth structural and chemical investigations of the metals deposited.

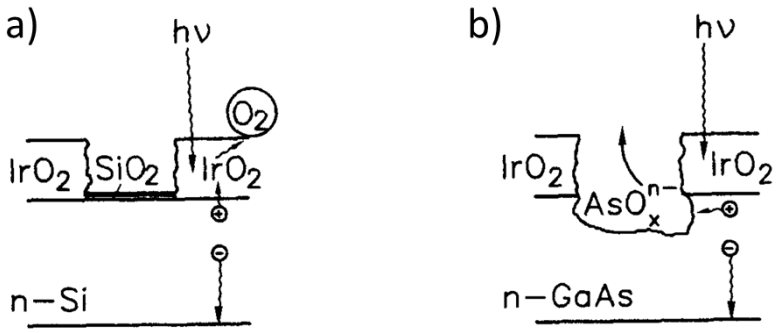

Figure 5. 24 Schematic representation of processes at the Ir/IrO_2 coated photoelectrodes during operation for (a) n-Si; (b) n-GaAs photoanodes. Adapted from [155]

Although promising perspectives are expected for the TiO_2 deposited by ALD as a protection layer due to conformal and controlled deposition, [85,119,144] the three samples studied here (CMP GaAs-Si, pristine GaAs-Si and GaAs wafer) have failed to provide a longer lifetime with robust stability in PEC water oxidation. Our results suggest that, independently of the grown material, the deposited TiO_2 cannot guarantee a 100% perfect protection. The studied TiO_2 may possess specific local structures or defects, where the electrolyte can reach the GaAs underneath. The GaAs is so reactive that one of these defects is enough to etch consequently the GaAs and kill the PA operation. It has to be noted that many contradictory reports exist in the literature about the use of TiO_2 as a protecting layer. Especially, it does exist a large variety of TiO_2 stoichiometries, defects and substructures from one experimental setup to the other. This highlights the importance of providing an in-depth understanding of the TiO_2 integration on III-V semiconductors. Especially, next steps of the work could focus on:

(i) **Pinholes:** Pinholes are crucial in the protection of III-V semiconductors with metal oxide layers, especially GaAs, where the corrosion products have a high solubility in the

electrolyte that may lead to partially or completely peel-off of the deposited protection layer. [91,156] The electrolyte may permeate to the bulk GaAs through the presence of only one surface pinhole and lead to progressive underneath corrosion of the sample. It is thus of high importance to be able to identify where the corrosion starts, and what is the relationship with some possible defects or inhomogeneities in the TiO_2.

(ii) **Annealing:** TiO_2 is the most promising and demonstrated protection layer for III-V and Si semiconductor photoelectrodes so far, and mostly deposited via ALD technique using organic precursors of Ti. Nevertheless, these precursors may dissolve when it comes into contact with the electrolyte. [145,154] A direct contact may establish between the electrolyte and bulk semiconductor photoelectrode through the tiny porosity of TiO_2 layer initiating the corrosion underneath and subsequently cracking the protective surface. Therefore, annealing of the ALD deposited TiO_2 layer plays a significant role: to remove Ti precursor ligands and transform the amorphous layer into polycrystalline anatase. It is worth to mention the importance of the annealing conditions as it may change physical properties of both TiO_2 protective layer and photoelectrode material (crystal structure, surface oxidation and intrinsic doping, etc). Thus, the incorrect annealing conditions may lead to the micro-failures or micro-cracks of the TiO_2 layer, even if the as-deposited layer was apparently pinhole-free at the beginning.

(iii) **Interfacial defects and surface states:** Generally, interfacial defects and surface states are known to act as recombination centers for the photogenerated charge carriers. [125,157,158] We may assume that, these interfacial defects and surface states might be present at the interface between GaAs and TiO_2 as any special surface treatment except rinsing it with ultrapure water and drying it with N_2 gas flow was not applied for the TiO_2-coated samples (CMP GaAs-Si, pristine GaAs-Si and commercial GaAs:n wafer). In this case, photogenerated minority carriers (holes) from the valence band may populate surface states leading to accelerated anodic corrosion at interface defects which become nucleation sites for etching pits. These etching pits become bigger and coagulate to form corrosion patterns undercutting the TiO_2 layer as corrosion progresses. 4

Conclusions and perspectives

This thesis was built up on the initial results obtained by FOTON Institute in collaboration with University College London for $GaP_{0.7}Sb_{0.3}$ photoelectrode grown on Si substrate, and extends further in collaboration with ISCR, with advanced assessment of new epitaxial III-V/Si photoanodes in comparison with commercial high-cost wafers. In particular, the concept of "band engineering" is demonstrated experimentally by showing how the optical and photoelectrochemical properties are deeply impacted, and, can be tuned by different band-lineups between the photoelectrode and the electrolyte. The main conclusions of each chapter are described as follows:

Conclusions:

In **Chapter 1**, the concept of solar energy storage in the form of H_2 fuel and its potential promises regarding the wide applicability and high energy density was presented. The research background of solar water splitting technology and the working principle of photoelectrochemical (PEC) were presented in details. Further, the physics of semiconductors and heterointerfaces (metal/semiconductor and semiconductor/ electrolyte junctions), as well as material requirements were discussed explicitly. Finally, the progresses and current challenges in the development of the state-of-the-art III-V and III-V/Si photoelectrodes were presented.

In **Chapter 2**, the experimental support of this thesis was given with the detailed description of the elaboration and physico-chemical characterizations of the III-V/Si thin-films and photoelectrodes. Molecular Beam Epitaxy (MBE) used in the growth of III-V thin films, photoelectrode preparation techniques and surface processing methods have been described. Structural, optical, photoelectrochemical characterization techniques were presented in details including working principles and the parameters used in this thesis. Technical aspects of water splitting with thermodynamical energy requirements and detailed description of the photoelectrochemical cell/setup was introduced.

In **Chapter 3**, the comparative assessment of a 1-μm thick epitaxial GaAs grown on a n-type Si substrate and a commercial GaAs wafer was realized with in-depth confrontation

of photoelectrochemical performances. Based on experimental results, a similar magnitude of light absorbtion and charge carriers generation was found for the 1-µm thick epitaxial GaAs/Si sample in comparison with the commercial GaAs wafer. The large measured photocurrent density for the III-V/Si photoanode was further analyzed relatively to the theoretical one using the absorption coefficient of the sample and the spectral photon flux density of the solar spectrum AM 1.5G. The origin of this finding was associated to the contribution of the Si substrate to the light absorption, resulting in an additional photocurrent, as demonstrated by an in-depth analysis of the incident photon-to-current conversion efficiency (IPCE) and the photocurrent density under tunable monochromatic light illumination.

In **Chapter 4**, the concept of band engineering, and its impact on photoelectrode's optical and photoelectrochemical properties were studied experimentally with $GaP_{1-x}As_x$ alloys grown epitaxially on Si substrate. A drastic improvement of quantum efficiency and high photocurrent density was observed for the alloys with large As contents. The origin of such improvement was assigned to the direct bandgap configuration with suitable energy gap to absorb efficiently the large fraction of the solar spectrum. The flat-band (V_{fb}) measurements were further carried out via Mott-Schottky characterizations to study the variation of band lineups between the photoanode and the electrolyte, and found to affect the onset potential of bandgap engineered photoanodes which is crucial as it describes the input energy in PEC water splitting.

In **Chapter 5**, the anodic corrosion of bare and surface protected photoelectrodes made of the epitaxially grown GaAs/Si and the commercial GaAs wafers were preliminary investigated in acidic and alkaline electrolytes. The two different surface protections: 1) with deposited metallic layers of iridium and nickel by sputtering technique and 2) TiO_2 deposited via atomic layer deposition technique were studied by measuring photocurrent density at applied voltage range with several consecutive scans. The protection efficiency was assessed by measuring the surface modification and elemental composition with optical microscopy, scanning electron microscopy (SEM) and energy-dispersive x-ray spectroscopy (EDX), respectively. In these preliminary studies, photoanodes were not successfully stabilized, indicating that further works are still needed to improve their protection.

Perspectives

On the one hand, the work presented in this thesis confirms the potential of III-V/Si photoelectrodes as a cost-effective solution to produce solar hydrogen with a very good efficiency, building on the large photocurrents measured, and on the ability to design at will the band structures, thanks to alloying (band engineering). This work thus opens a route toward efficient unassisted water splitting (i.e., without external applied bias). On the other hand, the presented results also indicate that a research effort still needs to be done on the protection of the photoanodes against corrosion during PEC operation.

In a short-term:

As cited in many research references, TiO_2 is the state-of-the-art protection layer for the majority of unstable photoelectrodes, including the III-V. However, in the present work, the atomic layer deposited TiO_2 layer did not succeed to efficiently protect epitaxial III-V/Si and commercial III-V wafers from the corrosion. A prior treatment of III-V/Si surfaces and optimization of ALD parameters could improve the protection of photoelectrodes. For this reason, more samples, preferably with moderate doping density have to be tested with optimization of the ALD processes and thicknesses deposited.

An effort should also be paid on the improvements of onset potentials for OER. Indeed, the photoanodes dedicated for the water OER often suffer from high onset potentials mainly due to the sluggish reaction kinetics and high rate recombinations of charges at surface states. Development and application of water OER catalysts, such as ruthenium aqua complex compounds could increase the reaction kinetics, and thus may improve the onset potential of the reaction as well as the stability of photoelectrodes. In the meantime, the application of surface passivation layers may contribute positively to reduce the charge accumulation at surface states and consecutively avoid recombinations.

In a mid-term:

Beyond the deposition of ALD TiO_2 protective layers, the alternatives for the surface protection can be developed in parallel. For instance, deposition of a transparent, robust polymer with a high stability in aqueous electrolyte could be considered. However, these polymers have a very poor conductivity and may induce a huge resistance for charge

transport. To this aim, transport channels could be designed through the polymer, using electrodeposited nickel (or iridium) with adapted technological lithography. Moreover, exploring different types of electrolytes other than 0.2 M H_2SO_4 and 1M KOH could be interesting to improve the efficiency/stability of the surface protection layers.

Long-term:

Electronic passivation of III-V/Si photoelectrodes with 2D materials could improve the stability and charge recombination. However, the surface preparation before using passivation methods is very challenging and not mature yet. The presence of a small un-passivated area could lead to the total failure of the device. Once the surface of the III-V/Si photoelectrodes are perfectly protected, the advanced photoelectrochemical characterization with intensity modulated photocurrent spectroscopy (IMPS) and electrochemical impedance spectroscopy (EIS) can be further developed to understand the physics more deeply. In addition to eutectic solution of In-Ga, different types of photoelectrode ohmic contacts could be tried and compared, respectively. Finally, the photocathodes from the similar alloy's used in thesis can be developed and co-integrated together with optimized photoanodes to demonstrate unassisted PEC water splitting device.

Appendices

A.1 Scanning Electron Microscopy

Scanning Electron Microscopy (SEM) is a powerful characterization technique, which uses a focused beam of electrons to produce high-resolution images of the sample's morphology. Moreover, the elemental composition of the analysed samples can be accessed through energy-dispersive X-ray spectroscopy (EDX) measurements. In this thesis, the SEM (ScanMat platform, Univ. Rennes 1) was used to characterize the morphology and the elemental analysis of the sample. The elemental analysis with EDS is carried out mainly to investigate the influence of the chemical treatment followed by physical polishing. Further, the EDS was used as well to check the elemental analysis before and after PEC activity for the samples with TiO_2 passivation layer.

A conventional SEM setup is presented in **Figure A. 1 (a)**. The electron gun emits the electrons that are accelerated by the anode to produce the primary electron beam. Several electromagnetic lenses are used to shape and focus the electron beam towards the sample. The specimen is fixed on a scanning stage located inside the vacuum chamber together with the detectors necessary for the data collection. As illustrated in **Figure A. 1 (b-c),** in SEM, the electron-matter interaction is mainly defined by three physical processes: (i) Back-scattering electrons (BSE) is the quasi-elastic interaction, when the primary electrons are emerging back from the sample surface. (ii) Emission of the secondary electrons (SE) – the kinetic energy of the primary electrons is partially transferred to the matter, leading to the emission of SE; (iii) Fluorescence - emission of characteristic X-rays upon transition of an electron from E_1 to E_2 subshells inside the atom. Depending on the maximum escape interaction depth illustrated relatively to SE (**Figure A. 1 (c)**) the first two processes are widely used in the morphological characterization, whereas the latter is element specific enabling the characterization of the chemical composition.

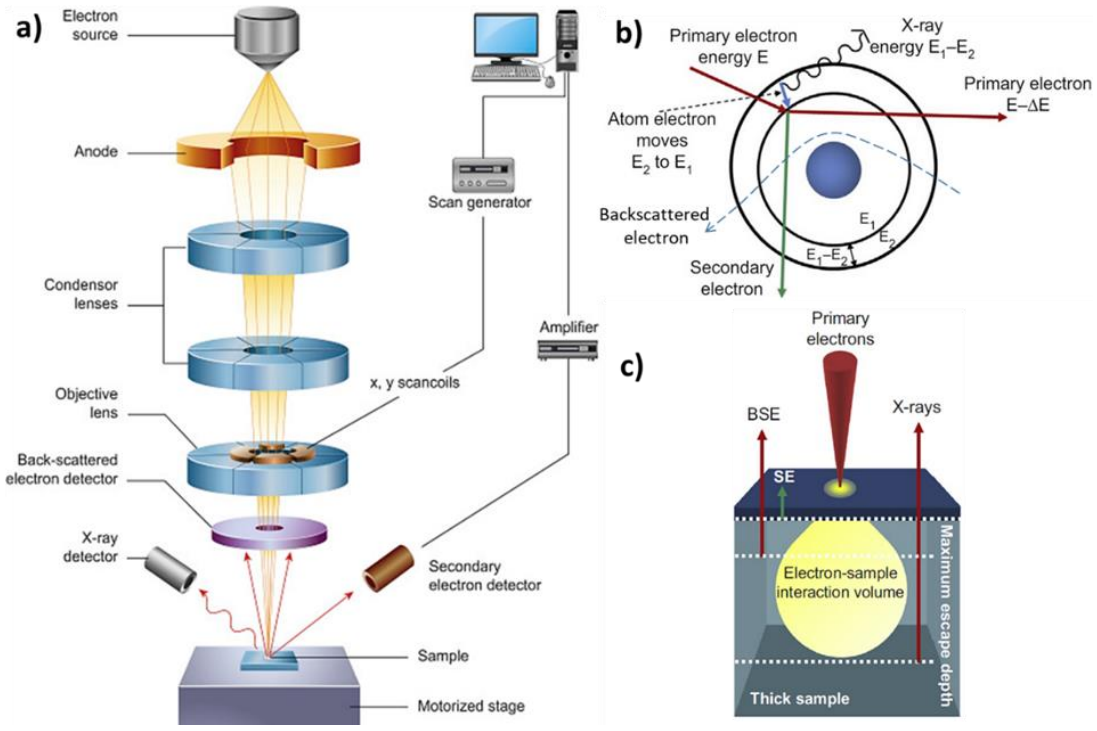

Figure A. 1 (a) Schematic representation of the conventional SEM setup, (b) the fundamentals electron-matter interactions used in SEM imaging contrast and (c) interaction of the primary electrons with the bulk of specimen [1]

A.2 Chemical mechanical polishing

Combination of the chemical and mechanical processes, together as called chemical-mechanical polishing (CMP) is used in order to smoothen the surface of the high roughness samples. In this thesis, some of the epitaxial $GaP_{1-x}As_x$ alloys were processed with CMP in order to improve the surface quality. Especially, the samples that have to be characterized with ellipsometry technique, as it requires smoother surface to avoid fitting artefacts. In addition, GaAs/Si was processed with CMP to study the influence of the surface roughness to the protecting efficiency of the TiO_2 passivation layer.

The sample is processed with CMP using an abrasive and chemical solution of H_3PO_4 or H_2O_2 (depending on the material) on the rotating disk. The sample is then

[1] https://doi.org/10.1016/B978-0-08-100040-3.00002-X

pressed towards the rotating disk that contains the abrasive and wetted consequently with the chemical solution. The schematic diagram illustrating the functional principle of CMP is shown in **Figure A. 2**

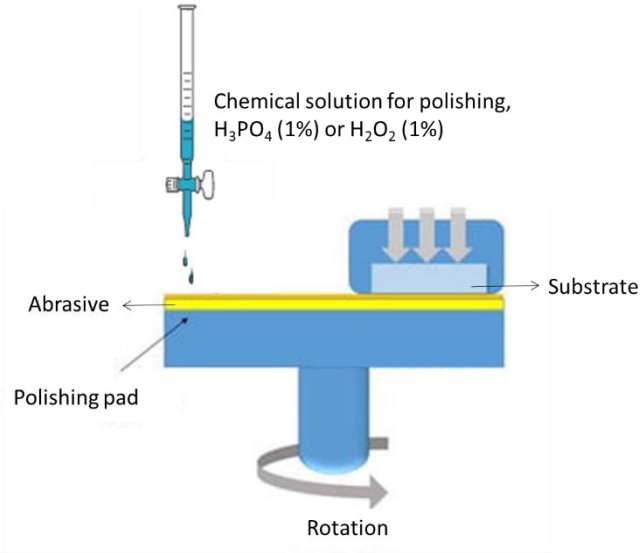

Figure A. 2 Schematic illustration of the CMP principle

A.3 Fitting & Analysis of the spectroscopic ellipsometry data

Horiba UVISEL 2 spectroscopic ellipsometer is used to characterize the optical properties, thickness and roughness of $GaP_{1-x}As_x$ alloys epitaxially grown on Si substrate. The approach is indirect, based on the fitting of the measured data with spectroscopic ellipsometry. Therefore, a fitting model suitable to the studied sample has to be developed before the interpretation of results. The main part of the fitting is developing a dispersion formula which consists of a set of two parametric equations describing the complex optical functions (n (real), k (imaginary)) and dielectric functions (ϵ_1 (real), ϵ_2 (imaginary)) as function of photon energy (E). Knowing which dispersion formula is appropriate for the studied set of samples is essential. For the semiconductors of the group III-V and their alloys, Tauc-Lorentz model is applied to better describe the absorption edge, avoiding an overestimation of ϵ_2 (imaginary) for energies lower than the bandgap. [106] The imaginary part of the Tauc-Lorentz dispersion formula (ϵ_2) is defined by inter-band optical transitions only and equals to zero for energies smaller than the optical bandgap, as shown below:

$$\begin{cases} \epsilon_2 = \frac{1}{E} \times \frac{A \times E_0 \times C \times (E - E_g)^2}{(E^2 - E_0^2)^2 + C^2 \times E^2} \; for \; E > E_g \\ \epsilon_2 = 0 \; for \; E < E_g \end{cases} \qquad \text{eq. A.1}$$

The real part (ϵ_1) of the dielectric function is derived from the expression of (ϵ_2) using the Kramers-Kronig integration. [106,107] **Figure A.3** shows an example of simplified a single peak Tauc-Lorentz model that can be used to fit direct bandgap materials. The fitting starts by adjusting the parameters described in the ϵ_2 (imaginary) part as following,

- A (in eV) is related to the absorption peak,
- C (in eV) is the broadening of the peak,
- E_g (in eV) is the optical bandgap energy,
- E_0 (in eV) is the center of the peak

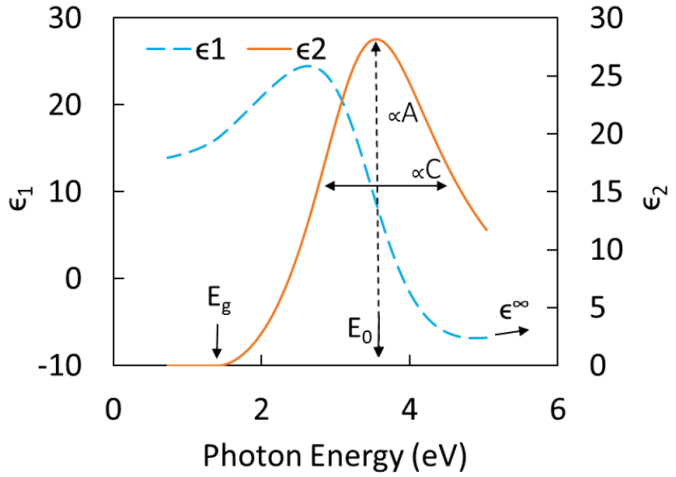

Figure A. 3 Tauc-Lorentz model. Dielectric functions ϵ_1 (real) in blue dashed-line and ϵ_2 (imaginary) in orange solid line plotted for a model material with A = 170 eV, C = 2.2 eV, Eg = 1.39 eV, E0 = 3.5 eV, and ϵ_∞ = 0.6. Produced using VASE software of Horiba UVISEL 2 spectroscopic ellipsometer.

Then, the fitting continues with the real part of the dielectric function at high frequency (ϵ_∞), accounting to all inter-band transition occurring at high energies. In the case of indirect bandgap materials that expose several absorption peaks, it is possible to include their respective contributions using additional Tauc-Lorentz oscillators in which for each absorption peak there will be added 3 additional A, C and E_0 fitting parameters.

After a successful fit of the raw data, the VASE software of Horiba UVISEL 2 spectroscopic ellipsometer converts the complex dielectric functions (ϵ_1 (real), ϵ_2 (imaginary)) into complex optical constant (n (real), k (imaginary)) in which the value of k is used to calculate absorption coefficient (α) in cm^{-1} using the following relation:

$$\alpha = \frac{4\pi k}{\lambda} \qquad \text{eq. A.2}$$

where λ is the photon wavelength.

List of publications/conferences

a) Publications and proceeding publications

- **Mekan Piriyev**, Gabriel Loget Yoan Léger, Hanh Vi Le, Lipin Chen, Antoine Létoublon, Tony Rohel, Christophe Levallois, Julie Le Pouliquen, Bruno Fabre, Nicolas Bertru, Charles Cornet. ” Photo-electrode/Electrolyte interface band engineering with alloyed III-V thin films grown on a cost-efficient Si substrate”, under preparation

- **Mekan Piriyev**, Gabriel Loget, Yoan Léger, Lipin Chen, Antoine Létoublon, Tony Rohel, Christophe Levallois, Julie Le Pouliquen, Bruno Fabre, Nicolas Bertru, Charles Cornet. “Dual bandgap operation of a GaAs/Si photoelectrode”, accepted for publication in Solar energy materials & Solar cells.

- Lipin Chen, Yoan Léger, Gabriel Loget, **Mekan Piriyev**, Imen Jadli, Sylvain Tricot, Tony Rohel, Rozen Bernard, Alexandre Beck, Jule Le-Pouliquen, Pascal Turban, Philippe Schieffer, Christophe Levallois, Bruno Fabre, Laurent Pedesseau, Jacky Even, Nicolas Bertru and Charles Cornet.” Epitaxial III-V/Si vertical heterostructures with hybrid 2D-semimetal/semiconductor ambipolar and photoactive properties”, Advanced Science. 9 (2022) 2101661.

- Dana Stanescu, **Mekan Piriyev**, Victoria Villard, Cristian Mocuta, Adrien Besson, Dris Ihiawakrim, Ovidiu Ersen, Jocelyne Leroy, Sorin G. Chiuzbaian, Adam P. Hitchcock and Stefan Stanescu. “Characterizing surface states in hematite nanorod photoanodes, both beneficial and detrimental to solar water splitting efficiency”, Journal of Materials Chemistry A, (2020) ,8, 20513-20530.

b) Invited talks

- Yoan Léger, Hanh Vi Le**, Mekan Piriyev**, Lipin Chen, Brieg Le Corre, Yiran Zhao, Gabriel Loget, Nicolas Bertru, Charles Cornet. "Transport in photoelectrochemical heterojunctions: Interface-controlled physics", 13th meeting on Nanoscience advances, C'Nano, Sept. 2022, Porquerolles, France

- Charles Cornet, Lipin Chen, **Mekan Piriyev**, Gabriel Loget, Bruno Fabre, Yoan Léger, Alexandre Beck, Anne Ponchet, Oliver Skibitzki, Pascal Turban, Philippe Schieffer, Laurent Pedesseau, Jacky Even, Nicolas Bertru. "Hétéro-épitaxie III-V/Si : contrôle des propriétés des surfaces et interfaces pour la photo-électrochimie", 35èmes Journées Surfaces et Interfaces, Jan. 2022, Dijon (virtual), France

c) Communication with international/national audience

- **Mekan Piriyev**, Hanh Vi Le, Yoan Léger, Gabriel Loget, Christophe Levallois, Tony Rohel, Antoine Létoublon, Bruno Fabre, Nicolas Bertru, Charles Cornet. "Tunable bandgap III-V alloys on a low-cost Si substrate for solar-assisted water splitting", International workshop on Emerging Solar Energy Materials & Applications (ESEMA), Jun. 2022, IGESA Porquerolles, France

- **Mekan Piriyev**, Lipin Chen, Yoan. Léger, Christophe Levallois, Tony Rohel, Antoine Létoublon, Gabriel Loget, Bruno Fabre, Nicolas Bertru, and Charles Cornet. "Engineering of energy gap and band lineups of III/V semiconductor alloys on silicon for solar hydrogen production" Journées Nationales du photovoltaïque, JNPV 2021, Dec. 2021, Dourdan, France, poster communication

- **Mekan Piriyev**, Lipin Chen, Yoan Léger, Tony Rohel, Antoine Létoublon, Gabriel Loget, Bruno Fabre, Nicolas Bertru, Charles Cornet. "Bandgap engineering of III-V semiconductors on silicon for solar hydrogen production", 5èmes Journées des Carburants Solaires, Sep. 2021, Saint Jacut de la Mer, France, poster communication

- **Mekan Piriyev**, Lipin Chen, Yoan Léger, Tony Rohel, Antoine Létoublon, Gabriel Loget, Bruno Fabre, Nicolas Bertru, Charles Cornet. “Epitaxial thin-films of GaAs(x)P(1-x)/Si photoelectrodes for solar hydrogen production”, 21st International Conference on Molecular-Beam Epitaxy (ICMBE 2018), Sep. 2021, Mexico (virtual), Mexico, poster communication

d) Selected seminars

- **Mekan Piriyev**, Nicolas Bertru, Charles Cornet. “Oral presentation in a video reunion about PhD works in front of members of three FOTON labs”, Nov. 2021, INSA Rennes

- **Mekan Piriyev**, Lipin Chen, Yoan Léger, Gabriel Loget, Bruno Fabre, Nicolas Bertru, Charles Cornet. “Oral presentation about the last achieved photoelectrochemical results on III-V alloys on Si substrate” Jul. 2021, INSA Rennes

- **Mekan Piriyev**, Nicolas Bertru, Charles Cornet. “Oral presentation for the status and progress of the PhD thesis in front of members of FOTON-OHM”, Sept. 2020, Institut Foton, Rennes.

References

[1] T.J. Jacobsson, V. Fjällström, M. Edoff, T. Edvinsson, Sustainable solar hydrogen production: from photoelectrochemical cells to PV-electrolyzers and back again, Energy Environ. Sci. 7 (2014) 2056–2070. https://doi.org/10.1039/C4EE00754A.

[2] T. Abbasi, S.A. Abbasi, 'Renewable' hydrogen: Prospects and challenges, Renewable and Sustainable Energy Reviews. 15 (2011) 3034–3040. https://doi.org/10.1016/j.rser.2011.02.026.

[3] R.J. Detz, J.N.H. Reek, B.C.C. van der Zwaan, The future of solar fuels: when could they become competitive?, Energy Environ. Sci. 11 (2018) 1653–1669. https://doi.org/10.1039/C8EE00111A.

[4] M. Grätzel, Photoelectrochemical cells, Nature. 414 (2001) 338–344. https://doi.org/10.1038/35104607.

[5] F. Decker, S. Cattarin, PHOTOELECTROCHEMICAL CELLS | Overview, in: J. Garche (Ed.), Encyclopedia of Electrochemical Power Sources, Elsevier, Amsterdam, 2009: pp. 1–9. https://doi.org/10.1016/B978-044452745-5.00035-6.

[6] Y.-H. Chiu, T.-H. Lai, M.-Y. Kuo, P.-Y. Hsieh, Y.-J. Hsu, Photoelectrochemical cells for solar hydrogen production: Challenges and opportunities, APL Materials. 7 (2019) 080901. https://doi.org/10.1063/1.5109785.

[7] H. Gerischer, On the stability of semiconductor electrodes against photodecomposition, Journal of Electroanalytical Chemistry and Interfacial Electrochemistry. 82 (1977) 133–143. https://doi.org/10.1016/S0022-0728(77)80253-2.

[8] D. Bae, B. Seger, P.C.K. Vesborg, O. Hansen, I. Chorkendorff, Strategies for stable water splitting via protected photoelectrodes, Chem. Soc. Rev. 46 (2017) 1933–1954. https://doi.org/10.1039/C6CS00918B.

[9] S. Hu, N.S. Lewis, J.W. Ager, J. Yang, J.R. McKone, N.C. Strandwitz, Thin-Film Materials for the Protection of Semiconducting Photoelectrodes in Solar-Fuel Generators, J. Phys. Chem. C. 119 (2015) 24201–24228. https://doi.org/10.1021/acs.jpcc.5b05976.

[10] J. Tournet, Y. Lee, S.K. Karuturi, H.H. Tan, C. Jagadish, III–V Semiconductor Materials for Solar Hydrogen Production: Status and Prospects, ACS Energy Lett. 5 (2020) 611–622. https://doi.org/10.1021/acsenergylett.9b02582.

[11] M.R. Shaner, H.A. Atwater, N.S. Lewis, E.W. McFarland, A comparative technoeconomic analysis of renewable hydrogen production using solar energy, Energy Environ. Sci. 9 (2016) 2354–2371. https://doi.org/10.1039/C5EE02573G.

[12] M. Bosi, C. Pelosi, The potential of III-V semiconductors as terrestrial photovoltaic devices, Progress in Photovoltaics: Research and Applications. 15 (2007) 51–68. https://doi.org/10.1002/pip.715.

[13] S. Saeidi, K.M. Awan, L. Sirbu, K. Dolgaleva, Nonlinear photonics on-a-chip in III-V semiconductors: quest for promising material candidates, Appl. Opt., AO. 56 (2017) 5532–5541. https://doi.org/10.1364/AO.56.005532.

[14] C.F. Blanco, S. Cucurachi, F. Dimroth, J.B. Guinée, W.J.G.M. Peijnenburg, M.G. Vijver, Environmental impacts of III–V/silicon photovoltaics: life cycle assessment and guidance for sustainable manufacturing, Energy Environ. Sci. 13 (2020) 4280–4290. https://doi.org/10.1039/D0EE01039A.

[15] P. Kumar, P.E.D.S. Rodriguez, V.J. Gómez, N.H. Alvi, E. Calleja, R. Nötzel, First Demonstration of Direct Growth of Planar High-In-Composition InGaN Layers on Si, Appl. Phys. Express. 6 (2013) 035501. https://doi.org/10.7567/APEX.6.035501.

[16] H. Döscher, O. Supplie, M.M. May, P. Sippel, C. Heine, A.G. Muñoz, R. Eichberger, H.-J. Lewerenz, T. Hannappel, Epitaxial III–V Films and Surfaces for Photoelectrocatalysis, ChemPhysChem. 13 (2012) 2899–2909. https://doi.org/10.1002/cphc.201200390.

[17] M. Alqahtani, S. Sathasivam, L. Chen, P. Jurczak, R. Piron, C. Levallois, A. Létoublon, Y. Léger, S. Boyer-Richard, N. Bertru, J.-M. Jancu, C. Cornet, J. Wu, I.P. Parkin, Photoelectrochemical water oxidation of GaP1−xSbx with a direct band gap of 1.65 eV for full spectrum solar energy harvesting, Sustainable Energy Fuels. 3 (2019) 1720–1729. https://doi.org/10.1039/C9SE00113A.

[18] L. Chen, Y. Léger, G. Loget, M. Piriyev, I. Jadli, S. Tricot, T. Rohel, R. Bernard, A. Beck, J. Le Pouliquen, P. Turban, P. Schieffer, C. Levallois, B. Fabre, L. Pedesseau, J. Even, N. Bertru, C. Cornet, Epitaxial III–V/Si Vertical Heterostructures with Hybrid 2D-Semimetal/Semiconductor Ambipolar and Photoactive Properties, Advanced Science. 9 (2022) 2101661. https://doi.org/10.1002/advs.202101661.

[19] P. Kumar, P. Devi, R. Jain, S.M. Shivaprasad, R.K. Sinha, G. Zhou, R. Nötzel, Quantum dot activated indium gallium nitride on silicon as photoanode for solar hydrogen generation, Commun Chem. 2 (2019) 1–7. https://doi.org/10.1038/s42004-018-0105-0.

[20] CO2 emissions – Global Energy Review 2021 – Analysis, IEA. (2022). https://www.iea.org/reports/global-energy-review-2021/co2-emissions (accessed January 25, 2022).

[21] N.S. Lewis, D.G. Nocera, Powering the planet: Chemical challenges in solar energy utilization, PNAS. 103 (2006) 15729–15735. https://doi.org/10.1073/pnas.0603395103.

[22] International Energy Agency, Renewables – Global Energy Review 2021 – Analysis, IEA. (2022). https://www.iea.org/reports/global-energy-review-2021/renewables (accessed April 19, 2022).

[23] K. Rajeshwar, R. McConnell, S. Licht, eds., Solar Hydrogen Generation: Toward a Renewable Energy Future, 2008. https://www.springer.com/gp/book/9780387728094 (accessed June 2, 2019).

[24] T. Yusaf, M. Laimon, W. Alrefae, K. Kadirgama, H.A. Dhahad, D. Ramasamy, M.K. Kamarulzaman, B. Yousif, Hydrogen Energy Demand Growth Prediction and Assessment (2021–2050) Using a System Thinking and System Dynamics Approach, Applied Sciences. 12 (2022) 781. https://doi.org/10.3390/app12020781.

[25] M. Ahmed, I. Dincer, A review on photoelectrochemical hydrogen production systems: Challenges and future directions, International Journal of Hydrogen Energy. 44 (2019) 2474–2507. https://doi.org/10.1016/j.ijhydene.2018.12.037.

[26] S. Ardo, D.F. Rivas, M.A. Modestino, V.S. Greiving, F.F. Abdi, E.A. Llado, V. Artero, Pathways to electrochemical solar-hydrogen technologies, Energy Environ. Sci. 11 (2018) 2768–2783. https://doi.org/10.1039/C7EE03639F.

[27] A. Fujishima, K. Honda, Electrochemical Photolysis of Water at a Semiconductor Electrode, Nature. 238 (1972) 37. https://doi.org/10.1038/238037a0.

[28] K. Sivula, R. van de Krol, Semiconducting materials for photoelectrochemical energy conversion, Nat Rev Mater. 1 (2016) 1–16. https://doi.org/10.1038/natrevmats.2015.10.

[29] Z. Wang, C. Li, K. Domen, Recent developments in heterogeneous photocatalysts for solar-driven overall water splitting, Chem. Soc. Rev. 48 (2019) 2109–2125. https://doi.org/10.1039/C8CS00542G.

[30] J.H. Kim, D. Hansora, P. Sharma, J.-W. Jang, J.S. Lee, Toward practical solar hydrogen production – an artificial photosynthetic leaf-to-farm challenge, Chem. Soc. Rev. 48 (2019) 1908–1971. https://doi.org/10.1039/C8CS00699G.

[31] W.-H. Cheng, M.H. Richter, M.M. May, J. Ohlmann, D. Lackner, F. Dimroth, T. Hannappel, H.A. Atwater, H.-J. Lewerenz, Monolithic Photoelectrochemical Device for Direct Water Splitting with 19% Efficiency, ACS Energy Lett. 3 (2018) 1795–1800. https://doi.org/10.1021/acsenergylett.8b00920.

[32] M. Grätzel, Photoelectrochemical cells, Nature. 414 (2001) 338. https://doi.org/10.1038/35104607.

[33] Z. Li, W. Luo, M. Zhang, J. Feng, Z. Zou, Photoelectrochemical cells for solar hydrogen production: current state of promising photoelectrodes, methods to improve their properties, and outlook, Energy Environ. Sci. 6 (2013) 347–370. https://doi.org/10.1039/C2EE22618A.

[34] S. S.M., N. Kwok K., Physics and Properties of Semiconductors—A Review, in: Physics of Semiconductor Devices, John Wiley & Sons, Ltd, 2006: pp. 5–75. https://doi.org/10.1002/9780470068328.ch1.

[35] L.M. Peter, Semiconductor Electrochemistry, in: S. Giménez, J. Bisquert (Eds.), Photoelectrochemical Solar Fuel Production: From Basic Principles to Advanced Devices, Springer International Publishing, Cham, 2016: pp. 3–40. https://doi.org/10.1007/978-3-319-29641-8_1.

[36] R.D. Lépinau, GaAs-on-Si solar cells based on nanowire arrays grown by molecular beam epitaxy, Thesis, University Paris Saclay, 2020.

[37] S. Hu, C. Xiang, S. Haussener, A.D. Berger, N.S. Lewis, An analysis of the optimal band gaps of light absorbers in integrated tandem photoelectrochemical water-splitting systems, Energy Environ. Sci. 6 (2013) 2984–2993. https://doi.org/10.1039/C3EE40453F.

[38] C.F. Klingshirn, Crystals, Lattices, Lattice Vibrations and Phonons, in: C.F. Klingshirn (Ed.), Semiconductor Optics, Springer, Berlin, Heidelberg, 2012: pp. 135–166. https://doi.org/10.1007/978-3-642-28362-8_7.

[39] D.E. Aspnes, A.A. Studna, Dielectric functions and optical parameters of Si, Ge, GaP, GaAs, GaSb, InP, InAs, and InSb from 1.5 to 6.0 eV, Phys. Rev. B. 27 (1983) 985–1009. https://doi.org/10.1103/PhysRevB.27.985.

[40] Z. Zhang, J.T. Yates, Band Bending in Semiconductors: Chemical and Physical Consequences at Surfaces and Interfaces, Chem. Rev. 112 (2012) 5520–5551. https://doi.org/10.1021/cr3000626.

[41] H. Gerischer, Solar photoelectrolysis with semiconductor electrodes, in: B.O. Seraphin (Ed.), Solar Energy Conversion: Solid-State Physics Aspects, Springer, Berlin, Heidelberg, 1979: pp. 115–172. https://doi.org/10.1007/3-540-09224-2_4.

[42] R. Memming, Solid–Liquid Interface, in: Semiconductor Electrochemistry, John Wiley & Sons, Ltd, 2015: pp. 89–125. https://doi.org/10.1002/9783527688685.ch5.

[43] M.G. Walter, E.L. Warren, J.R. McKone, S.W. Boettcher, Q. Mi, E.A. Santori, N.S. Lewis, Solar Water Splitting Cells, Chem. Rev. 110 (2010) 6446–6473. https://doi.org/10.1021/cr1002326.

[44] A. Hankin, F.E. Bedoya-Lora, J.C. Alexander, A. Regoutz, G.H. Kelsall, Flat band potential determination: avoiding the pitfalls, J. Mater. Chem. A. 7 (2019) 26162–26176. https://doi.org/10.1039/C9TA09569A.

[45] P. Babar, K. Patil, J. Mahmood, S. Kim, J.H. Kim, C.T. Yavuz, Low-overpotential overall water splitting by a cooperative interface of cobalt-iron hydroxide and iron oxyhydroxide, Cell Reports Physical Science. 3 (2022) 100762. https://doi.org/10.1016/j.xcrp.2022.100762.

[46] T. Yao, X. An, H. Han, J.Q. Chen, C. Li, Photoelectrocatalytic Materials for Solar Water Splitting, Advanced Energy Materials. 8 (2018) 1800210. https://doi.org/10.1002/aenm.201800210.

[47] M.T. Mayer, Photovoltage at semiconductor–electrolyte junctions, Current Opinion in Electrochemistry. 2 (2017) 104–110. https://doi.org/10.1016/j.coelec.2017.03.006.

[48] F. Nandjou, S. Haussener, Degradation in photoelectrochemical devices: review with an illustrative case study, J. Phys. D: Appl. Phys. 50 (2017) 124002. https://doi.org/10.1088/1361-6463/aa5b11.

[49] M. Pourbaix, Atlas of electrochemical equilibria in aqueous solutions, First English edition., Pergamon Press, Oxford, 1966.

[50] H. Gerischer, Electrolytic decomposition and photodecomposition of compound semiconductors in contact with electrolytes, Journal of Vacuum Science and Technology. 15 (1978) 1422–1428. https://doi.org/10.1116/1.569800.

[51] S. Chen, L.-W. Wang, Thermodynamic Oxidation and Reduction Potentials of Photocatalytic Semiconductors in Aqueous Solution, Chem. Mater. 24 (2012) 3659–3666. https://doi.org/10.1021/cm302533s.

[52] F. Nandjou, S. Haussener, Kinetic Competition between Water-Splitting and Photocorrosion Reactions in Photoelectrochemical Devices, ChemSusChem. 12 (2019) 1984–1994. https://doi.org/10.1002/cssc.201802558.

[53] W. Yu, J.L. Young, T.G. Deutsch, N.S. Lewis, Understanding the Stability of Etched or Platinized p-GaInP Photocathodes for Solar-Driven H2 Evolution, ACS Appl. Mater. Interfaces. 13 (2021) 57350–57361. https://doi.org/10.1021/acsami.1c18243.

[54] H.J. Lewerenz, Tailoring of Interfaces for the Photoelectrochemical Conversion of Solar Energy, in: Photoelectrochemical Materials and Energy Conversion Processes, John Wiley & Sons, Ltd, 2010: pp. 61–181. https://doi.org/10.1002/9783527633227.ch2.

[55] T. Schuler, T. Kimura, T.J. Schmidt, F.N. Büchi, Towards a generic understanding of oxygen evolution reaction kinetics in polymer electrolyte water electrolysis, Energy Environ. Sci. 13 (2020) 2153–2166. https://doi.org/10.1039/D0EE00673D.

[56] M. Bosi, C. Pelosi, The potential of III-V semiconductors as terrestrial photovoltaic devices, Progress in Photovoltaics: Research and Applications. 15 (2007) 51–68. https://doi.org/10.1002/pip.715.

[57] N.R.E.L. NREL, Best Research-Cell Efficiency Chart, Best Research-Cell Efficiency Chart. (2022). https://www.nrel.gov/pv/cell-efficiency.html (accessed May 22, 2022).

[58] O. Khaselev, J.A. Turner, A Monolithic Photovoltaic-Photoelectrochemical Device for Hydrogen Production via Water Splitting, Science. 280 (1998) 425–427. https://doi.org/10.1126/science.280.5362.425.

[59] H. Kroemer, Nobel Lecture: Quasielectric fields and band offsets: teaching electrons new tricks, Rev. Mod. Phys. 73 (2001) 783–793. https://doi.org/10.1103/RevModPhys.73.783.

[60] C.-Z. Ning, L. Dou, P. Yang, Bandgap engineering in semiconductor alloy nanomaterials with widely tunable compositions, Nat Rev Mater. 2 (2017) 1–14. https://doi.org/10.1038/natrevmats.2017.70.

[61] I. Lucci, S. Charbonnier, L. Pedesseau, M. Vallet, L. Cerutti, J.-B. Rodriguez, E. Tournié, R. Bernard, A. Létoublon, N. Bertru, A. Le Corre, S. Rennesson, F.

Semond, G. Patriarche, L. Largeau, P. Turban, A. Ponchet, C. Cornet, Universal description of III-V/Si epitaxial growth processes, Phys. Rev. Materials. 2 (2018) 060401. https://doi.org/10.1103/PhysRevMaterials.2.060401.

[62] E. Tournié, A.N. Baranov, Chapter 5 - Mid-Infrared Semiconductor Lasers: A Review, in: J.J. Coleman, A.C. Bryce, C. Jagadish (Eds.), Semiconductors and Semimetals, Elsevier, 2012: pp. 183–226. https://doi.org/10.1016/B978-0-12-391066-0.00005-8.

[63] T. Quinci, J. Kuyyalil, T.T. Nguyen, Y. Wang, S. Almosni, A. Létoublon, T. Rohel, K. Tavernier, N. Chevalier, O. Dehaese, N. Boudet, J.-F. Bérar, S. Loualiche, J. Even, N. Bertru, A. Le Corre, O. Durand, C. Cornet, Defects limitation in epitaxial GaP on bistepped Si surface using UHVCVD-MBE growth cluster, Journal of Crystal Growth. 380 (2013) 157–162. https://doi.org/10.1016/j.jcrysgro.2013.05.022.

[64] T. Nguyen Thanh, C. Robert, W. Guo, A. Létoublon, C. Cornet, G. Elias, A. Ponchet, T. Rohel, N. Bertru, A. Balocchi, O. Durand, J.S. Micha, M. Perrin, S. Loualiche, X. Marie, A. Le Corre, Structural and optical analyses of GaP/Si and (GaAsPN/GaPN)/GaP/Si nanolayers for integrated photonics on silicon, Journal of Applied Physics. 112 (2012) 053521. https://doi.org/10.1063/1.4751024.

[65] C. Cornet, S. Charbonnier, I. Lucci, L. Chen, A. Létoublon, A. Alvarez, K. Tavernier, T. Rohel, R. Bernard, J.-B. Rodriguez, L. Cerutti, E. Tournié, Y. Léger, M. Bahri, G. Patriarche, L. Largeau, A. Ponchet, P. Turban, N. Bertru, Zinc-blende group III-V/group IV epitaxy: Importance of the miscut, Phys. Rev. Materials. 4 (2020) 053401. https://doi.org/10.1103/PhysRevMaterials.4.053401.

[66] M. Rio Calvo, J.-B. Rodriguez, C. Cornet, L. Cerutti, M. Ramonda, A. Trampert, G. Patriarche, É. Tournié, Crystal Phase Control during Epitaxial Hybridization of III-V Semiconductors with Silicon, Advanced Electronic Materials. 8 (2022) 2100777. https://doi.org/10.1002/aelm.202100777.

[67] L. Chen, Optoelectronic, vibrational and transport properties of III-V/Si antiphase boundaries for photonics and solar energy harvesting, INSA Rennes, 2021.

[68] K. Sivula, F. Le Formal, M. Grätzel, Solar Water Splitting: Progress Using Hematite (α-Fe2O3) Photoelectrodes, ChemSusChem. 4 (2011) 432–449. https://doi.org/10.1002/cssc.201000416.

[69] T.W. Kim, Y. Ping, G.A. Galli, K.-S. Choi, Simultaneous enhancements in photon absorption and charge transport of bismuth vanadate photoanodes for solar water splitting, Nat Commun. 6 (2015) 8769. https://doi.org/10.1038/ncomms9769.

[70] Y. Wang, W. Tian, C. Chen, W. Xu, L. Li, Tungsten Trioxide Nanostructures for Photoelectrochemical Water Splitting: Material Engineering and Charge Carrier Dynamic Manipulation, Advanced Functional Materials. 29 (2019) 1809036. https://doi.org/10.1002/adfm.201809036.

[71] G.-L. Ke, B. Jia, H.-C. He, Y. Zhou, M. Zhou, State-of-the-art advancements of transition metal oxides as photoelectrode materials for solar water splitting, Rare Met. (2022). https://doi.org/10.1007/s12598-022-01968-5.

[72] I. Vurgaftman, J.R. Meyer, L.R. Ram-Mohan, Band parameters for III-V compound semiconductors and their alloys, Journal of Applied Physics. 89 (2001) 5815–5875. https://doi.org/10.1063/1.1368156.

[73] Y. Lin, R. Kapadia, J. Yang, M. Zheng, K. Chen, M. Hettick, X. Yin, C. Battaglia, I.D. Sharp, J.W. Ager, A. Javey, Role of TiO2 Surface Passivation on Improving the Performance of p-InP Photocathodes, J. Phys. Chem. C. 119 (2015) 2308–2313. https://doi.org/10.1021/jp5107313.

[74] N. Kornienko, N.A. Gibson, H. Zhang, S.W. Eaton, Y. Yu, S. Aloni, S.R. Leone, P. Yang, Growth and Photoelectrochemical Energy Conversion of Wurtzite Indium Phosphide Nanowire Arrays, ACS Nano. 10 (2016) 5525–5535. https://doi.org/10.1021/acsnano.6b02083.

[75] V. Bougrov, Properties of Advanced Semiconductor Materials: GaN, AIN, InN, BN, SiC, SiGe | Wiley, John Wiley & Sons, 2001.

[76] J. Kamimura, P. Bogdanoff, F.F. Abdi, J. Lähnemann, R. van de Krol, H. Riechert, L. Geelhaar, Photoelectrochemical Properties of GaN Photoanodes with Cobalt Phosphate Catalyst for Solar Water Splitting in Neutral Electrolyte, J. Phys. Chem. C. 121 (2017) 12540–12545. https://doi.org/10.1021/acs.jpcc.7b02253.

[77] H. Kim, H. Bae, S.W. Bang, S. Kim, S.H. Lee, S.-W. Ryu, J.-S. Ha, Enhanced photoelectrochemical stability of GaN photoelectrodes by Al2O3 surface passivation layer, Opt. Express, OE. 27 (2019) A206–A215. https://doi.org/10.1364/OE.27.00A206.

[78] M. Velazquez-Rizo, D. Iida, K. Ohkawa, Photoelectrochemical and crystalline properties of a GaN photoelectrode loaded with α-Fe2O3 as cocatalyst, Sci Rep. 10 (2020) 12586. https://doi.org/10.1038/s41598-020-69419-8.

[79] Y. Wang, J. Schwartz, J. Gim, R. Hovden, Z. Mi, Stable Unassisted Solar Water Splitting on Semiconductor Photocathodes Protected by Multifunctional GaN Nanostructures, ACS Energy Lett. 4 (2019) 1541–1548. https://doi.org/10.1021/acsenergylett.9b00549.

[80] C. Liu, J. Sun, J. Tang, P. Yang, Zn-Doped p-Type Gallium Phosphide Nanowire Photocathodes from a Surfactant-Free Solution Synthesis, Nano Lett. 12 (2012) 5407–5411. https://doi.org/10.1021/nl3028729.

[81] M. Malizia, B. Seger, I. Chorkendorff, P.C.K. Vesborg, Formation of a p–n heterojunction on GaP photocathodes for H2 production providing an open-circuit voltage of 710 mV, J. Mater. Chem. A. 2 (2014) 6847–6853. https://doi.org/10.1039/C4TA00752B.

[82] A. Standing, S. Assali, L. Gao, M.A. Verheijen, D. van Dam, Y. Cui, P.H.L. Notten, J.E.M. Haverkort, E.P.A.M. Bakkers, Efficient water reduction with gallium

phosphide nanowires, Nat Commun. 6 (2015) 7824. https://doi.org/10.1038/ncomms8824.

[83] S. Lee, A.R. Bielinski, E. Fahrenkrug, N.P. Dasgupta, S. Maldonado, Macroporous p-GaP Photocathodes Prepared by Anodic Etching and Atomic Layer Deposition Doping, ACS Appl. Mater. Interfaces. 8 (2016) 16178–16185. https://doi.org/10.1021/acsami.6b04825.

[84] J. Greil, S. Assali, Y. Isono, A. Belabbes, F. Bechstedt, F.O. Valega Mackenzie, A.Yu. Silov, E.P.A.M. Bakkers, J.E.M. Haverkort, Optical Properties of Strained Wurtzite Gallium Phosphide Nanowires, Nano Lett. 16 (2016) 3703–3709. https://doi.org/10.1021/acs.nanolett.6b01038.

[85] S. Hu, M.R. Shaner, J.A. Beardslee, M. Lichterman, B.S. Brunschwig, N.S. Lewis, Amorphous TiO2 coatings stabilize Si, GaAs, and GaP photoanodes for efficient water oxidation, Science. 344 (2014) 1005–1009. https://doi.org/10.1126/science.1251428.

[86] M. Alqahtani, S. Ben-Jabar, M. Ebaid, S. Sathasivam, P. Jurczak, X. Xia, A. Alromaeh, C. Blackman, Y. Qin, B. Zhang, B.S. Ooi, H. Liu, I.P. Parkin, J. Wu, Gallium Phosphide photoanode coated with TiO2 and CoOx for stable photoelectrochemical water oxidation, Opt. Express, OE. 27 (2019) A364–A371. https://doi.org/10.1364/OE.27.00A364.

[87] S. Pishgar, J.M. Strain, S. Gulati, G. Sumanasekera, G. Gupta, J.M. Spurgeon, Investigation of the photocorrosion of n-GaP photoanodes in acid with in situ UV-Vis spectroscopy, J. Mater. Chem. A. 7 (2019) 25377–25388. https://doi.org/10.1039/C9TA10106C.

[88] I.V. Bagal, M. Arunachalam, A. Waseem, A. Abdullah, S.H. Kang, S.-W. Ryu, Gallium phosphide photoanodes coated with nickel oxyhydroxide cocatalyst for stable photoelectrochemical water splitting reactions, Applied Surface Science. 558 (2021) 149873. https://doi.org/10.1016/j.apsusc.2021.149873.

[89] J.S. Blakemore, Semiconducting and other major properties of gallium arsenide, Journal of Applied Physics. 53 (1982) R123–R181. https://doi.org/10.1063/1.331665.

[90] J.L. Young, K.X. Steirer, M.J. Dzara, J.A. Turner, T.G. Deutsch, Remarkable stability of unmodified GaAs photocathodes during hydrogen evolution in acidic electrolyte, J. Mater. Chem. A. 4 (2016) 2831–2836. https://doi.org/10.1039/C5TA07648J.

[91] M.V. Lebedev, W. Calvet, T. Mayer, W. Jaegermann, Photoelectrochemical Processes at n-GaAs(100)/Aqueous HCl Electrolyte Interface: A Synchrotron Photoemission Spectroscopy Study of Emersed Electrodes, J. Phys. Chem. C. 118 (2014) 12774–12781. https://doi.org/10.1021/jp500564c.

[92] W. Yu, M.H. Richter, E. Simonoff, B.S. Brunschwig, N.S. Lewis, Investigations of the stability of GaAs for photoelectrochemical H2 evolution in acidic or alkaline

aqueous electrolytes, J. Mater. Chem. A. 9 (2021) 22958–22972. https://doi.org/10.1039/D1TA04145B.

[93] S.-M. Park, M.E. Barber, Thermodynamic stabilities of semiconductor electrodes, Journal of Electroanalytical Chemistry and Interfacial Electrochemistry. 99 (1979) 67–75. https://doi.org/10.1016/S0022-0728(79)80411-8.

[94] O. Khaselev, J.A. Turner, Electrochemical Stability of p - GaInP2 in Aqueous Electrolytes Toward Photoelectrochemical Water Splitting, J. Electrochem. Soc. 145 (1998) 3335. https://doi.org/10.1149/1.1838808.

[95] T.G. Deutsch, J.A. Turner, Semiconductor Materials for Photoelectrolysis, (2014). http://www.hydrogen.energy.gov/ pdfs/review14/pd035_deutsch_2014_o.pdf.

[96] F. Yang, A.C. Nielander, R.L. Grimm, N.S. Lewis, Photoelectrochemical Behavior of n-Type GaAs(100) Electrodes Coated by a Single Layer of Graphene, J. Phys. Chem. C. 120 (2016) 6989–6995. https://doi.org/10.1021/acs.jpcc.6b00232.

[97] C. Jiang, J. Wu, S.J.A. Moniz, D. Guo, M. Tang, Q. Jiang, S. Chen, H. Liu, A. Wang, T. Zhang, J. Tang, Stabilization of GaAs photoanodes by in situ deposition of nickel-borate surface catalysts as hole trapping sites, Sustainable Energy Fuels. 3 (2019) 814–822. https://doi.org/10.1039/C8SE00265G.

[98] D. Kang, J.L. Young, H. Lim, W.E. Klein, H. Chen, Y. Xi, B. Gai, T.G. Deutsch, J. Yoon, Printed assemblies of GaAs photoelectrodes with decoupled optical and reactive interfaces for unassisted solar water splitting, Nat Energy. 2 (2017) 1–5. https://doi.org/10.1038/nenergy.2017.43.

[99] I. Lucci, S. Charbonnier, M. Vallet, P. Turban, Y. Léger, T. Rohel, N. Bertru, A. Létoublon, J.-B. Rodriguez, L. Cerutti, E. Tournié, A. Ponchet, G. Patriarche, L. Pedesseau, C. Cornet, A Stress-Free and Textured GaP Template on Silicon for Solar Water Splitting, Advanced Functional Materials. 28 (2018) 1801585. https://doi.org/10.1002/adfm.201801585.

[100] M. Alqahtani, S. Sathasivam, F. Cui, L. Steier, X. Xia, C. Blackman, E. Kim, H. Shin, M. Benamara, Y.I. Mazur, G.J. Salamo, I.P. Parkin, H. Liu, J. Wu, Heteroepitaxy of GaP on silicon for efficient and cost-effective photoelectrochemical water splitting, J. Mater. Chem. A. 7 (2019) 8550–8558. https://doi.org/10.1039/C9TA01328H.

[101] L. Chen, M. Alqahtani, C. Levallois, A. Létoublon, J. Stervinou, R. Piron, S. Boyer-Richard, J.-M. Jancu, T. Rohel, R. Bernard, Y. Léger, N. Bertru, J. Wu, I.P. Parkin, C. Cornet, Assessment of GaPSb/Si tandem material association properties for photoelectrochemical cells, Solar Energy Materials and Solar Cells. 221 (2021) 110888. https://doi.org/10.1016/j.solmat.2020.110888.

[102] J. Wu, Y. Li, J. Kubota, K. Domen, M. Aagesen, T. Ward, A. Sanchez, R. Beanland, Y. Zhang, M. Tang, S. Hatch, A. Seeds, H. Liu, Wafer-Scale Fabrication of Self-Catalyzed 1.7 eV GaAsP Core–Shell Nanowire Photocathode on Silicon Substrates, Nano Lett. 14 (2014) 2013–2018. https://doi.org/10.1021/nl500170m.

[103] D. Wang, A. Pierre, M.G. Kibria, K. Cui, X. Han, K.H. Bevan, H. Guo, S. Paradis, A.-R. Hakima, Z. Mi, Wafer-Level Photocatalytic Water Splitting on GaN Nanowire Arrays Grown by Molecular Beam Epitaxy, Nano Lett. 11 (2011) 2353–2357. https://doi.org/10.1021/nl2006802.

[104] T. Tra Nguyen, Silicon photonics based on monolithic integration of III-V nanostructures on silicon, INSA Rennes, 2013.

[105] Oxford Instruments, Atomic Force Microscopy - An Overview from Asylum Research, Oxford Instruments. (2022). https://afm.oxinst.com/outreach/atomic-force-microscopy (accessed April 19, 2022).

[106] G.E. Jellison, Data analysis for spectroscopic ellipsometry, Thin Solid Films. 234 (1993) 416–422. https://doi.org/10.1016/0040-6090(93)90298-4.

[107] D.E. Aspnes, Spectroscopic ellipsometry — Past, present, and future, Thin Solid Films. 571 (2014) 334–344. https://doi.org/10.1016/j.tsf.2014.03.056.

[108] R. van de Krol, M. Grätzel, eds., Photoelectrochemical Hydrogen Production, Springer US, 2012. https://www.springer.com/fr/book/9781461413790 (accessed May 21, 2019).

[109] Y. Tachibana, L. Vayssieres, J.R. Durrant, Artificial photosynthesis for solar water-splitting, Nature Photonics. 6 (2012) 511–518. https://doi.org/10.1038/nphoton.2012.175.

[110] W.P. Gomes, F. Cardon, Electron energy levels in semiconductor electrochemistry, Progress in Surface Science. 12 (1982) 155–215. https://doi.org/10.1016/0079-6816(82)90002-8.

[111] T. Bak, J. Nowotny, M. Rekas, C.C. Sorrell, Photo-electrochemical hydrogen generation from water using solar energy. Materials-related aspects, International Journal of Hydrogen Energy. 27 (2002) 991–1022. https://doi.org/10.1016/S0360-3199(02)00022-8.

[112] C.G. Van de Walle, J. Neugebauer, Universal alignment of hydrogen levels in semiconductors, insulators and solutions, Nature. 423 (2003) 626–628. https://doi.org/10.1038/nature01665.

[113] D. Guyomard, Mise au Principes de base de l'électrochimie des semi-conducteurs, J. Chim. Phys. 83 (1986) 355–391. https://doi.org/10.1051/jcp/1986830355.

[114] N.R.E.L. NREL, Reference Air Mass 1.5 Spectra, (2022). https://www.nrel.gov/grid/solar-resource/spectra-am1.5.html (accessed November 16, 2021).

[115] Z. Chen, T.F. Jaramillo, T.G. Deutsch, A. Kleiman-Shwarsctein, A.J. Forman, N. Gaillard, R. Garland, K. Takanabe, C. Heske, M. Sunkara, E.W. McFarland, K. Domen, E.L. Miller, J.A. Turner, H.N. Dinh, Accelerating materials development for photoelectrochemical hydrogen production: Standards for methods, definitions,

and reporting protocols, Journal of Materials Research. 25 (2010) 3–16. https://doi.org/10.1557/JMR.2010.0020.

[116] Z. Chen, T.G. Deutsch, H.N. Dinh, K. Domen, K. Emery, A.J. Forman, N. Gaillard, R. Garland, C. Heske, T.F. Jaramillo, A. Kleiman-Shwarsctein, E. Miller, K. Takanabe, J. Turner, Experimental Considerations, in: Z. Chen, H.N. Dinh, E. Miller (Eds.), Photoelectrochemical Water Splitting: Standards, Experimental Methods, and Protocols, Springer, New York, NY, 2013: pp. 17–44. https://doi.org/10.1007/978-1-4614-8298-7_3.

[117] K. Gelderman, L. Lee, S.W. Donne, Flat-Band Potential of a Semiconductor: Using the Mott–Schottky Equation, J. Chem. Educ. 84 (2007) 685. https://doi.org/10.1021/ed084p685.

[118] A.G. Scheuermann, P.C. McIntyre, Atomic Layer Deposited Corrosion Protection: A Path to Stable and Efficient Photoelectrochemical Cells, J. Phys. Chem. Lett. 7 (2016) 2867–2878. https://doi.org/10.1021/acs.jpclett.6b00631.

[119] R. Liu, Z. Zheng, J. Spurgeon, X. Yang, Enhanced photoelectrochemical water-splitting performance of semiconductors by surface passivation layers, Energy Environ. Sci. 7 (2014) 2504–2517. https://doi.org/10.1039/C4EE00450G.

[120] C.F. Blanco, S. Cucurachi, F. Dimroth, J.B. Guinée, W.J.G.M. Peijnenburg, M.G. Vijver, Environmental impacts of III–V/silicon photovoltaics: life cycle assessment and guidance for sustainable manufacturing, Energy Environ. Sci. 13 (2020) 4280–4290. https://doi.org/10.1039/D0EE01039A.

[121] O. Supplie, M.M. May, H. Stange, C. Höhn, H.-J. Lewerenz, T. Hannappel, Materials for light-induced water splitting: In situ controlled surface preparation of GaPN epilayers grown lattice-matched on Si(100), Journal of Applied Physics. 115 (2014) 113509. https://doi.org/10.1063/1.4869121.

[122] I. Lucci, Surface and interface contributions to III-V/Si hetero-epitaxial growth : Theory and Experiments, INSA Rennes, 2019.

[123] J.-H. Yang, L. Shi, L.-W. Wang, S.-H. Wei, Non-Radiative Carrier Recombination Enhanced by Two-Level Process: A First-Principles Study, Sci Rep. 6 (2016) 21712. https://doi.org/10.1038/srep21712.

[124] H. Das, S. Sunkari, H. Naas, Classification of Killer and Non-Killer Silicon Carbide Epitaxial Defects and Accurate Prediction of Device Yield, ECS Trans. 80 (2017) 239. https://doi.org/10.1149/08007.0239ecst.

[125] J.E. Thorne, J.-W. Jang, E.Y. Liu, D. Wang, Understanding the origin of photoelectrode performance enhancement by probing surface kinetics, Chem. Sci. 7 (2016) 3347–3354. https://doi.org/10.1039/C5SC04519C.

[126] L.M. Peter, K.G.U. Wijayantha, A.A. Tahir, Kinetics of light-driven oxygen evolution at α-Fe2O3 electrodes, Faraday Discuss. 155 (2012) 309–322. https://doi.org/10.1039/C1FD00079A.

[127] L.W. Aukerman, M.F. Millea, M. McColl, Diffusion Lengths of Electrons and Holes in GaAs, Journal of Applied Physics. 38 (1967) 685–690. https://doi.org/10.1063/1.1709396.

[128] S. Pishgar, M.C. Mulvehill, S. Gulati, G.U. Sumanasekera, J.M. Spurgeon, Investigation of n-GaAs Photoanode Corrosion in Acidic Media with Various Thin Ir Cocatalyst Layers, ACS Appl. Energy Mater. 4 (2021) 10799–10809. https://doi.org/10.1021/acsaem.1c01768.

[129] A. Thakur, D. Ghosh, P. Devi, K.-H. Kim, P. Kumar, Current progress and challenges in photoelectrode materials for the production of hydrogen, Chemical Engineering Journal. 397 (2020) 125415. https://doi.org/10.1016/j.cej.2020.125415.

[130] S. Saeidi, K.M. Awan, L. Sirbu, K. Dolgaleva, Nonlinear photonics on-a-chip in III-V semiconductors: quest for promising material candidates, Appl. Opt., AO. 56 (2017) 5532–5541. https://doi.org/10.1364/AO.56.005532.

[131] S. Adachi, C.W. Tu, Physical Properties of III-V Semiconductor Compounds: InP, InAs, GaAs, GaP, InGaAs and lnGaAsP, Physics Today. 47 (1994) 99–100. https://doi.org/10.1063/1.2808406.

[132] H. Kroemer, Polar-on-nonpolar epitaxy, Journal of Crystal Growth. 81 (1987) 193–204. https://doi.org/10.1016/0022-0248(87)90391-5.

[133] O. Tejayadi, Y.L. Sun, J. Klem, R. Fischer, M.V. Klein, H. Morkoç, Effects of MBE growth conditions on carbon contamination in GaAs, Solid State Communications. 46 (1983) 251–254. https://doi.org/10.1016/0038-1098(83)90262-4.

[134] R.N. Sacks, R.A. Pastorello, Effects of hot sources on residual doping in GaAs grown by molecular beam epitaxy, Appl. Phys. Lett. 52 (1988) 996–998. https://doi.org/10.1063/1.99198.

[135] L. Chen, L. Pedesseau, Y. Léger, N. Bertru, J. Even, C. Cornet, Antiphase boundaries in III-V semiconductors: Atomic configurations, band structures and Fermi levels, (2022). https://doi.org/10.48550/arXiv.2206.01571.

[136] A. Dargys, J. Kundrotas, Handbook on physical properties of Ge, Si, GaAs and InP, Science and Encyclopedia Publishers, Vilnius, Lithuania, 1994.

[137] C. Robert, M. Perrin, C. Cornet, J. Even, J.M. Jancu, Atomistic calculations of Ga(NAsP)/GaP(N) quantum wells on silicon substrate: Band structure and optical gain, Appl. Phys. Lett. 100 (2012) 111901. https://doi.org/10.1063/1.3694028.

[138] B. Iandolo, H. Zhang, B. Wickman, I. Zorić, G. Conibeer, A. Hellman, Correlating flat band and onset potentials for solar water splitting on model hematite photoanodes, RSC Adv. 5 (2015) 61021–61030. https://doi.org/10.1039/C5RA10215D.

[139] I. Roger, M.A. Shipman, M.D. Symes, Earth-abundant catalysts for electrochemical and photoelectrochemical water splitting, Nat Rev Chem. 1 (2017) 1–13. https://doi.org/10.1038/s41570-016-0003.

[140] K.T. Fountaine, H.J. Lewerenz, H.A. Atwater, Efficiency limits for photoelectrochemical water-splitting, Nat Commun. 7 (2016) 13706. https://doi.org/10.1038/ncomms13706.

[141] C.U. Maier, M. Specht, G. Bilger, Hydrogen evolution on platinum-coated p-silicon photocathodes, International Journal of Hydrogen Energy. 21 (1996) 859–864. https://doi.org/10.1016/0360-3199(96)00023-7.

[142] J. Gu, Y. Yan, J.L. Young, K.X. Steirer, N.R. Neale, J.A. Turner, Water reduction by a p-GaInP2 photoelectrode stabilized by an amorphous TiO2 coating and a molecular cobalt catalyst, Nature Mater. 15 (2016) 456–460. https://doi.org/10.1038/nmat4511.

[143] D. Vanmaekelbergh, W.P. Gomes, F. Cardon, Studies on the n-GaAs Photoanode in Aqueous Electrolytes. 1. Behaviour of the Photocurrent in the Presence of a Stabilizing Agent, Berichte Der Bunsengesellschaft Für Physikalische Chemie. 89 (1985) 987–994. https://doi.org/10.1002/bbpc.19850890912.

[144] Y.W. Chen, J.D. Prange, S. Dühnen, Y. Park, M. Gunji, C.E.D. Chidsey, P.C. McIntyre, Atomic layer-deposited tunnel oxide stabilizes silicon photoanodes for water oxidation, Nature Mater. 10 (2011) 539–544. https://doi.org/10.1038/nmat3047.

[145] M.E. Dufond, J.-N. Chazalviel, L. Santinacci, Electrochemical Stability of n-Si Photoanodes Protected by TiO2 Thin Layers Grown by Atomic Layer Deposition, (2021). https://doi.org/10.1149/1945-7111/abeaf3.

[146] P.H.L. Notten, van de Meerakker J.E.A.M., J.J. Kelly, Etching of III-V semiconductors : an electrochemical approach, Elsevier Advanced Technology, Oxford, 1991.

[147] S. Pishgar, Ga-based III-V semiconductor photoanodes for solar fuels and novel techniques to investigate their photocorrosion, Electronic thesis, University of Louisville, 2021.

[148] Y. Pi, Y. Xu, L. Li, T. Sun, B. Huang, L. Bu, Y. Ma, Z. Hu, C.-W. Pao, X. Huang, Selective Surface Reconstruction of a Defective Iridium-Based Catalyst for High-Efficiency Water Splitting, Advanced Functional Materials. 30 (2020) 2004375. https://doi.org/10.1002/adfm.202004375.

[149] Z. Chen, X. Duan, W. Wei, S. Wang, B.-J. Ni, Iridium-based nanomaterials for electrochemical water splitting, Nano Energy. 78 (2020) 105270. https://doi.org/10.1016/j.nanoen.2020.105270.

[150] S. Cherevko, S. Geiger, O. Kasian, A. Mingers, K.J.J. Mayrhofer, Oxygen evolution activity and stability of iridium in acidic media. Part 1. – Metallic iridium,

Journal of Electroanalytical Chemistry. 773 (2016) 69–78. https://doi.org/10.1016/j.jelechem.2016.04.033.

[151] A. Singh, S.L.Y. Chang, R.K. Hocking, U. Bach, L. Spiccia, Highly active nickel oxide water oxidation catalysts deposited from molecular complexes, Energy Environ. Sci. 6 (2013) 579–586. https://doi.org/10.1039/C2EE23862D.

[152] K. Sun, F.H. Saadi, M.F. Lichterman, W.G. Hale, H.-P. Wang, X. Zhou, N.T. Plymale, S.T. Omelchenko, J.-H. He, K.M. Papadantonakis, B.S. Brunschwig, N.S. Lewis, Stable solar-driven oxidation of water by semiconducting photoanodes protected by transparent catalytic nickel oxide films, Proceedings of the National Academy of Sciences. 112 (2015) 3612–3617. https://doi.org/10.1073/pnas.1423034112.

[153] K. Oh, C. Mériadec, B. Lassalle-Kaiser, V. Dorcet, B. Fabre, S. Ababou-Girard, L. Joanny, F. Gouttefangeas, G. Loget, Elucidating the performance and unexpected stability of partially coated water-splitting silicon photoanodes, Energy Environ. Sci. 11 (2018) 2590–2599. https://doi.org/10.1039/C8EE00980E.

[154] M.E. Dufond, M.W. Diouf, C. Badie, C. Laffon, P. Parent, D. Ferry, D. Grosso, J.C.S. Kools, S.D. Elliott, L. Santinacci, Quantifying the Extent of Ligand Incorporation and the Effect on Properties of TiO2 Thin Films Grown by Atomic Layer Deposition Using an Alkoxide or an Alkylamide, Chem. Mater. 32 (2020) 1393–1407. https://doi.org/10.1021/acs.chemmater.9b03621.

[155] M. Wendt, H.-M. Kuhne, Sputtering of iridium-oxide films as protective layers for oxygen evolving photoanodes, in: Conference Record of the Twentieth IEEE Photovoltaic Specialists Conference, 1988: pp. 1656–1661 vol.2. https://doi.org/10.1109/PVSC.1988.105993.

[156] P. Buabthong, Z.P. Ifkovits, P.A. Kempler, Y. Chen, P.D. Nunez, B.S. Brunschwig, K.M. Papadantonakis, N.S. Lewis, Failure modes of protection layers produced by atomic layer deposition of amorphous TiO2 on GaAs anodes, Energy Environ. Sci. 13 (2020) 4269–4279. https://doi.org/10.1039/D0EE02032J.

[157] Y. Kuang, T. Yamada, K. Domen, Surface and Interface Engineering for Photoelectrochemical Water Oxidation, Joule. 1 (2017) 290–305. https://doi.org/10.1016/j.joule.2017.08.004.

[158] H. Wang, Y. Xia, N. Wen, Z. Shu, X. Jiao, D. Chen, Surface states regulation of sulfide-based photoanode for photoelectrochemical water splitting, Applied Catalysis B: Environmental. 300 (2022) 120717. https://doi.org/10.1016/j.apcatb.2021.120717.

DOCTORAT MATIERE BRETAGNE MOLECULES LOIRE ET MATERIAUX

INSA RENNES

Titre : Etude de photoélectrodes à couches minces épitaxiales III-V sur substrat Si pour la dissociation photoélectrochimique de l'eau

Mots clés : Ingénierie de bande, cellule photoélectrochimique, couches minces épitaxiales, semi-conducteurs III-V sur Si, photoélectrode GaAs/Si, alliages GaPAs

Résumé : La conversion de l'énergie solaire en énergie chimique sous forme de H_2 via la dissociation de l'eau présente un grand intérêt dans le cadre d'une politique énergétique zéro carbone. Dans ce contexte, le développement de photoélectrodes à haut rendement et à faible coût de fabrication reste encore difficile malgré les récents travaux dans le domaine. Les semi-conducteurs à bande interdite directe III–V apparaissent comme des candidats prometteurs, du fait de leurs propriétés optiques supérieures, en comparaison à celles des semi-conducteurs à oxyde métallique ou du silicium. Les alliages III-V permettent également de profiter du concept d'ingénierie de bande interdite permettant une grande flexibilité en vue du développement de photoélectrodes. Alors que de nombreuses études portaient jusqu'ici sur l'utilisation de substrats III-V commerciaux onéreux, le développement de ces photoélectrodes sur un substrat Si beaucoup moins cher est étudié ici. Dans ce travail, nous montrons que des films épitaxiaux III-V de 1 µm d'épaisseur développés sur un substrat Si à faible coût peuvent produire un photocourant compétitif par rapport à ceux mesurés avec des substrats III-V. En particulier, ce travail démontre que les performances optiques et photoélectro-chimiques des photoélectrodes GaAsP/Si sont profondément impactées par les variations de la bande interdite et des alignements de bande. Des tentatives préliminaires de protection contre la corrosion sont également présentées.

Title : Study of photoelectrodes with III-V epitaxial thin-films on Si substrate for photoelectro-chemical water splitting

Keywords : Band engineering, photoelectrochemical cell, epitaxial thin-films, III-V semiconductors on Si, GaAs/Si dual bandgap photoelectrode, GaPAs alloys

Abstract : Conversion of solar energy into chemical energy in the form of H_2 via water splitting is of great interest in the framework of zero-carbon energy policy. In this context, the development of high-efficiency photoelectrodes at low manufacturing cost remains still challenging despite the numerous recent researches in the field. The direct bandgap III–V semiconductors have emerged as promising candidates, as they provide a large photon-to-electron conversion rate, much higher than those of metal oxide semiconductors and traditional Si. Especially, the use of III-V alloys allows to benefit from bandgap engineering to achieve desired photoelectrodes requirements. While many research studies proposed the use of high-cost commercial III-V wafers, the development of these photoelectrodes on a low-cost Si substrate is explored here. In this work, we show that 1-µm thick epitaxial III-V films grown on a low-cost Si substrate can produce a competitive photocurrent to those measured for expensive III-V commercial wafers. Especially, we demonstrated that the optical and Photo-Electro-Chemical perfor-mances of GaAsP/Si photoelectrodes are deeply impacted by the variations of the bandgap and band-lineups. Attempts to protect the photoelectrodes against corrosion are also presented.